TEXTURE EVOLUTION IN Ti-6Al-4V

Simon James Wyatt

Imperial College London
Department of Materials

This thesis is submitted in partial fulfilment of the requirements for the degree of Doctor of Philosophy

November 2019

I declare that this thesis and the research reported in it is my own work and that the contributions of others have been acknowledged and appropriately referenced in the list of sources. Figures referenced from other works are reproduced under license from their respective copyright owners.

Simon James Wyatt

5th November 2019

Abstract

Crystallographic orientation and microstructural morphology control properties in engineering materials. Titanium alloys are used extensively in commercial turbofan aircraft engines, due to their high strength and excellent corrosion resistance. The formation of preferred crystallite orientations during manufacturing must be understood in order to maximise component lifespan and avoid failure. In this thesis, I present a methodology which generates virtual 3D microstructures representing a material, conforming to an approximation of a 2D reference surface characterised by electron backscatter diffraction (EBSD). The subsurface grains of this microstructure are instanced using statistical information taken from the map, controlling grain size and texture. The subsurface texture is controlled through optimisations of an orientation distribution function (ODF) and misorientation distribution function (MDF). The influence of this control is shown through simulating deformation within the DAMASK crystal plasticity fast Fourier transform (CP-FFT) solver, to demonstrate the effect of subsurface texture on the stress and strain partitioning on the reference surface. The textures of Ti-6Al-4V formed through hot-rolling at temperatures between 750 and 950 °C are characterised by EBSD. As this method measures spatial and orientation information describing a 2D surface the material, I investigate the mechanisms through which lattice orientations of crystallites evolve during processing. EBSD maps are segmented by preferred orientation to demonstrate the spatial distribution of texture fibres. By measuring phase composition through direct backscatter spectroscopy (DBS) and elemental composition through energy dispersive x-ray spectroscopy (EDS), I demonstrate the influence of the β-phase on the formation of texture fibres during rolling, with weak evolution of all existing texture fibres as the Ti-6Al-4V bar plastically deforms through slip. Through CP-FFT simulations of synthetic textured polycrystals in DAMASK, using the orientations of the texture fibres observed by EBSD, I simulate the texture evolution during deformation by hot rolling. Through examination of lattice rotation, slip shear rates and twinning shear rates, I demonstrate that the texture evolution resulting from plastic deformation at high temperatures is conducted entirely by crystal slip, resulting in only small lattice rotations and weak texture evolution. This is in agreement with the textures obtained through EBSD of hot-rolled Ti-6Al-4V.

Dedicated in loving memory of Natasha, Wendy, and Evelyn,
who inspired my quest for knowledge. You are my family.

Acknowledgements

I must begin by thanking my academic supervisor, Dr Ben Britton, for his unrelenting support during our four years of work together. In congratulating every success, and supporting me through every hardship, you have helped me through with wisdom, compassion, and a tireless (and occasionally, irritating,) pursuit of excellence. I am proud to call you my mentor and my friend.

My co-supervisors Prof. Fionn Dunne and Prof. David Rugg, thank you for your advice and insight into the worlds of crystal plasticity and titanium processing respectively.

The support of Rolls-Royce plc and Timet ltd is gratefully acknowledged. My academic collaborators around the world, and Prof. Philip Eisenlohr most of all; thank you for the opportunity to work with you and ask so many annoying questions.

It was my pleasure to co-supervise the research projects of Yi Qiu, Yusen Wang, Aditya Chandrasekhar and Cobi Allen. Our time together has been a two-way street and your ideas and questions have inspired many of the best thoughts I've had.

Technical wizards Ben Wood and Russell Stracey, without whose expertise I would have been lost in the lab, completely out of my depth. I'm extremely grateful to Dr Abigail Ackerman, Thomas Kwok, and all the others who rolled with me.

Dr Mahmoud Ardakani, for introducing me to the world of electron microscopy. I'm proud to say that I never broke anything on the microscopes.

Dr Saira Naeem, for encouraging me to see the bigger picture of science beyond Imperial and inspiring me to visit schools across London as a STEM ambassador. I hope we've encouraged many more children to become the first in their family to attend a university.

Vivian, Jim, Pete, Abi, Alex, Ruth, Suki, Lucy, Claire and the rest of the backscattered bandits of B301. Thanks for so many good times, the conferences and camaraderie, the characterisation and the coding. You've all helped me in so many ways and I'm privileged to be a friend of each one of you.

My parents, Chris and Sharron. Thank you for helping me become who I am today, and for raising me in a home filled with metallurgical textbooks. I keep the ones you gave me here on my desk.

Thanks to my church family at Abbey Road Baptist Church for their love, prayers and support. To God be the glory.

To Karen Buck MP, Barrie, Matt, Tim, Adam, Paul, Patricia, Margaret, Mohammed, Angela, and our many comrades in Westminster who taught me to believe in myself and to strive to change the world with every day I'm on it. I'm proud of all that we've achieved together. My macrozones are red in your honour.

And to my darling wife Tessa. Thank you for always being with me and sharing your joy when I need it most. I couldn't have done this without you. Every day I reflect on how grateful I am to love and be loved by you.

Contents

List of Figures

List of Tables

Glossary

Short Form	Interpretation
$\boldsymbol{A}_{11}, \boldsymbol{A}_{12}, \boldsymbol{A}_{22}$ etc.	Components of a rank-2 tensor $\boldsymbol{A}$
$\dot{\boldsymbol{A}}$	Rate of change of each component of tensor $\boldsymbol{A}$
$\overline{\boldsymbol{A}}$	Average value of each component of tensor $\boldsymbol{A}$
$\|\|\boldsymbol{M}\|\|$	Infinity norm of matrix $\boldsymbol{M}$, the largest element contained in it
$\boldsymbol{M}^{-1}$	Inverse of matrix $\boldsymbol{M}$
$\boldsymbol{M}^{T}$	Transpose of matrix $\boldsymbol{M}$
σ	Cauchy stress tensor
ϵ	Total strain tensor
τ	Shear stress
γ	Shear strain
$\boldsymbol{\nabla}$	Cartesian differential operator
Γ, gamma distribution	$\Gamma(\alpha) = \int_0^\infty x^{\alpha-1}\, e^{-x} dx$, One-parameter gamma distribution
% wt.	Atomic weight percentage
2D	Two-dimensional
3D	Three-dimensional
$\boldsymbol{a}, \boldsymbol{c}$	Unit cell vector basis directions
$\boldsymbol{b}$	Burgers vector
BC	Boundary condition
bcc	Body-centred cubic
BOR	Burgers orientation relationship
BVP	Boundary value problem
$\mathbf{C}$	Elasticity stiffness tensor
CCD	Charge-coupled device
CDF	Cumulative distribution function
CP	Crystal plasticity
CP-Ti	Commercially pure titanium
CP-FEA	Crystal plasticity finite element analysis
CP-FFT	Crystal plasticity fast Fourier transform analysis
CPU	Central processing unit
CRSS	Critical resolved shear stress
DAMASK	Düsseldorf advanced material simulation kit
DBS	Direct backscatter spectroscopy
Div($\boldsymbol{A}$)	Divergence of tensor $\boldsymbol{A}$
E	Young's modulus
EBSD	Electron backscatter diffraction
EBSP	Electro backscatter diffraction pattern
EDS	Energy dispersive x-ray spectroscopy
Euler angles, $[\phi_1 \; \Phi \; \phi_2]$	Orientations defined by the rotation of unit cell basis vectors, in clockwise rotations around the (Z X' Z") directions.
EVP	Elasto-viscoplastic
$\boldsymbol{F}$	Deformation gradient
FC	(Taylor) full constraints
FEA	Finite element analysis
FFT	Fast Fourier transform
FIB	Focused ion beam
GND	Geometrically necessary dislocation
hcp	Hexagonal close-packed
HEDM	High energy x-ray diffraction microscopy

Short Form	Interpretation
IPF	Inverse pole figure
LAMEL, ALAMEL	(Advanced) lamellar grain Taylor-like plasticity model
MDF	Misorientation distribution function
ND, RD, TD	Normal direction, rolling direction, transverse direction
ODF	Orientation distribution function
OPS	Colloidal silica solution
$\boldsymbol{P}$, PK	1st Piola-Kirchoff stress (material point reference frame)
PF	Pole figure
RC	(Taylor) relaxed constraints
RMS($\boldsymbol{A}$)	Root-mean-square of the components of tensor $\boldsymbol{A}$
RSS	Resolved shear stress
RVE	Representative volume element
$\boldsymbol{S}$	2nd Piola-Kirchoff stress (laboratory reference frame)
SEM	Scanning electron microscope
sgn(a)	Sign function, returns the sign of a
TCVT	Texture-controlled Voronoi tessellation
TEM	Transmission electron microscope
Ti-6Al-4V	Titanium, alloyed with 6% wt. aluminium and 4% wt. vanadium
VPSC	Viscoplastic self-consistent
XRD	x-ray diffraction
Z	Atomic number
Zr 2.5 Nb	Zirconium, alloyed with 2.5% wt. niobium

1 Introduction

1.1 Texture in titanium manufacturing processes

Titanium alloys are used in a wide range of applications, including sporting equipment and turbofan and turbojet aviation engine components, due to their high strength and corrosion resistance. Since the material is exceptionally biocompatible, it is used as jewellery and in biomedical devices such as joint replacements (Lutjering and Williams, 2007). The alloy Ti-6Al-4V is particularly widespread in its use, as its high strength allows for lightweight components such as aviation engine fan blades.

Titanium ores are extracted through the Kroll process and cast into an ingot after mixing with any other alloying elements. As columnar body-centred cubic (bcc) β grains form on the surface of Ti-6Al-4V ingots during solidification, they develop a strong $\langle 100 \rangle$ fibre texture of predominant orientations. The interior of the ingot has a weak texture of random orientations, comprising of both β grains and hexagonal close-packed (hcp) α grains (Glavicic *et al.*, 2003). The forming processes during thermomechanical processing of Ti-6Al-4V components such as forging within a hydraulic press, or rolling into a sheet within a mill, also develop the texture of the material, resulting from the plastic flow in the material (Le Biavant, Pommier and Prioul, 2002; Obasi, Birosca, Leo Prakash, *et al.*, 2012b). This can result in the formation of strongly textured regions of material with a common orientation. These are known as macrozones (Wielewski, Siviour and Petrinic, 2012), microtextured regions (Ma *et al.*, 2018), and effective structural units (Rugg, Dixon and Dunne, 2007).

The emergence of a strong texture leads to anisotropic plastic deformation, for example due the resolution of macroscopic shear stresses onto slip systems through the set of Schmid factors (Lebensohn, Sanchez and Pochettino, 1994). Therefore, the need to understand the influence of microstructure and texture during deformation motivates the computational modelling of materials through crystal plasticity. In the crystal plasticity framework, deformation is described for material points through constitutive equations, which relate local stresses and strains to material parameters and crystal orientations. Through physical or phenomenological constitutive equations, crystal slip resulting from dislocation motion upon slip planes couples deformation to the texture and microstructure.

Since anisotropic elastic and plastic deformation depends on the crystal orientations of grains and their neighbourhoods, accurate prediction of texture in materials is necessary in order to predict material performance and failure, since macrozones are known to contribute to crack initiation (Hémery *et al.*, 2019).

1.2 Motivation and aims

In this thesis I will present development of crystal plasticity methods investigating the effect of texture on plastic deformation in Ti-6Al-4V, accompanied by experimental characterisation of hot-rolled Ti-6Al-4V to examine texture evolution during thermomechanical processing.

The observation of stress and strain partitioning between the phases of martensitic steels by Diehl *et al.*, (2016) suggests that the contrast of material properties controls local stress and strain behaviour in grains. I examine the effect of subsurface texture within representative volume elements (RVEs) on a constrained reference surface through crystal plasticity simulations.

I develop textures and microstructures through hot rolling of Ti-6Al-4V, controlling the temperature and final thickness reduction to investigate the mechanisms behind the "texture flip" of macrozone grains observed by G.C. Obasi *et al.*, (2012).

Using crystal plasticity modelling, I simulate the texture development using synthetic RVEs to represent textures obtained through characterisation of rolled development to large strains, examining the mechanisms governing plastic deformation.

1.3 Thesis structure

Chapter 1 demonstrates the contextual importance of the crystallographic texture in governing the plastic deformation of titanium alloys during thermomechanical processing. It introduces the motivation and structure of this thesis.

Chapter 2 reflects on the current literature available, discussing the three topics central to this thesis. Firstly, the computational methods for modelling texture evolution are discussed, introducing the basis of crystal plasticity and comparing the relative advantages and disadvantages of modelling texture evolution using various available methods. Secondly, the plastic deformation of titanium alloys is examined, with a focus on the development of microstructures and textures. Thirdly, methods of instancing RVEs for crystal plasticity simulations are presented.

Chapter 3 describes the computational models and experimental techniques used within this work. A novel method of instancing RVEs for crystal plasticity models with controlled texture and morphology is introduced.

Chapter 4 presents the grain structures instanced through the RVE instantiation method described in chapter 3, investigating the control of surface and subsurface morphology and subsurface texture generated from a reference surface. The effect of subsurface texture on surface stress and strain partitioning during crystal plasticity fast Fourier transform (CP-FFT) simulations is demonstrated.

Chapter 5 characterises the texture and morphology of hot-rolled Ti-6Al-4V between 750 and 950 °C, to thickness reductions of 30% and 75%. Electron microscopy is used extensively to characterise the microstructure of the material, with direct backscatter spectroscopy (DBS) used to measure the phase composition of as-received Ti-6Al-4V. Electron backscatter diffraction (EBSD) is used to measure crystal orientations at material points on a 2D surface sectioned from as-received and deformed Ti-6Al-4V bars. Energy-dispersive x-ray spectroscopy (EDS) is used to measure the elemental composition in tandem with EBSD characterisation of hot-rolled material.

Chapter 6 models the texture evolution of Ti-6Al-4V during a single rolling pass using CP-FFT methods. Synthetic polycrystal structures are instanced to represent the texture of Ti-6Al-4V characterised in chapter 5. Using a constitutive equation with phenomenological parameters observed in Ti-6Al-4V at high temperature, slip and twinning behaviour is modelled, resulting in texture evolution equivalent to a single rolling pass.

Chapter 7 discusses the results presented in chapters 4, 5 and 6, in the context of the literature reviewed in chapter 2. The mechanistic basis of the "texture flip" hypothesis is examined, with the potential for texture evolution through inheritance of orientations through the Burgers orientation relationship (BOR) and deformation twinning of chief importance. The shortcomings of the rolling procedures and CP-FFT simulations are outlined and discussed. The control of subsurface texture through the RVE instantiation method is outlined, and its influence on the local stress and strain partitioning, and therefore material performance and failure, is detailed.

Chapter 8 concludes this research, summarising the key findings of the computational models and experimental techniques presented in this thesis. The results are synthesised into an understanding of plastic deformation behaviour and texture development during the hot rolling of Ti-6Al-4V, and future work to continue this research is proposed.

2 Literature review

2.1 Computational micromechanical modelling methods

2.1.1 Sachs and Taylor models

Numerical models for predicting texture development in polycrystals have existed since the beginning of the 20th century. Sachs and Taylor developed similar models for examining the coupling of plastic deformation between grains, which are each considered to be one homogeneous unit within the microstructure (Sachs, 1928, Taylor, 1938). In the Sachs "isostress" model, the total macroscopic strain is partitioned into individual grains through assuming that for each grain, shear strains are resolved solely onto the slip system with the largest Schmid factor. The Taylor "isostrain" model, conversely, partitions the total macroscopic stress by assuming each grain is subject to the same strain.

Bishop and Hill developed the Taylor method through a virtual work method, resolving the applied macroscopic force F and displacement x onto the slip directions in individual crystals arising from work increment $\mathrm{d}W$:

$$Fx = \mathrm{d}W = \tau s\, dV \tag{1}$$

Where τ is the shear stress for plastic deformation of a grain in a macroscopic direction, for slip increments s within a volume element dV. With the overall strain equal for each grain, the homogeneous stress within the individual grains can be computed based on their crystal orientation. The internal stresses of the grains are neglected by the assumption that the elastic moduli are infinitely large, limiting the deformation to plastic flow of the crystal lattice (Bishop and Hill, 1951). The Bishop-Hill model requires the assumption that all CRSS magnitudes are equal. Since the slip systems in hexagonal close packed (hcp) materials have different CRSS values due to the hexagonal symmetry of the unit cell, this model is unsuitable for modelling texture evolution in titanium alloys.

Taylor modelling of texture during cold rolling of titanium and zirconium alloys to 50% thickness reduction by Philippe *et al.*, (1995). produces good agreement with experimentally observed textures. Implementing a constitutive model to choose between available slip and twinning systems, this method departed from the Bishop-Hill model by considering the relative ratio of CRSS values for slip and twinning systems. Using the “full constraints” (FC) of the Taylor method, whether every crystallite is constrained to the same plastic strain, the grains aligned with their (0002) plane normals parallel to the normal direction (ND) preferentially deform by < c + a > pyramidal slip or by twinning, resulting in a reduction of the intensity of this texture fibre compared to the experimental result. Using a “relaxed constraint” (RC) by removing the constraint on the XZ shear strain, the < c + a > pyramidal slip and twinning activity was greatly reduced, retaining the (0002) | | ND fibre. The choice of CRSS ratios to promote < a > basal cross slip increases the intensity of the (0002) | | TD fibre, where TD represents the transverse direction (Philippe *et al.*, 1995). The FC and RC formalism used is described in (Van Houtte, 1988).

Contemporary developments using similar stress and strain homogenisation methods to evaluate texture evolution include the hierarchical approach of the Advanced “LAMEL” Monte Carlo model (Van Houtte *et al.*, 2012), which quantifies changes of orientations arising from plastic deformation in lamellae with reduced computational cost when compared to the crystal plasticity computational methods discussed in sections 2.1.3-7. The “ALAMEL” model is used to update the texture for each material point within a FEA deformation model, evaluating a virtual polycrystal of 5000 individual orthorhombic crystallites for each location, populated from the orientation distribution function of the initial material. Considering each grain boundary, the model computes the strain rates within a region of each of the two grains present at that boundary, with the constraint that the average over both regions combined should be equal to the macroscopic strain rate of that deformation increment. This coupling also allows for a relaxation of two deviatoric shear strain components acting on each region, satisfying the RC criterion.

2.1.2 Self-consistent homogenisation methods

The calculation of the elastic strain field for a single inclusion within a polycrystal by Eshelby, (1957) gives rise to self-consistent methods of modelling plastic deformation. By treating each grain as an inclusion within a homogeneous medium, the numerical description of stress and strain interactions between the inclusion and the medium are significantly reduced in complexity compared to a Taylor calculation by reducing the model to the local behaviour of each grain, but this must be computed independently for every grain. The average stress and strain rates of the grains is constrained to be consistent with the macroscopic stress and strain rates, but anisotropic deformation within each grain allows for deviation from the average, unlike the Taylor FC model (Lebensohn and Tomé, 1993).

Using the CRSS values for available slip and twinning systems in a material, a stress state with p independent components can be expressed by activity on p independent plastic deformation systems (Tomé and Kocks, 1985).

Texture in zirconium alloys has been incorporated into viscoplastic self-consistent (VPSC) modelling, calculating strains resulting from the resolved shear stresses using a model similar to the Hutchinson constitutive equation discussed in section 2.1.3 (Tomé and Christodoulou, 2000). From the experimental yield stress, Tomé and Christodoulou were able to estimate CRSS values for the slip systems in the Zr 2.5% Nb alloy.

Texture evolution of a cold-rolled sheet of Ti-6Al-4V was computed using a VPSC model by Galán-López and Verleysen, (2018), again calculating the strain rate using a Hutchinson model. After instancing the model using an ODF characterised by electron backscatter diffraction (EBSD), the observed grains were modelled as ellipses, and subjected to loading in uniaxial tension along the rolling direction. This resulted in a reorientation of the (0002) || ND fibre, which is dominant in the observed rolling texture, towards the TD and RD, the transverse and rolling directions. This arises as the result of extensive < a > prismatic and basal slip, with activity on both systems observed. Little < c + a > pyramidal slip was observed, and twinning was neglected from the model.

2.1.3 Crystal plasticity computational methods

Crystal plasticity is a theoretical framework for modelling the plastic deformation in materials through the activation of one or more crystal slip systems. It is principally concerned with computing behaviours on a microstructural lengthscale, i.e. within and between grains. The plastic strain is formally defined as the portion of the constrained equilibrium change in the Lagrange strain tensor (equation (2) in Rice, 1971), resulting from the change in internal variables describing thermodynamic rearrangement when the stress and temperature are held constant. The work done by the system must be described by explicit variables describing changes in lattice arrangement, i.e. crystal slip (Rice, 1971).

In computational models of slip behaviour, the critical resolved shear stress (CRSS) is the minimum magnitude of resolved shear stress (RSS) on a given slip system, in order to initiate slip activity. The value of the CRSS $\boldsymbol{\tau}_{crss}$ for given slip system a single crystal is the product of the macroscopic yield stress and the cosines of the angles of the crystal plane normal n and the slip direction s with the applied loading direction (1).

$$\boldsymbol{\tau}_{crss} = \boldsymbol{\sigma}_{yield} \cos(n) \cos(s) \tag{2}$$

The 'Schmid factor' $\cos(n) \cos(s)$ describes the resolution of the magnitude of the macroscopic uniaxial yield stress onto the individual slip system, and can be generalised into a tensorial form for a generic macroscopic stress state, obtaining the RSS on the slip system ξ (2), (Lebensohn, Sanchez and Pochettino, 1994):

$$\boldsymbol{\tau}_{\xi} = \boldsymbol{\sigma}_{\xi} \left(\boldsymbol{n}_{\xi} \otimes \boldsymbol{s}_{\xi}\right) \tag{3}$$

with the Schmid tensor $(\boldsymbol{n}_{\xi} \otimes \boldsymbol{s}_{\xi})$ describing the Cartesian basis vector transformation of the stress state for slip system ξ, where $\boldsymbol{n}_{\xi}$ is the slip plane normal vector and $\boldsymbol{s}_{\xi}$ is the slip direction.

Since the symmetry of the hcp unit cell is not easily described using Cartesian geometry, a "structure matrix" is used to relate the unit cell parameters with the Cartesian xyz basis directions:

$$\widehat{\mathbf{A}} = \begin{pmatrix} \boldsymbol{a}_x & 0 & 0 \\ \boldsymbol{a}_y & \boldsymbol{b}_y & 0 \\ \boldsymbol{a}_z & \boldsymbol{b}_z & c_z \end{pmatrix} = \begin{pmatrix} |\boldsymbol{a}| \dfrac{\sqrt{1 + 2\cos(\alpha)\cos(\beta) - (\cos^2(\alpha) + \cos^2(\beta) + \cos^2(\gamma))}}{\sin(\alpha)} & 0 & 0 \\ |\boldsymbol{a}| \dfrac{\cos(\gamma) - \cos(\alpha)\cos(\beta)}{\sin(\alpha)} & |\boldsymbol{b}| \sin(\alpha) & 0 \\ |\boldsymbol{a}| \cos(\beta) & |\boldsymbol{b}| \cos(\alpha) & |\boldsymbol{c}| \end{pmatrix} \tag{4}$$

With $\alpha = \beta = 90°, \gamma = 120°$, and $[\boldsymbol{a}, \boldsymbol{b}, \boldsymbol{c}]$ comprising the set of lattice parameters for a given hcp material, where $\boldsymbol{a} = \boldsymbol{b}$. The structure matrix is lower-triangular following McKie and McKie convention, with the $\boldsymbol{b}$ vector parallel to the y axis and the $\boldsymbol{c}$ vector parallel to the z axis (McKie and McKie, 1986). As a result, the c/a ratio of lattice parameters in the hcp unit cell must be known in order to compute the slip behaviour from an applied loading case. The reciprocal structure matrix is obtained for the structure matrix as the transpose of its inverse:

$$\widehat{\mathbf{A}}^{*} = \left(\widehat{\mathbf{A}}^{-1}\right)^{T} \tag{5}$$

Through projection of the macroscopic stress state onto the lattice directions, the Schmid tensor can be evaluated for the slip directions and plane normals in hcp crystals, while preserving their symmetries. This formalism underpins the computation of resolved shear stresses in micromechanical crystal plasticity modelling for hcp materials.

The deformation gradient tensor $\boldsymbol{F} = \frac{\partial \boldsymbol{X}}{\partial \boldsymbol{x}}$ describes the anisotropic deformation of a crystal through the positions of a material point in its undeformed reference configuration $\boldsymbol{X}$ and its deformed test configuration $\boldsymbol{x}$. The (3 x 3) deformation gradient tensor describes hydrostatic normal strains by its diagonal components, and deviatoric shear strains by its off-diagonal components. The deformation gradient may then be decomposed into the product of its elastic and plastic components $\boldsymbol{F} = \boldsymbol{F}_e\boldsymbol{F}_p$, where $\boldsymbol{F}_p$ is computed through a constitutive law. Through a viscoplastic model, the rate of change of the deformation gradient is given as $\dot{\boldsymbol{F}}_p, = \boldsymbol{L}_p\boldsymbol{F}_p$, with the plastic velocity gradients $\boldsymbol{L}_p$ computed as the sum of shear rates $\dot{\gamma}$ over all active slip systems (Roters, Eisenlohr, Hantcherli, *et al.*, 2010):

$$\boldsymbol{L}_p = \sum_{\xi=1}^{S} \dot{\gamma}_{\xi} \tag{6}$$

In crystal plasticity models, the shear rate on a given slip system ξ is related to the external forces through the stress or strain loading parameters by a constitutive equation. The external deformation is partitioned by the computation of this constitutive equation at each material point in the model, solving for the internal stresses and strains. An example is the phenomenological power law developed by Hutchinson (Hutchinson, 1976):

$$\dot{\gamma}_{\xi} = \dot{\gamma}_{0} \left| \frac{\boldsymbol{\tau}_{\xi,\ rss}}{\boldsymbol{\tau}_{\xi,\ crss}} \right|^{n} \operatorname{sgn}\left(\boldsymbol{\tau}_{\xi,\ rss}\right) \tag{7}$$

With the resolved shear stress computed by $\boldsymbol{\tau}_{\xi,\ rss} = \boldsymbol{S} \cdot (\boldsymbol{n}_{\xi} \otimes \boldsymbol{s}_{\xi})$ by Schmid's law, where $\boldsymbol{S}$ is the 2nd Piola-Kirchoff (PK) stress (i.e. the engineering stress in the reference frame). Strain-rate sensitivity is approximated by the exponent n, which reduces the shear strain when $\boldsymbol{\tau}_{\xi,\ rss} < \boldsymbol{\tau}_{\xi,\ crss}$, and increases the shear strain when $\boldsymbol{\tau}_{\xi,\ rss} > \boldsymbol{\tau}_{\xi,\ crss}$.

The elastic component of the deformation gradient tensor $\boldsymbol{F_e}$ also includes rigid body rotations in the generalised case, and is computed through the identity $\boldsymbol{F_e} = \boldsymbol{F}\boldsymbol{F_p^{-1}}$ enabling an efficient calculation of an updated stress $\boldsymbol{S}$ through Hooke's law.

The behaviour of the phenomenological material model described in equation (7) can be improved by implementing the hardening scheme proposed by Voce, (1955), although the extended scheme implemented in current crystal plasticity models uses a slightly different formalism (Steglich *et al.*, 2012; Upadhyay *et al.*, 2016). The CRSS for each slip system ξ is permitted to increase in magnitude from $\boldsymbol{\tau}_{\xi,\ initial}$ up to a saturation value $\boldsymbol{\tau}_{\xi,\ sat}$:

$$\boldsymbol{\tau}_{\xi,\ crss} = \boldsymbol{\tau}_{\xi,\ initial} + (\boldsymbol{\tau}_{\xi,\ sat} + h_{\xi,\ sat}\,\gamma_{\xi}) \cdot e^{\left(1-\frac{h_{\xi,\ initial}}{\boldsymbol{\tau}_{\xi,\ sat}}\right)\cdot\gamma_{\xi}} \tag{8}$$

Where γ_{ξ} is the accumulated plastic strain on the slip system, with $h_{\xi,\ initial}$ and $h_{\xi,\ sat}$ being the initial and saturation hardening rates on the slip system.

Latent hardening mechanisms estimate the increased difficulty of achieving slip based on the accumulated plastic slip on all slip systems. As with the Voce scheme, it represents a work-hardening, with progressive hardening of all the slip systems when a single system is activated. It can be represented in Hill-Mandel notation (Boyle, 2005):

$$\boldsymbol{\tau}_{\xi,\ i+1} = \boldsymbol{\tau}_{\xi,\ i} + \dot{\boldsymbol{\tau}}_{\xi,\ i} \cdot \Delta t \tag{9}$$

$$\dot{\boldsymbol{\tau}}_{\xi,\ i} = h_{\xi} \cdot |\dot{\gamma}| \tag{10}$$

Where the rate of change of the resolved shear stress $\dot{\boldsymbol{\tau}}_{\xi,\ i}$ for the specific time increment depends on the magnitude of the shear rate $\dot{\gamma}$ and the hardening coefficient h_{ξ}. The formulation of h_{ξ} is extremely complex, as it depends upon the relative increase in difficulty for all different slip families available for a given material (Boyle, 2005). I consider it to be a free parameter used to fit the curves that desired, since the model must be tuned to the hardening behaviour required. It is useful to understand the limitations of the model in its predictive capability prior to running the simulation, to prevent extrapolation of the model beyond the scope where it is numerically or physically sound.

An alternative to phenomenological approaches is the physically-based lengthscale-dependent constitutive slip model proposed by Fionn P.E. Dunne, Rugg and Walker, (2007):

$$\dot{\gamma}_{\xi} = \rho_{SSD,\ m} \cdot b^2 \cdot \omega \cdot e^{\frac{-\Delta F}{kT}} \cdot \sinh\left(\frac{(\boldsymbol{\tau}_{\xi,\ rss} - \boldsymbol{\tau}_{\xi,\ crss} - x_{\xi})\Delta \mathrm{V}}{kT}\right) \tag{11}$$

This relation can be derived from the Gibbs energy formulation of dislocation slip through thermal activation events with Boltzmann factor of $e^{\frac{-\Delta F}{kT}}$, occurring with frequency ω (Gibbs, 1969). The model relates the shear on slip systems to the thermal motion of mobile statistically stored dislocations (SSDs), denoted by $\rho_{SSD,\ m}$. The activation volume is defined as $\Delta \mathrm{V} = \frac{b^2}{\sqrt{\rho_{GND}}}$, where ρ_{GND} is the density of geometrically necessary dislocations (GNDs) describing the lattice curvature in the material. GNDs are a measurable quantity, which allows this model to make physical predictions. The hardening term x_{ξ} analogously increases the CRSS through "back stresses" produced from the interaction of mobile dislocations with static dislocations, which increases the forces required to overcome these interactions as ρ_{GND} increases. This mechanism is known as "forest hardening" (Motz *et al.*, 2008).

The choice of constitutive model evaluated in a crystal plasticity model defines what physics can be captured by the simulation. The predictions of material behaviour and performance made through simulations should be considered with the purpose of their constitutive model in mind. In VPSC modelling of texture evolution in the magnesium alloy AZ31, Steglich *et al.*, (2012) have used a phenomenological model in order to compare the preference of available deformation modes. The same model has been used within FEA frameworks to evaluate lattice strain evolution under biaxial loading conditions (Upadhyay *et al.*, 2016), and for crystal plasticity simulations of the breakup of macrozones in titanium during uniaxial compression (Ma *et al.*, 2018). The development of a finite-strain elasto-viscoplastic FFT method which will be explored in section 2.1.6 began using this phenomenological model (Eisenlohr *et al.*, 2013). The endurance of the Hutchinson phenomenological constitutive equation and the Voce hardening scheme result in an advantage for any computational work which uses it, as there is a body of literature for comparison, and their characteristics are well-understood.

2.1.4 Finite element analysis

The constitutive model used in crystal plasticity must be evaluated within a numerical framework that evaluates the time-dependent differential equation for each material point within the model. The technique of finite element analysis (FEA) is an established technique in micromechanical modelling, which has been developed during the twentieth century (Courant, 1943; Zienkiewicz and Cheung, 1967; Peirce, Asaro and Needleman, 1982; Dunne, Rugg and Walker, 2007; Roters, Eisenlohr, Bieler, *et al.*, 2010). A versatile numerical method for computing partial differential equations, FEA is not explicitly connected to any physics and has applications beyond micromechanics, such as the propagation of vibrations within solids (Courant, 1943).

Solutions for deformation through an applied boundary condition are obtained using finite elements by approximating the system through ordinary differential equations, solving for the unknown quantities of the constitutive equation at each node for each element. Crystal plasticity FEA methods are constrained by requirement of compatibility of displacement at each node (Roters, Eisenlohr, Bieler, *et al.*, 2010). While the numerical methods used for solving the differential equations are varied (e.g. Euler's method, Runge-Kutta, or Adams-Moulton multi-step methods), there exist several commercially available software packages for solving finite-element problems, including Abaqus, Autodesk and Marc.

For a full derivation of the FEA formalism, see section 4.2 of (Dunne and Petrinic, 2005) and section 4.3 of (Quey, Dawson and Barbe, 2011). The discretisation of the global fields requires a choice of interpolation functions into a "mesh" of elements through shaped interpolation functions. This allows the simulation to vary in resolution around certain microstructural features within the model, where the field values calculated are important to the constitutive model, or the material performance problem under investigation, such as the stress and strain within a notched four-point bending simulation to investigate crack initiation (Figure 1, Sweeney *et al.*, 2013). The process of meshing can be time-consuming, both through the computational cost of calculating the interpolation functions, and through user action while defining them.

The process of meshing can be mitigated by using pre-processing tools such as Neper (Quey, Dawson and Barbe, 2011) to instance a representative volume element (RVE), generating a 3D microstructure through instantiation methods such as Voronoi or Laguerre tessellation (section 2.3.3, page 49) to represent a characterised polycrystal. At large strains, Neper can be used to re-mesh the finite element grid, ensuring that the simulation accurately describes the morphology. With integration into the FEpX FEA solver (Dawson and Boyce, 2015), Neper offers a convenient software package for FEA modelling, with the capability for distributed computing across a cluster of CPU cores.

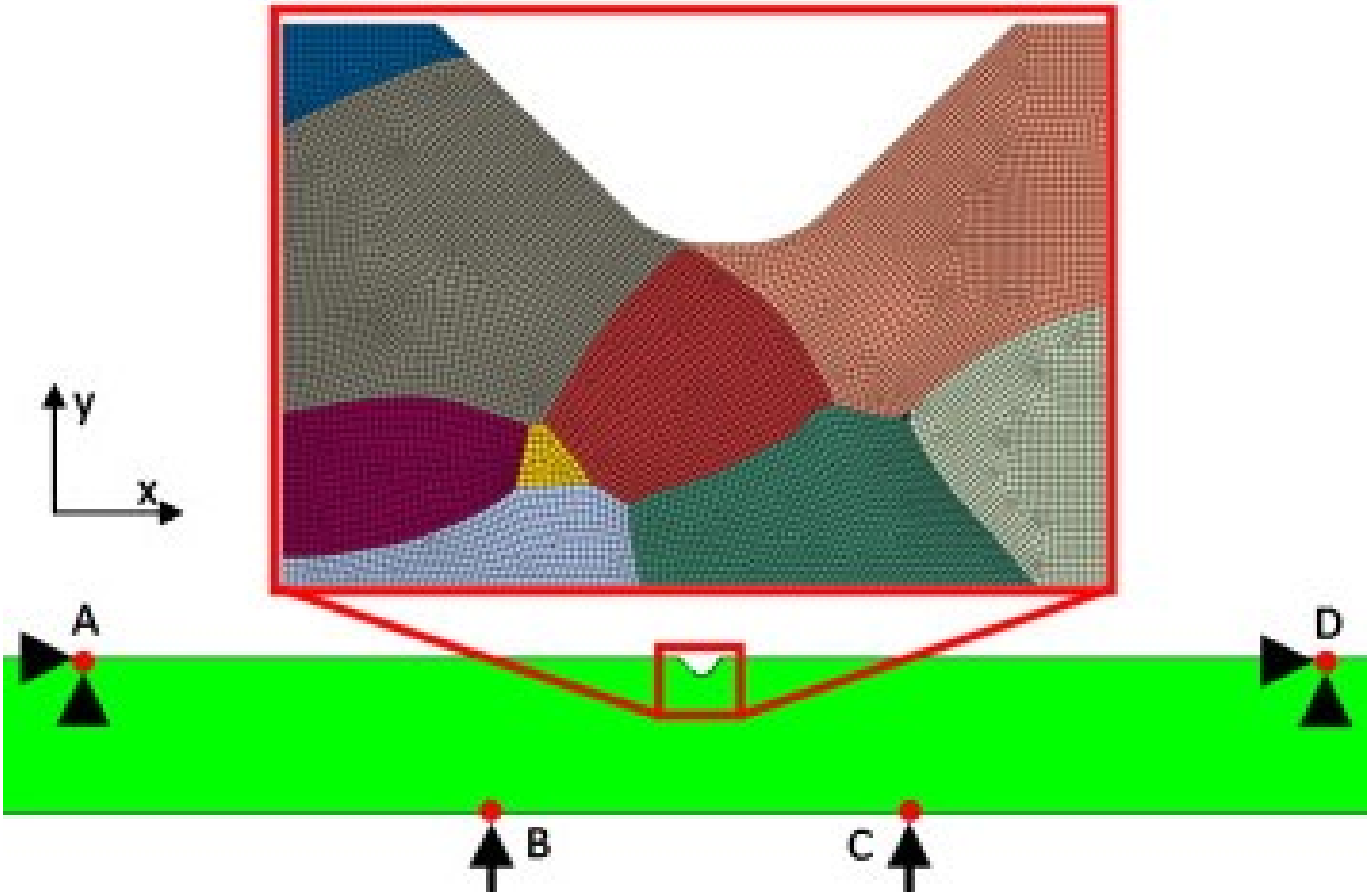

Figure 1: FEA mesh of grains in a notched four-point bending simulation. The finite element mesh has been selected to increase the resolution around the notch and at the grain boundaries, while reducing the resolution of large grain interiors. (Adapted from Sweeney et al., 2013 ©)

2.1.5 Crystal plasticity FFT methods

An alternative to FEA, a fast Fourier-transform (FFT) method was originally proposed by Moulinec and Suquet for computing the elastic and inelastic behaviour of composites (Moulinec and Suquet, 1998). This original model was advanced upon to include a viscoplastic model of non-linear shear, with the differential strain response computed through Green's function by an augmented Lagrangian method (Michel, Moulinec and Suquet, 2001). Large regions of interest can be modelled using CP-FFT methods, in order to evaluate strain localisation and texture evolution in polycrystals, evaluating a constitutive equation at each material point within the simulation, similar to the FEA method (Lebensohn, 2001).

The advantage of CP-FFT methods lies in the computational efficiency of solving the boundary-value problems of the constitutive equation within the Fourier domain. The algorithms to solve the boundary value problem formed by the differential strain response are computationally efficient compared to FEA methods, due to a reduction of the number of degrees of freedom through the periodic convolution with Green's function. As this requires a rectilinear voxelization of the integration points of the domain, the computationally expensive meshing process is also eliminated. This can result in the solution of equivalent crystal plasticity problems in significantly shorter durations (Prakash and Lebensohn, 2009; Liu *et al.*, 2010; Eisenlohr *et al.*, 2013). This improvement in computational speed per-element allows for the simulation of much more computationally intensive problems with a greater number of elements with CP-FFT models, than could be achieved through CP-FEA.

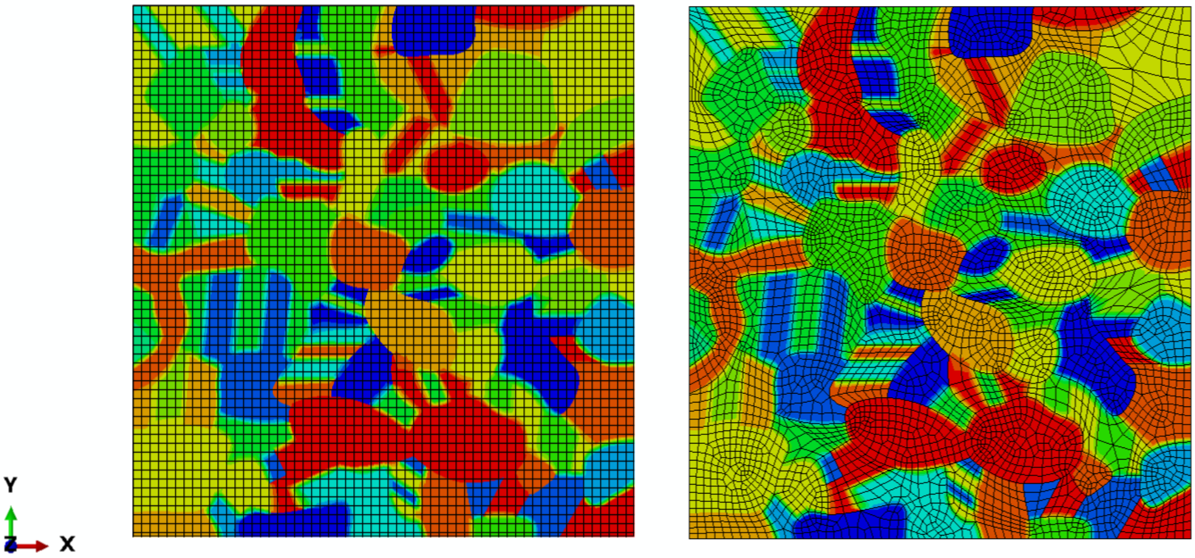

Figure 2: Comparison of a 64 x 64 element Fourier grid and finite element mesh for the same microstructure. The shape functions of the mesh demonstrate the difference in microstructural information which would be computed for the same loading conditions and constitutive equation (Zheng, 2017).

The onset of plastic slip was modelled in macrozones through a CP-FFT framework developed by (Hémery *et al.*, 2019). The instancing of a synthetic 3D microstructure allows for a comparison of plastic deformation in macrozones with other primary-α grains. Following uniaxial tension to 2% strain in displacement-controlled loading, regions of high local stress and strain were observed within macrozones, with a large stress gradient at the interface of the macrozones and primary-α. This is a potential cause of crack initiation in titanium alloys.

Texture evolution of the AZ31 magnesium alloy following deformation through rolling has been observed experimentally and modelled through CP-FFT simulations, during uniaxial loading in tension along RD, or compression along either RD or ND to 10% strain (Paramatmuni and Kanjarla, 2019). The initial texture was populated from the ODF of an experimentally characterised rolled sheet. Modelling slip using the Hutchinson constitutive equation (equation 7) and twinning as a pseudo-slip, the nucleation of T1 tension twins during uniaxial RD tension leads to a characteristic reorientation of grains by 86°, producing a fibre of grains with their (0002) plane aligned parallel to the RD which is not seen in textures characterised after experimental deformation of the material. In uniaxial RD compression, $< a >$ basal slip is initially the most active deformation mode at the onset of plasticity, but T1 twinning becomes the dominant mode of plastic deformation after 0.5% strain, resulting in a strong (0002) || TD fibre. For the uniaxial compression along ND, the (0002) pole figure saw a strengthening of the (0002) || ND fibre in both experimental and computational characterisation, with $< c + a >$ pyramidal slip being the only favourable deformation system.

One important caveat to the performance of CP-FFT methods is that the resolution of the Fourier grid and a finite element mesh are not directly equivalent. As the Fourier grid must be rectilinear, the finite element mesh can be selected to improve the resolution at grain boundaries and around triple junctions, with a corresponding lower resolution in other regions.

The CP-FFT method imposes a periodicity of the boundary conditions through the convolution of strain increments with Green's function. Consequently, the RVE used in a CP-FFT simulation could be considered as repeating in all directions (Lebensohn, 2001). If the boundary of the RVE represents a highly heterogeneous microstructure, the stress and strain fields may interact spuriously across it. This is one of the most serious disadvantages of the CP-FFT method.

2.1.6 The DAMASK FFT method

The Düsseldorf Advanced Materials Simulation Kit (DAMASK, http://damask.mpie.de) is an open-source hierarchical framework which combines material pre- and post-processing routines with a crystal plasticity frontend which can be coupled to several commercial FEA solvers. Alternatively, DAMASK can implement constitutive material-point models through its own CP-FFT solver (Roters *et al.*, 2012). The hierarchical nature of DAMASK's crystal plasticity model allows for customisation of crystallite-level homogenisation schemes and constitutive equations.

The spectral method uses the efficient FFTW libraries to compute the PK stresses and deformation gradients in the Fourier domain, implementing a constitutive equation at each material point. This is computationally inexpensive compared to implementations of FEA (Eisenlohr *et al.*, 2013). The boundary-value problems are solved after a minimum number of iterations, when the divergence of the first PK stress (equation 12) is minimised below a specified tolerance, indicating that the solver has reached an equilibrium. A residual representing satisfaction of the applied boundary conditions (equation 13) is also minimised, as a criterion demonstrating compatibility and consistency of the deformation gradient under the specified loading conditions.

$$\text{Divergence error} = \frac{\text{RMS}\big(\text{Div}(\boldsymbol{P})\big)}{\|\overline{\boldsymbol{P}}\|} \tag{12}$$

$$\text{Boundary condition error} = \left\|\dot{\boldsymbol{F}}_{BC}(\overline{\boldsymbol{P}} - \boldsymbol{P}_{\boldsymbol{BC}})\right\| \tag{13}$$

Parseval's theorem, which states that the integral of the square of a function is equal to the integral of the square of its Fourier transform, is used to calculate the divergence of the PK stress, as this is computationally cheaper than calculating it in real space (Woan, 2000). A full implementation of the numerical model used in the DAMASK spectral solver is detailed in (Roters *et al.*, 2019).

Using the Hutchinson phenomenological power law described in equation (7) as a constitutive model, Eisenlohr *et al.* (2013). compared the computational performance of the commercial FEA package MSC.Marc with DAMASK's CP-FFT spectral solver, for grids of 16^3, 32^3, and 64^3 finite elements or Fourier points. Additional models with 128^3 and 256^3 Fourier points were examined, to demonstrate an improved resolution of simulations made possible due to the reduced computational cost. Periodic boundary conditions were imposed upon the FEA model by connecting the nodes on opposite faces of the geometry.

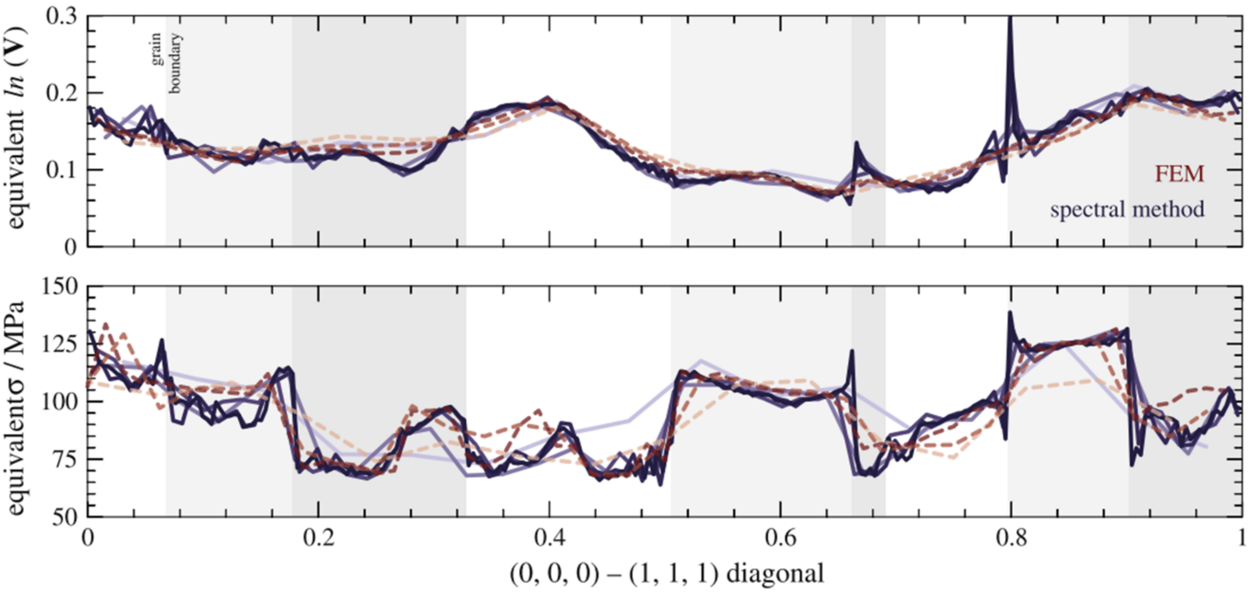

Figure 3: Local Von Mises stress (σ) and strain (V) in crystal plasticity FEA and FFT models along the [000] to [111] diagonal, at a macroscopic applied strain of 20%. Red indicates FEA modelling, blue indicates FFT modelling, with darker colours indicating a greater number of material points in the model. (Adapted from Eisenlohr et al., 2013 ©)

An equivalence of the macroscopic stress and strain behaviour is seen up to 40% applied strain following deformation in uniaxial tension (Figure 1 of Eisenlohr *et al.*, 2013). However, the local stress and strain responses of the microstructure vary significantly at the grain boundaries in the CP-FFT model (Figure 3). This is caused due to the orientation contrast introducing artifacts into the periodic stress and strain functions in the Fourier domain.

The computation time for the two methods was compared for a series of convergence tolerances (Figure 4). For equal resolution and tolerance, the FFT solver is approximately an order of magnitude faster than the FEA method. While this demonstrates the potential for increased computation speed, the resolution of a of the finite element mesh is not directly equivalent to the Fourier grid (Figure 2). As a mesh of an equal number of elements offers superior resolution of local material behaviour at grain boundaries, the CP-FFT method is only guaranteed to offer an order of magnitude improvement in performance for simulations of texture without reproduction of morphology. For fairness when simulating morphology, it is my opinion that doubling the resolution of the Fourier grid is necessary. Considering the computation times presented in Figure 4 this results in a more modest, yet consistent, reduction in computational cost.

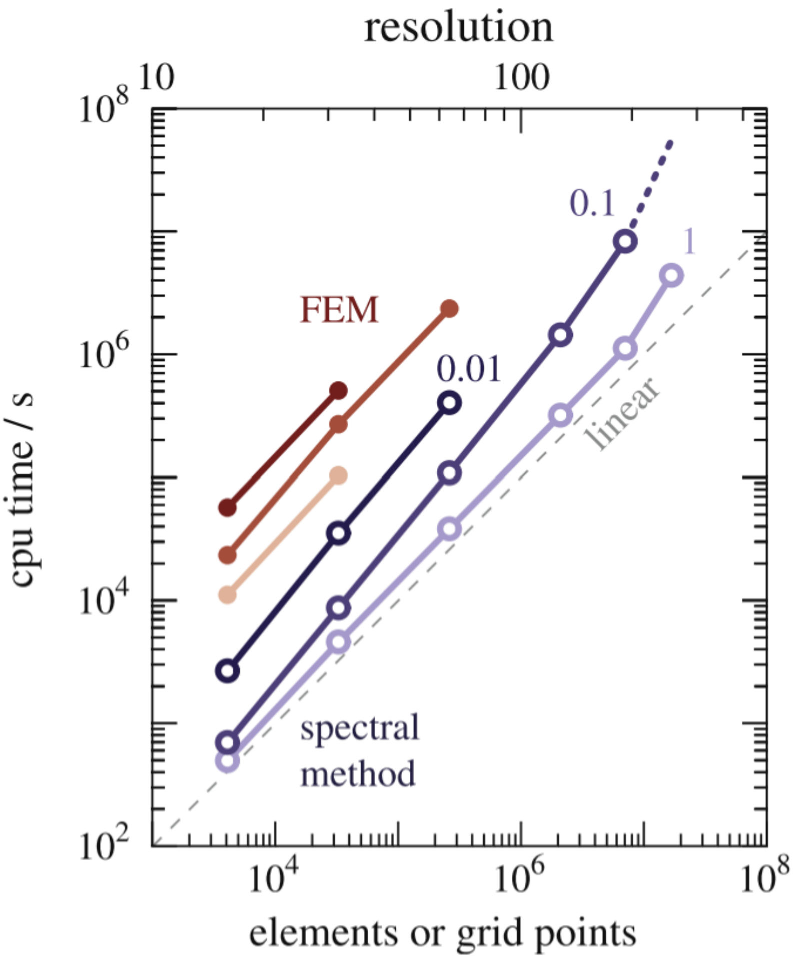

Figure 4: Computation time of FEA (red) and FFT (blue) simulations, using the same constitutive equation and boundary conditions, for a variety of element/grid resolutions. Darker colour indicates lower convergence tolerance. (Eisenlohr et al., 2013 ©)

2.1.7 Summary

A multitude of computational methods are used to model texture evolution, which both physical and phenomenological constitutive models used in crystal plasticity models, in addition to Taylor relaxed constraint and VPSC models. Hardening parameters are frequently calculated by fitting to experimental data (Leo Prakash *et al.*, 2015), although their uniqueness and strain path dependence is rarely explored.

The advantages and disadvantages of these models is found in Table 1. Given the advantages of CP-FEA methods for solving physically based problems, its extensive use in contemporary deformation mechanics is justified. CP-FFT methods offer comparable features in principle, with the possibility of a significant decrease in computational cost under specific circumstances. The disadvantage of being unable to select a polygonal mesh around microstructural features can be negated by increasing the density of Fourier-points in the domain, ensuring accurate computation of the material response. CP-FFT methods can also be used for the analysis of two-phase materials through DAMASK's material-point description of material properties.

Advantages	Taylor RC	VPSC	CP-FEA	CP-FFT
Computationally cheap?	✓	✓	✗	✓
Sub-grain resolution?	✗	✗	✓	✓
Capability of modelling large strains?	✓	✓	With remeshing	✓
Capability of modelling multi-phase materials?	✗	✗	✓	✓
Lengthscale-dependent constitutive equations?	✗	✓	✓	✓
Capability of modelling twinning?	✗	✓	✓	✓
Capability of modelling texture evolution?	✓	✓	✓	✓
Capability of directly instancing a polycrystal microstructure?	✗	✗	✓	✓
Tailored polygonal mesh of integration points for regions of interest?	N/A	N/A	✓	✗
Ensuring compatibility and equilibrium of deformation?	✗	✗	✓	✓

Table 1: Comparison of the advantages of computational micromechanical modelling methods reviewed in this chapter.

2.2 Plastic deformation and texture formation in titanium

2.2.1 Crystal structure and dual-phase behaviour during processing

Commercially pure titanium (CP-Ti) exhibits a two-phase crystal structure, with a stable hexagonal close-packed (hcp) α-phase at room temperature, and a stable body-centred cubic (bcc) β-phase above a transus temperature of 882 °C. This transus can be altered by the presence of interstitial or substitutional alloying elements, with α-phase stabilisers raising the transus temperature locally within the material, and β-phase stabilisers reducing the transus temperature (figure 1, Lutjering and Williams, 2007).

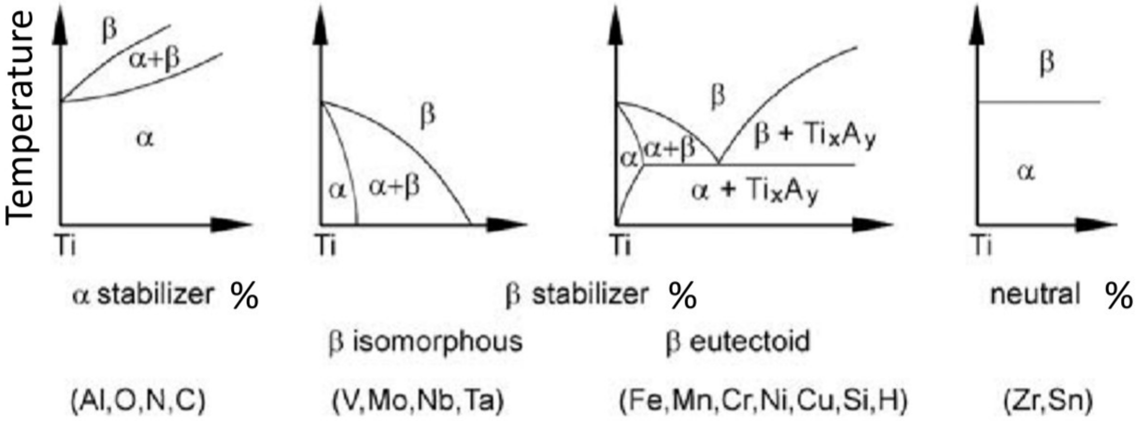

Figure 5: Effects of alloying elements on the phase composition in titanium alloys (Lutjering and Williams, 2007, pp 24 ©)

The combination of alloying 6% wt. aluminium and 4% wt. vanadium in Ti-6Al-4V produces an α + β -phase structure with metastable β at room temperature (Kolli and Devaraj, 2018), with a β-transus of 985-1005 °C in commercially available Ti-6Al-4V (Timet UK Ltd., 1997). During cooling, the parent β grains transform into child α grains, with the resulting α-phase morphology dependent on both the thermomechanical processing and cooling rate (Ahmed and Rack, 1998; Lutjering and Williams, 2007). The kinetics of the phase transformation between α and β can be martensitic or controlled by nucleation and growth. As martensitic phase transformations are diffusionless, the local variation in alloying elements enables α and β-phases to be present during processing and at room temperature, depending on the composition of the titanium alloy (James and Moon, 1970).

As Ti-6Al-4V is heated above room temperature, the β-fraction increases from below 10% at <700 °C, to 35% at 800 °C and 70% at 900 °C (Pederson *et al.*, 2003). Considering trinary phase diagrams (Figure 6), it is apparent that local changes in elemental composition support the retention of α and β-phases during thermomechanical processing at high temperatures. From this phenomenon I expect to see an effect of heterogeneous β grains distributed through the material during deformation at high temperatures, resulting in different constraints on the deformation in α grains and the retained β grains at room temperature. Thermomechanical processing of Ti-6Al-4V conducts deformation at high temperature, but my characterisation of the material will only be conducted at room temperature, after the processing has concluded. Therefore, almost all of the β will have transformed into α, and I will be investigating the resulting transformed α texture in an attempt to understand how it was produced.

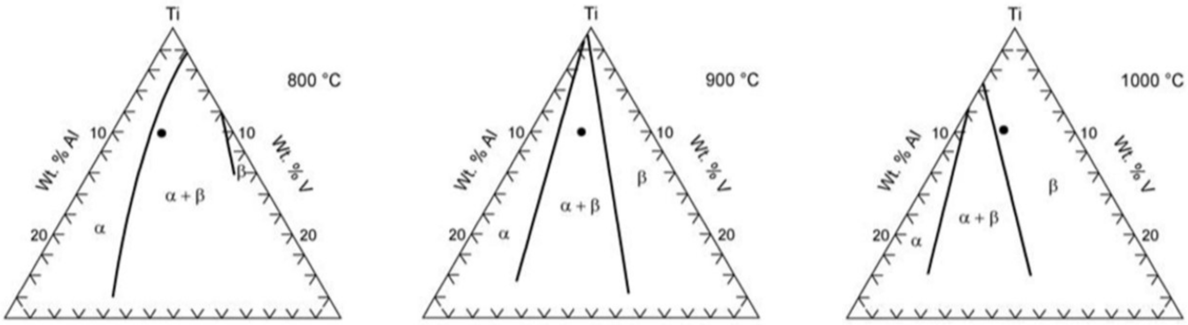

Figure 6: Trinary phase diagrams of titanium, alloyed with aluminium and vanadium at 800, 900 & 1000 °C. Ti-6Al-4V marked with ● (Lutjering and Williams, 2007, pp 28 ©).

Each step in the processing of Ti-6Al-4V is conducted at a specific termperature, in balance between the microstructural control at lower temperatures, and the greater ductility and easier workability at higher temperatures (Semiatin, Seetharaman and Weiss, 1997). The first step is homogenisation of the β at 100-150 °C above the transus, followed by recrystallisation and cooling to form an α + β colony structure. Since the laths formed are thin, and therefore only accommodate significant slip in a single direction, α + β working is conducted to break apart colony laths through β penetration, followed by a heat treatment to promote the growth of equiaxed primary-α grains. The recipe of α + β-phase field processing of Ti-6Al-4V can achieve greater improvements strength and ductility of the final material, and is therefore of considerable interest to commercial users of the alloy, such as aerospace engine manufacturers.

2.2.2 The Burgers orientation relationship of hcp phase transformations

The bcc β → hcp α-phase transformation results in the Burgers crystallographic orientation relationship (BOR), named after its discovery in zirconium (Burgers, 1934) but also observed in titanium (Newkirk and Geisler, 1953). The relationship constrains the crystallographic equivalence of the close-packed $(110)_\beta$ bcc planes with the close-packed $(0002)_\alpha$ hcp planes, and $(1\bar{1}1)_\beta$ with $(11\bar{2}0)_\alpha$ planes. Through the BOR a single β grain can transform to any one, or combination, of 12 possible α variants, but with each having a different crystallographic orientation with respect to the parent β (Lutjering and Williams, 2007).

The misorientations between the α variants formed from the same parent β grain are restricted to a set of 5 specific angles described in Table 2, according to the possible rotations between variants which the BOR for a given β orientation (Beladi, Chao and Rohrer, 2014).

Misorientation angle (°)	**Rotation axis**
10.529	$[0001]$
60.000	$[11\bar{2}0]$
60.832	$[\overline{1.377}\ \bar{1}\ 2.377\ 0]$
63.262	$[\overline{10}\ 5\ 5\ \bar{3}]$
90.000	$[1\ \overline{2.38}\ 1.38\ 0]$

Table 2: Misorientations between α variants formed by the β → α-phase transformation, as constrained by the BOR.

Where the misorientation angle and rotation axis describe the rotation between a given variant and $(1\bar{1}0)_\beta \parallel (0002)_\alpha$, $[111]_\beta \parallel [11\bar{2}0]_\alpha$.The transformation requires the alignment of the $\{110\}_\beta$ close-packed plane family in bcc with the $\{0002\}_\alpha$ close-packed plane family in hcp, producing the 12 possible variants through the symmetry of the unit cells.

After heating Ti-6Al-4V above the β-transus and cooling slowing in air, the formation of new recrystallised α-variants should produce these characteristic misorientations frequently throughout the material. Since at temperatures closer to the β-transus, a higher fraction of the bar is comprised of β-phase (Pederson *et al.*, 2003), I expect to see a greater relative frequency of the inter-variant misorientations with increasing rolling temperature.

2.2.3 Formation of macrozone microstructures in Ti-6Al-4V

The formation of colony-α in Ti-6Al-4V during cooling after high temperature thermomechanical processing can result in regions of lenticular α grains with a common long axis (laths), within a β matrix of refined grains (Lutjering and Williams, 2007; Wielewski, Siviour and Petrinic, 2012). These α laths share a common crystallographic orientation, from which arises the name "micro-textured regions", and their overall lenticular shape aligned along the long axis of the constituent laths inspires their alternate name, "macrozones". This alignment has been noted to follow a direction of material flow during forging in the β-phase (Le Biavant, Pommier and Prioul, 2002). X-ray diffraction (XRD) analysis of Ti-6Al-4V containing macrozones demonstrates a dominant texture fibre resulting from the common crystallographic orientation (Le Biavant, Pommier and Prioul, 2002; G. C. Obasi *et al.*, 2012a; G.C. Obasi *et al.*, 2012b). Macrozones therefore have an important role in the texture development of Ti-6Al-4V during thermomechanical processing, since they are a significant and unusual component of the material texture and morphology.

In the near-α titanium alloy IMI 834, macrozones are observed at room temperature following hot forging, below the β-transus. As the material presented equiaxed primary-α with a distribution of < c > axis orientations, Humbert et al. inferred that the macrozone orientations formed as a result of variant selection during the β → α-phase transformation (Humbert *et al.*, 2006). They propose a mechanism of minimisation of local elastic strain energies for each variant secondary-α lath formed, in relation to its neighbourhood during cooling.

Examination of the microstructure formed following rolling and recrystallisation at 950 °C by Warwick et al. (Warwick *et al.*, 2012) reveals extensive globularisation of the colony secondary-α laths, for annealing times for 2 hours or greater. Observing a more lenticular primary-α grain shape following an anneal of 2 hours, Warwick et al. propose that this represents an intermediate step in the formation of the non-macrozone equiaxed α seen after 16 hours of annealing, with the primary-α grains growing into neighbouring β and secondary-α laths. The observation of kinked α laths in the as-rolled texture, whose characteristic spread of orientations are not present after the heat treatment, suggests that highly deformed secondary-α laths represent nucleation sites for the growth of this equiaxed primary-α during heating. Le Biavant, Pommier and Prioul report the formation of a bimodal microstructure of equiaxed primary-α and lamellar secondary-α after hot forging below the β-transus (Le Biavant, Pommier and Prioul, 2002), after annealing at 700 °C for 2 hours. They believe that the equiaxed primary-α is formed as a direct result of forging at 955 °C, not through the recrystallisation. Zhang et al. report a 75% composition of equiaxed primary-α grains alongside macrozones after hot forging below the β-transus and a series of heat treatments, with the final heating of 300 °C (K. Zhang *et al.*, 2015).

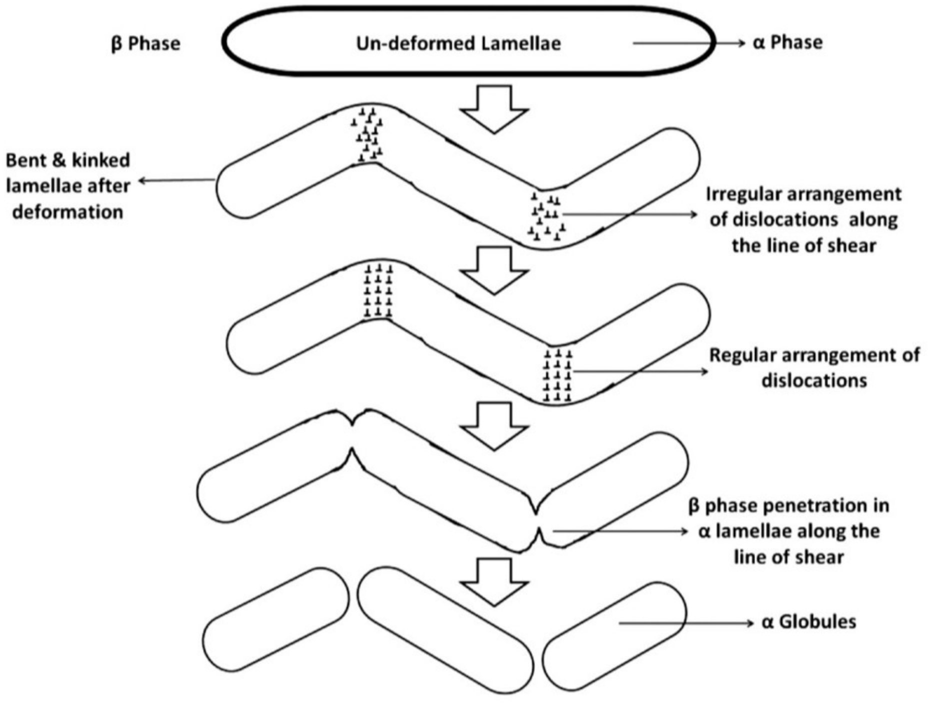

Figure 7: Formation of globular α from kinked colony laths by β penetration (Roy, Madhavan and Suwas, 2014 © tandfonline.com)

The equiaxed α grains form through the breakup of secondary-α colony laths during thermomechanical processing at high strain rates. As dislocations within laths impinge upon other grain boundaries in the direction of the shear, this results in a kink in the lath, as different lattice rotations change the shape. As β-phase penetrates into the lath along the direction of shear during hot working, the lath is "pinched" off and forms a new grain (Roy, Madhavan and Suwas, 2014). During further heat treatment, the globular α are nucleation sites for equiaxed α grains with different crystallographic orientations to the original colony lath (Figure 7).

The effect of the cooling rate following annealing was investigated by Semiatin *et al.*, (2003), heating hot-forged Ti-6Al-4V to 955 °C for 20 minutes, then cooling at a rate of 11 °C/min, 42 °C/min, or 194 °C/min. A variety of microstructures were obtained through quenching the heated samples at 870, 815, 760 and 705 °C, with a higher volume fraction of equiaxed primary-α obtained at slower cooling rates, and when quenching at 705 °C. Cooling at 194 °C/min and quenching at 705 °C produced a bimodal equiaxed primary-α and colony secondary-α microstructure.

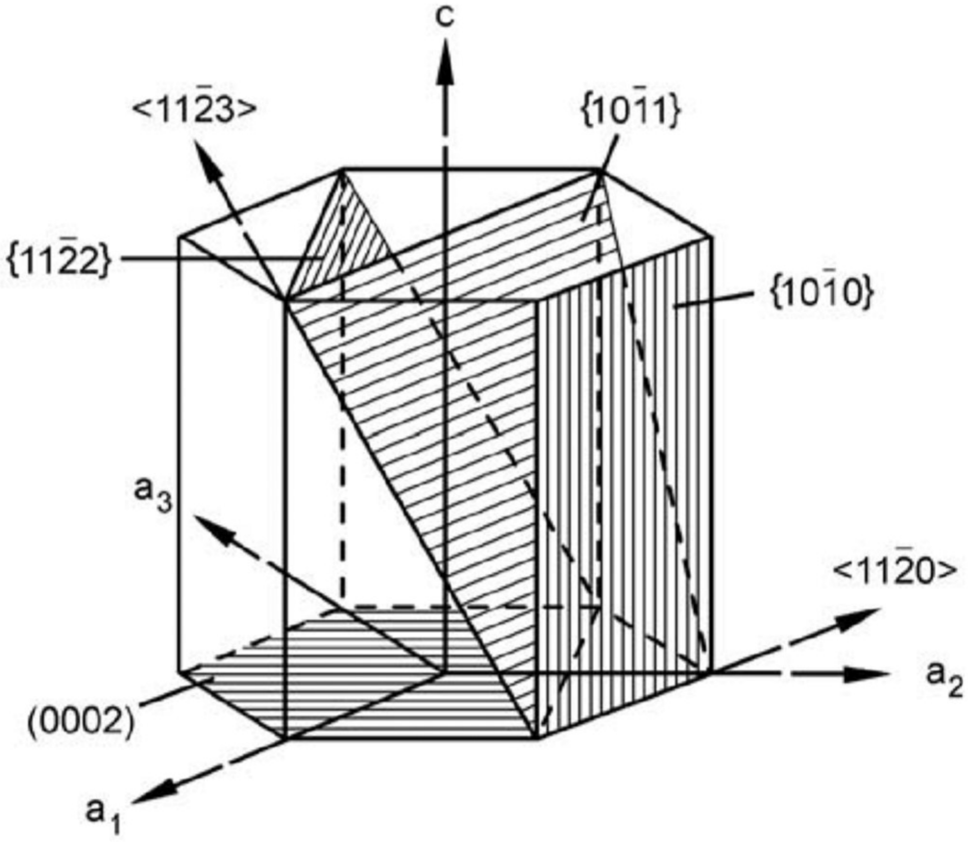

Figure 8: Slip planes and directions of the hcp unit cell (Lutjering and Williams, 2007, p 20 ©)

The cooling rate has a significant influence on the variant selection in other hcp alloys. For the zirconium alloy Zircaloy-2, which also inherits its secondary-α texture through the BOR, rapid cooling at 50 °C/s resulted in selection of secondary-α variants which produced a strong texture, i.e. favourability of specific variant selection during the β → α-phase transformation (Romero, Preuss and Quinta da Fonseca, 2009). This produces a similar texture to that seen in a cold-rolled and recrystallised CP-Ti sheet (Gey and Humbert, 2002), which was cooled at a rate of 10 °C/s. The strength of the texture formed by variant selection after the annealing of cold-rolled Ti-5Ta-1.8Nb sheet just below its β-transus notably increases with slower cooling rates, with furnace-cooling resulting in a complete colony-α microstructure at room temperature (Karthikeyan *et al.*, 2010). Considering the elastic strain-energy minimisation mechanism proposed by Humbert et al. (Humbert *et al.*, 2006), if the surface layer is rapidly cooled, and this results in a strongly selected texture, I would expect a residual strain resulting from the thermal contraction, which would provide nucleation sites for the growth of equiaxed primary-α.

In hot-rolled Ti-6242, the uneven distribution of macrozones is seen through the thickness of the bar, with an outer layer formed with few macrozones, and the greatest concentration of macrozones formed in the "mid-radius" between the centre of the bar and the surface (Pilchak *et al.*, 2013). Pilchak infers that this occurs as the result of a difference in cooling rate after rolling, but it could also be the result of the different strain rates throughout the material, as well as the friction of the material surface against the rollers.

2.2.4 Crystal slip in titanium alloys

Crystal slip is an important mode of plastic deformation in titanium alloys. The α titanium hcp unit cell has its close-packed direction along $< 11\bar{2}0 >$, with the slip of atoms within the crystal lattice along this direction translating either the (0002) plane, the < a > basal slip system, the three planes of the $\{10\bar{1}0\}$ family, the < a > prismatic slip system, or the six planes of the $\{10\bar{1}1\}$ family, the < a > pyramidal slip system. Since the shape change resulting from combined < a > basal and < a > prismatic slip is identical to that of < a > pyramidal slip, these systems are reduced to four independent modes of deformation (Lutjering and Williams, 2007). Since the Von Mises yield criterion requires 5 independent deformation modes to ensure heterogeneous deformation of a crystal without the formation of voids, a fifth deformation mode is necessary (Groves and Kelly, 1963). Geometrically, the four < a > basal and prismatic slip systems operate upon planes and in directions which are perpendicular to the < c > axis (Figure 8). In order to accommodate plastic strain parallel to the < c > axis, < c + a > pyramidal slip occurs along the $\{10\bar{1}1\} < 11\bar{2}3 >$ family, providing the necessary mode of deformation to enable shape change (Groves and Kelly, 1963). However, the< c + a > pyramidal slip system has a greater critical resolved shear stress (CRSS) than the other systems, reported at 631 MPa in compression and 441

MPa in tension for Ti-6Al-4V, with < a > prismatic CRSS values measured to be below 400 MPa for both loading conditions (Jones and Hutchinson, 1981).

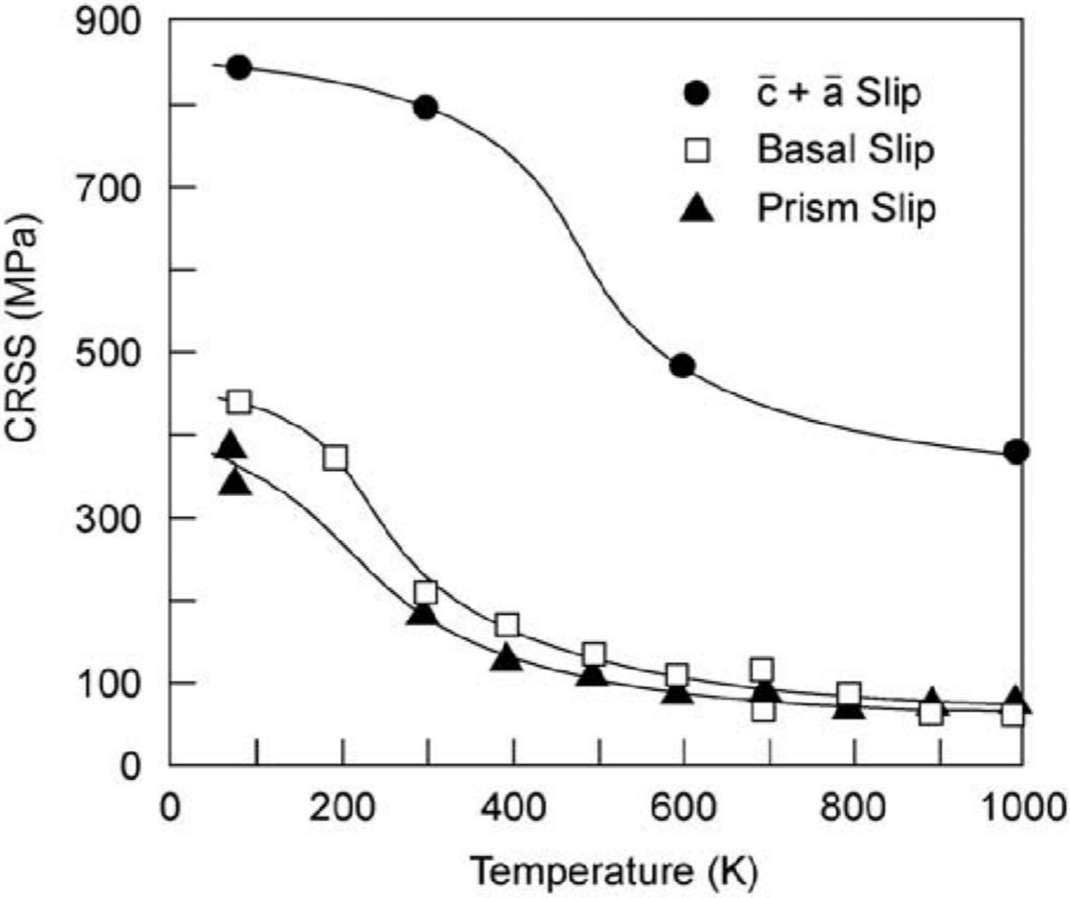

Figure 9: Temperature dependence of CRSS values for the basal, prismatic, and < c + a > slip systems in Ti-6.6Al single crystals (Lutjering and Williams, 2007, p 19 ©).

In Ti-6.6Al the temperature dependence of the CRSS values requires much greater stresses to activate the < c + a > pyramidal slip mode than the < a > basal and prismatic slip modes at all temperatures, with the CRSS for deformation at room temperature or below double the magnitude of the CRSS at 1000 K as seen in Figure 9 (Baggerly, Paton and Williams, 1976). This indicates the difficulty in achieving < c + a > pyramidal slip at low temperatures, requiring twinning as an additional mode of deformation to enable plastic deformation at low temperatures (Williams, Baggerly and Paton, 2002; Prakash *et al.*, 2010; Wielewski, Siviour and Petrinic, 2012).

The lattice rotation $\boldsymbol{W}^c$ resulting from crystal slip is calculated by the product of the plastic shear $\dot{\gamma}$ with difference of the tensor products of the slip plane normal $\boldsymbol{s}_i$ and slip direction $\boldsymbol{m}_i$ across each slip system i as expressed in equation 14 (Kocks, Tomé and Wenk, 2000).

Investigating lattice rotation at the onset of plastic deformation in Ti-6Al-4V, Hémery and Villechaise, (2019) deformed 10 mm x 2 mm x 0.8 mm dogbone samples of Ti-6Al-4V in stress-controlled loading up to 978 MPa, and observed a linear increase in plastic rotation with increasing macroscopic shear in both equiaxed primary-α grains and colony-α laths. However, as the maximum load stress resulted in 0.025% macroscopic strain, the lattice rotations observed were not larger than 3°.

Following uniaxial compressions at 600 °C to 70% thickness reduction, Mironov *et al.*, (2009) observe lattice rotations within macrozones in Ti-6Al-4V of between 5° and 15°, around a rotation axis close to the [0001] direction. This results in a spread of orientations within the macrozone fibre, resulting from the deformation of the macrozones by prismatic slip. Therefore, during rolling at temperatures below the β-transus, I expect to see broadening of the texture fibre indicating the macrozones which are well-oriented for prismatic and basal slip. This would indicate significant recrystallisation and formation of the macrozones prior to deformation.

The soft prismatic and basal slip within macrozones results in only low-angle grain boundaries forming between laths. Mironov *et al.*, (2009) observe the preferential alignment of low-angle grain boundaries with the macrozone lath long axis, forming “walls” of edge dislocations. Without significant strain hardening, the formation of high-angle grain boundaries is not possible. Globularisation of new equiaxed α grains is observed only where macrozone laths are kinked, forming high-angle grain boundaries with their neighbourhood. This explains why globularisation occurs extensively after hot-forging (Le Biavant, Pommier and Prioul, 2002; Semiatin *et al.*, 2003; Humbert *et al.*, 2006; C. Zhang *et al.*, 2015), but not rolling (Warwick *et al.*, 2012).

2.2.5 Deformation twinning in titanium alloys

Twinning provides an additional plastic deformation mechanism for hexagonal materials, which would otherwise not have enough deformation modes to satisfy the Von Mises yield criterion under certain strain conditions. Twinning is observed during cold rolling of many titanium alloys, playing a significant role in texture evolution (Philippe, Esling and Hoicheid, 1988; Zheng *et al.*, 2019). Although observed in CP-Ti through the T1 $\{10\bar{1}2\} < 10\bar{1}\bar{1} >$, T2 $\{11\bar{2}1\} < \bar{1}\bar{1}26 >$, C1 $\{11\bar{2}2\} < 11\bar{2}\bar{3} >$, and C2 $\{10\bar{1}1\} < \bar{1}012 >$ systems (Jia, Marthinsen and Li, 2019), the alloying elements in Ti-6Al-4V and solutes such as oxygen suppress twinning (Williams, Baggerly and Paton, 2002; Lutjering and Williams, 2007). As the parent-child planes are determined for each twinning system, the characteristic misorientations for each twinning system are defined, as listed in Table 3.

Misorientation angle (°)	**Twinning system**
84.8	**Tension (T1)** $\{\mathbf{10\bar{1}2}\} < \mathbf{10\bar{1}\bar{1}} >$
35.1	**Tension (T2)** $\{\mathbf{11\bar{2}1}\} < \mathbf{\bar{1}\bar{1}26} >$
64.6	**Compression (C1)** $\{\mathbf{11\bar{2}2}\} < \mathbf{11\bar{2}\bar{3}} >$
57.2	**Compression (C2)** $\{\mathbf{10\bar{1}1}\} < \mathbf{\bar{1}012} >$

Table 3: Misorientation angles for twinning systems in commercially pure titanium (Jia, Marthinsen and Li, 2019).

If twinning occurs during the processing of Ti-6Al-4V, I would expect to see a high frequency of the characteristic twin misorientations. The temperature and strain rate of processing plays a crucial role in controlling which deformation modes are available. At room temperature, twinning has been observed following uniaxial compression of Ti-6Al-4V to 14% thickness reduction (Leo Prakash *et al.*, 2010), at a strain rate of $10^{-6}\ \mathrm{s}^{-1}$, verified through SEM channelling-contrast imaging and TEM micrographs.

Single crystal Ti-6.6%Al compression testing indicates that grains aligned for basal and prism slip will not deform by twinning (Williams, Baggerly and Paton, 2002). At 5% wt. Al, twinning occurred in a single crystal aligned for basal slip during compression at 300 K and below. Light microscopy of titanium alloyed with 2.9% wt. shows the presence of twins after a thickness reduction of 50% at 500 K with single crystals aligned for prismatic slip. With single crystals aligned for $< c + a >$ pyramidal slip, twinning did occur during compression of an alloy of titanium with 1% wt. Al at 77 K, but was almost completely suppressed at 1000 K. Regardless of elemental composition, deformation above room temperature results in suppression of twin activation, and regardless of compression temperature, an increase in the % wt. of aluminium also suppresses twinning.

Following deformation by compression to 10% thickness reduction at a strain rate of $5000\ \mathrm{s}^{-1}$ at room temperature by Follansbee and Gray, (1989), twinning was observed in Ti-6Al-4V, segregated within the grains which were larger than average. However, twinning is not reported during compression at a strain rate of $10^{-3}\ \mathrm{s}^{-1}$, conflicting with the result observed by Prakash *et al.*, (2010). Follansbee and Gray, (1989) report that < a > basal and prismatic slip are responsible for suppressing twin activity, through their TEM micrographs demonstrating a significant presence of slip bands in grains after deformation by compression to 10% thickness reduction at a strain rate of $10^{-3}\ \mathrm{s}^{-1}$. T1 and T2 tension twinning has also been observed to occur in Ti-6Al-4V macrozones oriented for easy < a > basal and prismatic slip, during room temperature compression impact testing (Wielewski, Siviour and Petrinic, 2012).

Comparing their computational Taylor modelling of texture evolution with hot and cold rolling studies of titanium alloys including Ti-6Al-4, Philippe *et al.*, (1995) note that the activation of < c + a > pyramidal slip can suppress activity on the T1 $\{10\bar{1}2\} < 10\bar{1}\bar{1} >$ twinning system, which can reorient the < c > axis by 84.8°. Using a Taylor full constraints model, the ND fibre twinned away to form TD fibre, while in the Taylor relaxed constraints model, < a > prismatic slip is favoured, which retains the ND fibre. Modelling cold rolling to 50% thickness reduction, a twinned volume fraction of 5% is reported for Ti-6Al-4V, compared with 25% for CP-Ti.

Considering the presence of twinning in Ti-6Al-4V and other Ti-Al alloys, it is clear to me that I should not expect to see twinning occurring during hot rolling of Ti-6Al-4V. The effect of aluminium content supressing deformation twinning has been reported widely in the literature (Williams, Baggerly and Paton, 2002; Lutjering and Williams, 2007). While it is possible that some regions in the material may be locally depleted of aluminium, especially if they are rich in vanadium, at higher temperatures I expect these regions of the material to be primarily β-phase as per Pederson *et al.*, (2003), and therefore their effect on the texture evolution will produce the multiple secondary-α variants expected in a transformed texture. Additionally, if the twinning in titanium alloys is segregated to the largest grains (Follansbee and Gray, 1989), these will be equiaxed α grains, not macrozone α laths. This would exclude the possibility of the formation of new ND texture fibre through the reorientation of TD fibre macrozone laths, by T1 $\{10\bar{1}2\} < 10\bar{1}\bar{1} >$ tension twinning.

2.2.6 Textures of Ti-6Al-4V after hot working

The texture formed in Ti-6Al-4V during rolling is strongly influenced by the rolling temperature, resulting from both the microstructure formed and the presence of the softer β-phase to accommodate deformation (Semiatin, Seetharaman and Weiss, 1997). For α + β-phase field processing, the emergence of strong fibres of (0002) normal directions aligned with TD occurs at most temperatures, with an additional (0002) normal alignment with ND for working below 900 °C. Curiously, this is contradicted by the observation of rotated α-laths during the hot-forging of Ti-6Al-4V at 955 °C by Weiss et al. to 22% thickness reduction, where the final orientation of the laths aligned their < c > axis, and morphologically their long axis, with the direction of compression (Weiss *et al.*, 1986). Subsequent annealing for 30 minutes at 955 °C and a further 2 hours at 925 °C, followed by water quenching preserved this texture and microstructure. Weiss et al. identify a mechanism of β penetration into the lenticular α laths, along sub-grain boundaries or heavily sheared zones. Thin lamellae are noted to be much easier to break apart than thick lamellae.

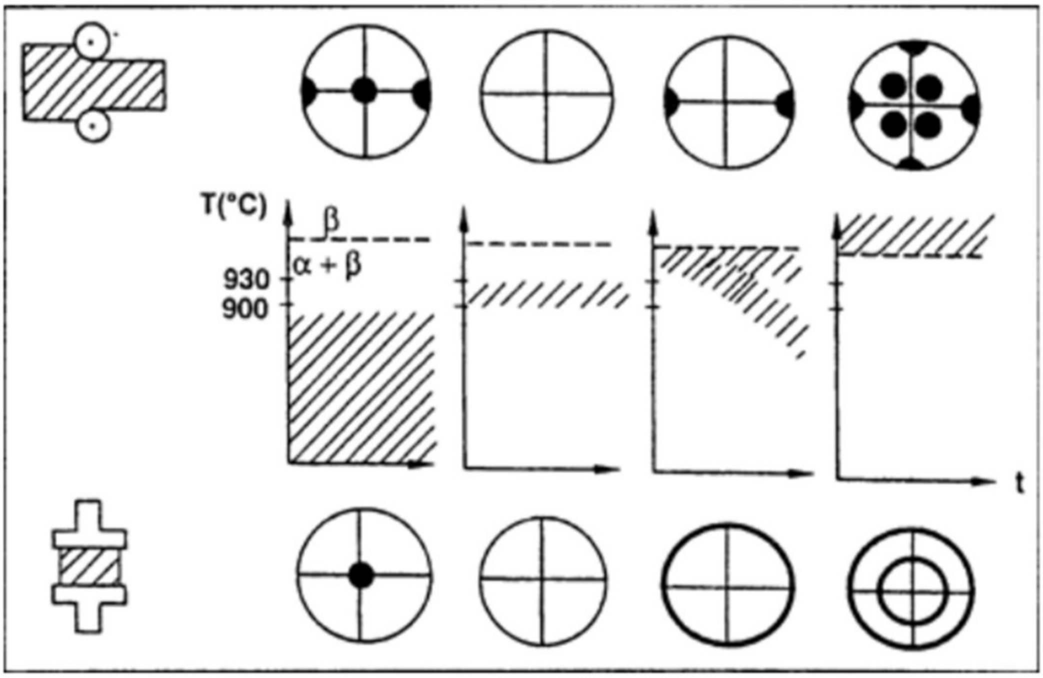

Figure 10: Schematic of the α textures indicated by the (0002) pole figure, as formed by rolling (top) and forging (bottom) for specific temperature ranges (Semiatin, Seetharaman and Weiss, 1997 ©).

The texture of Ti-6Al-4V formed by rolling at 900 °C, followed by recrystallisation at 980 °C are preserved after an additional rolling step along the same direction at 800 °C of 30% thickness reduction

(Morii *et al.*, 1986). The observed texture has strong (0002) poles aligned 15 ° away from the ND, towards the RD. After rolling at 900 °C, the intensity of this texture was significantly reduced. Since at this temperature, the material is > 50% β-phase, Morii et al. suggest that the mechanistic cause of this change in the texture is the whole rotation of undeformed α grains within the surrounding β.

XRD studies by G. C. Obasi *et al.*, (2012) demonstrate a characteristic (0002) | | ND texture fibre emerging after unidirectionally hot rolling to a thickness reduction of 75% at 800 °C, combined with a (0002) | | TD texture. This combination of fibres is frequently observed by XRD following uniaxial compression or unidirectional rolling at 800 - 900 °C (Chao, Hodgson and Beladi, 2016; Roy and Suwas, 2017).

In their work, G. C. Obasi *et al.*, (2012) chose 800 °C and 950 °C to demonstrate the combination of these fibres at 800 °C, and the exclusion of the ND texture, forming only the TD texture fibre, at 950 °C. Their 40 x 40 x 20 mm samples were heated at 1050 °C, rolled at 800 or 950 °C, then recrystalised for 8 hours at 950 °C. Smaller samples of 10 x 10 x 5 mm were cut and subsequently heat-treated in the β-field at 1150 °C for 30 min and furnace-cooled, with the final α texture forming through the BOR. After this heat treatment, the TD fibre is removed entirely from both the 800 °C and 950 °C rolled material, suggesting a thermal mechanism favouring the selection of α variants during the β → α transformation is crucial in controlling the final α texture. XRD characterisation of Ti-6Al-4V by Roy and Suwas, (2017) has identified ND textured colony laths forming after rolling at 700 °C to a 90% thickness reduction and heating for 75 minutes at 900 °C.

Despite this, the ND texture fibre is visible in the Obasi as-rolled material condition after 800 °C rolling, with the texture sharpened by the 950 °C recrystallisation heat treatment. This is to be expected, as the heating will cause primary α grain growth (G. C. Obasi *et al.*, 2012). During rolling of 5.75 mm thick Ti-6Al-4V plate at 750 °C to a 70% thickness reduction in a single pass, layers of ultra-fine grains form near the rolling surfaces, with equiaxed grains c. 200 nm in width, with a strong ND texture fibre. However, the same ND fibre is formed at the centre of the bar, with a weaker intensity (Chao, Hodgson and Beladi, 2016).

The hot compression of Ti-6Al-4V by Roy, Madhavan and Suwas, (2014) at 750-1000 °C resulted in globularisation resulting for lath kinking resulting from basal slip, with equiaxed primary-α growth at temperatures near the transus. Notably, the authors reference the β-transus to be 1040 °C which I believe to be in error, therefore their hottest compression tests are carried out in the β-phase field. This would explain the change in texture seen between the trend of softening of the (0002) pole figure maximum intensity from 850 – 950 °C, with substantial strengthening at 1000 °C, since the orientations for that temperature form entirely through recrystallisation and variant selection by the BOR, without any orientation spreading due to deformed primary-α. For deformation above 850 °C a reorientation away from the compression axis is observed, likely due to variant selection of secondary-α. Below this, the initial texture is broadened, indicating deformation in primary-α.

I aim to explore the mechanism responsible for the "texture flip" from combined TD and ND texture fibres, to TD fibre only, through hot rolling at a range of temperatures between 750 °C and 950 °C.

2.2.7 Aluminium and vanadium diffusion in Ti-6Al-4V

Due to the influence of alloying elements on phase composition of Ti-6Al-4V at high temperature, the mobility of α-stabilising aluminium and β-stabilising vanadium must be evaluated. Semiatin *et al.*, (2004) examine the diffusivity of aluminium and vanadium in the β-phase for Ti-6Al-4V through heating experimental couples of two titanium-aluminium-vanadium alloys with different compositions. The diffusivity of aluminium was found to be greater in a couple of 7.5% wt. % vanadium alloyed with 1.95% or 4.95% wt. % aluminium (A1/B1, Figure 11), than in the couple of 12.7% vanadium alloyed with 1.06% or 3.96% wt. aluminium (A5/B5, Figure 11). This suggests that the diffusion of alloying elements occurs fastest within the regions where the concentration of that element is greatest. Comparing their results with the estimated intrinsic diffusion coefficients for aluminium (Araki *et al.*, 1994) and vanadium (Zwicker, 1974), Semiatin *et al.*, (2004) observe lower diffusivity for all compositions, at all temperatures for their experiments (Figure 11).

The diffusivity of both aluminium and vanadium increases during heating as the temperature approaches the transus. At 950 °C calculated and empirical values are greater than 0.05 $\mu m^2/s$. By calculating the diffusivity as a function of temperature below the experimental range of temperatures, the diffusivity is seen to reduce exponentially, with values below 0.01 $\mu\mathrm{m}^2/\mathrm{s}$ at 750 °C. This suggests that for hot rolling at this temperature, the diffusion of alloying elements is minimal, and their spatial distribution will remain consistent.

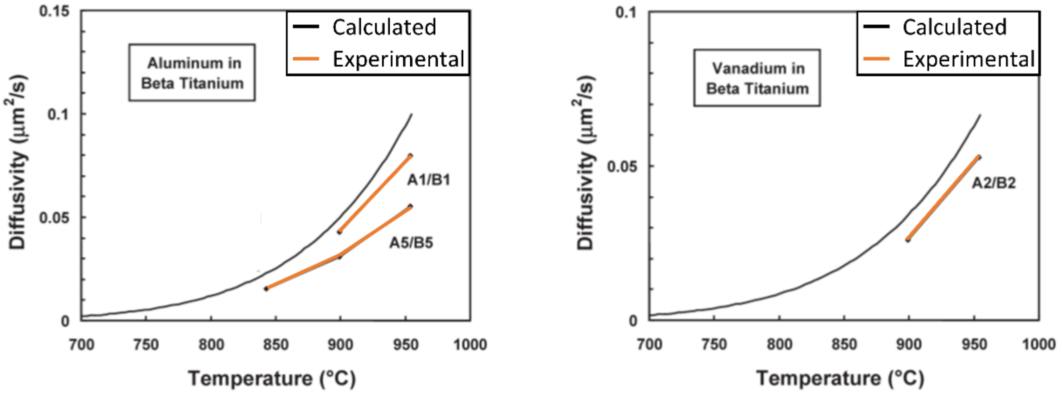

Figure 11: Comparison of measured and calculated diffusivity of aluminium (left) and vanadium (right), in β-titanium. (Adapted from Semiatin et al., 2004 ©)

From rearranging Fick's first law we find the average distance of diffusion at time *t* is given by:

$$\bar{x} = \sqrt{6Dt} \tag{15}$$

For every hour of heat treatment at 950 °C, with $D = 0.05$ for aluminium and vanadium, atoms of both elements will diffuse on average by 33 μm.

2.3 Instancing virtual microstructures in crystal plasticity simulations

2.3.1 Direct instantiation through 3D sectioning or x-ray tomography

Destructive methods can be used to characterise a material through repeated measurement of a 2D surface, such as focussed ion beam (FIB) 3D sectioning with EBSD (Groeber *et al.*, 2006; Borgh *et al.*, 2013). There is an issue of practicality with such methods, as the time required to characterise a 50 x 50 x 50 μm volume can require 4 days of FIB-SEM time (Groeber *et al.*, 2006). This experiment was conducted on an undeformed sample of the IN100 nickel superalloy, which readily diffracts "high-quality" electron backscatter patterns (EBSPs) with multiple clear, easily indexed diffraction bands which describe the lattice orientation at each inspection point. Deformed samples requiring complex sample preparation are unsuitable for characterisation through serial FIB sectioning.

An alternative to destructive characterisation are x-ray tomography technique, such as high-energy diffraction microscopy (HEDM, Lienert et al., 2011) and diffraction contrast tomography (DCT, Renversade et al., 2016). The 43 layers of grains characterised through HEDM by Lienert et al. were meshed into a CP-FEA model, but as with FIB-SEM serial sectioning, this presents good 2D resolution of the microstructure and comparably coarse resolution through the third dimension. Both these methods require use of synchrotron x-ray beamline facilities, which limits access to the methods and greatly restricts the number of samples which may be processed for a given project.

2.3.2 Oligocrystal "2.5D" modelling of a reference surface

The simplest possible method of instancing a 3D microstructure is extrusion of a characterised 2D surface in the third dimension, creating a "2.5D" microstructure of columnar grains which extend throughout the bulk of the material. In CP-FFT modelling, a plane-stress condition can be applied through the representation of a free surface, controlled by a compliant layer of voxels subject to isotropic plasticity (Maiti and Eisenlohr, 2018). This method has the advantage of representing the morphology and texture of grains characterised through methods such as EBSD. All grains within the model experience the real neighbourhood of orientations present in the reference material, as the ODF and MDF is identical to the characterised 2D surface.

In CP-FFT simulations of dual-phase steels, instanced by Voronoi tessellation, Diehl *et al.*, (2016) have demonstrated the influence of neighbourhood phase composition on the stress and strain partitioning. Modelling hard martensite grains within a soft ferrite matrix, a martensite volume fraction of 0.4 led to localisation of strains at the ferrite grain boundaries, with relaxation in their interiors. By refining the height of the RVE used in the model (Figure 12), the periodic boundary condition becomes a closer and closer approximation of a columnar microstructure.

As $h \rightarrow 0.01$ for the microstructures modelled, the variance of the von Mises stress and strain increased, with the greatest variations present at grain boundaries. While the combination of this effect with larger martensite volume fractions lead to the most significant variations in strain behaviour, significant variation of the strain partitioning is seen in the models comprising a 0.1 martensite fraction, suggesting an influence of texture as well. For damage and failure predictions, which depend on strongly localised effects such as the stresses at grain boundaries and triple junctions, I believe it is unacceptable to use a "2.5D" simulation due to this phenomenon.

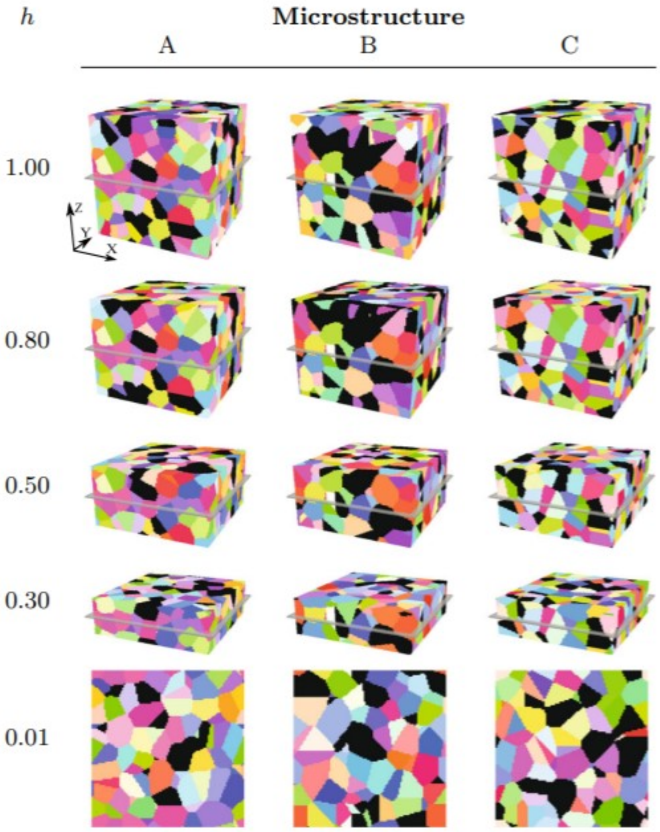

Figure 12: Three synthetic microstructures A, B, and C, populated by Voronoi tessellation in a 100 x 100 x 100 grid. The columnarity of the microstructures is tuned by constraining the height of the model to a fraction h around the central voxel layer. (Adapted from Diehl et al., 2016 ©).

2.3.3 Generating synthetic microstructures through tessellation

The Voronoi tessellation is a system of generating cells of the set S, such that a cell is formed around the seed point c_s for all points x within a domain V which satisfy equation (16). This represents a minimization of the Euclidean distance $d(x, c_s)$ from the seed point to each material point in the grain, compared with the Euclidean distances from the material point to every other seed point in the tessellation (Aurenhammer, 1987).

$$R(s) = \{x \in V |\, d(x, c_s) < d(x, c_t), \text{for all } t \in S - \{s\}\} \tag{16}$$

This enables the modelling of reference grains with a direct equivalence, and the Voronoi method is frequently used to populate RVEs for crystal plasticity (Zeghadi *et al.*, 2007; Quey, Dawson and Barbe, 2011; Diehl *et al.*, 2016).

Greater control of the size of individual cells in the tessellation can be obtained using the Laguerre tessellation (Aurenhammer, 1987; Redenbach, Shklyar and Andrä, 2012). This method defines S as a set of spheres, such that a cell is formed by a sphere s in the region containing all points x in the domain V, where the power of the point is minimized:

$$R(s) = \{x \in V \,|\, pow(x, c_s) < pow(x, c_t), \text{ for all } t \in S - \{s\}\} \tag{17}$$

$$pow(x, s) = d(x, c_s)^2 - r_s{}^2 \tag{18}$$

With the power of sphere s at point x given by equation (18). The radius of the sphere r_s is parameter which reduces the power of the sphere, making the corresponding cell larger by allowing points further from c_s to be included in the cell associated with c_s (Figure 13).

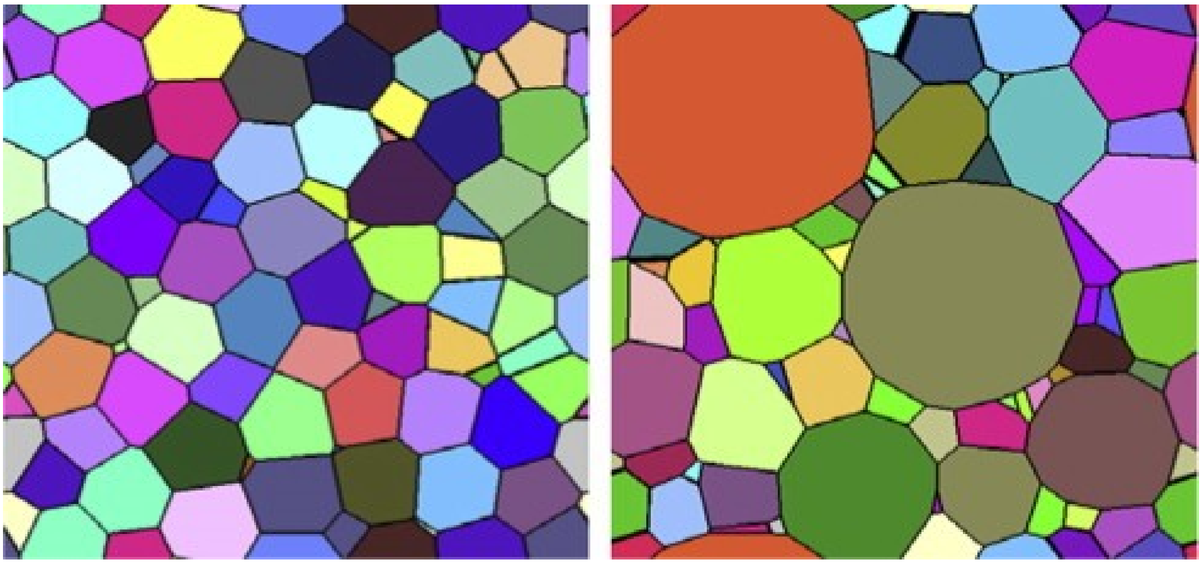

Figure 13: Laguerre tessellations of the same set of seed vertices, with equal sphere radii (left) and with sphere radii generated by a one-parameter gamma distribution with c = 4.0. (Redenbach, Shklyar, & Andrä, 2012 ©)

The Laguerre tessellation offers a significant advantage over the Voronoi tessellation, in that through the parameter r_s, the size of an individual grain can be controlled (Aurenhammer, 1987). This offers an advantage in generating RVEs from a characterised 2D reference surface, as the grain areas may be used as a parameter to improve the representation of grain morphology, for example with a bimodal grain structure.

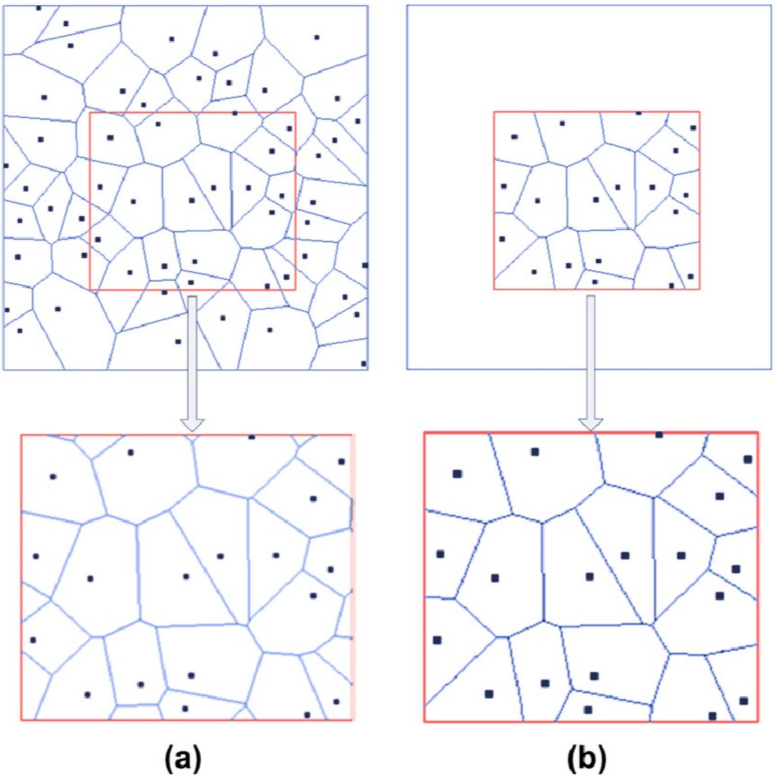

Figure 14: Voronoi diagrams constrained to an interior boundary, with seeds populated outside the region of interest (a), and only within the region of interest (b). (Zhang, Balint and Lin, 2011 ©).

A similar method to the Laguerre tessellation is presented by Zhang, Balint and Lin, (2011), where the grain sizes are constrained according to the distribution of grain sizes in a reference surface. Using a one-parameter gamma distribution, the mean grain size and any two other percentile grain sizes can be reproduced. The VGRAIN RVE generation program computes the gamma control parameter from a reference surface and tessellates a volume of cells with controlled grain size.

One consideration when generating volumes through a tessellation is to populate grains outside the geometry boundary. If grain seed points only exist within the domain of the tessellation, the boundary grains will be increased in size (Figure 14). When populating beyond this volume, other small boundary grains are seen whose seeds lie outside the boundary. When generating RVEs through any method, a method of domain subsampling is necessary to preserve the morphology of the boundary grains (Zhang, Balint and Lin, 2011).

2.3.4 Representing the texture of a reference surface

2.3.4.1 ODF reconstruction

For a 2D surface, the grain lattice orientations can be directly matched to the reference. 3D RVEs can be assigned orientations using the orientation distribution function (ODF), which defines the probability of a given orientation g representing a volume fraction $\frac{dV}{V}$ (Eisenlohr and Roters, 2008a):

$$\frac{dV}{V} = f(g)dg \tag{19}$$

With the infinitesimal volume of orientation space, dg, calculated as:

$$dg = \frac{1}{8\pi^2} d\phi_1 \, d\phi_2 \, d\cos\Phi \tag{20}$$

Which is normalised such that the integral over all Euler orientation space is exactly equal to 1. The numerical approximation of the ODF can be partitioned into bins in Euler space, and the discrete volume fraction which exists within each bin reproduced in a synthetic volume. Eisenlohr and Roters, (2008) utilise a method of "integral approximation", in order to address the repeated sampling of orientations in the fundamental zone due to the sample symmetry. If a small number of orientations have been sampled, the method overrepresents orientations which are present in the initial texture. This can be addressed through probabilistic sampling of randomly generated orientations to satisfy the ODF, at increased computational cost.

Measurements of bulk texture through EBSD by Humphreys, (2001) indicate a minimum number of measurements of between 500 and 1500 points on a reference surface are necessary to appropriately sample texture. The average grain size of the material will influence the number of grains that this measurement represents, but it is to be expected that this is of the order of hundreds of grains.

In a VPSC model, orientations can be sampled directly from an experimentally characterised ODF (Galán-López and Verleysen, 2018), as the number of grains modelled in a VPSC simulation is of the order of 1000. Since each grain is deformed independently, the neighbourhood misorientations do not contribute to the partitioning of deformation.

2.3.4.2 MDF reconstruction

In order to consider the effect of neighbourhood orientations resulting from the texture of a material on the deformation mechanics, the misorientation distribution function (MDF) is computed. In a similar manner to the ODF, is it is the probability of a misorientation arising as a volume fraction of the constituent grains:

$$\frac{dV}{V} = f(\Delta g)dg = \int_{\Delta\Omega} f(g)dg \tag{21}$$

Where only orientations from a given misorientation interval $\Delta\Omega$ are considered (Qiu, 2016).

Saylor *et al.*, (2004) developed a method to optimise the MDF of a 3D RVE through the use of a cost function (equation 22), which accounts for the ODF and MDF of a referenced surface. The cost function λ computes the total deviation across O ODF bins and M MDF bins. Since this method computes the difference between the modelled and reference texture across each bin, it does not constrain the resolution of either ODF or MDF binning to a particular orientation or misorientation space. The user is therefore free to specify O and M in order to constrain the reproduction of the texture.

$$\lambda = \sum_{i}^{O}\left(f_{model}(g)_i - f_{ref}(g)_i\right)^2 + \sum_{j}^{M}\left(f_{model}(\Delta g)_j - f_{ref}(\Delta g)_j\right)^2 = \lambda_{ODF} + \lambda_{MDF} \tag{22}$$

Through swapping the orientations of grains present in the RVE or replacing the orientation of a grain with a different orientation present in the ODF, the total deviation is minimised through a Monte Carlo process.

3 Experimental and computational methods

3.1 Acquisition of material mapping through electron microscopy

3.1.1 Sample preparation

Production of a high-quality metallographic finish is necessary in order to observe the internal microstructure of a material, rather than merely observing the defects introduced into the material during preparation. This is of critical importance for surface-sensitive techniques such as EBSD. Since the typical area of an EBSD map is less than 1 mm^2, the material is first cut to size using a displacement-controlled precision saw with a silicon carbide blade, using a cutting rate of 0.005 mm/s and coolant fluid.

Next, the samples are then mounted using Bakelite, to present one surface for grinding and polishing. The grinding process uses silicon carbide grains adhered to paper wafers, removing damaged layers of the material through friction. Several samples may be polished simultaneously, pressed into the silicon carbide paper by a piston with a force of 10 N, with the sample and paper rotated to maximise abrasion. Water is used to cool the sample and wash away any debris, in order to reduce further damage to the surface. It is important to replace the silicon carbide paper after a minute of grinding, since as the binding agent weakens, particles of silicon carbide can break away from the paper and scratch the sample surface. The coarsest papers are used first, to eliminate the surface damage induced by cutting and subsequent preparation, moving to progressively finer papers with a greater density of silicon carbide particles, and a smaller average grain size. At each stage, the scratches and subsurface damage introduced by the previous grinding step are removed.

Following the completion of grinding with 4000 grit papers (a particle diameter of 5 μm), the sample is polished using a dilute neutralised colloidal silica (OPS) solution of 70 ml OPS with a particle diameter of 0.25 μm, 30 ml hydrogen peroxide, and 150 ml deionised water. Held in a drum with other samples, the material is buffed by a soft cloth for 30 minutes. Following this, the sample is washed with deionised water to prevent contamination. The sample is then inspected using polarised optical microscopy. The polishing process must be repeated several times in order to produce a clean, smooth surface with a "mirror" finish free from scratches. Depending on the prior deformation of the sample, between 2 and 10 hours of polishing may be required.

Between each hour of polishing with OPS, the samples were etched in order to selectively remove material in order to reveal the microstructure. Due to the relative softness of the β-phase, damage accumulates within it and the EBSPs produced by it are unlikely to indexed. Kroll's reagent is used, comprising 91 ml water, 3 ml hydrofluoric acid and 6 ml nitric acid. The samples were immersed in the etchant for 30 seconds, in order to attack the damaged surface layer and reveal undeformed material for future polishing steps.

Additionally, after the polishing was completed, the sample was etched for 3 seconds, in order to give a strong contrast under unpolarised light between the α and β-phases. This allowed for polarised optical microscopy of the microstructure at low magnification, in order to rapidly obtain information about the morphology across an area similar in size to the maps characterised through EBSD. When this was achieved, the sample was polished for 5 further minutes to remove the etch and ensure no topography was present on the sample.

After washing thoroughly with deionised water, isopropanol, and acetone, the samples were mechanically broken out of their Bakelite mounts and adhered to an aluminium stub with silver paint, to ensure electrical conductivity and prevent charging of the sample during electron microscopy. At all times during the sample preparation process, which takes several days for a single sample, the samples were stored between preparation steps in a controlled environment free from dust, water, and volatile organic compounds (such as may be found on human skin).

3.1.2 Electron backscatter diffraction (EBSD)

By rastering the electron beam of a scanning electron microscope (SEM) over a series of inspection points, the electron backscatter can be collected through a scintillator and charge-coupled device (CCD). The diffraction patterns produced, known as EBSPs, describe the crystallographic orientation of the material point inspected by the electron beam through its Kikuchi bands (Wilkinson and Britton, 2012). As the patterns can be efficiently computed as points through the Hough transform algorithm, a lookup table of orientations is used by computer software to interpret the orientations of each inspected point.

EBSD patterns are typically obtained with a sample tilt of 70° relative to the incident electron beam, in order to increase the quality of the EBSPs obtained (Wilkinson and Britton, 2012).

The Hough indexing method requires clear EBSPs with several bands projected onto the CCD. In highly deformed materials, the lattice curvature arising from high GND density can result in poor quality patterns, which are difficult to index. As a result, highly deformed materials are more difficult to index than undeformed materials and must be measured using greater CCD resolution (and therefore longer inspection durations at each material point). Since the use SEM equipment is time-restricted, this limits the number of points which may be examined in a single mapping through EBSD. Therefore, there must be a balance of the dual needs of mapping enough points to obtain a valid texture, while ensuring an acceptable indexing fraction to have confidence in the orientations produced. In particular, it is difficult to observe the β-phase in Ti-6Al-4V during large-scale EBSD mapping, due to the preferential deformation of this phase.

3.1.3 Energy dispersive spectroscopy

The excitation of valance shell electrons to higher energy states results in spontaneous photon emission as the electron transitions to its ground state. In Siegbahn notation, the Kα emission lines describe the characteristic photon energy describing the transition from a $2p$ to an $1s$ orbital. For all elements except hydrogen, the wavelength of the photon of the Kα_1 emission line falls within the x-ray band.

Using a Bruker XFlash 6|60 EDS x-ray detector, the spectrum of x-ray photons observed after inspection of the material by the SEM electron beam can be resolved into individual peaks through Gaussian decomposition, using the eSprit 2.1 software. The Kα peaks for user-specified elements are computed through a series fit of Gaussians computed through the known peak locations. As a result, elements may only be resolved if the Kα peaks are separate in energy space, which makes the resolution of the instrument crucial for discriminating Kα peaks with similar energies, such as for titanium and vanadium.

The eSprit software computes the ZAF (atomic number, atomic absorption, and fluorescence) correction through proprietary methods. This computes an expected difference in intensity according to three characteristics of each element (Goldstein *et al.*, 2018).

The proportion of x-rays scattered increases with Z, but the energy lost from each scattering event is inversely proportional to Z. Therefore, the relative intensity for a low Z element is reduced when it is

alloyed with a higher Z element. In Ti-6Al-4V, we should expect the intensity of Al Kα peaks to be reduced compared to pure Al, due to the reduced availability of electrons due to increased scattering with Ti and V.
The absorption effect reduces the intensity of x-rays which were generated below the surface in the material, since some will be absorbed during their path to the detector. The fluorescence effect is the excitation of transitions in other elements in the material by source photons, which would result in a reduced intensity of light element emission spectra and increased intensity of higher-order transitions in heavier elements. (Goldstein *et al.*, 2018). Both the absorption and fluorescence effects are smaller in magnitude than the Z scattering effect.

The eSprit software only uses the most intense lines for each element within its computation of the elemental fractions, making the fluorescence correction unnecessary, due to the separation in energy-space of the Kα peaks. The Gaussians for each element are integrated, and the intensity compared against a reference peak for that element, generated by a 15 kV incident electron beam. Since the EDS acquisition in chapter 5 was conducted using a 20 kV electron beam, the emission peak heights of the reference could be expected to be lower in magnitude in the reference compared with the experimental results. This introduces an uncertainty which is difficult to account for.

3.1.4 Direct backscatter spectroscopy

Using a direct electron detector clipped to the SEM objective lens, the electron backscatter can rapidly be obtained by rastering the beam across the sample, measuring the intensity at each inspection point. This allows for the discrimination of phase within the material, since the atomic density of the bcc β-phase is greater than the hcp α-phase. As this increase in density means an incident electron is more likely to undergo scattering with a titanium atom, the intensity of backscatter is greater when β-phase is present at the inspection point.

Inside the chamber of the SEM used for EBSD acquisition, I installed a DBS detector comprising of concentric circular electrodes illustrated in Figure 15. When the collection diodes are optimised (in terms of solid angle set with a working distance of 10 mm, and an acceleration voltage of 20kV, spot size of 5.0 and a working distance of 10mm) the signal can be summed over electrodes A, B, and C maximising the collection of electron backscatter and optimising Z-number and atomic density contrast. The β-grains appear brighter (due to the higher average atomic density of this phase). There is weaker grain orientation contrast, from electron channelling, in the α-grains.

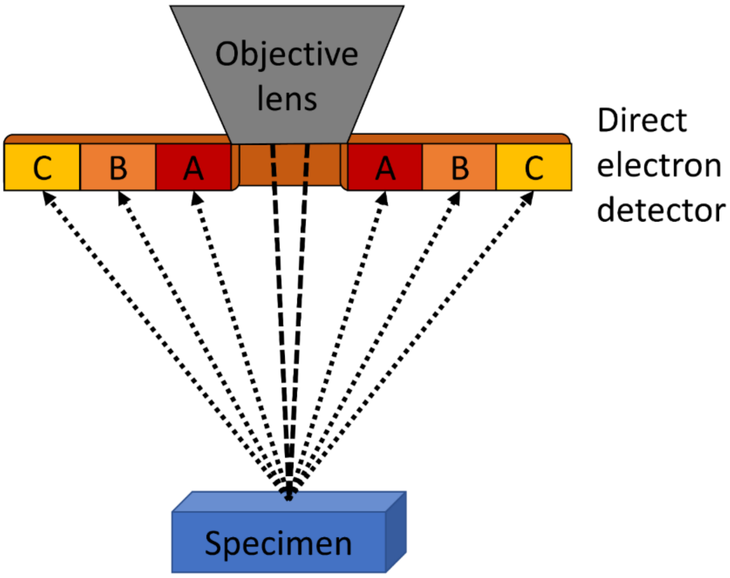

Figure 15: Schematic of the interior of an SEM chamber, featuring a direct electron detector

Micrographs were collected with a scanning step size of 1 μm to provide multiple pixels in both the α-grains, as well as in the β-ligaments. These were analysed offline to calculate the phase factions. Two methods were employed – thresholding based upon a threshold brightness value; and Gaussian decomposition of the frequency histograms of electron intensity.

3.2 Texture-controlled Voronoi tessellation (TCVT) method

3.2.1 Proof of the overdetermination of near-surface seed positions

Euler's polyhedron formula relates the numbers of faces, vertices, and edges in a convex 3D polyhedron:

$$F + V - E = 2 \qquad (23)$$

Where F is the number of faces, V is the number of vertices, and E is the number of edges (Cromwell, 1997, p 189). For a Voronoi tessellation, each cell is bounded by straight edges which connect at vertices. Since only the division of a diagram into quadrants would require a vertex which connects four edges, any practical tessellation is described by the minimal configuration of edges connecting two vertices, with three edges terminating at each vertex. Therefore;

$$V = \frac{2}{3}E \tag{24}$$

Considering the Voronoi tessellation as a flat 2D surface, the number of grains is equal to the number of faces, and can be divided into interior and boundary grains by:

$$G = F = G_e + G_i \tag{25}$$

Where G is the number of grains, G_e is the number of external grains, with at least one edge along the boundary of the tessellation, and G_i is the number of the internal grains, with no edges along the boundary of the tessellation. We can define grains, vertices, and edges accordingly:

$$\begin{gathered} G = G_e + G_i \\ V = V_e + V_i \\ E = E_e + E_i \end{gathered} \tag{26}$$

By substituting equations (24), (25) and (26) into (23),

$$E = 3(G_e + G_i - 2) \tag{27}$$

Since each external grain corresponds to an edge which reaches the domain boundary, it creates an external vertex, in addition to the four corner vertices of the domain.

$$V_e = G_e + 4 \tag{28}$$

where V_e is the number of vertices on the boundary of the tessellation. The number of vertices can be expressed through rearrangement of equation (27) into (24),

$$V = (V_e + V_i) = \frac{2}{3}E = \frac{2}{3}(E_e + E_i) = 2(G_e + G_i - 2) \tag{29}$$

And the number of internal vertices can be found by rearrangement of equation (28) into (29)

$$V_i = G_e + 2G_i - 8 \tag{30}$$

At each vertex, the Euclidean distances from the vertex to the seed points of the surrounding grains are known. For each boundary vertex V_e, we are free to perturb the seed locations, generating one equation defining the Euclidean distances. For each internal vertex V_i, perturbations to two of the three seed locations constrains the perturbation of the third, which is necessary in order to retain the vertex position. Therefore, each internal vertex generates two equations which define all three Euclidean differences. As the seed positions must be calculated in 3D space, the number of unknowns is equal to $3G$. Therefore, an exact solution is possible in the condition:

$$V_e + 2V_i \ \geq \ 3(G_e \ + \ G_i) \tag{31}$$

Substituting for equations (28) and (30) and equation (31):

$$(G_e + 4) + 2(G_e + 2G_i - 8) \ \geq \ 3(G_e \ + \ G_i)$$
$$\therefore \ G_e \geq 6G_i \tag{32}$$

This provides the limiting ratio edge grains to interior grains for an exact solution to exist within this method. In cases where this is no longer satisfied, we must select the *a priori* inclination of a few grain boundaries to provide a suitable solution from this method. Without this intervention only a columnar solution where all seeds are located on the z = 0 surface is possible.

Since solving many simultaneous equations exactly will be computationally expensive and can be difficult to linearize, it is advantageous to limit the problem to overdetermined systems, where more equations are constructed than unknowns to be found, and minimise the error of the Euclidean distances from seed points to their corresponding vertices, given by:

$$\begin{aligned}\varphi_{sys} = \sum_a \left(d\left(P_a, A_{P_a}\right) = \ d\left(P_a, B_{P_a}\right)\right)^2 + \sum_a \left(d\left(V_a, A_{V_a}\right) - d\left(V_a, B_{V_a}\right)\right)^2 \\ + \sum_a \left(d\left(V_a, A_{V_a}\right) - d\left(V_a, C_{V_a}\right)\right)^2\end{aligned} \tag{33}$$

The coordinates of seeds, $x_{v,i}$, can then be estimated by placing the initial seed locations x_i, within a bounded domain:

$$x_{v,i} \in [x_i - \sqrt{A_i}, \quad x_i + \sqrt{A_i}] \tag{34}$$

Where A_i is the corresponding set of observed grain areas, used as an assumption of the confinement of the seed coordinates.

3.2.2 Representing a surface by a Laguerre tessellation

A typical EBSD map consists of an X-Y rectilinear measurement of crystal orientations and phase to resolve a microstructure with a fixed step size. Microstructure maps can be rendered from these data using the MTEX libraries for MATLAB (Bachmann, Hielscher and Schaeben, 2011), and in particular, regions of common orientation representing grains can be demarked. These grains are separated by grain boundaries, where the local difference in orientation exceeds a specified tolerance. The morphology of the material is described through the grain boundary network, with knowledge of the orientation of the grain retained.

Approximating the grain boundary network using the Laguerre tessellation (Aurenhammer, 1987), which will be used to represent the reference surface on one face of the RVE. The Laguerre tessellation is a modification of the Voronoi tessellation (section 2.3.3, page 49), with weighting for the cell area accounted for in order to give control over the grain size. Due to the weighting, the cell boundaries of the Laguerre tessellation are not equidistant from the two seed points defining it, unless the weightings of those seed points are equal. This enables the generation of a specific grain size distribution.

To reproduce cells associated with grains from the reference microstructure, I compute the Laguerre tessellation associated with the grain centroids c by assuming that our reference microstructure is approximated as a set of circular grains, giving $r^2 = \frac{A}{\pi}$ where A is the set of grain areas. This approximation is well suited for equiaxed grains, but may not accurately represent other structures, such as highly lenticular grains.

This Laguerre tessellation describes a surface approximating the EBSD map, as a vertex diagram that can be used to generate inclined grain boundaries with respect to the subsurface. The average crystallographic orientation of each grain is associated with the corresponding cell, to be transcribed into the RVE for use in crystal plasticity simulations.

3.2.3 Instancing a RVE with a single constrained surface morphology

If the Laguerre tessellation of cells of the X-Y plane is extended in the Z dimension, with its seeds located on that plane, all the grain boundaries of those grains will be columnar along the Z dimension. This is equivalent to extrusion of the surface microstructure and may not be appropriate (Diehl *et al.*, 2016). To produce inclined boundaries, I adjust the seed points relative to each other, along the Z dimension, while maintaining the threading line which is the cross product of the surface and the grain boundary plane. In order to achieve this, I use an optimisation scheme designed by Qiu, (2016) to minimise the error introduced to the trace of the grain boundaries on the Z = 0 surface.

In order to produce inclined subsurface grain boundaries, I reposition the seed points from the location of the corresponding grain centroids to anywhere within the 3D domain, requiring that the vertices of the surface grain traces satisfy the constraint of the reference Laguerre tessellation. The subsurface seed positions $c_v = (x_v, y_v, z_v)$ must lie within the interval defined by:

$$\begin{aligned} x_v &\in \left[x_s - 3\sqrt{A_s}\,, \quad x_s + 3\sqrt{A_s}\right] \\ y_v &\in \left[y_s - 3\sqrt{A_s}\,, \quad y_s + 3\sqrt{A_s}\right] \\ z_v &\in \left[z_s - 3\sqrt{A_s}\,, \quad z_s + 3\sqrt{A_s}\right] \end{aligned} \tag{35}$$

where A_s is the grain area for the centroid located at (x_s, y_s, z_s).

To simplify the computation of the new seed positions, I recalculate 3D surface cells using a pure Voronoi tessellation (noting that their 2D cross section will be optimised to minimise the error of the surface trace with the Laguerre tessellation), where the points x defined by $x \in V|\, d(x, c_s) \leq d(x, c_t)$, for the set of centroids $c_t = c - \{c_s\}$.

Each non-edge vertex represents a triple-junction between three grains, and the line segments between non-corner vertices are defined by the perpendicular bisector of the line between seeds. Since the scalar product of two perpendicular vectors is zero, the following equality holds for vertices v_1 and v_2 between two seeds, A and B:

$$-a_1 x_A - a_2 y_A - a_3 z_A + a_1 x_B + a_2 y_B + a_3 z_B = 0 \tag{36}$$

Where

$$a_1 = x_{v_2} - x_{v_1} \;\; a_2 = y_{v_2} - y_{v_1} \;\; a_3 = z_{v_2} - z_{v_1} \tag{37}$$

The location of the surface trace vertices can therefore be described as the set of simultaneous equations arising from the choice of position for each of the Voronoi grain seeds. Solving these equations exactly becomes challenging for a geometry of more than two seed points, since the system becomes overdetermined when the condition of equation (32) is satisfied.

I obtain the solution for the surface structure using an optimisation routine, utilising the MATLAB fmincon function to minimise the sum of the squared distances for each of the vertices solved by the set of simultaneous equations (36).

With near-surface seeds in place, the remainder of the volume beneath the surface seeds can be populated using routines that are based upon the approach in VGRAIN (Zhang, Balint and Lin, 2011) which have been ported into MATLAB.

3.2.4 Optimising the subsurface texture

The average grain orientations from the reference EBSD characterisation are applied to the corresponding surface grains in the 3D synthetic microstructure. This ensures a close approximation of the surface microstructure between simulation and experiment.

The orientations of the subsurface microstructure are statistically populated from the reference surface. First, we sample orientations from the orientation distribution function (ODF) which matches the reference surface characterised through EBSD. This assumes that the ODF of the surface plane is similar to the ODF of the subsurface volume.

Although constrained on the surface through the direct instancing of orientations in the reference EBSD map, throughout the 3D volume the neighbourhood texture of the misorientation distribution function (MDF), will be uncorrelated. This rarely matches with experimental data, and this is undesirable as the local neighbourhood of orientations is likely to play an important role in controlling deformation partitioning (Diehl *et al.*, 2016). Therefore, the initial texture population can be improved through a Monte Carlo based optimisation scheme.

Following a method like the one developed by Saylor *et al.*, (2004), the optimisation scheme relies of improving the selection of individual grain orientations based upon reducing a total cost function. This function consists of measuring the difference in spherical harmonic components for the MDF and ODF distributions and iterating until a satisfactory similarity is achieved (e.g. limited numbers of relative changes between Monte Carlo steps or a total difference below a threshold).

By partitioning the orientation space into 2000 bins of equal volume, the difference between two ODFs can be quantified by the binning of all the orientation observations. The MDF is also partitioned into 23 bins of 0.05 radians, for misorientation angles between 0 and 1.15 radians.

Therefore, an orientation bin is given by $g = \iiint \sin\Phi \; d\phi_1 d\Phi \; d\phi_2$ and a misorientation bin is given by $\Delta g = \iiint \frac{\sin\Phi}{-\sin\Phi} d\phi_1 d\cos\Phi \; d\phi_2 = \Delta\phi_1 \, \Delta\phi_2 \Delta\cos\Phi$. By considering the binned orientations $f(g)$ and misorientations $f(\Delta g)$, I can establish a cost function:

$$\lambda = \sum_{i}^{2000} \left(f_{model}(g)_i - f_{ref}(g)_i\right)^2 + \sum_{j}^{23} \left(f_{model}(\Delta g)_j - f_{ref}(\Delta g)_j\right)^2 = \lambda_{ODF} + \lambda_{MDF} \tag{38}$$

Each Monte Carlo step involves choosing at random between changing or swapping the orientation for a given grain, selecting randomly from grains whose orientation lies in the bins with the largest contribution to λ.

The swap operation simply exchanges the orientations corresponding to two subsurface grains, which changes the ODF slightly due to differences in volume, but more significantly changes the MDF.

The change operation selects a grain whose orientation bin has an excess contribution to the ODF when compared to the reference (i.e. $f_{model}(g)_i - f_{ref}(g)_i > 0$), then assigns a random orientation from generated from Euler angles within a bin which does not have an excess. Since the change operation alters the ODF contribution significantly more than a swap operation, the probability of choosing the change operation instead of the swap operation is controlled by $P(change) = \frac{\lambda_{ODF}}{\lambda}$. In RVEs with large numbers of subsurface grains, the λ_{ODF} contribution will be much smaller than λ_{MDF}, so $P(change)$ will be negligible and almost all the operations will be swaps.

Each iteration is performed on multiple cores (typically 16) and the best solution from the parallel computation is selected.

Overall, this iterative procedure results in a closer match between the synthetic and experimental textures, including neighbourhood effects. In practice, I have found that terminating this process after 20,000 iterations is sufficient for a volume with around 100 or more grains.

3.3 CP-FFT Simulation parameters

The crystal plasticity simulations in chapters 4 and 6 were computed using the DAMASK spectral solver. The material configuration parameters used are described in this section.

3.3.1 Stress and strain partitioning in TVCT volume elements

Two constitutive equations are used in the CP-FFT modelling of volume elements instanced through the TCVT method.

In order to break periodicity, the RVE instanced through TCVT was embedded in an isotropic medium across the domain boundaries. Another isotropic layer, designed to plastically deform easily and dilate, was applied to the reference surface, in order to enforce a plane stress condition.

Isotropic parameters	**Hard uniform layer**	**Compliant uniform layer**
C_{11}	169 GPa	1.69 GPa
C_{12}	122 GPa	0 GPa
C_{44}	75.3 GPa	750 MPa
$\dot{\gamma}_0$	0.001	0.001
n	20	5
h_0	100 MPa	1 MPa
τ_0	17.0 MPa	0.17 MPa
τ_{sat}	35.8 MPa	0.6 MPa
w	2.25	2.25
M	3	3

Table 4: Constitutive parameters for the uniformly plasticly-deforming layers used to break periodicity in TCVT-instanced RVEs.

These layers use a computationally cheap constitutive equation:

$$\dot{\gamma} = \dot{\gamma}_0 \left(\sqrt{\frac{3}{2}} \frac{\|\boldsymbol{S}^*\|}{M\,\tau} \right)^n \tag{39}$$

Where the slip rate $\dot{\gamma}$ is calculated from a reference slip rate $\dot{\gamma}_0$, the stress exponent n, the Taylor orientation factor M, and the absolute deviatoric 2nd PK stress tensor $\|\boldsymbol{S}^*\| = \left\|\boldsymbol{S} - \frac{1}{3}\mathrm{tr}(\boldsymbol{S})\right\|$. The hardening of the model is governed by the flow stress, which evolves for each timestep dt according to

$\tau = \tau_0 + \sum(\dot{\gamma} h_0 \left|1 - \frac{\tau}{\tau_{sat}}\right|^w dt)$, asymptotically approaching a chosen saturation value τ_{sat} with free parameters h_0 and w.

The RVE itself was modelled using the Hutchinson phenomenological constitutive equation (page 22).

Phenomenological parameters	
$\boldsymbol{C_{11}}$	169 GPa
$\boldsymbol{C_{12}}$	122 GPa
$\boldsymbol{C_{44}}$	75.3 GPa
$\boldsymbol{\dot{\gamma}_0}$	0.001
n	20
$\boldsymbol{h_0}$	100 MPa
$\boldsymbol{\tau_0}$	17.0 MPa
$\boldsymbol{\tau_{sat}}$	35.8 MPa
$\boldsymbol{a}$	10

Table 5: Constitutive parameters for the TCVT-instanced RVEs describing polycrystalline copper microstructures.

Hardening of the individual slip systems was conducted using a Voce-like hardening scheme:

$$\tau^{\xi}_{CRSS} = \tau^{\xi}_0 + \sum(h_0 \left|1 - \frac{\tau^{\xi}_{CRSS}}{\tau^{\xi}_{sat}}\right|^a \sum_k^N (\beta^{\xi k} \dot{\gamma}^k)\ dt) \tag{40}$$

As with the isotropic constitutive equation, the hardening asymptotically approaches a saturation value τ^{ξ}_{sat}, from the initial value τ^{ξ}_0. The matrix β describes hardening on the ξ^{th} slip system as a result of the hardening on the k slip systems in its family, differentiating between basal, prismatic, and pyramidal slip systems in hexagonal close-packed materials. The CRSS is then evolved based on the slip activity upon the k systems of that family. h_0 and a are phenomenological parameters.

3.3.2 Texture evolution of Ti-6Al-4V during high-temperature loading

In order to demonstrate the different material response during room temperature and high temperature deformation of Ti-6Al-4V, constitutive parameters for the elastic and plastic material parameters were devised, using computations of elastic stiffness constants through single crystal calculations at 25 °C and 550 °C (Simmons and Wang, 1971) . The CRSS values were taken from measurements at 20 °C (Zambaldi *et al.*, 2012). Using empirical measurements of the stress at 0.2% strain, at 20 °C and 538 °C, (Lerch and

Arnold, 2016), the CRSS values obtained by Zambaldi are adjusted by a factor of $\frac{1}{4.6}$. The initial CRSS value for pseudo-slip twinning was estimated as 125% of the $< c + a >$ pyramidal slip CRSS value, as per Philippe et al., (1995).

Isotropic parameters	Room temperature	High temperature
C_{11}	162.4 GPa	134.5 GPa
C_{12}	92.0 GPa	99.6 GPa
C_{13}	69.0 GPa	68.8 GPa
C_{33}	181.7 GPa	161.0 GPa
C_{44}	46.0 GPa	750 MPa
$\dot{\gamma}_0$	0.001	0.001
n	20	20
h_0	15 MPa	15 MPa
$\tau_{0,\ basal}$	349.3 MPa	49.1 MPa
$\tau_{sat,\ basal}$	568.6 MPa	192.7 MPa
$\tau_{0,\ prism}$	150 MPa	18.0 MPa
$\tau_{sat,\ prism}$	1502.2 MPa	82.8 MPa
$\tau_{0,\ pyramidal}$	1107.9 MPa	132.8 MPa
$\tau_{sat,\ pyramidal}$	3420.1 MPa	610.9 MPa
$\tau_{0,\ twin}$	1384.9 MPa	166.0 MPa
a	2	2

Table 6: Constitutive parameters for CP-FFT simulations of Ti-6Al-4V at room temperature and hot-rolling temperatures. Elastic constants obtained from Simmons and Wang, (1971). Room temperature CRSS values obtained from Zambaldi et al., (2012). Twinning CRSS estimated according to the method used by Philippe et al., (1995). High temperature CRSS values estimated to reproduce empirical values obtained by Lerch and Arnold, (2016).

4 Instancing of 3D microstructures from limited statistical information

This chapter demonstrates a method for generation of 3D microstructures which is useful for crystal plasticity simulations which emulate experimental tests, from 2D electron backscatter diffraction (EBSD) characterisation of a reference microstructure surface. Following the TCVT method outlined in section 3.2 (page 58), I create virtual instances of 3D microstructures with a surface which conforms to an approximation of a 2D copper dataset. The subsurface grains are controlled to ensure a representative population of grain sizes. The average crystal orientations of grains are controlled through an orientation distribution function (ODF) and the neighbourhood of grain orientations is controlled through a misorientation distribution function (MDF), in order to reproduce the texture of the characterised surface in the subsurface.

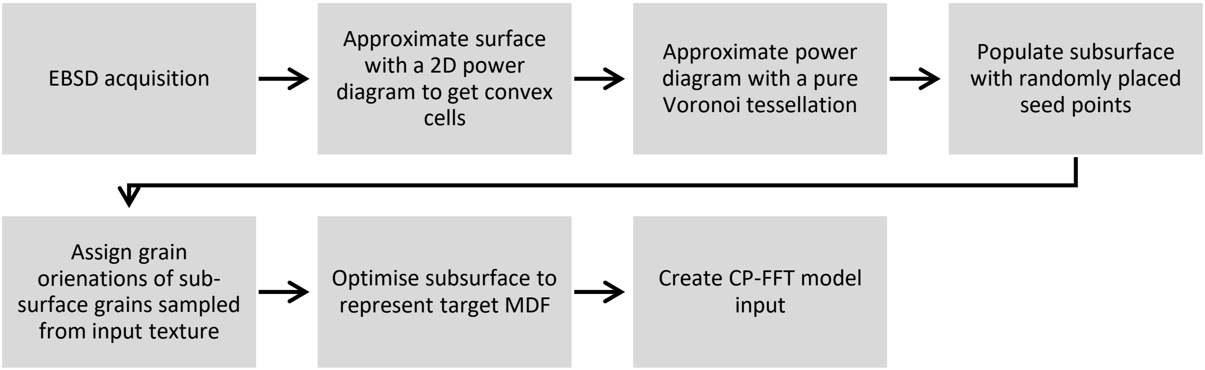

Figure 16: Flowchart describing the method for instancing 3D RVEs from 2D EBSD characterisation.

In this chapter I investigate this approach of generating microstructures by simulating deformation using the DAMASK FFT-based crystal plasticity solver. I break the periodicity of the loading conditions inherent to the spectral method through the addition of a plastic isotropic layer and impose a plane stress boundary condition on the surface constrained to the original reference through a dilatational "air" layer. I explore the utility of virtual instancing in order to evaluate surface stress field variation due to the underlying subsurface microstructure.

4.1 3D reproduction of a microstructure characterised in 2D by EBSD

While the method detailed in this chapter is applicable to any material system, EBSD characterisation of a copper oligocrystal microstructure provided an ideal dataset for 3D reproduction, with a small number of large, equiaxed grains. A lamellar microstructure, as seen in titanium alloys, becomes more difficult to reproduce when Voronoi seed points are moved to produce inclined out-of-plane grain boundaries, as seen in the small lenticular grains in Figure 17. This is due to the Voronoi tessellation requiring convex cells when reproducing the reference surface.

4.1.1 Controlling the surface grain size through Laguerre tessellation

The initial placement of near-surface grain seeds is constrained to the reference grain centroids, as seen in Figure 17. This does not neatly reproduce the grain boundaries observed in the reference map, with the smallest grains growing to be much larger than their original area, and the inclination of grain boundaries surrounding them being altered. Triple junctions have moved to describe the new shapes of the smallest grains, but the largest and most equiaxed grains have the most accurate reproduction of their morphology, with some triple junctions close to their original locations. The morphology of larger

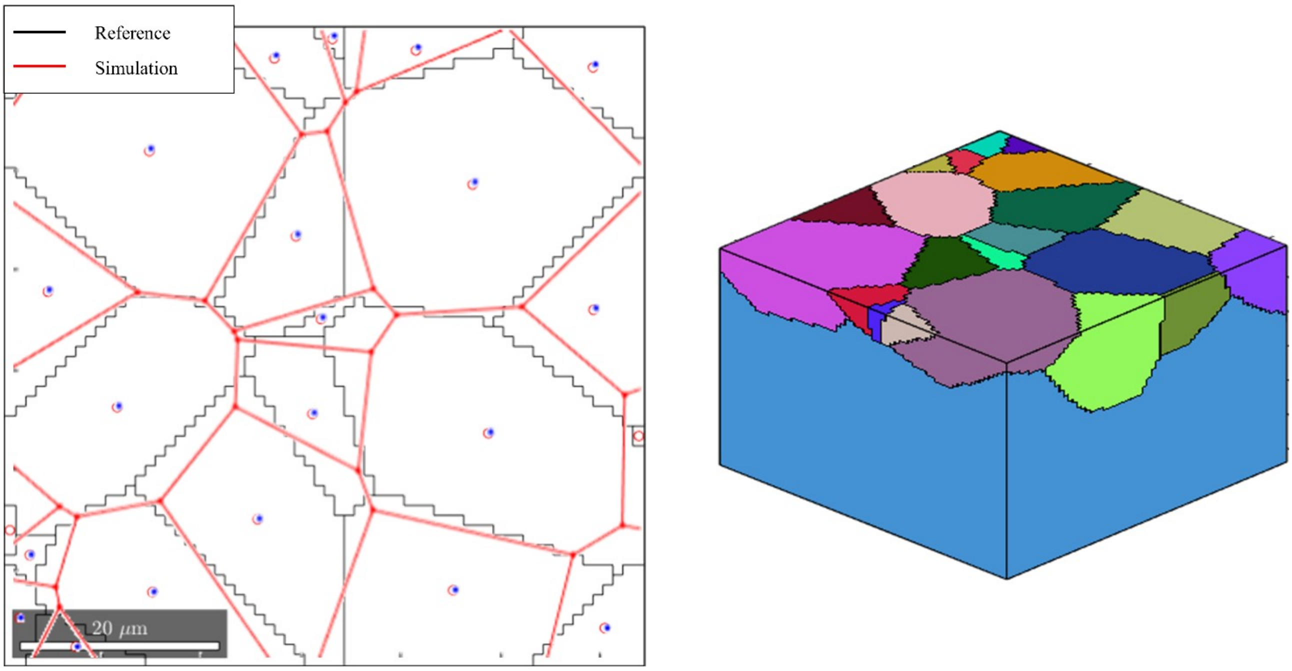

Figure 17: Comparison of voxelised computation of reference grains with MTEX, denoting their centroids, and the Laguerre tessellation of regions seeded at the centroids and weighted by the grain area.

lenticular grains is poorly reproduced, with additional triple junctions which are not present in the reference surface.

The areas of the grains generated by the Laguerre tessellation are strongly affected by the weighting assigned to each grain. This weighting determines where the grain boundary can be located. When the weighting of the points in the tessellation is assigned as a circle with an area equal to the corresponding reference grain, the resulting output grain area follows a strongly linear relationship with the reference grain area (Figure 18). This relationship does not hold when the Laguerre tessellation weighting is selected randomly from the areas of the reference grains. The clustering of grains around the origin demonstrates the incompatibility of generating the smallest grains observed in the reference, with areas significantly greater than their reference as seen in Figure 17.

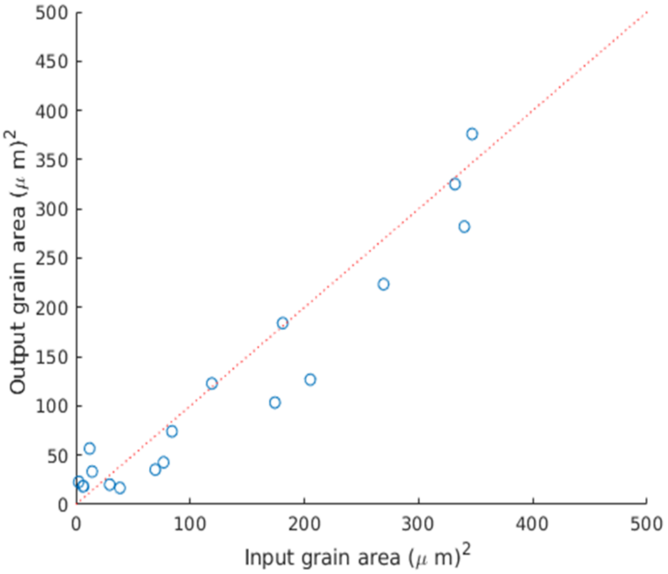

Figure 18: Comparison of the reference and generated near-surface grain areas for a Laguerre tessellation weighted by the corresponding grain area, demonstrating reproduction of the surface morphology.

After populating the subsurface grains, the distribution of volumes of the generated grains is dominated by the smallest grains (Figure 19), with observed frequency inversely proportional to grain volume due to the random packing of new grain seeds through a distance criterion, which will preferentially fit the largest voids. Using a stereological approximation of the reference surface grain areas as cubes, there is a similar dominance of very small volume grains, but no obvious relationship between larger grain areas and frequency is seen. Since the approximation of the surface grains as cubes does not account for the spatial exclusivity of the grains within the volume, it likely represents an overestimate of size, notably in the three largest grains, which would occupy a volume of 13000 equivalent voxels or greater, with 262144 voxels present in a 64 x 64 x 64 grid.

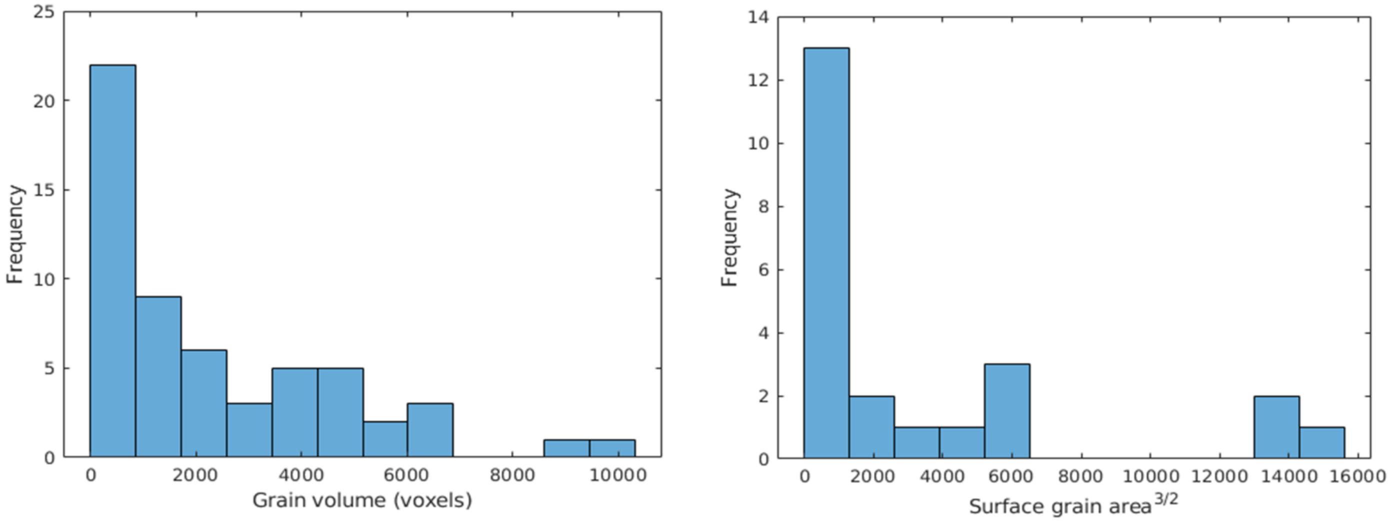

Figure 19: The volumes of all grains after population of the subsurface, and the stereological approximation of the reference grain volumes, as grain area raised to the power 3/2.

4.1.2 Measuring the inclination of subsurface grain boundaries

The extension of the surface grains in the Z direction is limited by the population of subsurface grains, which are shaded blue in Figure 17. The varying inclination of near-surface grain boundaries demonstrates the positioning of seed positions above the surface (outside the volume element) and below (inside the volume element), with a similar fraction of seeds above and below (Figure 20).

The vertical spacing of the seeds is close to linearity, between a range of 15 µm above and below the surface. The median z-position is very slightly below the surface. If all the near-surface seeds were constrained to the z = 0 surface layer, the grain boundaries depicted in Figure 17 would be columnar since their placement is excluded from the minimum distance constraint used for the assignment of the subsurface seeds. The empirical cumulative frequency of grain boundary inclinations with respected to the vertical direction, between the grains generated by the near-surface seeds, indicates a median inclination of around 8°. The maximum inclination is approximately 83°, with largest grain boundary inclinations being less frequent since this requires a pair of seeds to have a very large difference in Z-spacing, with very small differences in Euclidean distance in X and Y.

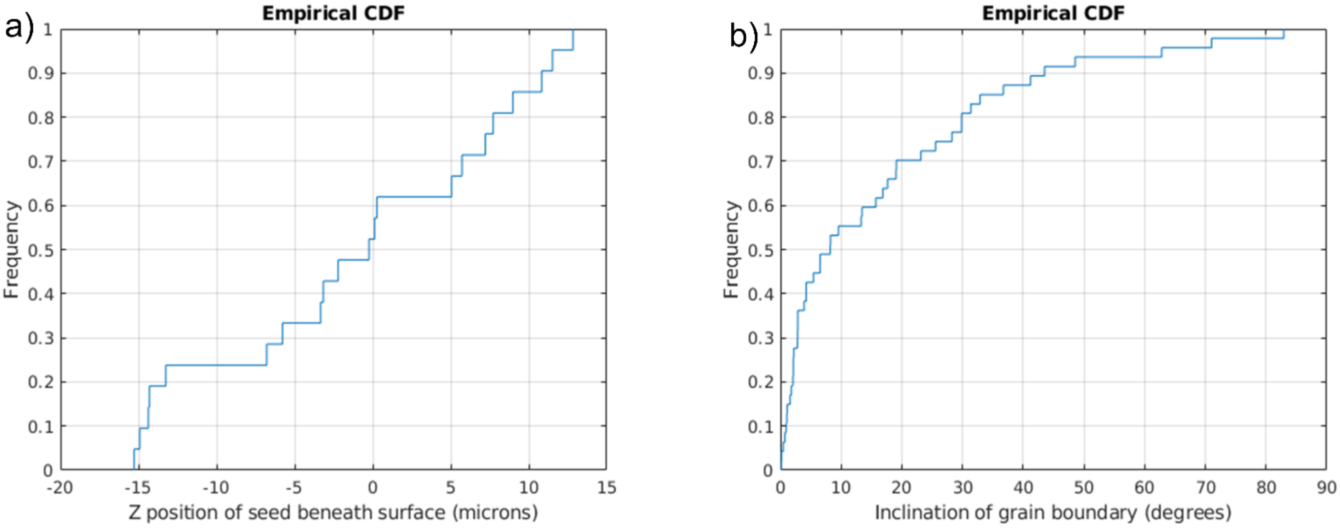

Figure 20: Cumulative distributions of the 3D near-surface grain structures, through the Z-positions and grain boundary inclination angles.

4.1.3 Validation of the method by comparison to Voronoi tessellation

For the reference surface described in 4.1.1 which contains 23 grains, 97 grains have been assigned to the volume element. By generating 10 microstructures of 64 x 64 x 64 voxels through Voronoi tessellation with randomly placed seed points, I can compare the morphology of the TCVT-instanced microstructure with another method used in crystal plasticity simulations.

From the empirical cumulative distribution function (CDF) of surface grain boundary inclinations with the vertical direction, calculated for the 10 RVEs, there is a bimodal distribution of grain inclinations, between 0-10° and between 80-90° Figure 21). The former grouping resembles the near-vertical grain boundaries seen in Figure 20. However, since there is no exclusion-zone below the reference surface, which is necessary in the 3D instantiation to preserve the morphology of the reference surface, new seeds may be placed in the Z dimension close to the seeds which produce the grains visible on the surface, which produces the second grouping of grain boundaries with inclinations between 80-90°. This potentially indicates that the subsurface exclusion-zone is too large.

The grain volumes generated by Voronoi tessellation (Figure 21) are dominated by moderately-sized, equiaxed grains of 2000-3000 voxels (out of a total volume of 262144 voxels), which is to be expected as a uniform random distribution of 100 grains would assign 1% of the total volume to each grain on average. However, by taking a stereological approximation of the grain volumes, from the areas of 23 grains of the plane Z=1 raised to the power 3/2, I observe a similar pattern to that seen in Figure 19. The smallest grain areas in a 2D-characterised dataset are therefore underestimated in volume within the 3D RVE. There is an associated increase in the estimated volume of the very largest grains of the reference surface as a result, seen from the group of grains on the surface with stereological volume estimates of between 4000 and 5000 voxels.

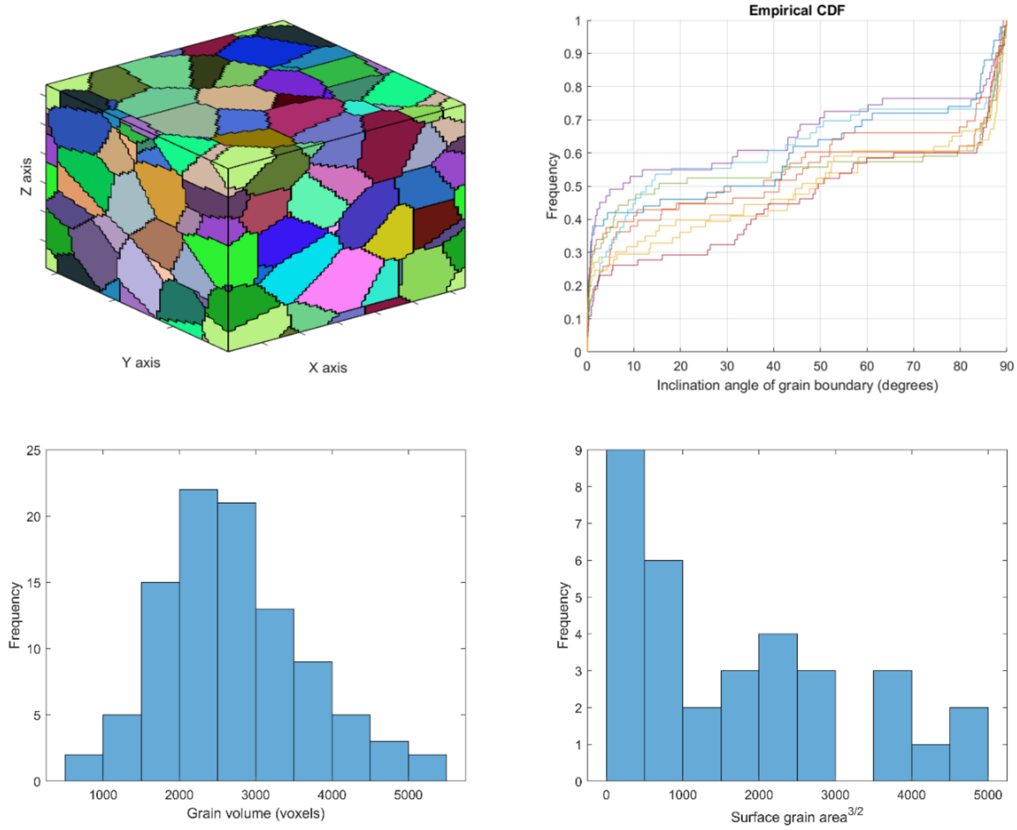

Figure 21: Representative volume element generated by Voronoi tessellation generated from 97 randomly-located seeds, with the histogram of the grain volumes, and a stereological approximation of the Z=1 surface grain areas, raised to the power 3/2. The empirical cumulative distribution functions (CDFs) of grain boundary inclination for 10 separate volumes are shown.

4.2 Texture reproduction in the subsurface microstructure

For the reference surface generated in 4.1 which contains 23 grains, the 74 subsurface grains have been randomly assigned orientations selected from the surface. The reference surface ODF is matched by the ODF of the 97 grains in the instantiated microstructure, since the orientations of the subsurface grains of the volume element are assigned at random according to their frequency within the ODF. With a convolution width of 5°, the pole figures do not show any features which are easy to distinguish. Despite this, the neighbourhood of orientations has not been reproduced after random assignment, resulting in a very different MDF in the assigned subsurface compared to the MDF of the reference surface (Figure 22a, b). Due to the relatively low number of grains present in the surface and the RVE simulation, 23 and 97 respectively, the MDF assigned to the subsurface is not initially random, since there is a limited number of misorientations that can be generated from the 23 orientations assigned.

Following the optimisation of the texture through 20000 grain orientation swap and change operations, the ODF has not evolved significantly (Figure 22c). However, the MDF has been transformed, with some of the characteristic features of the MDF emerging. Through the histograms of misorientations present in the surface, and each of the two RVEs generated (Figure 22a, b, c), the lack of agreement between the MDF of the reference and after random assignment is clear, and the improvement of the MDF after 20000 texture operations is notable, although it does resemble a Mackenzie-like distribution, due to the low degree of freedom in reproducing the texture from only 74 sub-surface grains available to replicate the surface texture MDF.

The record of the ODF and MDF contributions of the cost function (equation (38), page 59), after each accepted operation (Figure 22g), demonstrates that after random assignment, the contributions from the two components are similar, but the ODF contribution reduces to become negligible after around 30 accepted operations for this surface. For the 20000 operations attempted, only 114 successfully reduced the cost function of the ODF and MDF and were accepted.

Reproducing a reference surface with 157 grains also shows agreement of the ODF between the surface and subsurface before optimisation (Figure 22d, e). After 20000 texture operations, the ODF is sharpened, with orientations which are common in the random assignment increased further in frequency. The MDF for the subsurface of the microstructure after random assignment is much more uniformly random than the microstructure with fewer grains (Figure 22b, e), with the histogram of misorientation angles following the Mackenzie distribution. Since this volume contains more than 1000 grains, there are enough grain boundaries to reproduce the MDF with good agreement after 20000 texture operations (Figure 22f).

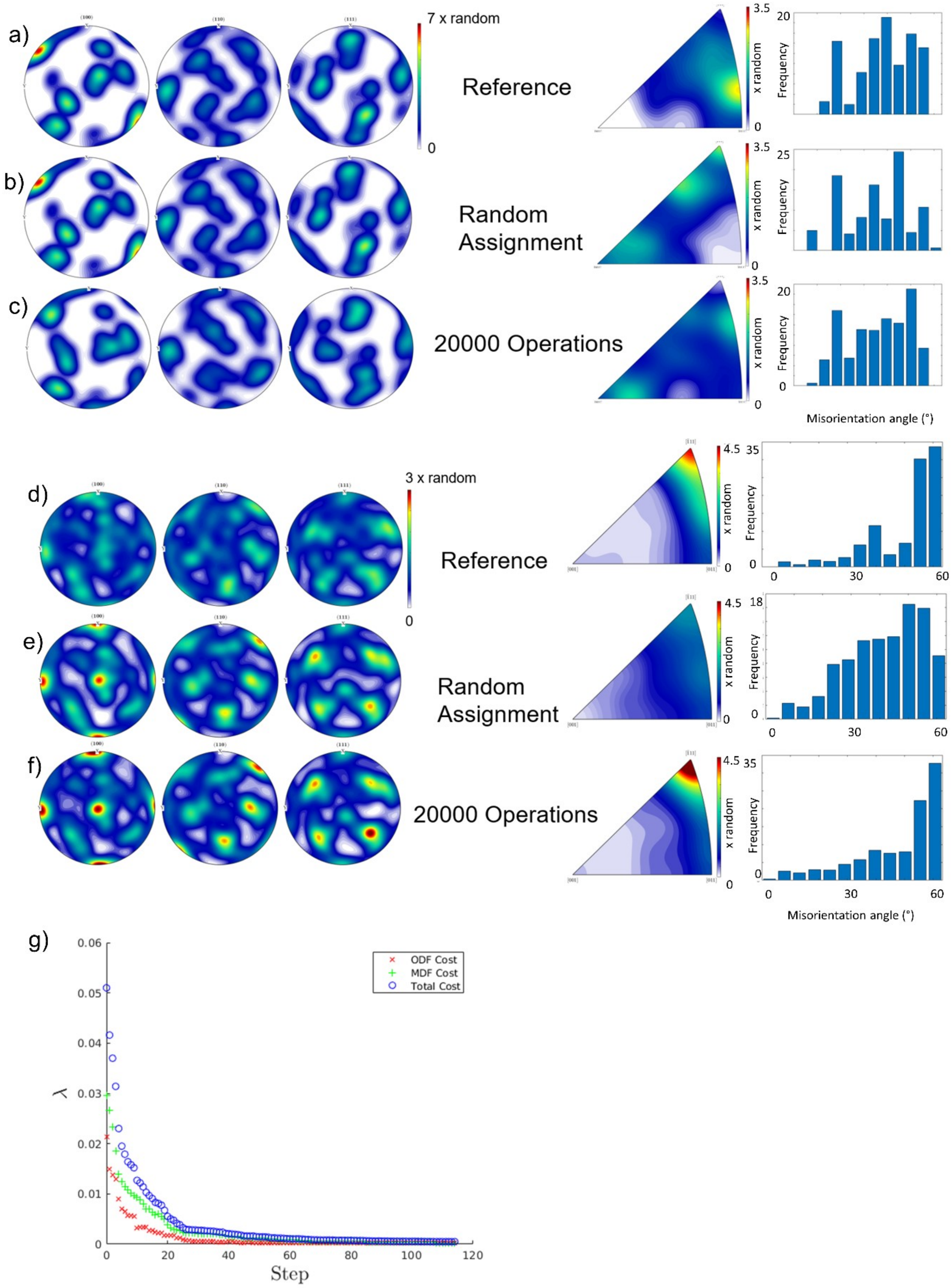

Figure 22: Demonstration of 3D texture population using the Monte Carlo method from two reference surfaces, one containing 23 grains (a, b, c) and one containing 157 grains (d, e, f), comparing the reference (a, d), initial assignment (b, e), final assignment (c, f), and the convergence of the cost function for the 23 grain case (g), given by equation (38), page 59, calculated after each accepted texture operation.

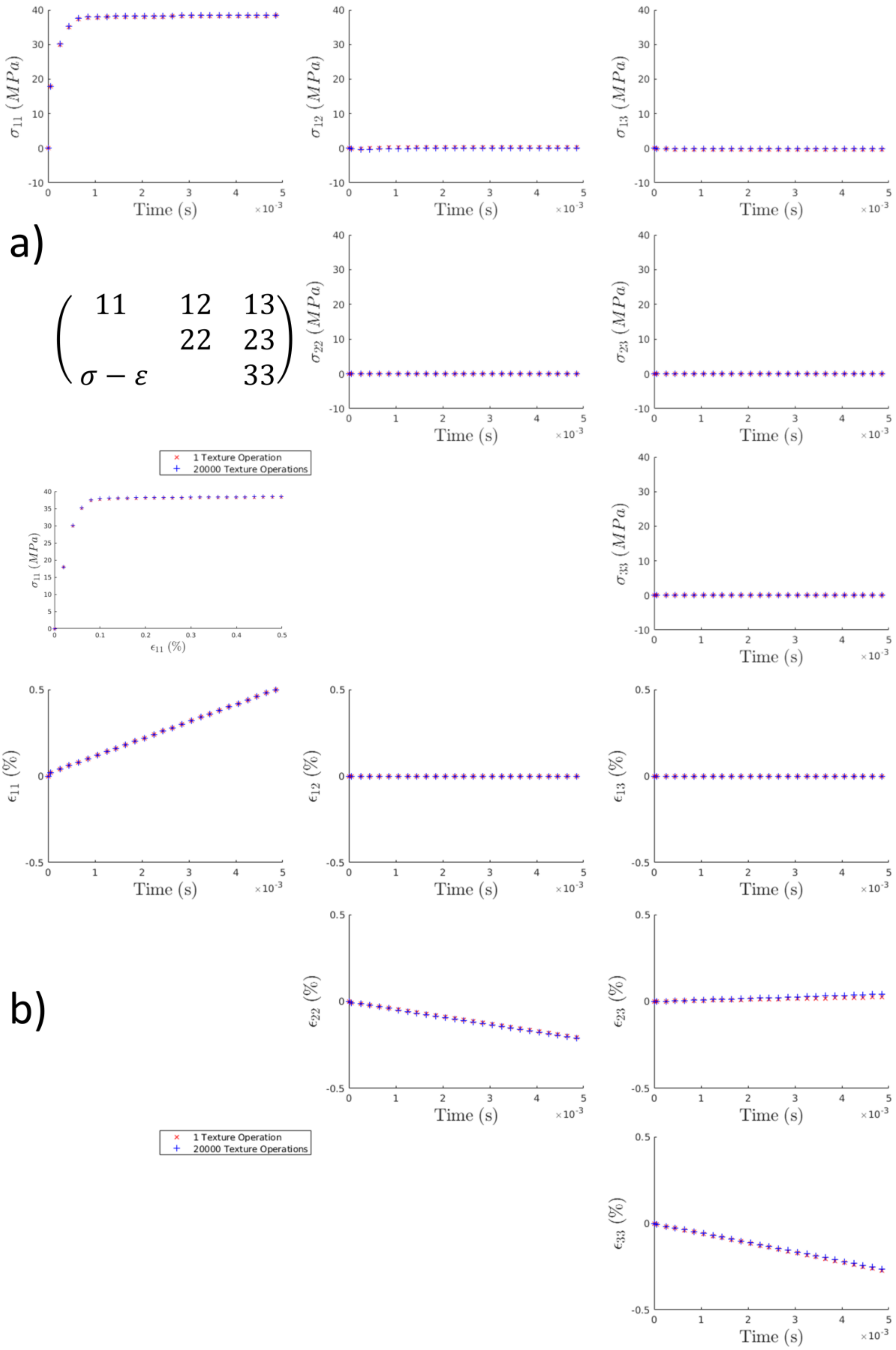

Figure 23: Macroscopic time-plots of stress (a) and strain (b) tensor components, showing the similarity of the macroscopic performance is similar in RVEs with and without MDF texture optimisation. Stress-strain 11 component plot show as inset.

The misorientation histograms for the reference surface containing 157 demonstrate the improvement of recreating the texture with such a large number of grains, over the reference of 23 grains. The reference surface misorientation histogram is very different from the Mackenzie distribution, and is recreated by the texture optimisation.

4.3 Macroscopic stress and strain behaviour

For the grain morphology instanced from the 23-grain surface, two CP-FFT models have been produced, corresponding with the textures shown in Figure 22b, and Figure 22c. During deformation to 0.5% strain along the X-axis of the volume element, I recorded the average stress and strain states of the polycrystal after increments of 2 seconds, corresponding to 0.02% in incremental applied strain. The macroscopic stress tensor for both models shows that for the duration of the loading, only the σ_{11} component is non-vanishing, with only very slight differences in the magnitude of the stress at each increment (Figure 23a).

Similarly, for both textures, the hydrostatic strain tensor components ε_{11}, ε_{22} and ε_{33} are linear (Figure 23b), with extension in the 11 direction per increment of applied load, and corresponding compression in the 22 and 33 directions ensuring that the overall volume of the models are conserved. It follows that the macroscopic stress-strain behaviour $\sigma_{11} - \varepsilon_{11}$ is also equivalent (Figure 23a, inset).

4.4 Local variation of surface stress and strain behaviour due to subsurface texture

Measuring the stress and strain states of the model reference surface, after the final increment of deformation, we observe strongly localised partitioning of the stress and strain tensor components, according to the influence of the subsurface texture in both the randomly assigned case (Figure 24a) and the optimised texture after 20000 operations (Figure 24b). This leads to calculation of the differences between both maps (Figure 24c), with differences at grain boundaries and near triple junctions of up to 30 MPa, a magnitude similar to the yield point observed empirically in Figure 23a, approximately 38 MPa. This relationship holds true for all 6 unique components of the stress and strain tensors, suggesting some differences in plastic deformation resulting from all hydrostatic and all deviatoric strains.

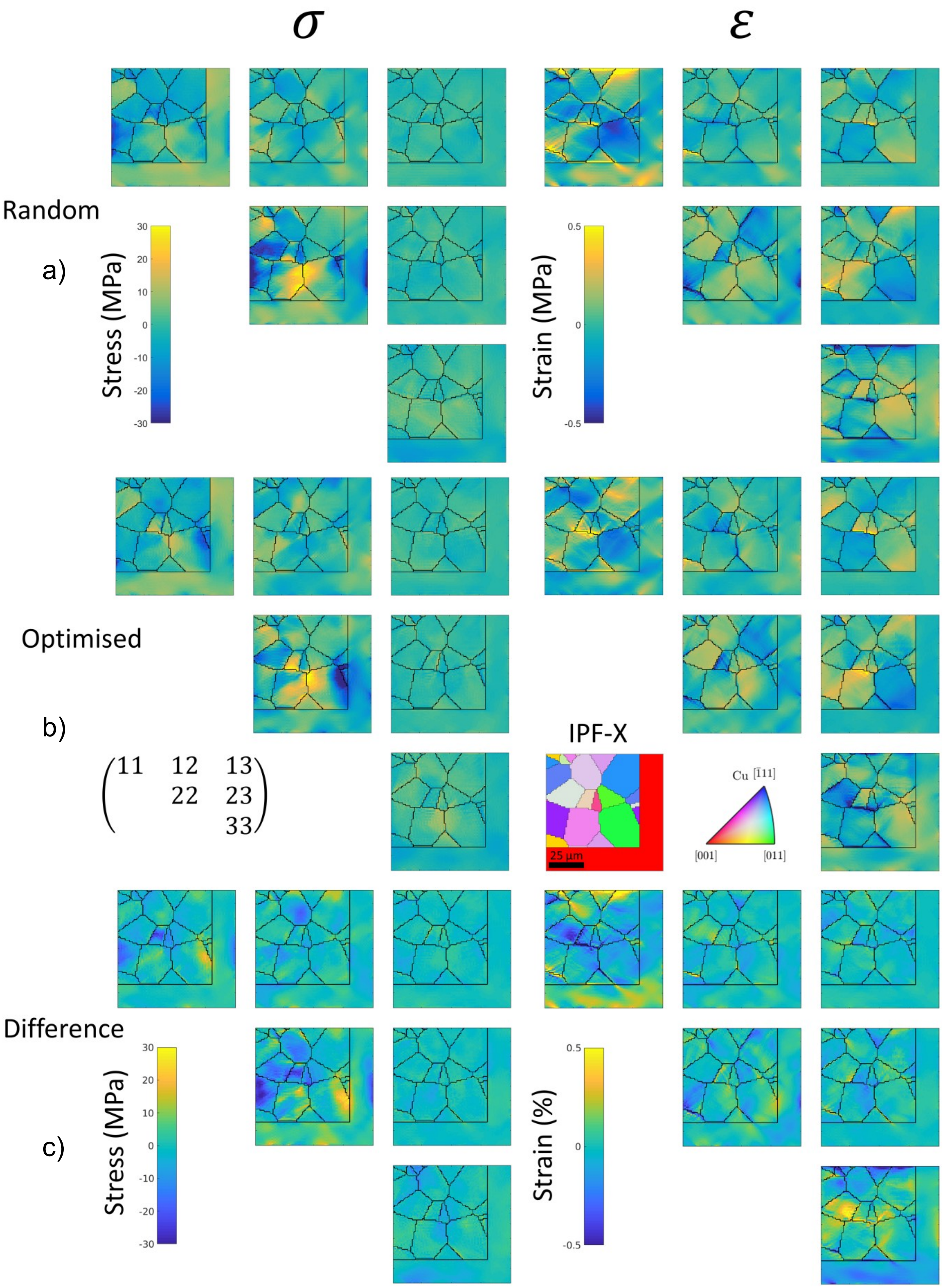

Figure 24: Stress and strain maps for the reference surface, after instantiation of a CP-FFT model under 0.5% strain in X, with randomised subsurface texture (MDF) (a), subsurface texture optimised to represent the surface MDF (b), and the difference plot between the two models (c).

5 Thermomechanical processing of Ti-6Al-4V

This chapter examines the evolution of texture during deformation of Ti-6Al-4V by hot rolling. Through measurement of local crystal orientations through EBSD, I present changes in the microstructure morphology and crystallographic texture together, showing the changes in structure which occur during thermomechanical processing. I characterised the material in an as received condition (supplied kindly by TIMET) and measured the initial texture and phase composition. The material was heated in a furnace at a temperature of 950 °C for one hour and air-cooled, and I measured the changes of the texture and microstructure through EBSD. Next, I rolled the material at temperatures of 750 °C and 900 °C with 30% thickness reduction, and to 75% thickness reduction. Before each rolling trial began, the material was heated for one hour at the target temperature and reheated between rolling passes. After the final thickness reduction had been achieved, the material was air-cooled. I selected these temperatures and strains to compare the textures formed after rolling at different temperatures below the β-transus with an aim to recreate a texture reported in the literature, which I could not achieve. I designed the rolling trials and subsequent texture analysis to explore why this might be the case and have used crystal plasticity methods (in chapter 6) to test these hypotheses.

5.1 EBSD measurement of texture in unidirectionally rolled Ti-6Al-4V plate

5.1.1 As-received material

The Ti-6Al-4V material supplied by TIMET has been forged firstly in the β-phase field and secondly in the α + β-phase field. This route was selected with the intention of forming a fully recrystallised material structure comprising of many refined grains. This forged ingot has been rolled in the α + β-phase field at 950 °C, just below the β transus of 980 °C, through a proprietary method of rolling gap reductions, until a reduction to 20 mm thickness has been achieved, with a microstructure comprising of equiaxed primary-α grains. The rolled plate is lastly creep-flattened below the α + β-phase field to ensure a cuboid shape with flat, perpendicular faces (Timet UK Ltd., 2019).

EBSD mapping of as received and heat-treated material was performed in the RD plane. Maps were captured for an area which is 820 μm in height by 550 μm in width, with a step size of 1μm.

Crystal orientations with respect to the TD are represented and are coloured using the IPF colour key, as shown in Figure 25. These maps reveal regions of common orientation called 'macrozones'. The macrozones are typically seen as large regions of 'red' (i.e. < c > along TD) where the finer scale α-grain structure is nearly contiguous. In this RD section, the macrozones present as long elliptical features with their long axes along TD.

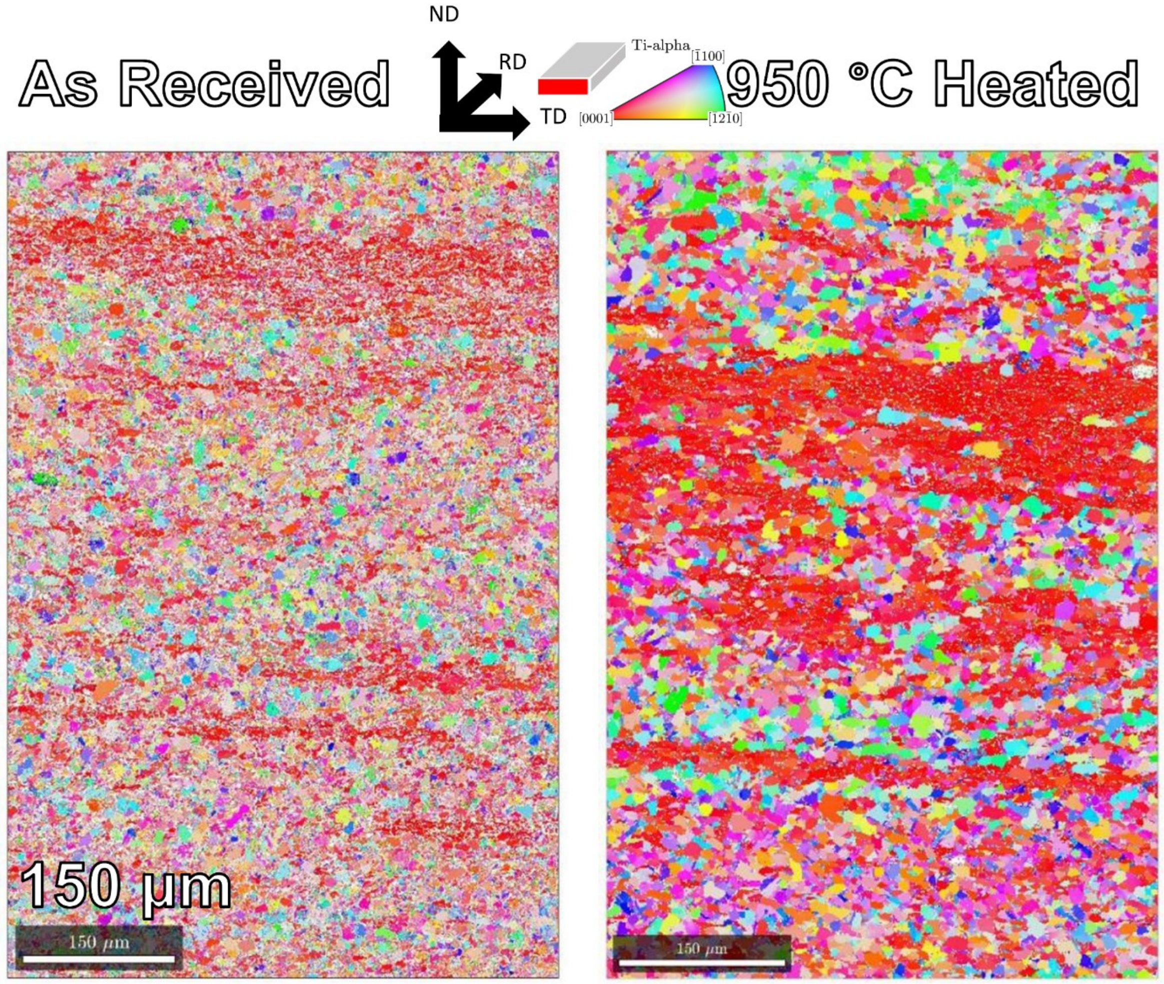

Figure 25: EBSD characterisation of as-received and heat-treated Ti-6Al-4V material, coloured by the IPF-TD.

These EBSD-based observations are supported with polarised light microscopy of the as-received and as-rolled material (Figure 27). From these micrographs, the sample contains lenticular α grains which are 10-20 µm in size. Clusters of these grains have similar crystal orientations (indicated by their colour in the polarised light micrographs, which varies according to the <c> axis of the crystal in the α-phase) and these are lenticular regions of more than one millimetre in length. These are macrozones. The long axis of the grains and the macrozones are colinear and aligned with the TD. The macrozones are around 200 µm in thickness along ND. The macrozone appears to be interlaced with equiaxed α-phase along its long edges, breaking up the region of common orientation into bands. It is more challenging to observe these features consistently within the polarised light micrographs than with EBSD. The region containing a macrozone does not index completely and contains some fine scaled retained β-phase at room temperature.

Between the individual macrozones are regions containing equiaxed α-phase grains, with a variety of different crystallographic orientations. The crystallographic texture is revealed in the (0002) pole figure seen in fig 5.2. In the texture plots, the spatial data is removed, but the area fraction of the different orientations is encoded in this rendering of the frequency distribution. There is a central pole of grains with their <c> axis aligned with the ND, these correspond to cyan-coloured grains within the IPF-TD colouring of Figure 25. Spatially, this texture fibre is distributed throughout the map and is comprised of some of the regions of common orientation within the microstructure.

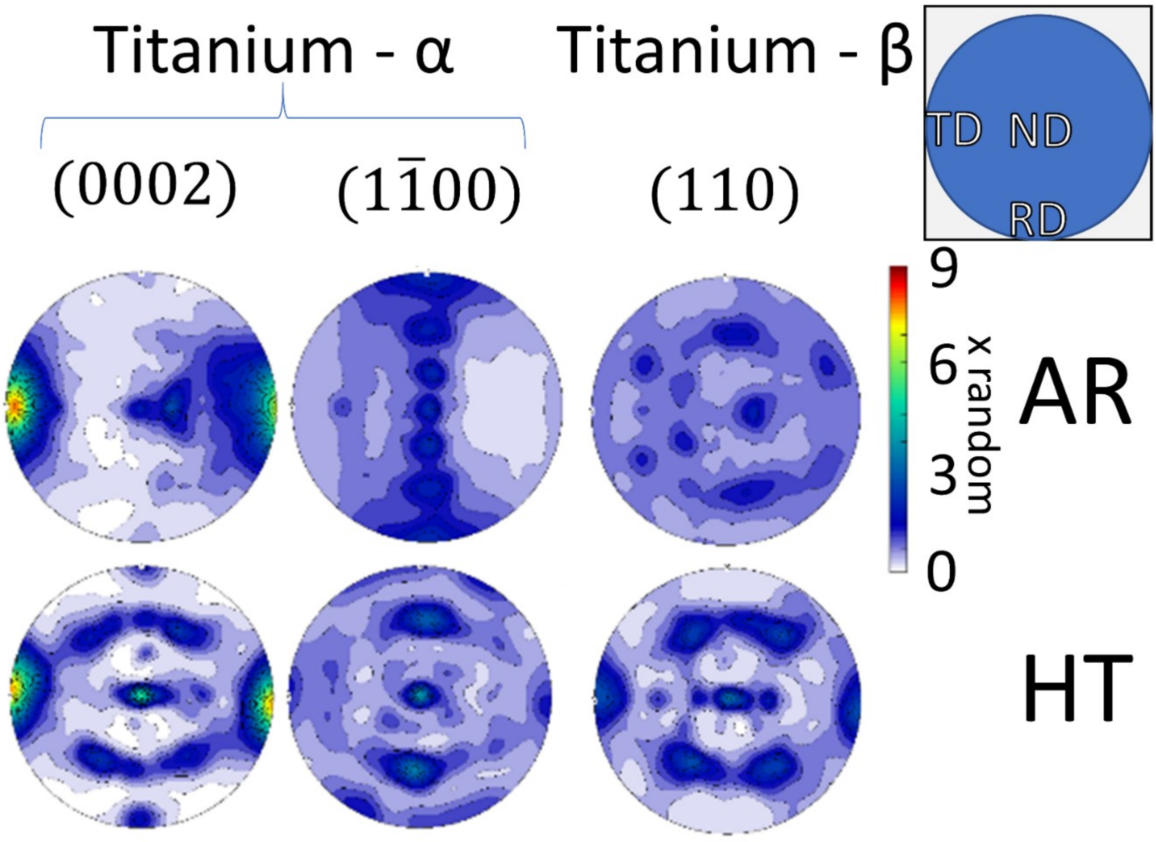

Figure 26: Pole figures displaying the orientations present in the texture of as-received and 950 °C heat-treated Ti-6Al-4V.

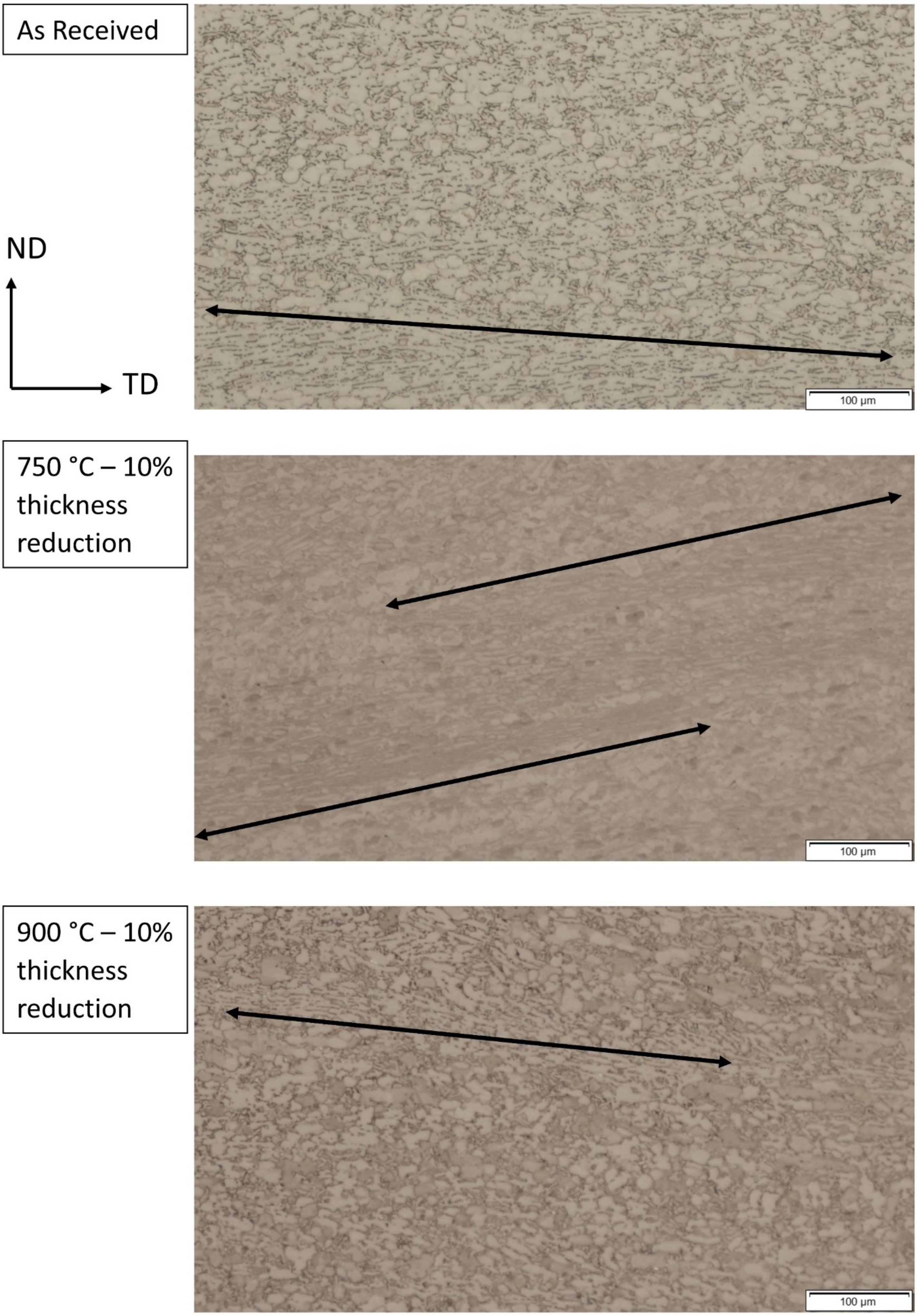

Figure 27: Polarised light microscopy of Ti-6Al-4V, as-received and as-rolled at 750 °C and 900 °C to 10% thickness reduction. Light indicates α-phase and dark indicates β-phase.

5.1.2 950 °C heat treatment

Compared to the as-received condition, a 950 °C heat treatment for one hour increases the EBSD pattern indexing rate from 83% to 96%, for an area of 823 μm in height and 548 μm in width, observed with a beam step size of 1 μm. This is likely energetically driven due to a reduction in strain gradients within the grains, as well as coarsening of the microstructure.

For both samples, the texture is dominated by the TD fibre, with this orientation occurring 7x more frequently than would appear at random, when the pole figure is binned to within 5°. However, the IPF map of the 950 °C heated material shows primary-α grain growth, both for grains aligned with the macrozones (Figure 25, red grains), and grains aligned away from them. The growth of off-macrozone grains contributes a new off-macrozone texture fibre, with cube on-edge β grains visible in the (110) β pole figure and these related to the (0002) α pole figure through the BOR. This results in a strong pole indicating a fibre grains with their basal plane normal direction aligned with ND (Figure 26). A faint pole with a basal plane normal direction aligned with RD is visible in the heat-treated material figure, indicating growth of RD-aligned alpha grains.

A rotation of the on-macrozone grains is notable from the $(1\bar{1}00)$ pole figures, as in the as-received case there are two superimposed fibres, separated by a 30° ϕ_1 rotation of the hcp unit cell, from on-edge to on-face.

5.1.3 Estimation of phase fractions of Ti-6Al-4V measured by DBS

Measurement of the phase faction of the two phases is difficult, especially when there is relatively poor indexing of the β-phase in the EBSD maps.

Following acquisition of direct electron backscatter across a sample, a range of backscatter intensities are collected across the sample surface. In the thresholding method, to separate the two phases, a suitable threshold value is selected to partition the data between the two phases. Pixels with intensity values below the threshold value are considered to be the α-phase and pixels above this value are the β-phase. This binarization is well described, provided that the two phases are well separated in intensity space. However, for this data this is not the case as shown in Figure 28, where several diffuse noisy alpha grains have intensity values above 30, while some of the β grain centres have values below 30. The white balances of the images are inconsistent due to changes in sample cleanliness, so the threshold must be changed for each image. This reliance on human intuition makes the systematic error difficult to quantify. In figure 1, 14.58% of pixels lie above a white level of 35, but only 6.98% are above 50. Since for this material, the β-fraction is typically around 10%, this confirms that a threshold binning is not an acceptable method to measure the phase contrast reliably, as there is no way to know which threshold is more appropriate.

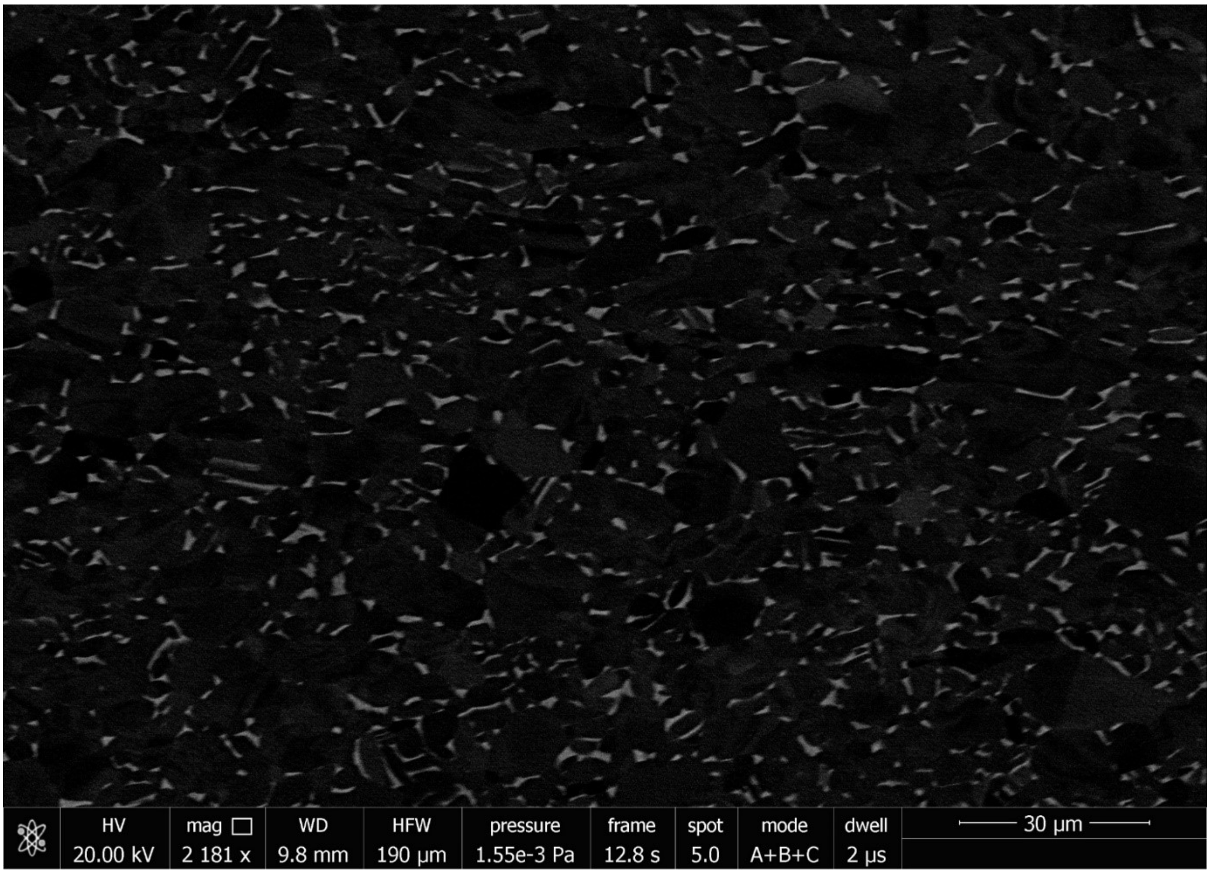

Figure 28: Electron backscatter image, optimised for phase contrast in Ti-6Al-4V. The lighter colour is the higher atomic density β-phase which plates the equiaxed primary α-phase.

As an alternative analysis, we can use a statistical deconvolution method. In this case the distributions of intensity values for the two phases are considered to be described by two independent Gaussian distributions. These two distributions can overlap. I can extract the phase fractions by fitting two Gaussian functions to the data and counting the area under each. This method is reasonable when considering the total area fractions assigned to each phase, but for points within the map with a white intensity located in the intersection of the distributions, I am unable to determine which phase is present.

A schematic of this deconvolution method is shown in Figure 29, with the histogram of white intensities marked by open circles, and the Gaussian fits superimposed as lines.

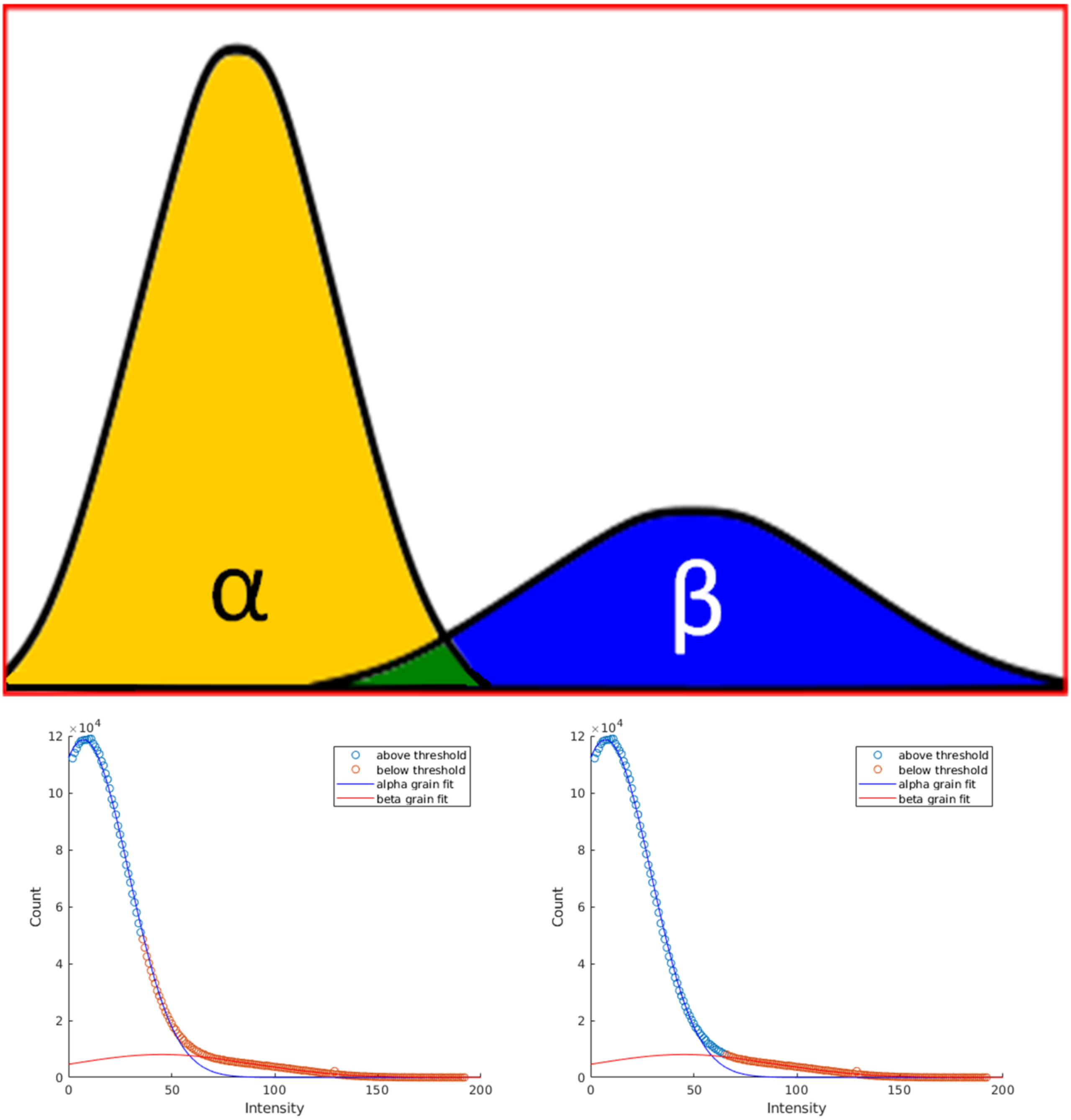

Figure 29: (Top) Schematic representation of the frequency-intensity histogram for a dual phase backscatter image, with α-phase in yellow, β-phase in blue, and an overlapping region in green. (Bottom) of the Gaussian decomposition with thresholding at 35 (left) and 65 (right).

A comparison of the phase fractions for ten regions from the RD face of as-received Ti-6Al-4V recovered using thresholding and the Gaussian decomposition method are shown in Table 7. I have chosen to consider the intersection of the two Gaussian distributions as the uncertainty of the beta phase which is indistinguishable from alpha.

ImageJ thresholded histogram			Gaussian decomposition	
50 bin (%)	35 bin (%)	Image	Integrated Beta Gaussian area fraction (%)	Area fraction of Gaussian intersection (%)
6.8	14.4	1	6.3	0.64
7.0	14.6	2	15.1	9.83
7.7	15.6	3	13.7	7.91
7.0	14.5	4	14.1	8.52
7.5	16.8	5	14.0	8.26
7.6	16.2	6	13.2	7.38
7.8	16.5	7	14.5	8.96
7.4	15.0	8	15.9	10.37
6.5	14.3	9	6.6	1.14
5.2	11.4	10	16.3	12.62
7.0	14.9	average	13.0	7.56

Table 7: Beta fractions estimated from 10 separate locations of an as-received Ti-6Al-4V sample, estimated from thresholded histograms in ImageJ, and through Gaussian decomposition.

For almost all the regions, the beta fraction found by Gaussian decomposition is between the two values found by thresholding the histograms in ImageJ, with the average area calculated by Gaussian decomposition being 13.0% ± 7.56. The β-fraction of Ti-6Al-4V observed in literature is typically towards the lower end of this estimate, but values greatly above this range have been reported after rapid quenching from near the β-transus. As the as received material was mechanically deformed by creep flattening in its final processing step, I feel this estimate is reasonable.

5.2 Small rolling strains in Ti-6Al-4V

5.2.1 Rolling procedure

Each rolling bar was cut to 25 mm in width and 50 mm in length by electric discharge machining, and then milled down to 15 mm in thickness (to provide a fixed width and remove surface contamination). Before rolling, each bar was heated in a furnace at the indicated temperature for the rolling trial for 30 minutes, and the temperature of the sample was measured. The bars were taken from the surface and rolled to a total thickness reduction target in passes of 10% of the thickness before each rolling step, using a mill with (room temperature) steel rollers of 5” diameter, sequentially at an initial rolling speed of 25 revolutions per minute. Note that as the rollers were at room temperature, the bars a significant die chill as they passed through the mill.

After each bar completed a pass through the mill, its thickness was measured with Vernier callipers to the nearest 100th of a millimetre. For bars subject to several rolling passes, I reheated them for two minutes to restore them to the rolling temperature. When the final pass for each bar had been achieved, it was placed on a metal block to cool in air.

5.2.2 Comparison of morphologies and textures formed

In all six samples rolled to 30% thickness reduction or lower, the α texture remains dominated by the macrozones of the TD fibre (Figure 31, red grains of Figure 30) and this texture is spread over 20-30 degrees. In these samples the off-macrozone grains are randomly oriented. For the as-received material the macrozones are contained within a narrower distribution of orientations. This is indicative of slip and whole grain rotation within the macrozones. The spatial arrangement of the overarching macrozone as a potential structural unit is retained, indicating that deformation is not sufficient in this temperature, strain, and strain rate deformation state to result in macrozone breakup.

In all maps except 20% reduction at 950 °C, the macrozones are contiguous and spatially oriented along the TD. For these maps, the macrozones themselves contain several of the largest grains present in the map and these are separated spatially and by orientation.

In all maps except 20% reduction at 950 °C, the macrozones are contiguous and spatially oriented along the TD. For these maps, the macrozones themselves contain several of the largest grains present in the map and these are separated spatially and by orientation.

Morphologically in these cross sections, the macrozones are lenticular in shape, and are comprised of lenticular primary α grains contained within a β matrix. Although the fine β grains produce poor EBSPs which have not indexed well, they are apparent from the pattern quality map (Figure 32), where the softness of the β allows for high relative plastic deformation compared to the α, with the increased GND density reducing the pattern quality. The off-macrozone primary α grains are relatively equiaxed, but with significant variation of grain size.

Some orientations aligned towards the ND are present in the α (0002) pole figures after 10% and 20% thickness reduction, which may be retained from the as-received texture.

After 10% thickness reduction at 750 °C there is an insufficient number of β grains observed to compare the texture of this phase confidently, with less than 3% of the map area indexed as β.

Thickness reduction	750 °C	900 °C
10 %	3340 grains	2669
20 %	2033	3119
30 %	1963	3288

Table 8: Number of grains calculated by MTEX in Ti-6Al-4V rolled at 750 and 900 °C, using a neighbouring-pixel threshold misorientation angle of 20°.

After 30% thickness reduction, there is little of the original ND-aligned basal fibre remaining in the α (0002) pole figure. As this EBSD map observed 1963 grains (Table *8*: Number of grains calculated by MTEX in Ti-6Al-4V rolled at 750 and 900 °C, using a neighbouring-pixel threshold misorientation angle of 20°.Table 8), with a minimum grain size of 5 pixels, this demonstrates that α grains with basal planes aligned with the ND are not present in the material.

For the 30% thickness reduction, the β (110) figures show the β texture evolving away from the as-received configuration, towards an edge-on cube texture, with the differences of the pole figures becoming more apparent with increasing strain for both temperatures. The presence in the β (110) pole figure and absence in the α (0002) pole figure shows that this texture has formed through deformation of the β titanium which has been retained below the transus, without any transformation to α titanium, since these orientations would be inherited through the BOR.

For the 900 °C rolling to 30% thickness reduction, the ND || (0002) fibre is not removed from the α pole figures. In the β (110) pole figures, the texture is rotated from the as-received condition, towards the rolling direction after 10% thickness reduction, with 9.20% of the EBSD map is indexed as β. After 20% reduction , a new texture fibre has formed with two bands of frequent orientations (Figure 31, centre-right), one a ring centred 20° away from the rolling direction, with a width of around 15°, and the other a band connecting the axes of the TD. Further deformation to 30% reduction shows the emergence of the x-shaped fibres present in the 750 °C rolling, but with similarities to the as-received β texture.

From the quality maps in figure 5.4 it is evident that large equiaxed grains are brighter than the rest of the map, indicating better pattern quality when compared to the macrozone primary α and macrozone β matrix. This indicates that there are low strain gradients across the equiaxed primary α and explains the lower intensity of the fibres present in the β pole figures, as non-indexed points between the macrozone grains can be inferred to represent highly deformed β-phase.

Notably, the number of indexed grains with five or more contiguous pixels within 20° decreases with increased strain for the 750 °C rolling, but the number of grains increases with strain for 900 °C rolling. As the material undergoes plastic deformation, changes to the lattice curvature such as an increase in GND density will impede the formation of diffraction patterns. From the image quality map, it is apparent that recrystallisation has taken place within the macrozones, forming new α grains which readily index, visible as bright white spots within the macrozone. Other equiaxed α grains, which are around 25 μm in width, are visible in all six quality maps. These correspond to off-macrozone primary α grains, which may present a harder orientation for slip during ND compression.

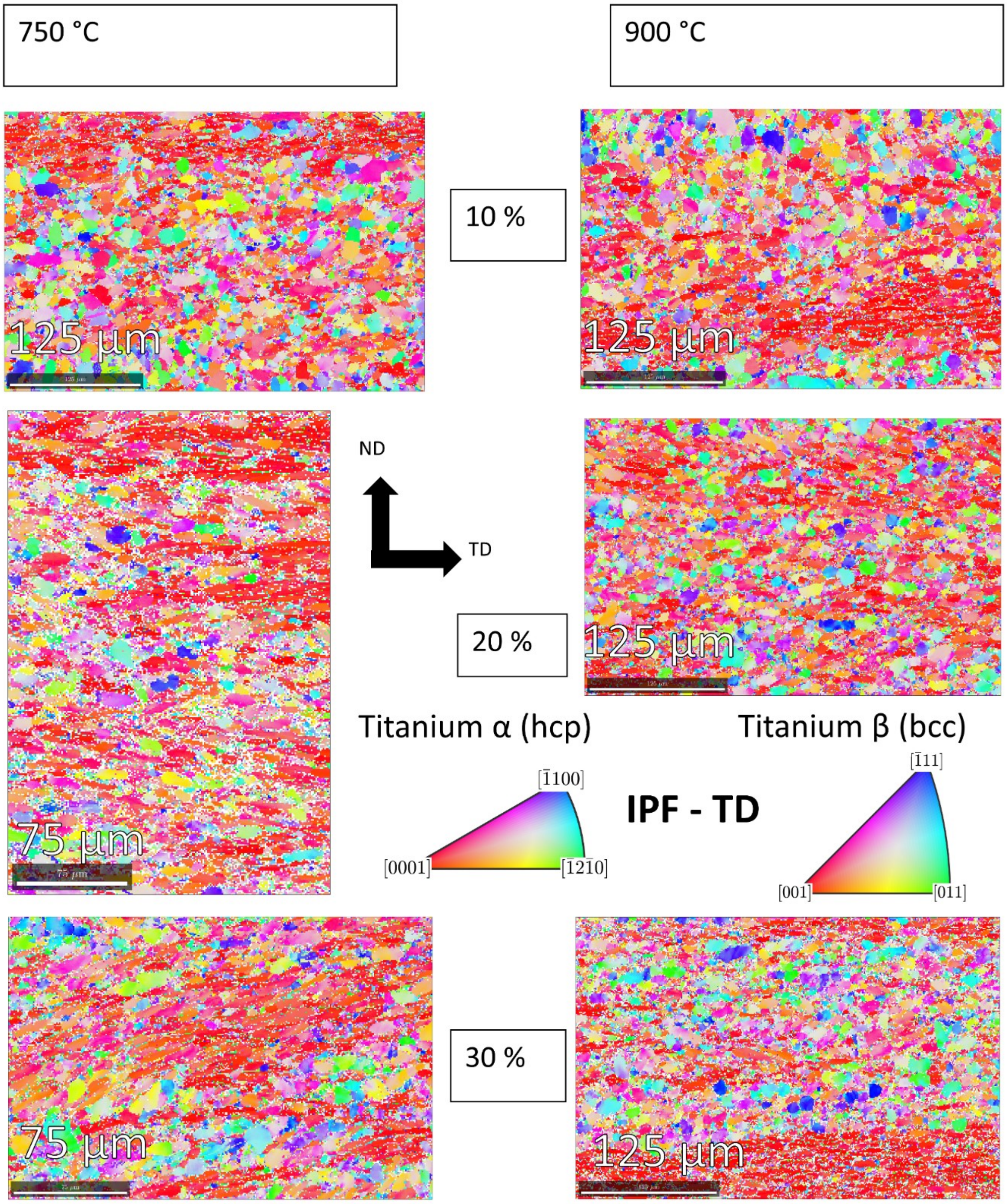

Figure 30: IPF-TD maps of rolled Ti-6Al-4V at 750 °C (left) and 900 °C (right) to 10%, 20% and 30% thickness reduction.

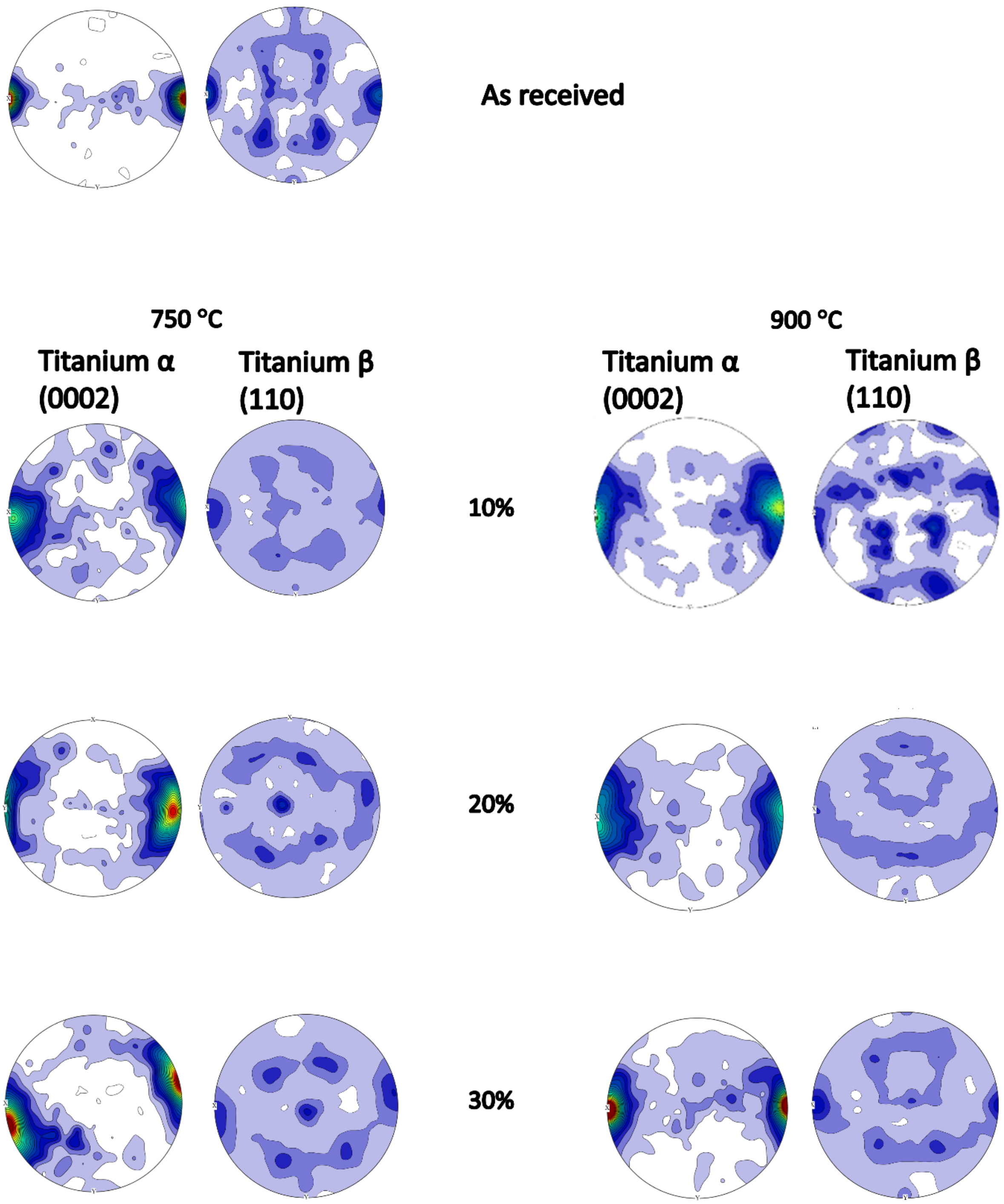

Figure 31: Pole figures presenting the texture of rolled Ti-6Al-4V at 750 °C (left) and 900 °C (right) to 10%, 20% and 30% thickness reduction. A partial inheritance of the β texture is visible, due to the BOR.

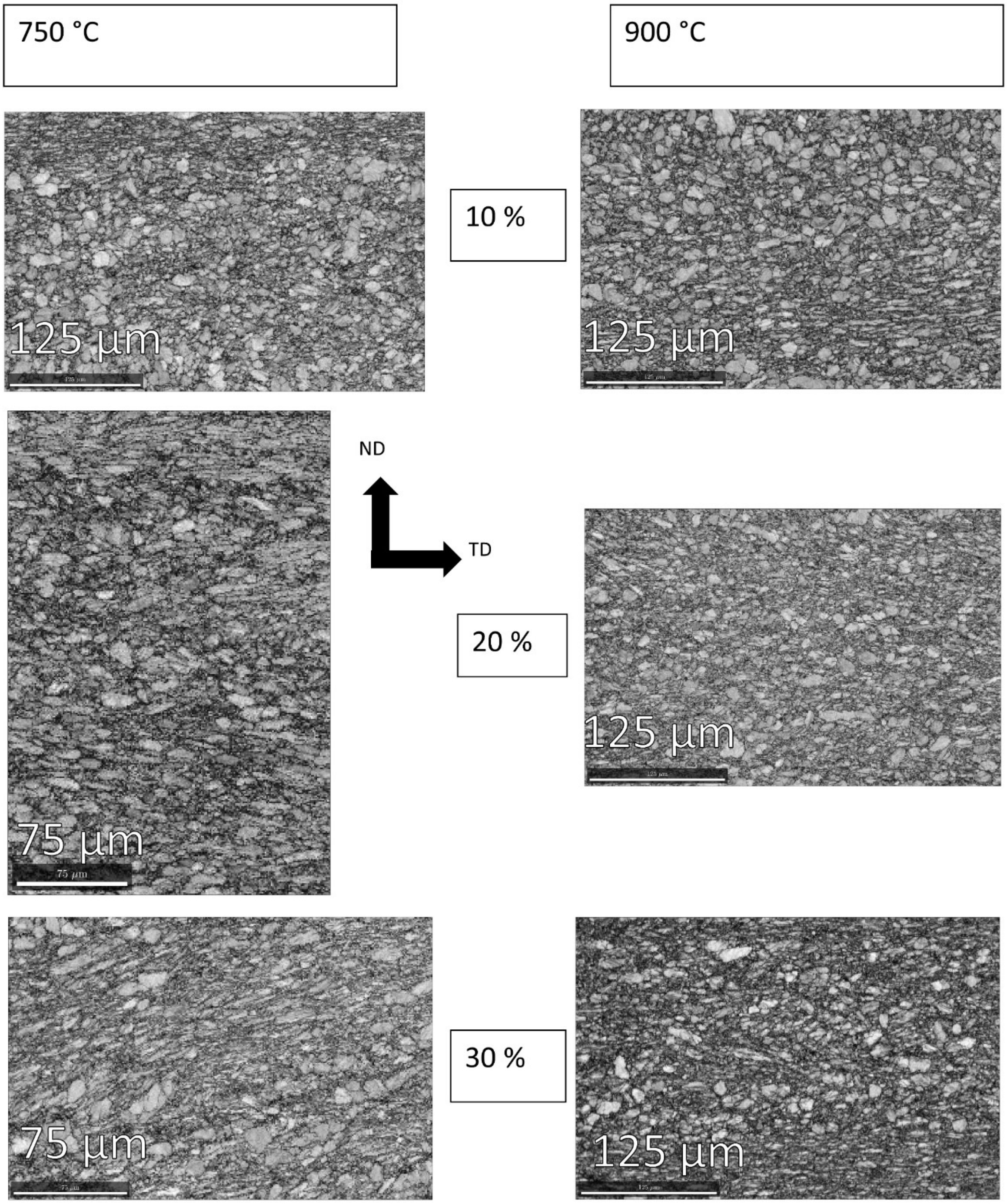

Figure 32: EBSD pattern quality maps of rolled Ti-6Al-4V at 750 °C (left) and 900 °C (right) to 10%, 20% and 30% thickness reduction. Low pattern quality indicates lattice distortion due to GNDs.

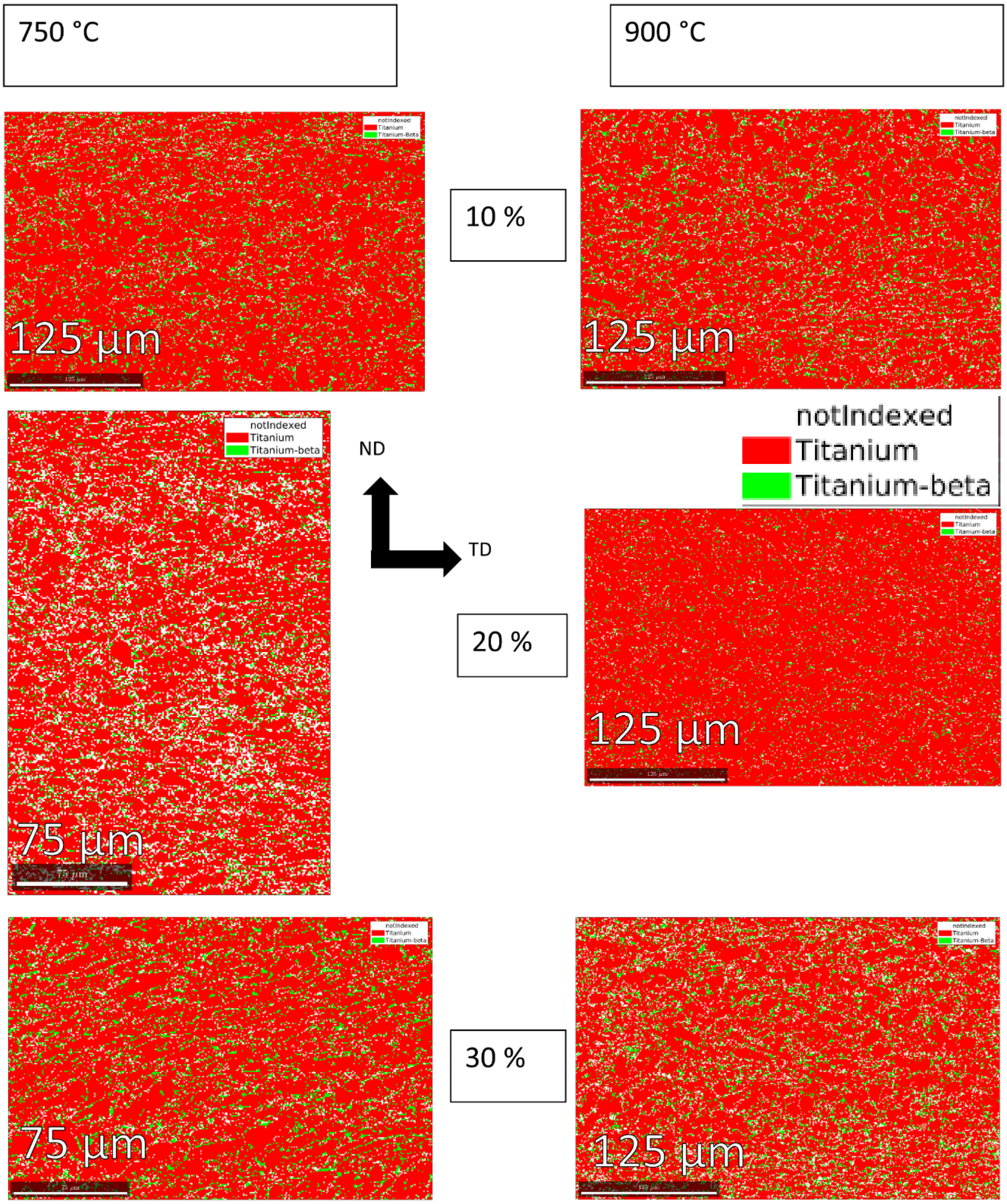

Figure 33: phase maps of rolled Ti-6Al-4V at 750 °C (left) and 900 °C (right) to 10%, 20% and 30% thickness reduction, showing the predominance of large α grains (red) and the clustering of β grains (green) at the α grain boundaries.

5.3 Characterisation of texture fibres at 75% thickness reduction

Due the lack of appearance of the twinning texture with 30% strain, I rolled 5 additional bars of Ti-6Al-4V to a thickness reduction of 75%, at furnace temperatures of 750, 800, 850, 900 and 950 °C.

5.3.1 Measurement of morphology and texture through EBSD

At 750 °C and 800 °C, after rolling to 75% thickness reduction, the macrozones have been broken up and redistributed throughout the material. This contrasts with rolling at 850 °C, where the macrozones are contiguous and parallel along TD, between 25-50 μm in width (Figure 34). The morphology has been changed considerably following the increase in total thickness reduction from 30% to 75% along the ND, as the macrozones are consistently larger than 100 μm after 30% thickness reduction at 750°C

Between 800 and 900 °C, the non-macrozone primary α contains large orientation gradients, which indicate a strain gradient across them, as well as rotation of α grains within a highly deformed β matrix. In the 900 °C IPF map, there are only two lenticular non-macrozone grains, with one showing a complete orientation transition from $(1\bar{1}00)$ to $(\bar{1}2\bar{1}0)$, but the other being aligned with its major axis parallel to the ND. At 950 °C the primary α seen at all lower temperatures is partially replaced by colony α laths which have grown, sharing the same orientation as one nearby off-macrozone grain.

Considering the frequency of grain boundary misorientations seen in Figure 38, there is no indication of significant numbers of grains differing by 84.8° for any rolling temperature, which would indicate T1 tension twins of the $\{10\bar{1}2\}\langle 10\bar{1}1\rangle$ system. This is the only twinning mode that could reorient primary α grains of the TD fibre into the ND fibre. There is a singlet peak of frequent misorientations of 74° present for samples rolled at 750 – 850 °C, which is diminished above 850 °C, which does not correspond to a misorientation expected through twinning or from neighbouring BOR variants. This indicates the rotation of α grains has occurred through another mechanism. The doublet peak of 60° and 63° is strengthened above 850 °C, indicating the preferential selection of secondary α variants from the same parent β grain (Karthikeyan, Saroja and Vijayalakshmi, 2006).

At all temperatures the pattern quality for the β-phase and fine α grains present is very poor (Figure 36). This implies a high GND density in the β-phase, resulting in lattice curvature, indicating that deformation is partitioned to the β. This increases the difficulty of indexing the β-phase, reducing the β fraction for all

75% thickness reduction rolling maps, compared to the 10-30% reduction at 750 and 900 °C. The large primary α grains are brighter, but not uniformly white, indicating plastic deformation at all temperatures. After rolling at 750 °C, a fine α grain structure forms, necessitating a comparably high magnification to characterise the texture. As this allows for a reduced step size, the indexing fraction is higher (94%) than at any other temperature except 950 °C (97%). In this case, small recrystalised grains are brightly visible, along with the pronounced colony laths which are evident in the quality map but are hidden within the structure of a macrozone α region in the IPF map. These secondary α grains are relaxed and produce EBSPs that are easy to index.

Through comparing the pole figures, there is no evidence of any "texture flip" from the TD fibre to the ND fibre, as the macrozones remain the strongest texture component at all temperatures, and there is very low intensity at the centre of the (0002) pole figures for all rolling temperatures below 900 °C. At these rolling temperatures, there is an emergence of orientations aligned 90° away from the ND, including alignment with RD. The TD fibre is broadened in both directions towards RD, indicating the spatial rotations of primary α macrozone laths within the β matrix. The pole figure for the 800 °C rolling shows a strong pole of orientations 20° away from the RD, with apparent connection of the fibres to the macrozones visible on the figure, implying an emergence through rotation of individual macrozone grains. In the β (110) pole figures there is little resemblance to the α texture.

After rolling at 900 and 950 °C, the α (0002) pole figures represent inheritance of the off-macrozone texture from the β-phase through the BOR. For the 950 °C rolled material, this matches with the texture apparent in the β (110) pole figure of the 950 °C heat-treated material. In the 900 °C rolled material, there is no resemblance of the cube on-edge β texture visible in the 950 °C heat-treated material. At both temperatures the indexed β fraction is below 5% of the map, despite the expectation of over 10% β-phase present at room temperature. Given that the most deformed grains become more difficult to index, likely due to the increase in dislocation density within the grains introducing lattice curvature, it is possible that the corresponding contribution to the texture fibres of these most deformed grains are missing from the pole figures.

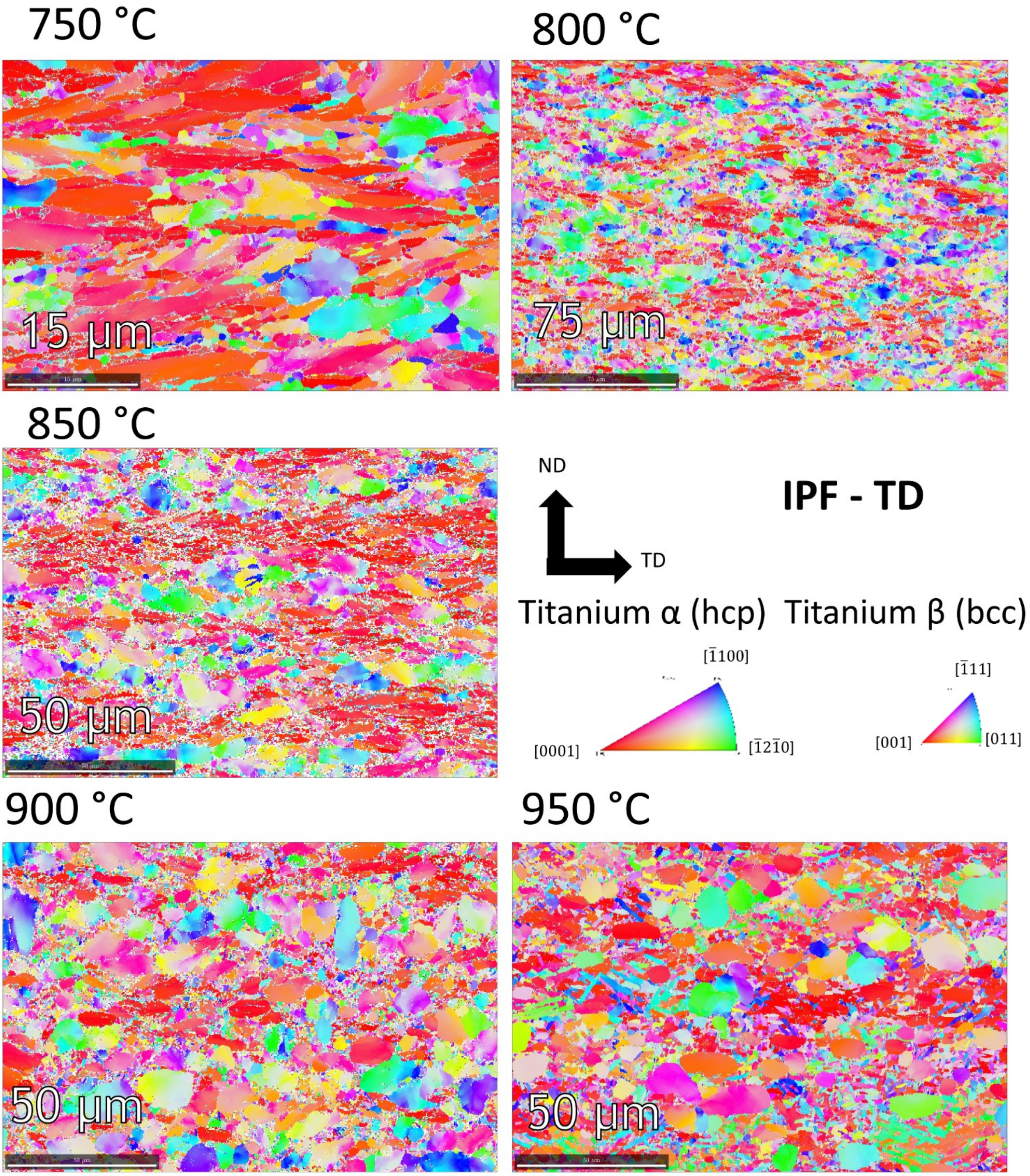

Figure 34: IPF-TD maps of rolled Ti-6Al-4V to 75% thickness reduction, at temperatures between 750 °C and 950 °C. Please note the difference in scale for 750 °C and 800 °C rolling.

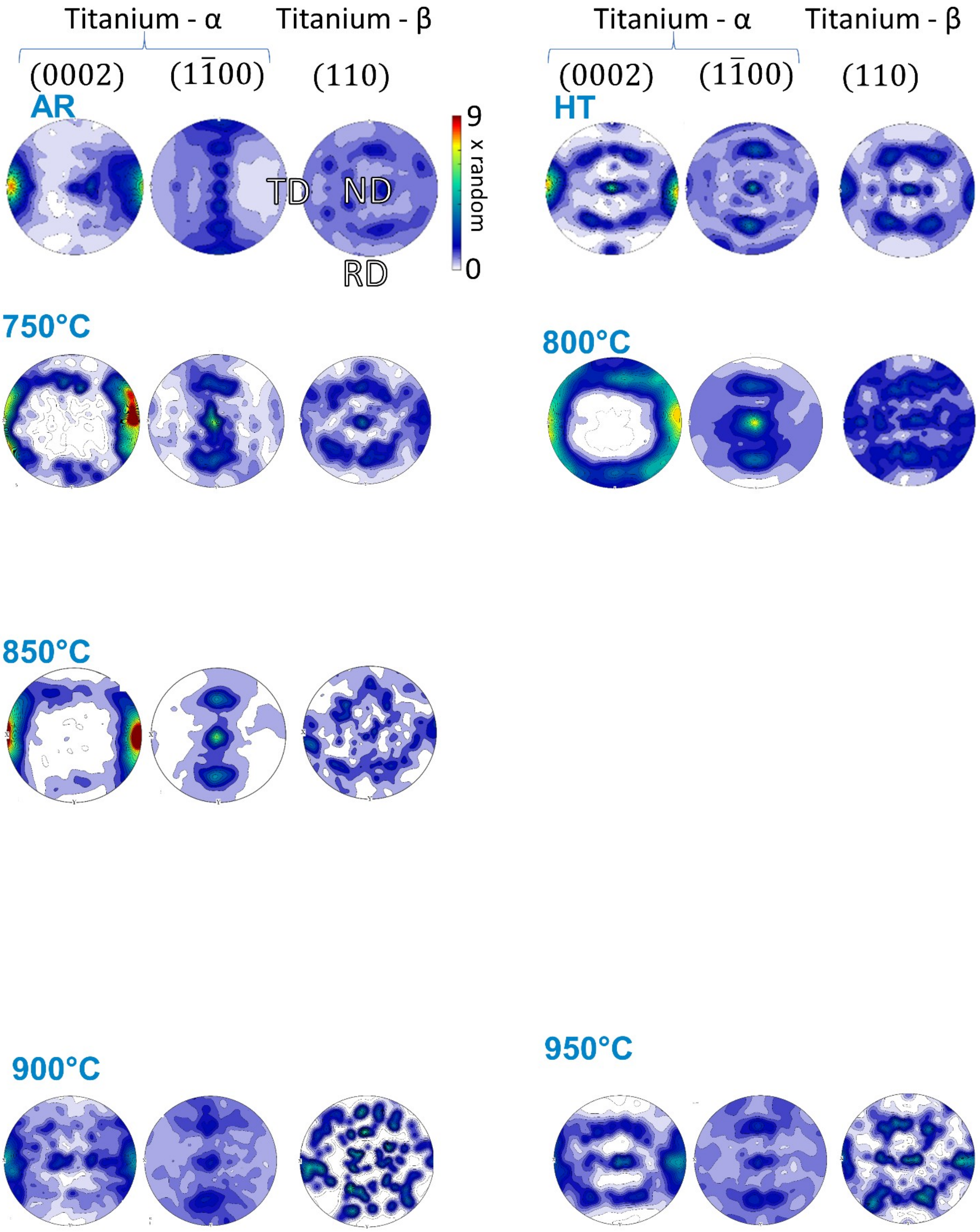

Figure 35: Pole figures displaying the texture of rolled Ti-6Al-4V to 75% thickness reduction, at temperatures between 750 °C and 950 °C.

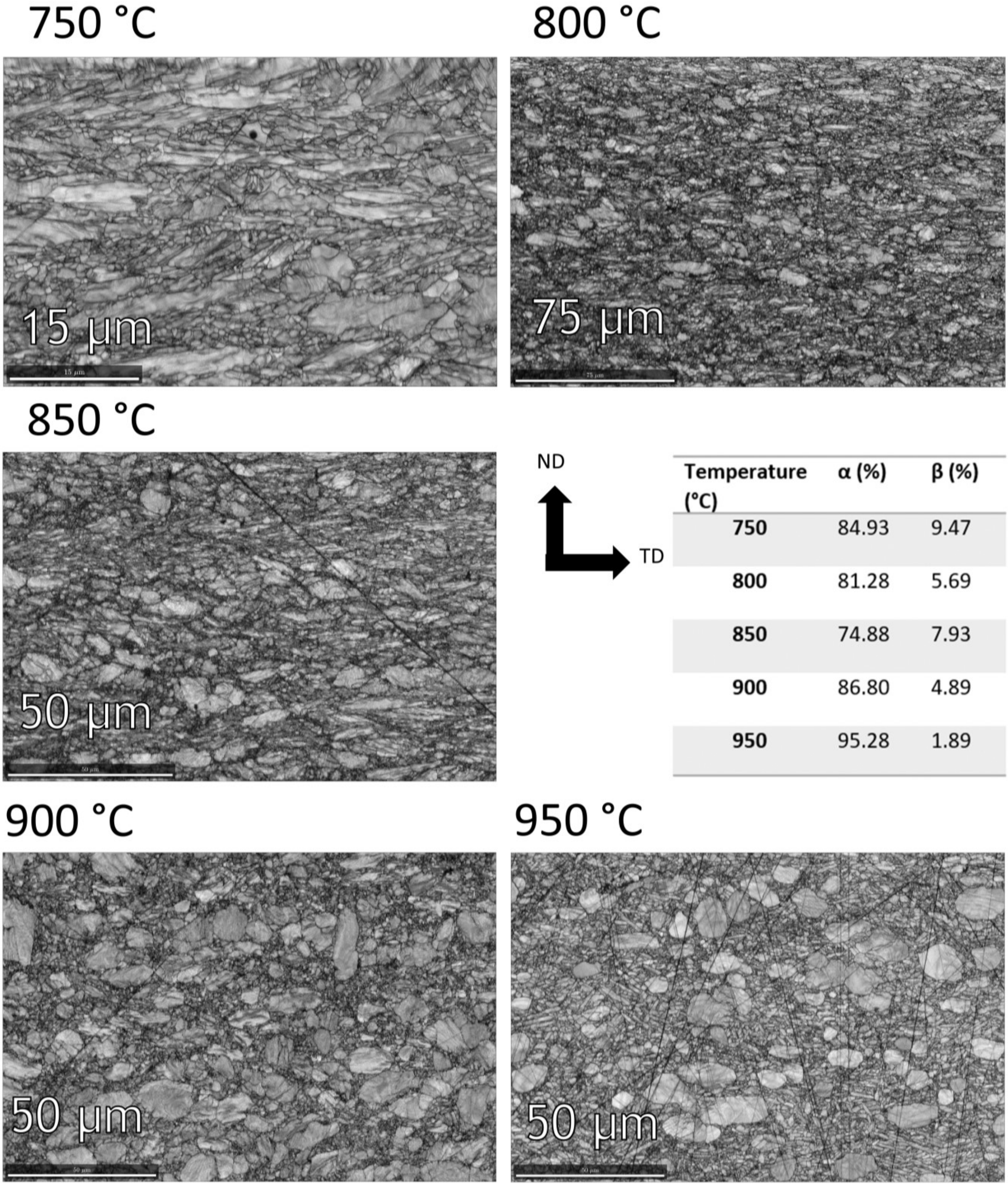

Temperature (°C)	α (%)	β (%)
750	84.93	9.47
800	81.28	5.69
850	74.88	7.93
900	86.80	4.89
950	95.28	1.89

Figure 36: EBSD pattern quality maps of rolled Ti-6Al-4V to 75% thickness reduction, at temperatures between 750 °C and 950 °C. Please note the difference in scale for 750 °C and 800 °C rolling.

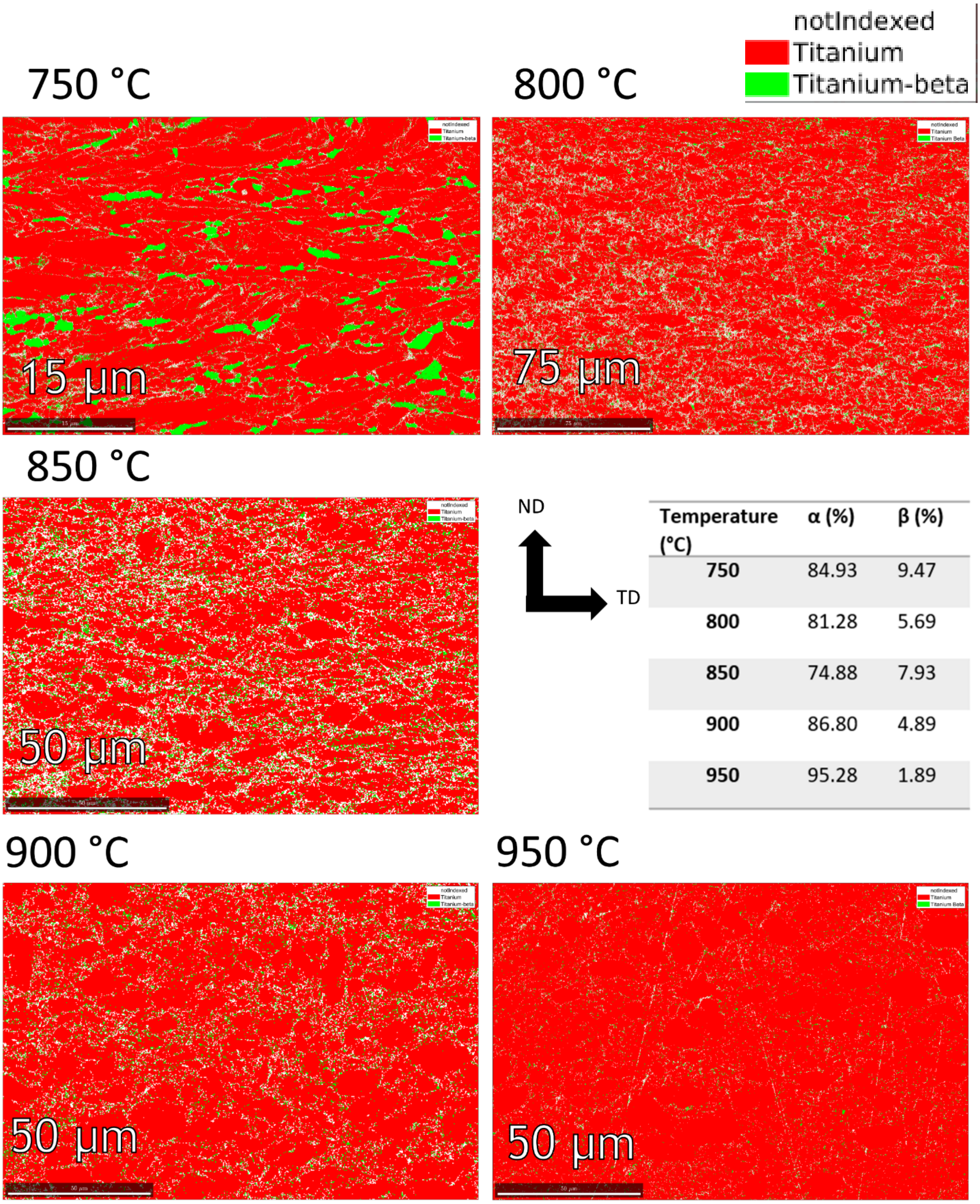

Temperature (°C)	α (%)	β (%)
750	84.93	9.47
800	81.28	5.69
850	74.88	7.93
900	86.80	4.89
950	95.28	1.89

Figure 37: EBSD phase maps of rolled Ti-6Al-4V to 75% thickness reduction, at temperatures between 750 °C and 950 °C. Please note the difference in scale for 750 °C and 800 °C rolling.

750 °C

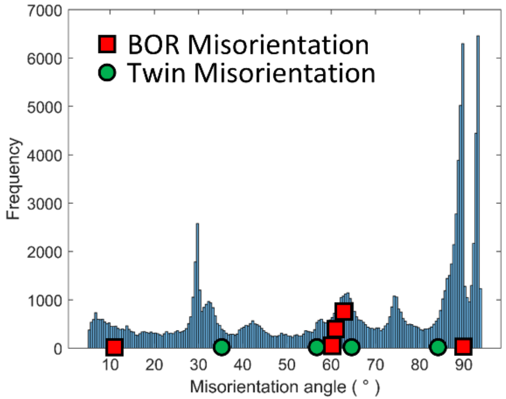

800 °C

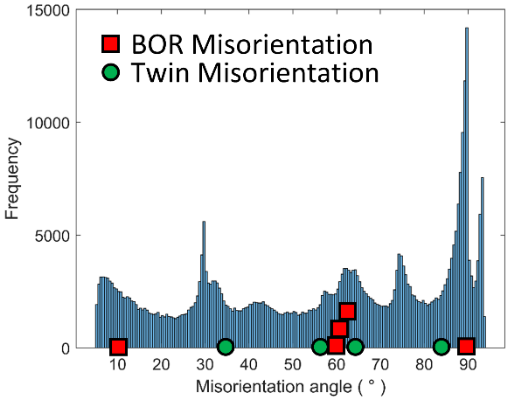

850 °C

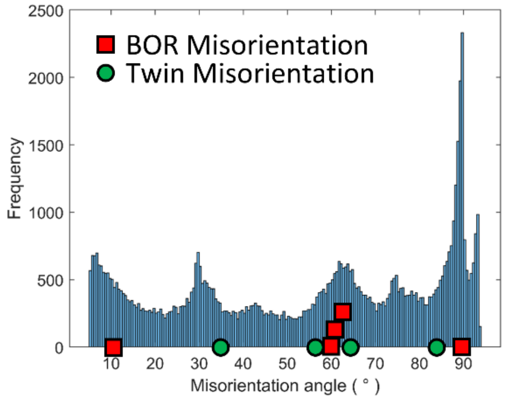

Twin system	Misorientation Angle (°)	Rotation axis	BOR Misorientation angle (°)
T1	84.8	[0001]	10.529
T2	35.1	$[11\bar{2}0]$	60.000
C1	64.6	$[\bar{1}.377\ \bar{1}\ 2.377\ 0]$	60.832
C2	57.2	$[\overline{10}\ 5\ 5\ \bar{3}]$	63.262
		$[1\ \overline{2.38}\ 1.38\ 0]$	90.000

900 °C

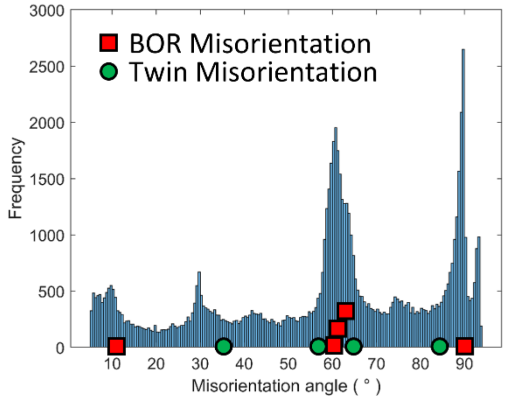

950 °C

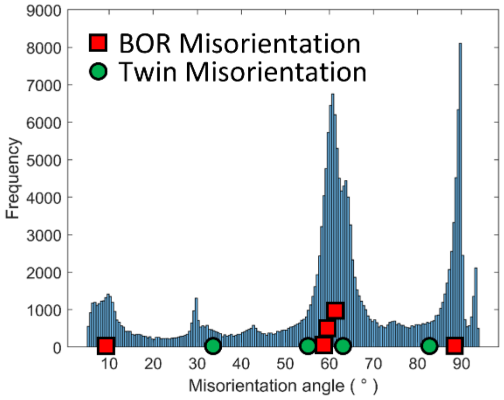

Figure 38: Histograms of the α-α grain boundary misorientations for rolled Ti-6Al-4V to 75% thickness reduction, at temperatures between 750 °C and 950 °C, inset with the specific misorientations resulting from twinning systems in titanium, and arising from the BOR through neighbouring α variants with a common parent β grain.

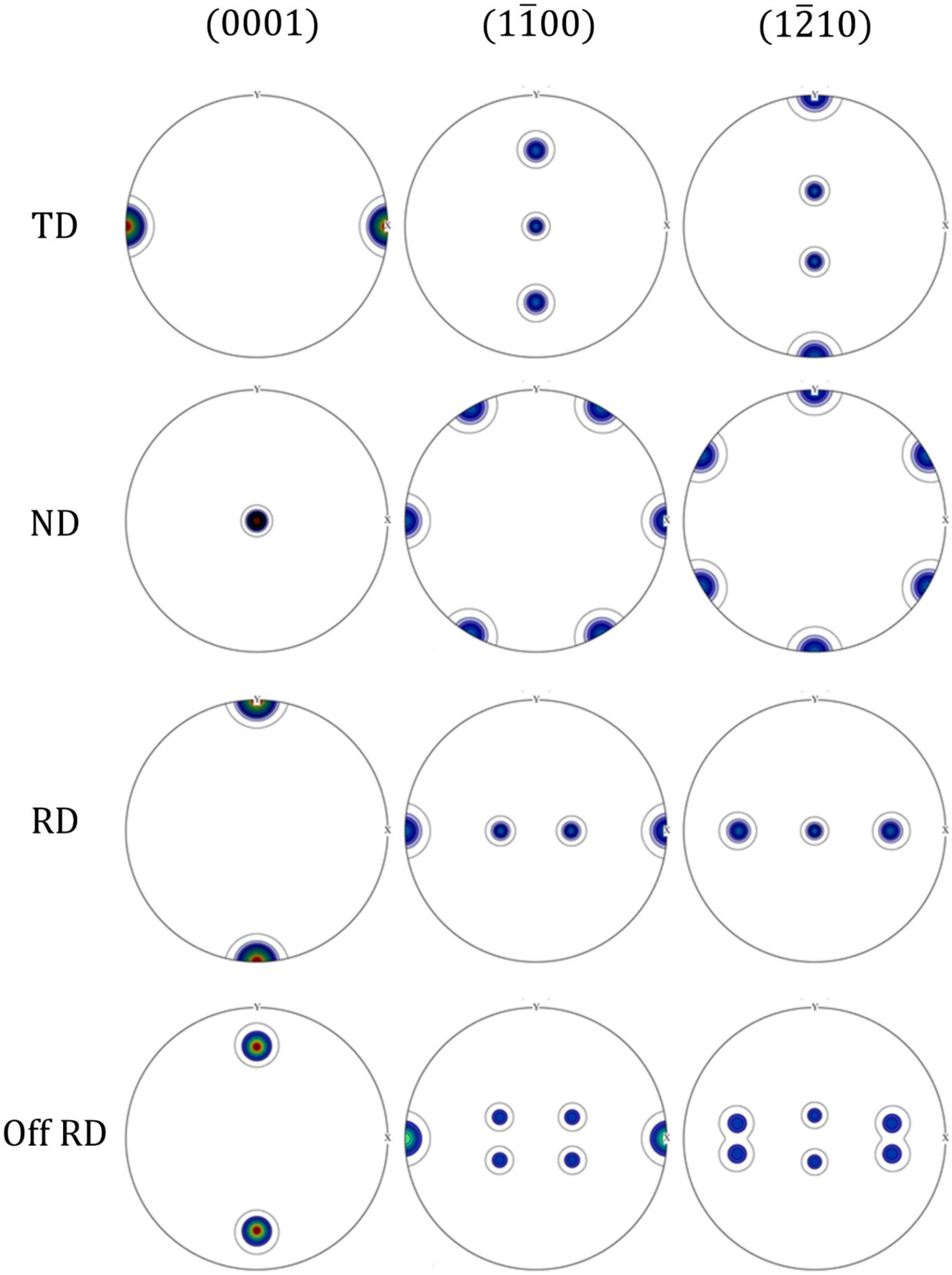

Figure 39: Pole figures representing the individual texture fibres present in rolled Ti-6Al-4V

5.3.2 Segmenting texture fibres

This far, analysis of the morphology and texture has been disconnected. However, the EBSD maps enable us to explore the spatial distribution of texture fibres. I will classify the segmentation according to the three fibres aligned with TD, ND and RD are described by a single Euler angle, with the off-RD fibre (IV) requiring two to describe the symmetry. These are segmented within MTEX with an allowable deviation of 30° from the centre of each fibre and examples are plotted as subsets of the original EBSD maps in Figure 40. Next, I can sum the area fraction of these fibres with respect to the TD, ND and RD for the rolling procedure.

The contributions to the overall crystallographic texture are indicated with the texture fibre area fraction analysis shown in Figure 41 for the 75% reduction in thickness rolling trials.

The TD texture fibre, which we observe in the macrozones, has a significant area fraction (>0.2) for all samples. For both unrolled material conditions, and the 750, 850 and 950 °C rolled material, the area fraction is greatest, and after rolling at 800 and 900 °C, it is slightly less than the area fraction of the off-RD fibre.

There is overlap in the RD fibre and the off-RD fibre, as they are separated by 20° in Euler space, but the binning is to within 30°. This is apparent as the relative intensities of the two fibres are similar for four of the five rolled datasets, with the exception being the 950 °C rolled material, which has a small fraction of grains aligned with the RD fibre. The as-received material and 950 °C heat-treated material also each have a very small fraction of RD-oriented grains. The off-RD fibre consistently accounts for a greater area fraction, which combined with the representation of the fibre in the α (0002) pole figures, suggests that the RD fibre is not present at all, and only the off-RD fibre is physically present in the rolled material.

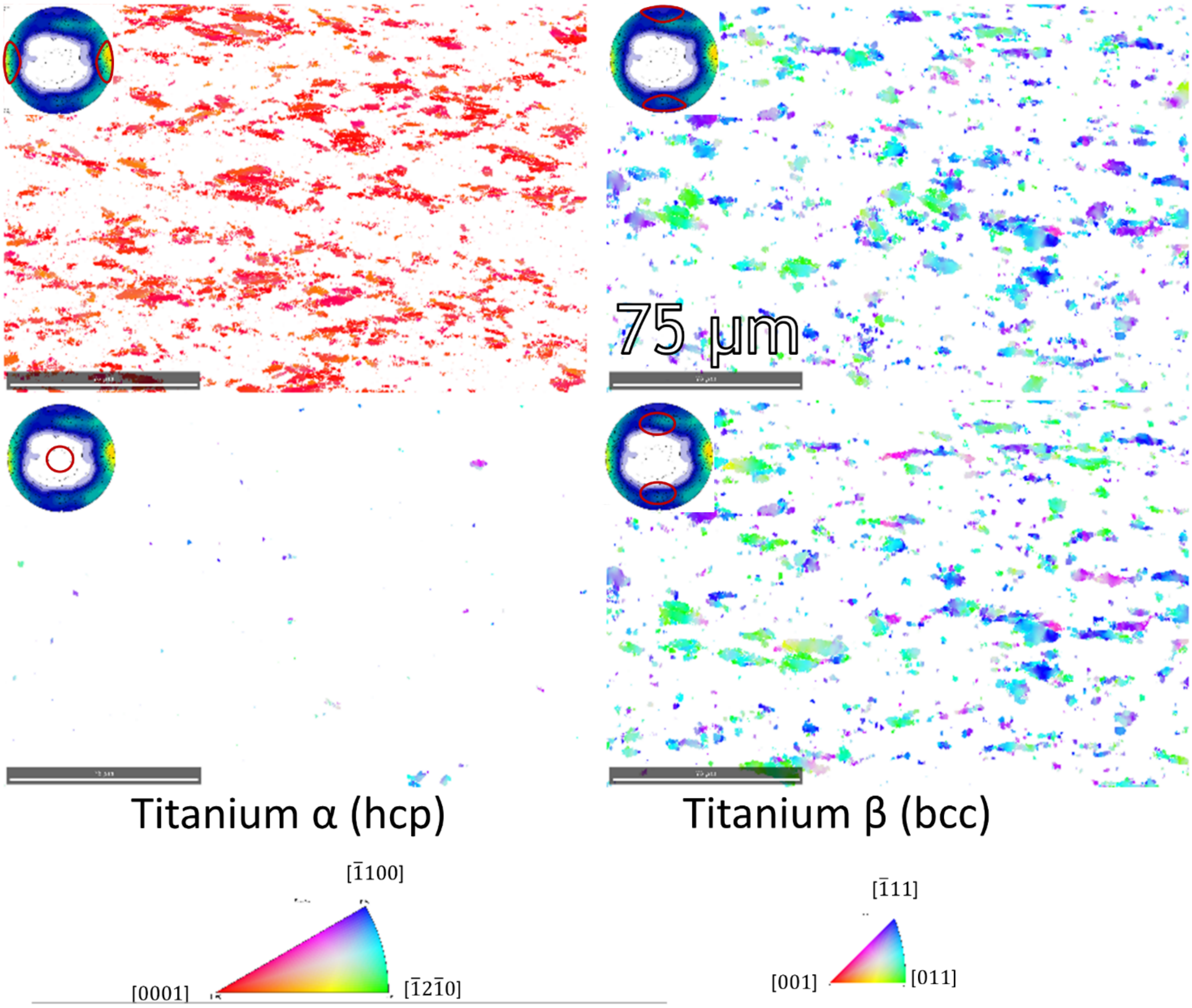

Fibre	ϕ_1 (°)	Φ (°)	ϕ_2 (°)	
(0001) || TD	270	90	90	🟥
(0001) || ND	0	0	0	🟦
(0001) || RD	180	90	180	🟩
Off-RD (1)	0	70	0	🟪
Off-RD (2)	180	70	0	

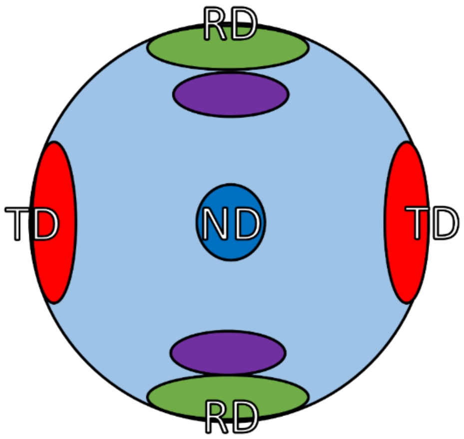

Figure 40: IPF-TD map of Ti-6Al-4V rolled at 800 °C, segmented by the orientations comprising the four texture fibres. Segmentation uses a 30° tolerance.

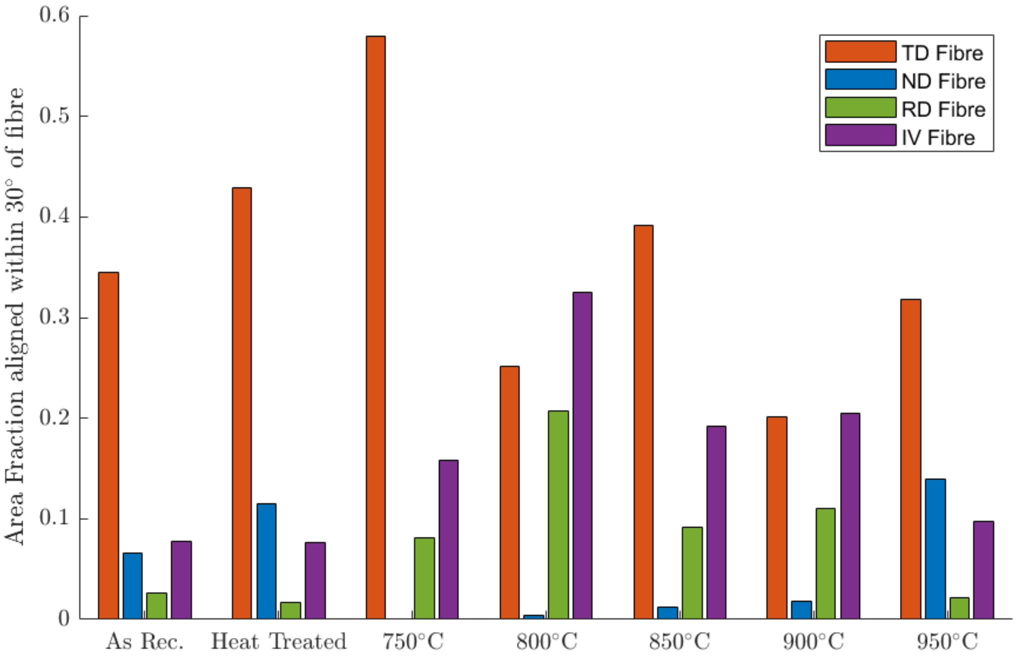

Figure 41: Histogram of texture fibre composition from EBSD characterisation of Ti-6Al-4V, in as-received, as-heated, and as-rolled conditions at 750 - 950 °C.

Despite its presence in the as-received material, after rolling the ND fibre is present in only the 950 °C rolled material. However, it accounts for almost 10% of the 950 °C heat-treated material, which while being more than the as-received material, remains lower than the 950 °C rolled material, of which around 15% of the α titanium grains are aligned with the ND texture fibre.

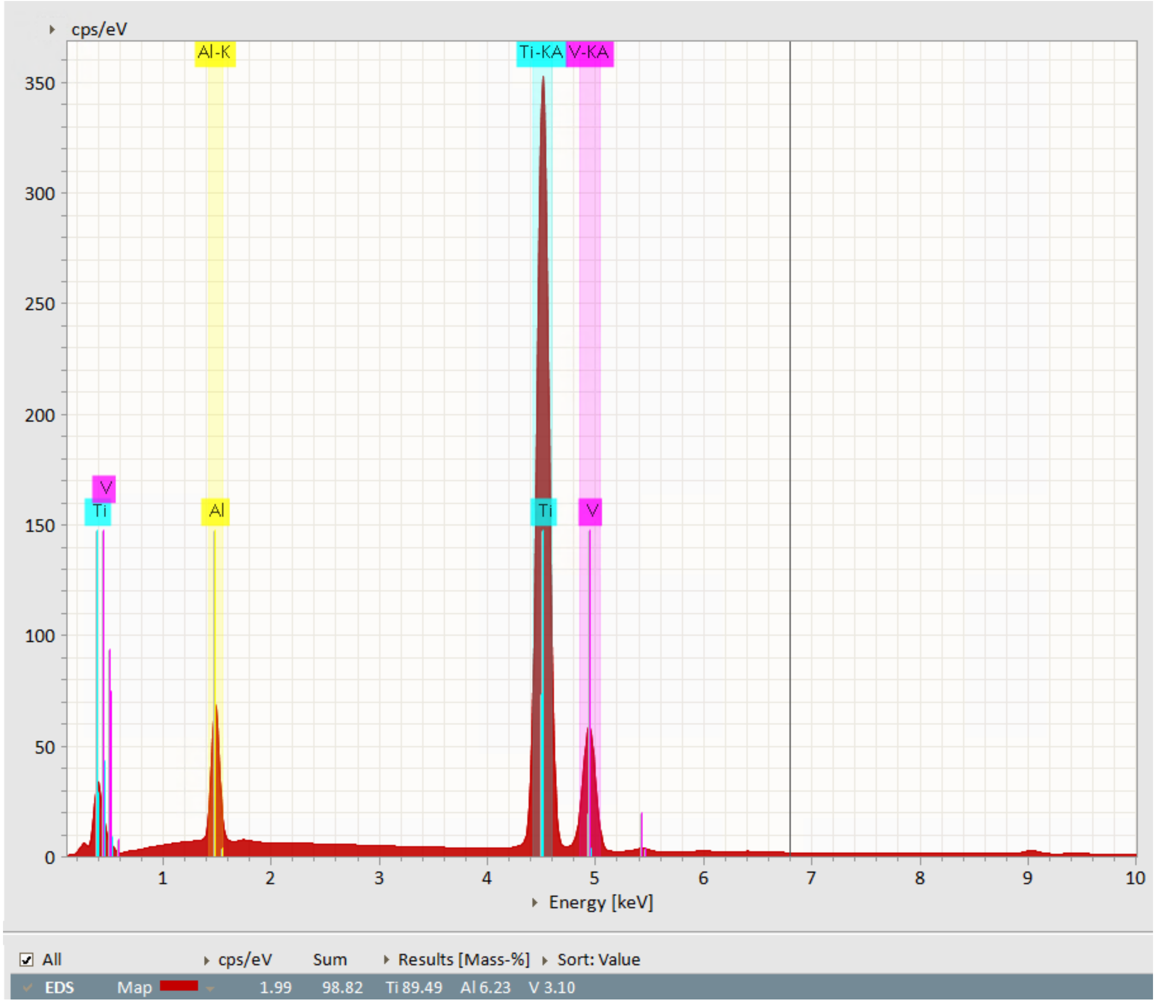

☑ All ▸ cps/eV Sum ▸ Results [Mass-%] ▸ Sort: Value

EDS Map 1.99 98.82 Ti 89.49 Al 6.23 V 3.10

Ti: 90.55% Al: 6.31% V: 3.14%

Figure 42: Spectrum of x-ray emission energies from energy absorption in Ti-6Al-4V, with normalised elemental composition.

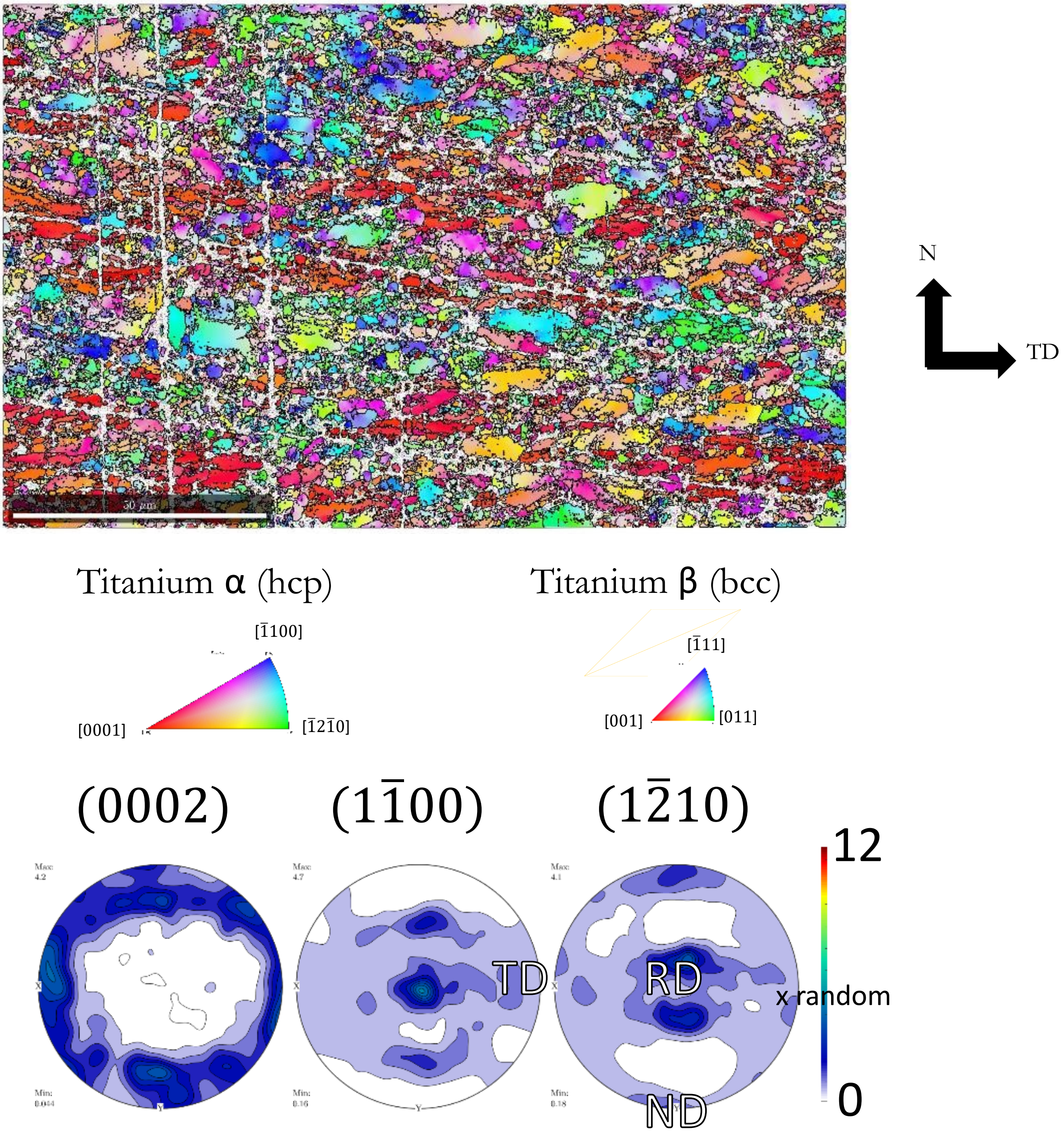

Figure 43: IPF-TD map of Ti-6Al-4V rolled at 800 °C characterised with simultaneous EDS acquisition, with the pole figure displaying the texture.

5.3.3 Measuring elemental composition by Energy Dispersive Spectroscopy

From the characteristic electron energy absorption and subsequent x-ray emission spectra, the elemental composition of Ti-6Al-4V can be measured with EDS simultaneously with EBSD acquisition. Due to the 126 eV resolution of the Bruker XFlash 6|60 EDS detector at the Mn Kα emission peak, it can distinguish between the Ti and V Kα peaks, which have a difference of 500 eV.

Characterising a sample from the centre of the Ti-6Al-4V bar rolled to 75% thickness reduction at 800 °C, I have computed its elemental composition to be 90.55% titanium, 6.31% aluminium, and 3.14% vanadium (Figure 42) from the relative intensities of the x-ray spectra and analysis using Bruker eSprit v2.1, integrating the peak intensities using a gaussian series convolution and ZAF correction.

Combining EBSD and EDS in simultaneous acquisition has enabled me to segment the EDS spectra based upon microtexture. In Figure 43, I compare an area of interest with significant variation in texture, containing several large primary α grains which are aligned with the TD macrozones, and away from the TD in a variety of different orientations.

From the qualitative EDS data presented in Figure 44, the aluminium-rich regions of the material are shown to be correspondingly vanadium-poor, and vice versa. The relative segregation of the two alloying elements results in large primary α grains being formed in aluminium-rich regions, for both on-macrozone and off-macrozone aligned grains. However, large off-macrozone grains are consistently close to the vanadium-rich regions, particularly when they are located between two such regions on opposite edges. As vanadium stabilises the β-phase, these off-macrozone grains are located in β-rich regions during rolling, which preferentially plastically deforms first due to its relative softness. This allows for the rotation of entire primary α grains within their β matrix at rolling temperatures, resulting in the emergence of the off-RD texture fibre seen during rolling at 750-850 °C.

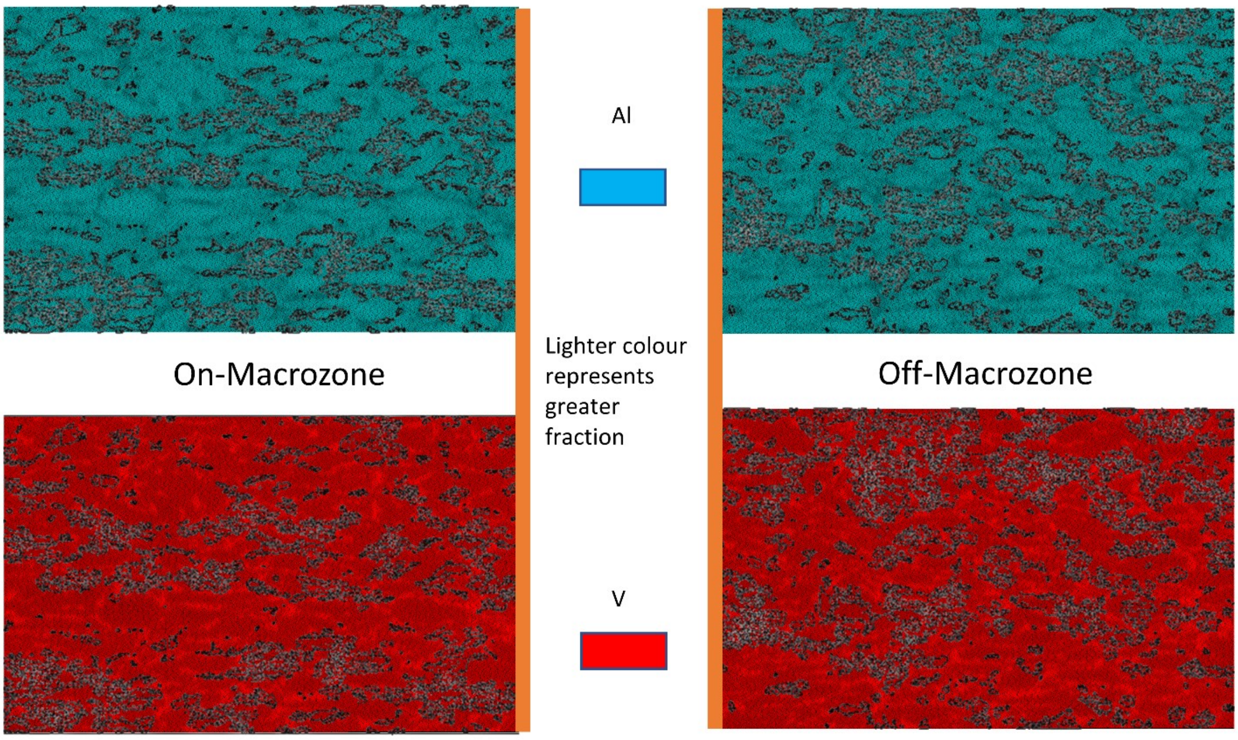

Figure 44: Mapping of relative composition of aluminium and vanadium obtained through EDS of Ti-6Al-4V rolled at 800 °C, overlaid with the grain boundaries of macrozone and non-macrozone primary α grains.

5.4 Thermocouple measurements of heated bar temperature

5.4.1 Measurement of die chill

As noted, rolling was performed using cold rollers. This results in significant die chill during the rolling process, and this is further complicated by the low thermal mass of the samples used in this study.

In conjunction with the 950 °C heat treatment recorded in 5.1.2, I recorded the temperature within the furnace and during air-cooling using a pair of two thermocouples spot-welded to one bar from unprocessed Ti-6Al-4V. This bar was withdrawn from the furnace and allowed to cool in air to 300 °C, which it reached after 450 seconds of cooling.

A second bar had a thermocouple attached, and the bar was withdrawn from the furnace after 1 hour of heating and rolled through the mill to a thickness reduction of 15%, with the temperature recorded at a rate of 1 s^{-1}. As the bar entered the mill, the change in geometry caused the weld to detach immediately, so the measurement is only minimally representative of the effect of cold rollers. The temperature log indicates that the sample had cooled by 150 °C before it was inserted into the rollers.

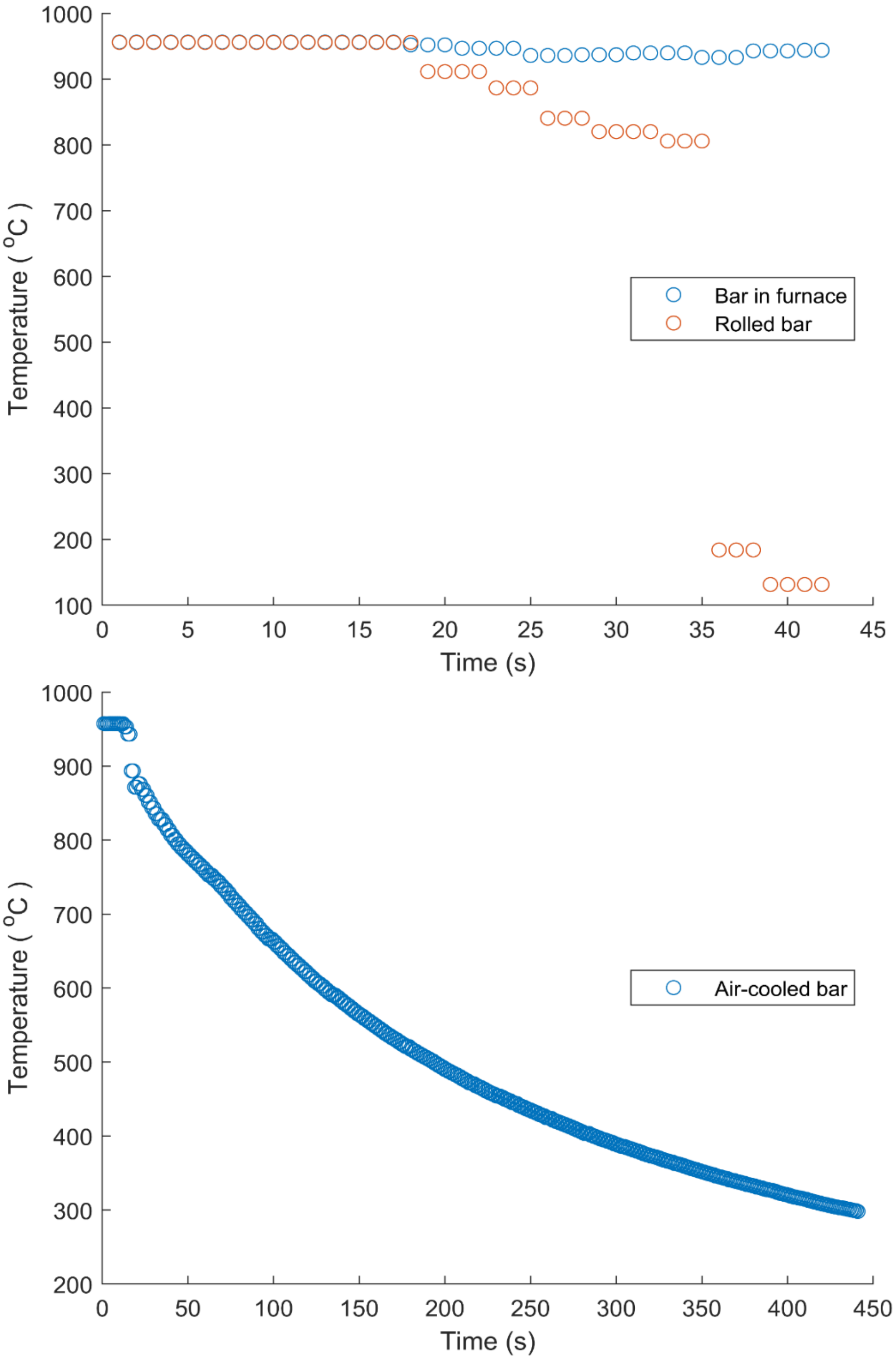

Figure 45: Thermocouple datalogging of the temperature of two Ti-6Al-4V bars heated to 950 °C , showing the thermal effect of rolling and opening of the furnace (above), and the temperature recorded as a bar is cooled in air (below).

6 Modelling texture evolution using CP-FFT methods

In order to investigate the texture evolution of Ti-6Al-4V during thermomechanical processing, this chapter explores the textures formed during simulations of deformation in uniaxial compression, and biaxial tension and compression. Slip is modelled through crystal plasticity using a constitutive, with elastic behaviour modelled by Hooke's law and plastic behaviour modelled through the phenomenological Hutchinson power law (Hutchinson, 1976). Considering the influence of slip behaviour during the forming of Ti-6Al-4V as seen in section 2.2.4, the model is validated with constitutive parameters for Ti-6Al-4V obtained at room temperature and elevated temperature (550 °C) for single crystals. The lattice rotation due to slip of contrasting orientations at grain boundaries is examined in bicrystals.

Through constructing synthetic polycrystal volume elements I investigate the slip and twinning behaviour contributing to texture evolution during forming of Ti-6Al-4V. The orientations assigned to the volume elements are representative of the textures observed after hot rolling between 750 – 950 °C at 75% thickness reduction, in chapter 5. In order to examine the possibility of twinning in macrozone laths, I have spatially consolidated the grains comprising the macrozone into a 3 x 5 x 1 grain "Frankfurter" or a 5 x 5 x 1 grain "Hamburger" geometry, which may only plasticly deform by twinning.

The texture evolution of these synthetic polycrystals is investigated through crystal plasticity simulations, with boundary conditions upon the volume elements simulating an equivalent strain to a single rolling pass from the processing routines presented in chapter 5. The textures obtained after uniaxial Z compression, and biaxial tension along either X or Y with compression along Z are presented. Slip and twinning shear rates in the final strain increment are presented, to demonstrate the relative importance of slip or twinning to the plastic deformation during thermomechanical processing of Ti-6Al-4V.

The constitutive equations in the DAMASK spectral method require calibration through the material parameters which describe elasticity according to Hooke's law, and plasticity according to the Hutchinson phenomenological power law (Hutchinson, 1976). The elastic constants were obtained through single crystal calculations at 25 °C and 550 °C (Simmons and Wang, 1971), while the CRSS values were taken from measurements at 20 °C (Zambaldi *et al.*, 2012). Using empirical measurements of the stress at 0.2%

strain, at 20 °C and 538 °C, (Lerch and Arnold, 2016), I observed that the ratio of stress between measurements at 20 °C and 538 °C at the onset of plasticity was 4.6:1 respectively. Therefore, I calculated estimates for the CRSS values at 538 °C by dividing the values measured at 20 °C by 4.6. In this phenomenological model, the orientations of the RVE are updated as a result of the lattice rotation due to plastic deformation (Roters *et al.*, 2019). The choice of which deformation mode is activated depends in part on the relative ratio of the CRSS values and the Voce hardening parameters, since hardening on the slip system with the largest Schmid factor may make it less favourable than a slip system with a lower Schmid factor and therefore a lower RSS.

In CP-FFT simulations, the compatibility of the deformation gradient requires spatial partitioning of the stress function in the Fourier domain across several voxels. In a polycrystal the need to satisfy compatibility and equilibrium in neighbouring grains with different orientations results in a "contrast" of the spectral frequencies of the stress function in those grains. In order to limit the computational cost of my simulations, I chose to construct my polycrystal models from grains comprising 5 x 5 x 5 voxel cubes.

6.1 Building textured polycrystal volume elements

6.1.1 Bicrystal simulations

During simulated deformation by crystal slip, the voxels of a CP-FFT simulation, or the elements of a CP-FEA simulation must remain connected in the regular grid describing the volume element in order to satisfy the condition of compatibility. However, in a real crystal the deformation of the lattice through dislocations creates defects which may be mobile within the grain, as the shear upon the lattice moves dislocations through the grain until they impinge upon a pinning object. As the grain boundaries also constrain the shape of the grain, this results in a reorientation of the crystal lattice.

In order to demonstrate the appropriate texture evolution due to lattice reorientation resulting from crystal slip in DAMASK, I constructed a computationally cheap bicrystal model of 64 voxels in a 4 x 4 x 4 grid. For this geometry I introduced two grains, one with 8 voxels arranged in a 2 x 2 x 2 cube, embedded in the corner of the geometry (Figure 47), with the remaining 56 voxels comprising the other grain. I chose this geometry to demonstrate the numerical artifacts that can be generated in small grains in the CP-FFT method, justifying my choice of 5 x 5 x 5 voxel grains. Considering an applied uniaxial shear strain in the X-direction, I have selected two orientation pairs for the grain, wherein one case the smaller grain is preferentially oriented for < a > prismatic slip, with the other case orienting the smaller grain for preferential < c + a > pyramidal slip. In both cases, the larger grain is oriented poorly for all forms of slip, with its slip plane normal oriented in parallel to the applied shear direction.

	"Soft-hard" geometry		"Hard-hard" geometry	
	Soft orientation	Hard orientation	Soft orientation	Hard orientation
ϕ_1 (°)	15	90	80	90
Φ (°)	0	90	90	90
ϕ_2 (°)	0	0	0	0

Table 9: Euler angles describing the orientations of bicrystals with strong and weak orientation contrast.

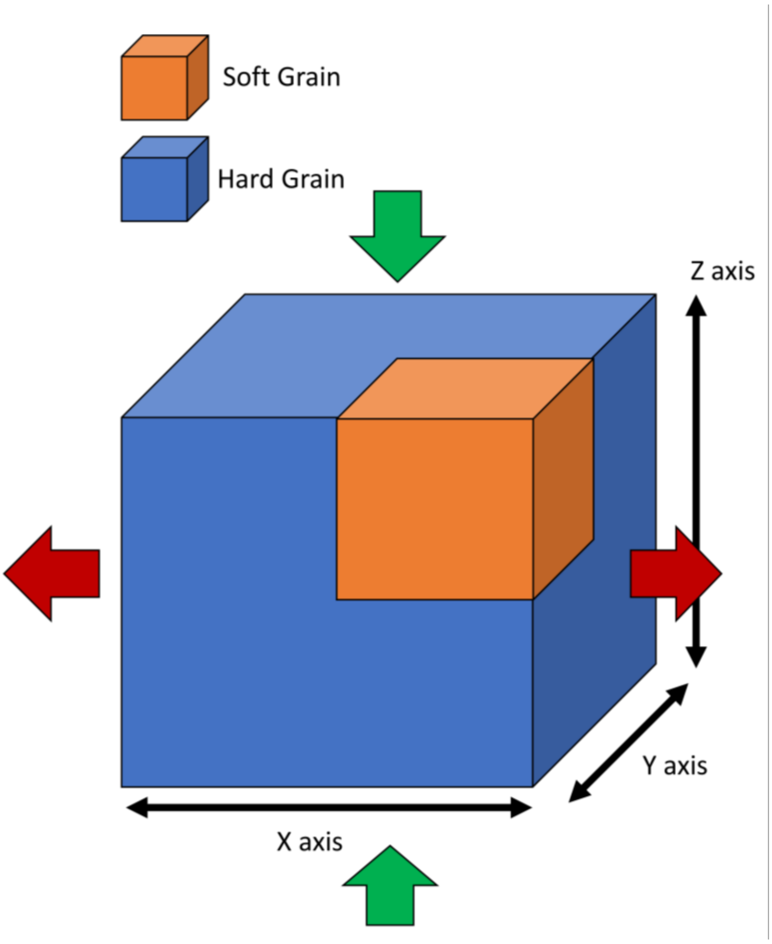

Figure 46: Bicrystal model of soft and hard grains, indicating the boundary condition of tensile loading along the x direction with red arrows, and compressive loading along the z direction with green arrows.

These two geometries were then deformed in three loading configurations:

1. 1% tension in X
2. 75% tension in X
3. 75% tension in X, 75% compression in Z

I used the elastic constants and CRSS values corresponding to the high temperature model (500 °C) in section 6.1.1 (page 111).

shows the resulting grain rotations for these three simulations. For the “soft-hard” grain pair, we see a repeated partition of the grain rotation into the smaller grain, which was well oriented to deform by slip. The smaller grain undergoes a rotation of magnitude between 0.4° and 0.6°, while the larger grain undergoes a maximum rotation of 0.2°. This ratio of 3:1 is maintained for the 75% tensile loading and the biaxial loading case, demonstrating the partitioning of slip onto the appropriate slip systems, and the resulting crystallite rotation in the DAMASK crystal plasticity model. However, in this case, the maximum magnitudes of the grain rotations are 7.0° and 2.4° in the smaller grain and the larger grain respectively. As in chapter 5, the internal misorientations are observed to be approximately 15° after rolling to 75% thickness reduction in Figure 47, demonstrating that these reorientations are large considering only 2% strain has been achieved.

The biaxial loading case reduces the maximum grain rotation to 0.5° and 0.3° for the smaller grain and the larger grain respectively, since the biaxial loading condition results in more complicated slip behaviour since both grains are now well oriented for slip resulting from the compressive shear in Z.

The slip behaviour of the “hard-hard” grain pair is very different to the “soft-hard” grain pair. Since the smaller grain is no longer oriented for easy < a > prismatic slip, the Burgers vector of the easiest slip direction is oriented with reasonable alignment to the macroscopic shear direction in both grains, and a large lattice rotation is not required in order to preserve compatibility of the voxel faces. This results in grain rotations of less than 0.05° within all voxels following the 1% tensile shear simulation and the 75% shear biaxial tensile and compressive loading conditions. The 75% tensile shear in X resulted in a simulation that did not readily converge. A tenfold increase in the number of permitted increments was required to reduce the divergence of the 1st PK stress $\boldsymbol{P}$ (i.e., in the material reference frame) below the set tolerance $\left(\frac{\mathrm{RMS}(\mathrm{Div}(\boldsymbol{P}))}{\|\bar{\boldsymbol{P}}\|} \leq 5 * 10^{-3}\right)$, which demonstrates that numerical equilibrium of the stress state was not achieved. This results in an anomalous result with voxels throughout the geometry rotating significantly further than 7°, which should not be expected for this geometry.

In all six simulations, the grain rotation within the two grains is not uniform. The smaller grain forms clear bands of increased grain rotation in the larger grain, due to the periodic boundary conditions of the CP-FFT method. The small grain forms a distinctive checkerboard pattern due to its small size, as there are not enough voxels to accommodate the sharp contrast of the different slip behaviours of the two grains. This artifact is the numerically optimised solution, pairing the grain rotation arising from heterogeneous slip behaviour in diagonally opposite corners of the grain. This demonstrates that when considering the texture evolution in these models, a grain size of greater than two voxels along any dimension is necessary to ensure that the Fourier transform of the stress state does not result similar spatial discontinuities for other grains.

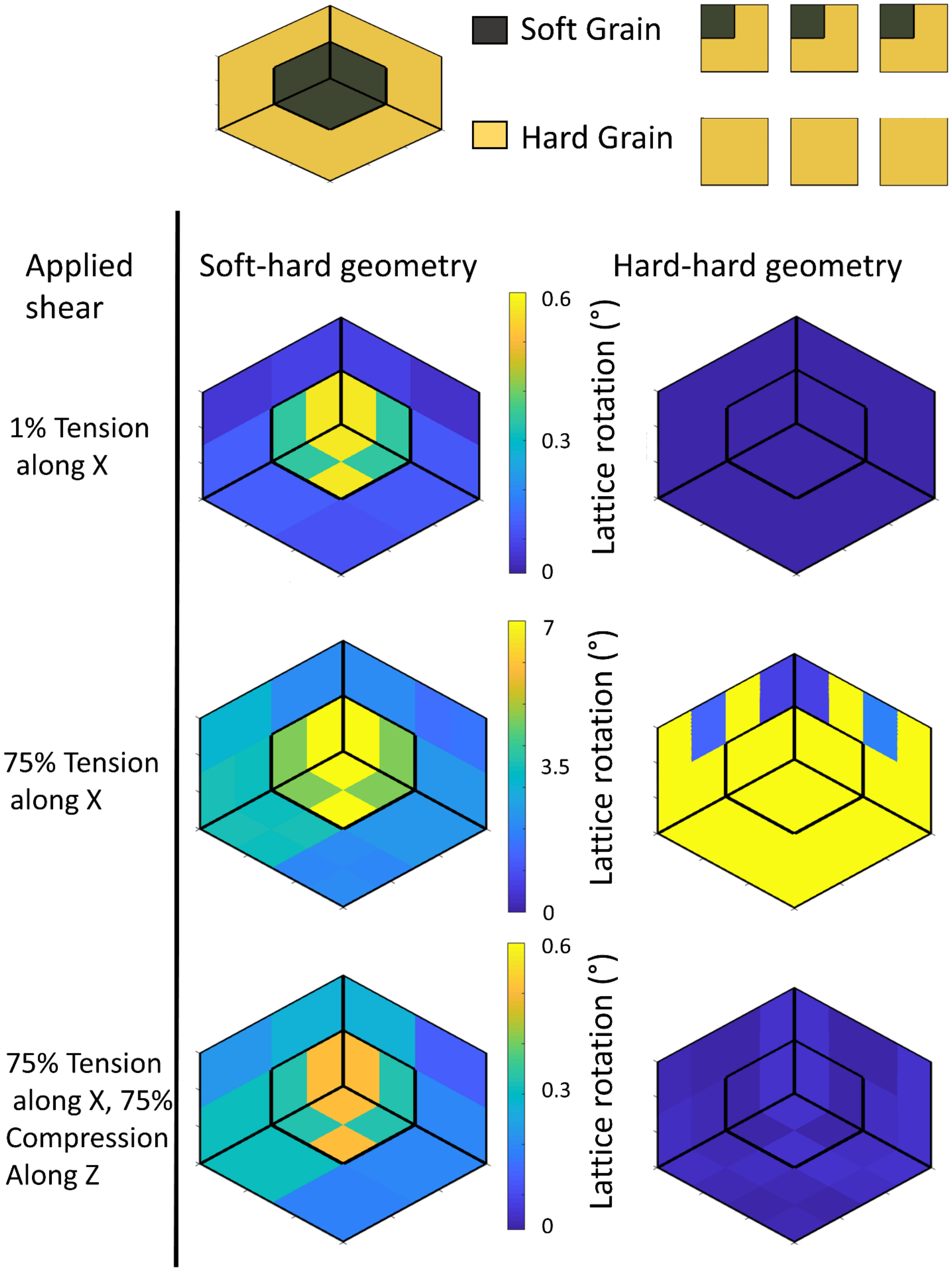

Figure 47: Lattice rotation of voxels in bicrystal volumes deformed under periodic boundary conditions in uniaxial tension to 1% and 75% total shear, and 75% in biaxial compression and tension, for a geometry with a small soft grain and hard grain pair. Lattice rotation is plotted with respect to the initial configuration of the grains.

6.1.2 RVE reproducing the texture of rolled Ti-6Al-4V

To replicate the texture of rolled Ti-6Al-4V, I created volume elements formed of 125 grains, each formed of 125 voxels in a 5 x 5 x 5 cube. The total size of the volume element is therefore 25 x 25 x 25 voxels. I assigned orientations to the grains corresponding to the TD, ND, RD, and off-RD texture fibres, or a randomly generated orientation.

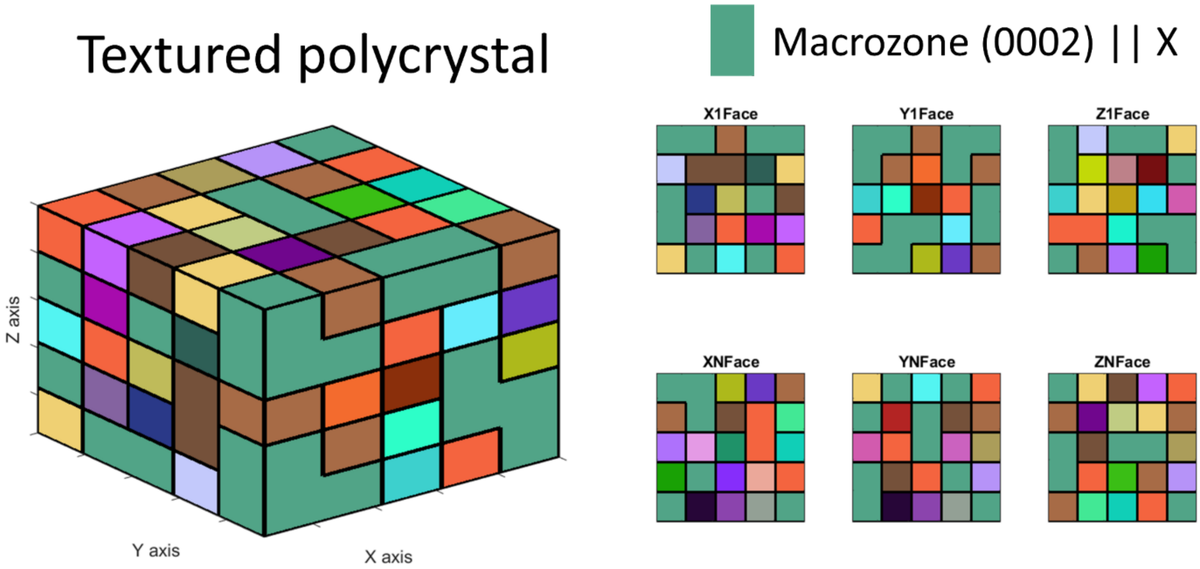

Figure 48: Grain ID map of a randomly constructed textured polycrystal representing the texture fibres observed following rolling of Ti-6Al-4V.

To represent the macrozone fibres, the probability that a given grain is of the TD fibre is 30%, greater than for any other fibre, each of which has a 10% chance to be assigned. The off-RD texture fibre is randomly chosen between the two possible variants with equal probability. With 40% probability, the assignment randomly generates a new orientation from Euler angles, $\phi_1 \in [0\ 90]°$, $\Phi \in [0\ 180]°$ and $\phi_2 \in [0\ 90]°$. The angles generated are uniformly distributed between the limits and recorded as a new grain in the DAMASK geometry. This controls the texture through imposition of the ODF, while not attempting to control the MDF. This initial texture is seen in Figure 50.

This geometry represents the texture of hot-rolled TI-6Al-4V, and the DAMASK simulations of it used the elastic constants and CRSS values corresponding to the high temperature model described in section 6.1 (page 111).

6.1.3 Spatially reconstructing a macrozone as an inclusion within the polycrystal

Randomly assigning the voxel orientations does not appropriately reproduce the large-scale structures present in hot-rolled Ti-6Al-4V, which forms macrozones of large structural features where grains whose orientations correspond to the TD texture fibre are lenticular in shape, with a long axis aligned with the TD.

To reflect this, the method of constructing a randomly textured polycrystal has been altered. The TD fibre is not randomly assigned, but instead is described by either a 5 x 5 x 1 “hamburger” grid of 5 x 5 x 5 voxel grains, or a 5 x 3 x 1 “frankfurter”, with its long axis aligned with X and its semi-long axis aligned with Y (Figure 49). By setting these grains to be a second phase which only permits twinning, I can test the possibility of T1 tension twinning being a permissible deformation mode in the macrozones. Because the < a > prismatic slip or < c + a > pyramidal slip modes are almost always crystallographically favourable, I expect that twinning will only occur in the hamburger volume, and never in the frankfurter volume, when the RVE is deformed in compression along Z. The contribution this has to the texture will demonstrate what mechanisms explain the texture evolution we see (and do not see) in rolled Ti-6Al-4V.

While generating the layers of the RVE, I instanced a new set of pseudorandom numbers through:

```
stream = RandStream('twister','Seed',sum(100*clock));
```

This ensures that the same random stream cannot be called while assigning layers, which ensures that the orientations of the textured grains, which are repeated, are not repeated in a pattern which forms similar structures within the volume.

Both models use the same constitutive parameters for the high temperature model in section 6.1.1 (page 116), described in section 3.3.2 (page 66).

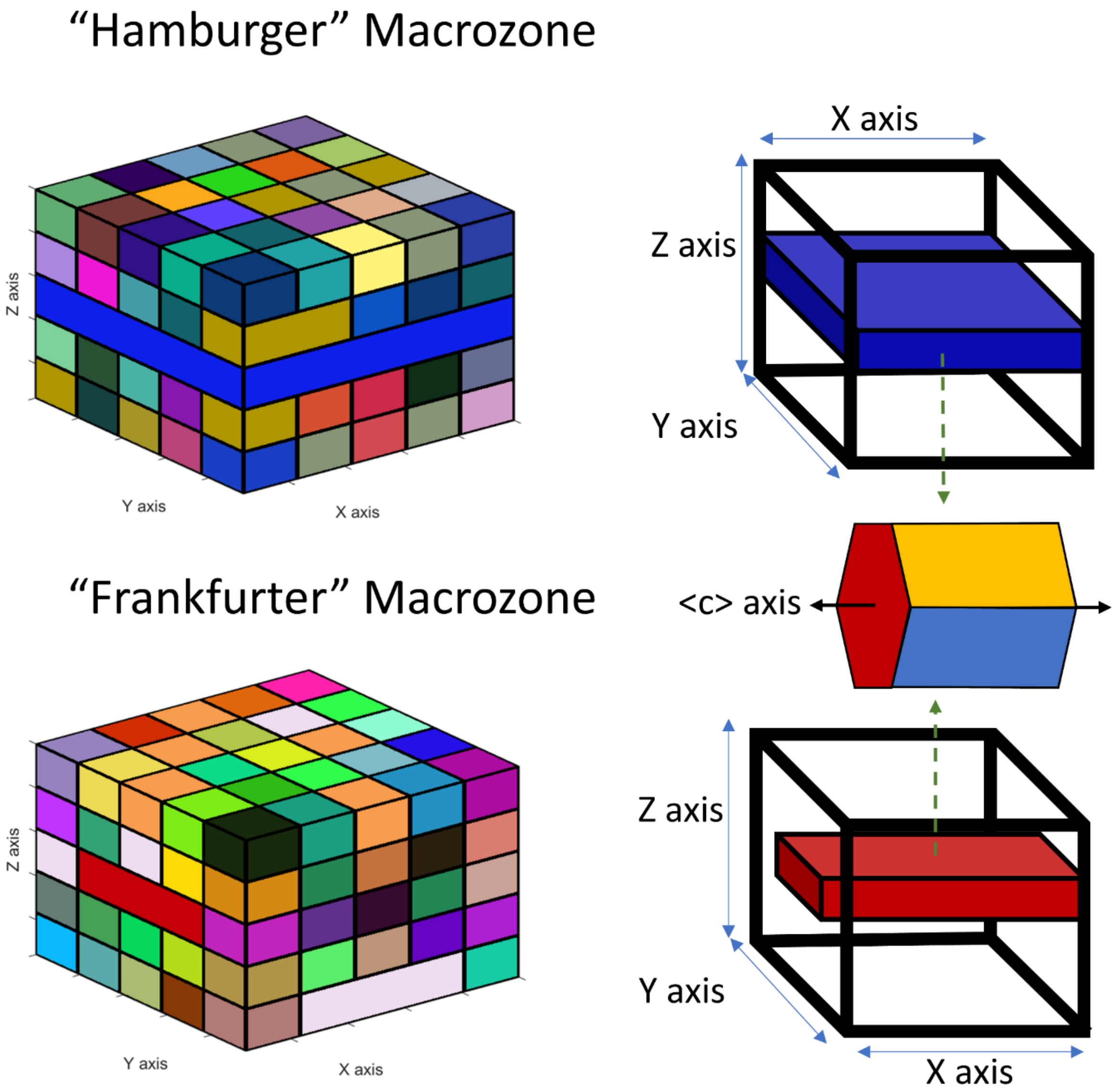

Figure 49: Grain ID map of a randomly constructed textured polycrystal with spatially coherent macrozone grains in the central Z layer, as a 5 x 5 x 1 "hamburger" or a 5 x 3 x 1 "frankfurter".

6.2 Texture evolution in CP-FFT simulations of textured polycrystals

6.2.1 25% Deformation of a textured synthetic polycrystal

Through deformation of the representative polycrystal produced in 6.2.1 (page 116), I calculated the changes in the texture after deformation in tension along the X direction to 25% strain, and biaxial deformation in tension along either of the X or Y directions (for references to the axes, see figure X) with compression along Z to 25% strain. In the DAMASK loadcase specification, the deformation is instanced in two parts, with different target deformation gradient rates ($\dot{\boldsymbol{F}}$). As the numerical instability in the method is greatest during the transition from fully elastic to fully plastic behaviour, I chose to reduce the amount of strain per-increment during the first 1% of deformation. The $\dot{\boldsymbol{F}}$ for the loading axes is reduced to 10^{-4}, for 100 seconds over 100 increments. At this point the behaviour should be fully plastic, which permits us to switch to an $\boldsymbol{F}$ of 10^{-3} on the loading axes, since the behaviour established in the elastic-plastic transition should be numerically favourable and continue until the conclusion of the simulation.

Considering the differences in texture evolution seen by Taylor FC and RC modelling (Section 2.1.1, p 18), I deformed the polycrystal using several loading conditions, to examine whether a different texture could be obtained by constraining a stress relaxation of the macroscopic XY, XZ, and YZ shears. I employed mixed boundary conditions with a relaxation on the hydrostatic stress component not subjected to a shear strain component, in combination with either all three deviatoric stresses, the XY and YZ stresses, or no deviatoric stress relaxation. The final DAMASK loading conditions (i.e. for fully plastic deformation of the RVE) are described in tensorial form in Table 10.

Load case	**Deformation gradient boundary condition ($\dot{\boldsymbol{F}}$)**	**Stress boundary condition ($\boldsymbol{P_{BC}}$)**
Uniaxial	$\begin{bmatrix} 0 & * & * \\ 0 & * & * \\ 0 & 0 & -10^{-3} \end{bmatrix}$	$\begin{bmatrix} * & 0 & 0 \\ * & 0 & 0 \\ * & * & * \end{bmatrix}$
XZ Biaxial	$\begin{bmatrix} 10^{-3} & * & * \\ 0 & * & * \\ 0 & 0 & -10^{-3} \end{bmatrix}$	$\begin{bmatrix} * & 0 & 0 \\ * & 0 & 0 \\ * & * & * \end{bmatrix}$
YZ Biaxial	$\begin{bmatrix} 0 & * & * \\ 0 & 10^{-3} & * \\ 0 & 0 & -10^{-3} \end{bmatrix}$	$\begin{bmatrix} * & 0 & 0 \\ * & * & 0 \\ * & * & * \end{bmatrix}$

Table 10: Constrained (numerical) and relaxed (*) components of the DAMASK deformation gradient and stress boundary conditions imposed during plastic deformation.

As the polycrystal RVE contains 83 unique grains, I have not attempted to capture the statistics of the equiaxed grains present in rolled Ti-6Al-4V. Instead, I focussed on the behaviour of the grains comprising the dominant texture fibres to explore whether these fibres can describe the change in crystal orientations, and whether the 'texture flip' described by G. C. Obasi *et al.*, (2012) and lack of a flip in my rolling trials (described in chapter 5) can be understood. Observing the pole figures of the textures produced through the simulations, the directly assigned grains of the rolled texture are dominant after 25% plastic deformation (Figure 50). Through the broadening of the poles produced for each fibre I observe that small variations within the grains appear, altering the orientations by around 5-20°. The TD fibre lattice rotation is the lowest in magnitude out of all the fibres (Table 11), demonstrating that the macrozones do not contribute to a "texture flip" through reorientation due to slip.

In the case of deformation by tension, the off-RD fibre (type IV, Figure 39) weakens in its intensity, with voxels from both variants of the texture reorienting slightly towards ND, the centre of the pole figure. In the YZ biaxial loading case, this phenomenon is particularly prominent. Considering the other frequently occurring grain orientations assigned to represent the rolled texture, there is no evidence of any evolution due to slip.

Under the YZ biaxial loading condition, a boundary condition of 25% total strain could only be achieved without constraining the deviatoric shear stresses to relaxation. However, considering the small differences in lattice rotation between the other boundary conditions, I consider this to be a representative simulation result. The pole figures shown in Figure 50, Figure 52 and Figure 54, the lattice rotations presented in Figure 51, Figure 53 and Figure 55, and the slip and twinning shear rates listed in Table 12, Table 15 and Table 16 are taken from the simulation results using this loading conditions.

By investigating the slip and twin shear rates computed during the final increment of deformation and lattice rotations for biaxial and uniaxial loading cases, with relaxations imposed on different deviatoric stress and strain conditions, I observe that there is no change in the average grain rotations for relaxations of XY, XZ and YZ deviatoric $\dot{\boldsymbol{F}}$ terms (Table 11).

Since only T1 tension twinning was permitted, in neither load-case was this mechanism preferable for the ND fibre grains, no twinning activity is observed in this fibre (Table 12). For all other fibres, under all loading conditions, the slip shear rate is at least an order of magnitude greater in the final increment of strain, indicating that deformation by slip is dominant during high temperature rolling.

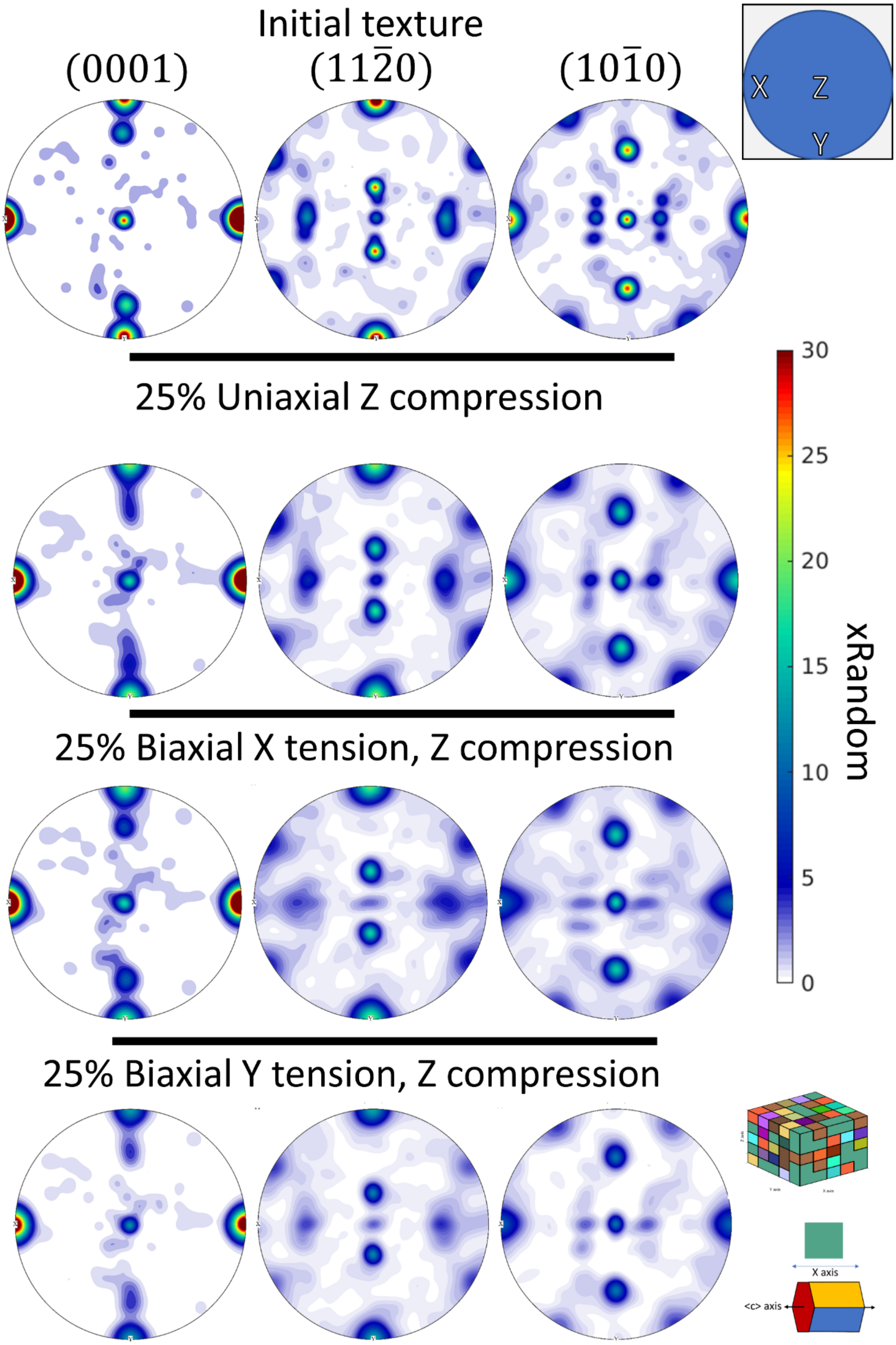

Figure 50: Smoothed (5° FWHM) pole figure displaying the texture of the synthetic Ti-6Al-4V polycrystal, before and after 25% deformation in tension and biaxial tension and compression

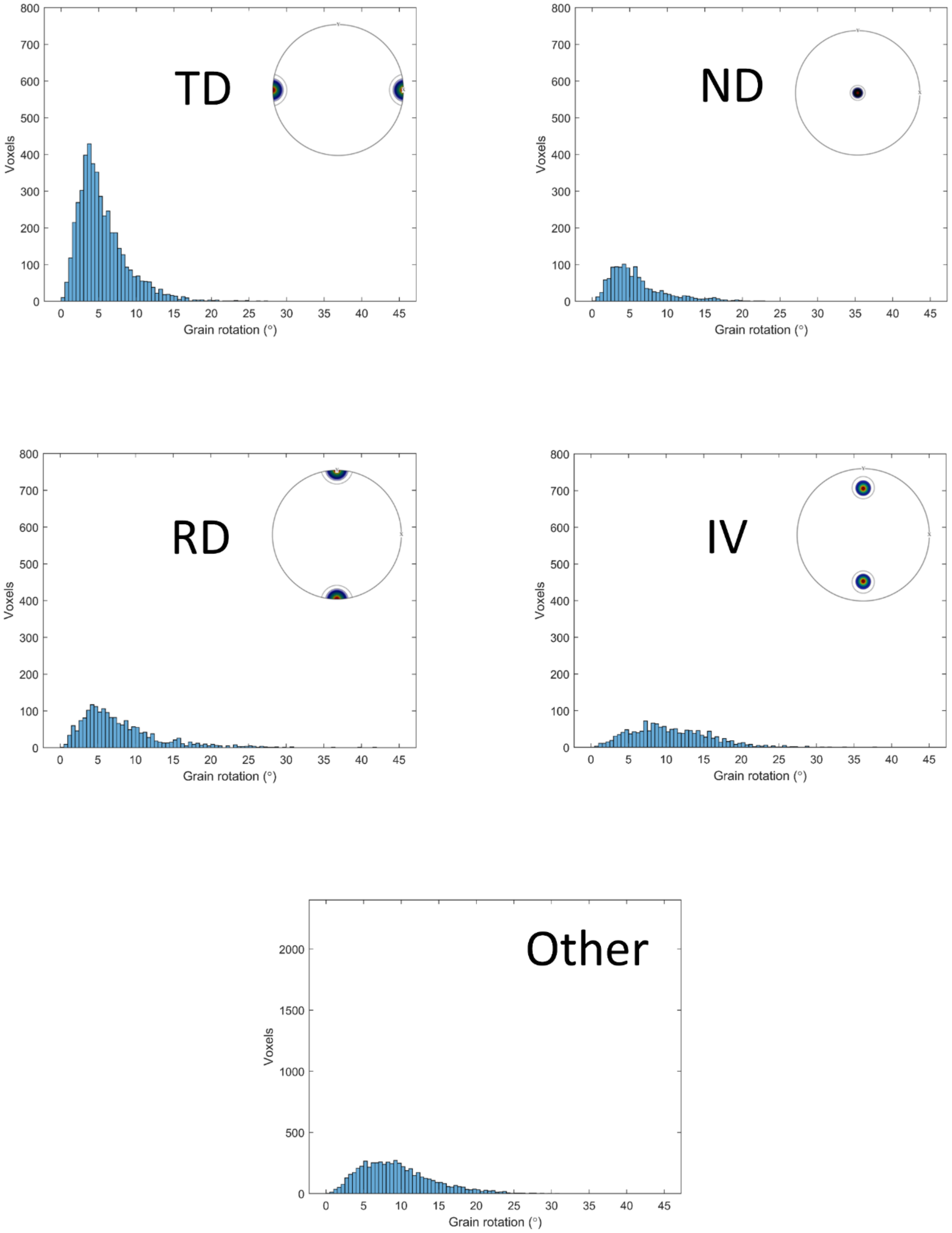

Figure 51: Lattice rotations within voxels of grains segmented by texture fibre, in a textured synthetic polycrystal, deformed to 25% biaxial tension along Y and compression along Z.

Average grain rotation (°)									
	XY, XZ, YZ relaxed deviatoric stresses			XY, YZ relaxed deviatoric stresses			No relaxed deviatoric stresses		
Loading condition	XZ Biaxial	YZ Biaxial	Z Uniaxial	XZ Biaxial	YZ Biaxial	Z Uniaxial	XZ Biaxial	YZ Biaxial	Z Uniaxial
TD Fibre	5.8296	N/A	5.6363	5.8221	N/A	5.6385	5.8285	5.4833	5.6649
ND Fibre	7.1476	N/A	6.5189	7.0825	N/A	6.5204	7.0966	5.9818	6.5607
RD Fibre	10.7277	N/A	6.3004	10.7264	N/A	6.2942	10.7365	7.8488	6.2894
IV Fibre	10.8013	N/A	11.2270	10.8288	N/A	11.2295	10.8388	11.0625	11.2482
Other	9.3613	N/A	10.6079	9.3424	N/A	10.6067	9.3350	17.9959	10.6254

Table 11: Average lattice rotation in degrees within grains comprising the different texture fibres after 25% simulated deformation in compression, and biaxial tension and compression. Column headings indicate the relaxed components of the 1st PK stress tensor in the loading condition.

	Slip shear rate in final increment			Twin shear rate in final increment		
Loading condition	XZ Biaxial	YZ Biaxial	Z Uniaxial	XZ Biaxial	YZ Biaxial	Z Uniaxial
TD Fibre	5.58E-04	1.74E-04	2.51E-04	6.93E-05	5.43E-05	1.26E-05
ND Fibre	3.20E-04	1.77E-04	1.67E-04	0.00E+00	0.00E+00	0.00E+00
RD Fibre	6.22E-04	2.36E-04	7.39E-04	2.69E-05	2.76E-05	5.98E-05
IV Fibre	4.33E-04	1.71E-04	3.36E-04	9.53E-06	1.25E-05	3.79E-05
Other	1.03E-03	8.69E-04	1.18E-03	7.19E-06	5.91E-06	9.10E-06

Table 12: Largest slip and twinning shear rates across all slip systems in synthetic polycrystals representing the texture of rolled Ti-6Al-4V, deformed to 25% strain in various loading conditions.

Lattice rotation distributions segmented by the fibres following deformation in biaxial tension along Y and compression along Z (Figure 51), due to the additional degree of directional freedom of the < c+ a > pyramidal slip system. Almost all voxels rotate by 20° or less, irrespective of texture fibre. The average lattice rotation is consistent for each fibre, regardless of boundary condition (Table 11), but the lower average rotation in the TD and ND fibres is evident.

6.2.2 Slip and twinning behaviour in a contiguous macrozone geometry

By arranging the grains of the TD fibre into a spatially contiguous unit, I have attempted to replicate the geometry of a macrozone within the volume, as described in section 6.2.2 (Figure 49). Considering a macrozone which is unbounded along one dimension, a 5 x 3 x 1 “frankfurter” grain, or a 5 x 5 x 1 “hamburger” grain, I have constrained it to allow plastic deformation through T1 tension twinning only. Through uniaxial compression along the Z direction, and biaxial compression along Z and tension along the X or Y direction, I have examined a selection of loading conditions in order to investigate the twinning behaviour in the macrozones within a rolling pass.

The boundary conditions were set using DAMASK's mixed boundary conditions, with hydrostatic deformation gradient aims of 7.5% shear, along the tensile (X/Y) or compression (Z) axis. Simulations attempting strains of greater magnitude than this failed to converge. In section 5.3 (page 94), the titanium bars were rolled to a thickness reduction of 10% in a single pass. While this represents a greater strain than the loading conditions for this simulation, it is similar in magnitude and the plastic slip and twinning mechanisms of the constitutive equation will evolve during the simulation according to what is numerically favourable at the onset of plastic deformation, unless the hardening behaviour results in another slip or twinning system becoming favourable.

Comparing the average grain rotations across the texture fibres in both models, there is no deviation of average rotation in a given texture fibre greater in magnitude than 0.01°, for any of the loading conditions used (Table 13, Table 14). The texture evolution is therefore the same, regardless of deviatoric stress relaxation terms used in the loading condition. In the XZ biaxial loading condition, tension along X should result in RD-fibre grains being well aligned for easy basal and prismatic slip, but more grain rotation is seen in this fibre in the YZ biaxial loading condition. The grain rotations in the "hamburger" geometry are lower in magnitude (Table 14) than those in the "frankfurter" geometry (Table 13), suggesting that the interruption of the macrozone throughout the whole layer reduces the plastic deformation in neighbouring layers above and below it.

As there are no observed differences in texture evolution based on the relaxation of the loading conditions, I restricted my data loading constraints with no relaxed deviatoric shear stresses only, in order to match the loading conditions which converged in section 6.2.1.

	Average grain rotation (°)								
	XY, XZ, YZ relaxed deviatoric stresses			XY, YZ relaxed deviatoric stresses			No relaxed deviatoric stresses		
Loading condition	XZ Biaxial	YZ Biaxial	Z Uniaxial	XZ Biaxial	YZ Biaxial	Z Uniaxial	XZ Biaxial	YZ Biaxial	Z Uniaxial
TD Fibre	0.5225	0.5030	0.4610	0.5228	0.5210	0.4610	0.5210	0.5376	0.4646
ND Fibre	1.8762	2.7086	2.9149	1.8757	1.9220	2.9135	1.9220	2.6848	2.9069
RD Fibre	2.9700	3.8515	4.1082	2.9659	2.9421	4.1068	2.9421	3.8390	4.0652
IV Fibre	3.1018	6.0438	6.4550	3.1000	3.3614	6.4545	3.3614	6.2360	6.4154
Other	6.7727	7.6985	8.3045	6.7720	7.2222	8.3394	7.2222	7.9452	8.4907

Table 13: Average lattice rotation in degrees in grains segmented by texture fibre, in textured polycrystals with a 5 x 3 x 1 macrozone, deformed to 7.5% strain in various loading conditions.

	Average grain rotation (°)								
	XY, XZ, YZ relaxed deviatoric stresses			XY, YZ relaxed deviatoric stresses			No relaxed deviatoric stresses		
Loading condition	XZ Biaxial	YZ Biaxial	Z Uniaxial	XZ Biaxial	YZ Biaxial	Z Uniaxial	XZ Biaxial	YZ Biaxial	Z Uniaxial
TD Fibre	0.4273	0.1470	0.0962	0.4237	0.1508	0.0973	0.4286	0.1660	0.0984
ND Fibre	1.7392	1.7854	1.7558	1.7298	1.7731	1.7421	1.7494	1.7863	1.7729
RD Fibre	2.3686	1.9107	1.9063	2.4347	1.9441	1.9365	2.4789	1.9330	1.8961
IV Fibre	2.7902	5.2730	4.4085	2.8143	5.2935	4.1454	2.8231	5.3315	4.4237
Other	3.7403	3.9464	3.8615	3.6995	4.0672	4.0222	3.8467	4.0656	4.0969

Table 14: Average lattice rotation in degrees in grains segmented by texture fibre, in textured polycrystals with a 5 x 5 x 1 macrozone, deformed to 7.5% strain in various loading conditions.

Examining the largest shear rates on the slip and twin systems for the final increment of deformation in each of the biaxial and uniaxial loading conditions for the two geometries, there is greater shear on the most active slip system in all cases for the “frankfurter” macrozone geometry, for all texture fibres allowed to deform by slip, except the RD fibre under uniaxial compression (Table 15). In the case of the “hamburger” geometry, slip shears are greater than twinning shears by two orders of magnitude in all fibres.

Neither TD fibre, which was not allowed to deform by slip, nor the ND fibre have deformed by twinning. Since this indicates that the macrozone grains are not plastically deformed at all, with the strains accommodated by the neighbouring grains.

	Slip shear rate in final increment			Twin shear rate in final increment		
Loading condition	**XZ Biaxial**	**YZ Biaxial**	**Z Uniaxial**	**XZ Biaxial**	**YZ Biaxial**	**Z Uniaxial**
TD Fibre	0.00E+00	0.00E+00	0.00E+00	0.00E+00	0.00E+00	0.00E+00
ND Fibre	2.05E-04	1.28E-04	1.33E-06	0.00E+00	3.58E-13	0.00E+00
RD Fibre	1.77E-04	2.63E-04	2.84E-06	1.02E-05	6.77E-07	6.19E-05
IV Fibre	1.30E-04	1.90E-04	2.11E-06	4.34E-06	5.58E-07	5.13E-05
Other	7.01E-04	8.30E-04	8.91E-06	8.06E-06	1.09E-07	9.90E-06

Table 15: Largest slip and twinning shear rates across all slip systems in textured polycrystals with a 5 x 3 x 1 macrozone, deformed to 7.5% strain in various loading conditions.

	Slip shear rate in final increment			Twin shear rate in final increment		
Loading condition	**XZ Biaxial**	**YZ Biaxial**	**Z Uniaxial**	**XZ Biaxial**	**YZ Biaxial**	**Z Uniaxial**
TD Fibre	0.00E+00	0.00E+00	0.00E+00	0.00E+00	0.00E+00	0.00E+00
ND Fibre	2.19E-04	1.31E-04	1.31E-06	0.00E+00	0.00E+00	0.00E+00
RD Fibre	1.46E-04	1.46E-04	1.48E-06	4.80E-06	6.36E-05	6.23E-07
IV Fibre	1.18E-04	1.07E-04	1.11E-06	1.83E-06	3.99E-05	3.87E-07
Other	8.35E-04	8.87E-04	8.83E-06	9.64E-06	8.63E-06	8.38E-08

Table 16: Largest slip and twinning shear rates across all slip systems in textured polycrystals with a 5 x 5 x 1 macrozone, deformed to 7.5% strain in various loading conditions.

There is no visible change in the texture observed in the pole figures for either “frankfurter” or “hamburger” macrozones, for either biaxial loading condition or the uniaxial compression loading condition. Figure 52 and Figure 54 have been selected, showing the result of the simulations with mixed boundary conditions with relaxed deviatoric stress constraints on the XY, XZ and YZ stress tensor components.

The slight difference in mechanical response between the two macrozone geometries is seen in the lattice rotations of the voxels segmented into their respective texture fibres. The orientations of the “hamburger” macrozone voxels are unchanged (Table 14), which is expected as no plastic deformation of these grains have occurred. In the corresponding macrozone voxels of the “frankfurter” model, up to 5° of rotation is observed in a minority of voxels (Table 13). As the two geometries are differentiated by 1 x 5 strips of grains along two parallel edges of the “frankfurter” macrozone, the plastic deformation of these grains results in a shape change of the grain boundaries, causing this reorientation.

The “frankfurter” geometry has 110 non-macrozone grains, each comprising of 5 x 5 x 5 voxels, compared with 100 in the “hamburger” geometry. This results in a greater number of voxels with non-zero lattice rotations in the “frankfurter” model, but lattice rotations of voxels in this model are also greater in magnitude, across all the texture fibres. The largest rotations are seen in the off-RD fibre (IV), and in the grains with orientations populated by randomly generated Euler angles. These correspond to the equiaxed primary-α grains in titanium, deforming readily by slip.

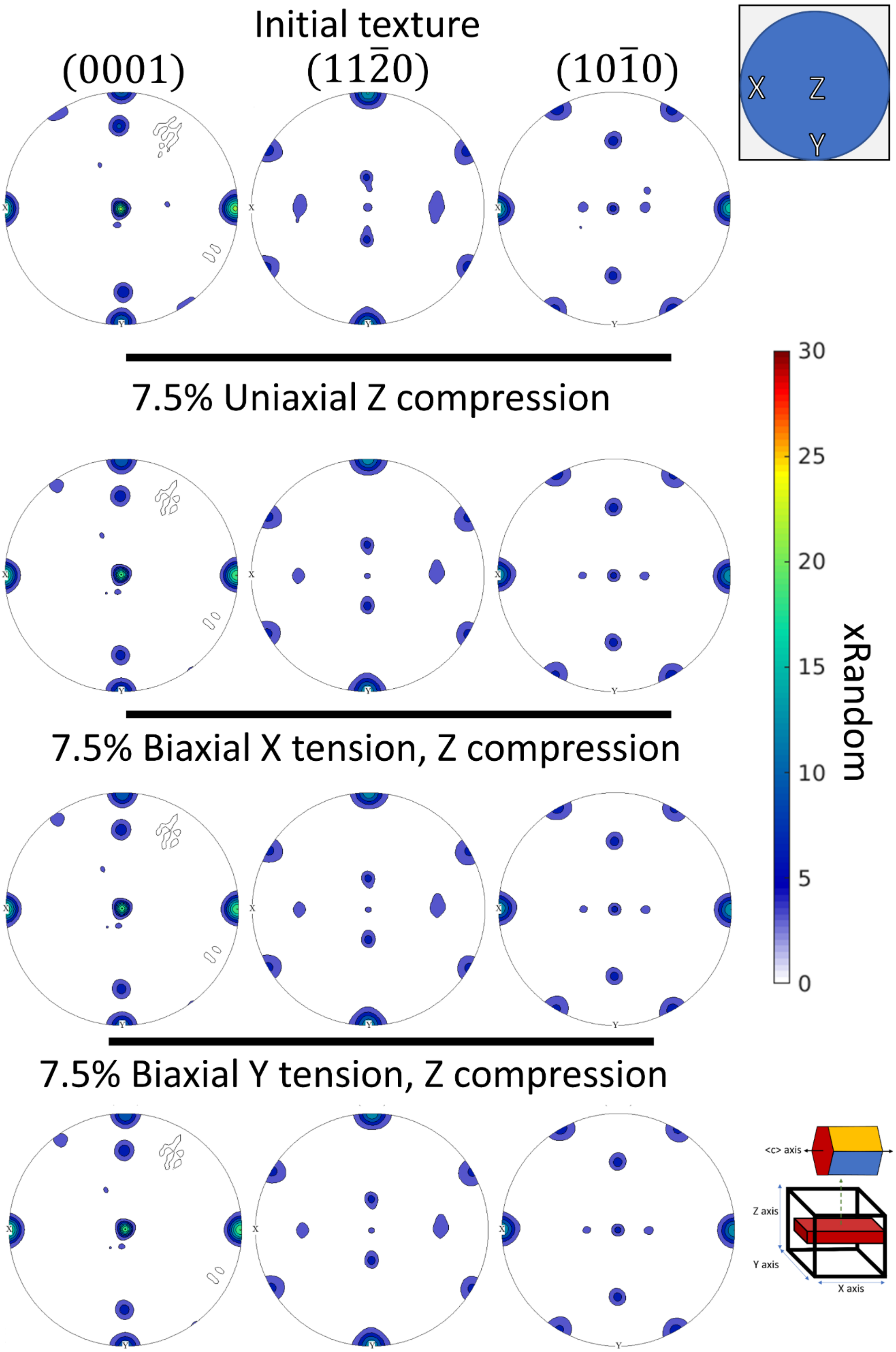

Figure 52: Smoothed (5° FWHM) pole figures of textured synthetic polycrystals, with a 5 x 3 x 1 grain macrozone, deformed to 7.5% strain in uniaxial compression, and biaxial tension and compression.

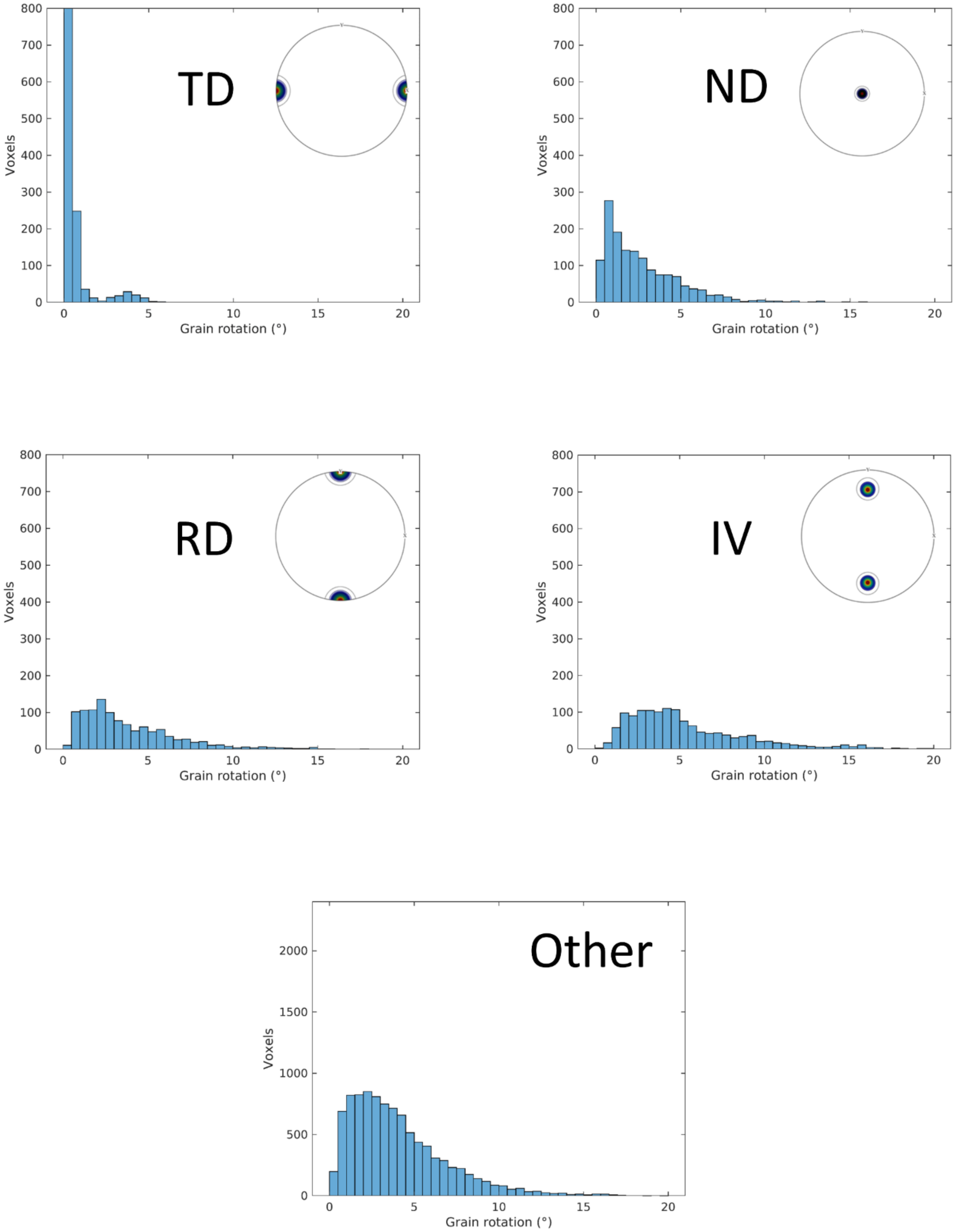

Figure 53: Lattice rotations within voxels of grains segmented by texture fibre, in a textured synthetic polycrystal containing a 5 x 3 x 1 macrozone, deformed to 7.5% biaxial tension along Y and compression along Z.

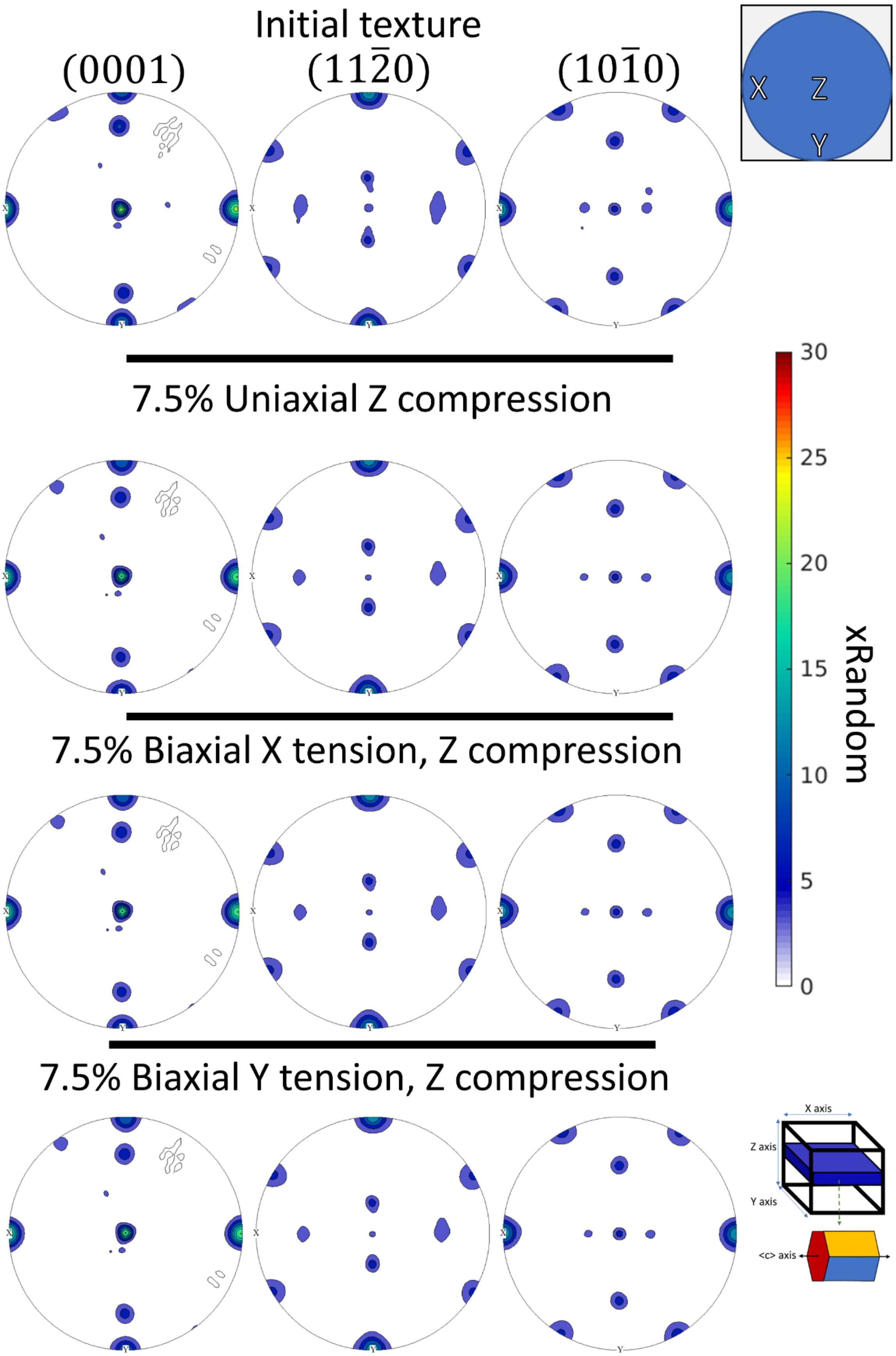

Figure 54: Smoothed (5° FWHM) pole figures of textured synthetic polycrystals, with a 5 x 5 x 1 grain macrozone, deformed to 7.5% strain in uniaxial compression, and biaxial tension and compression.

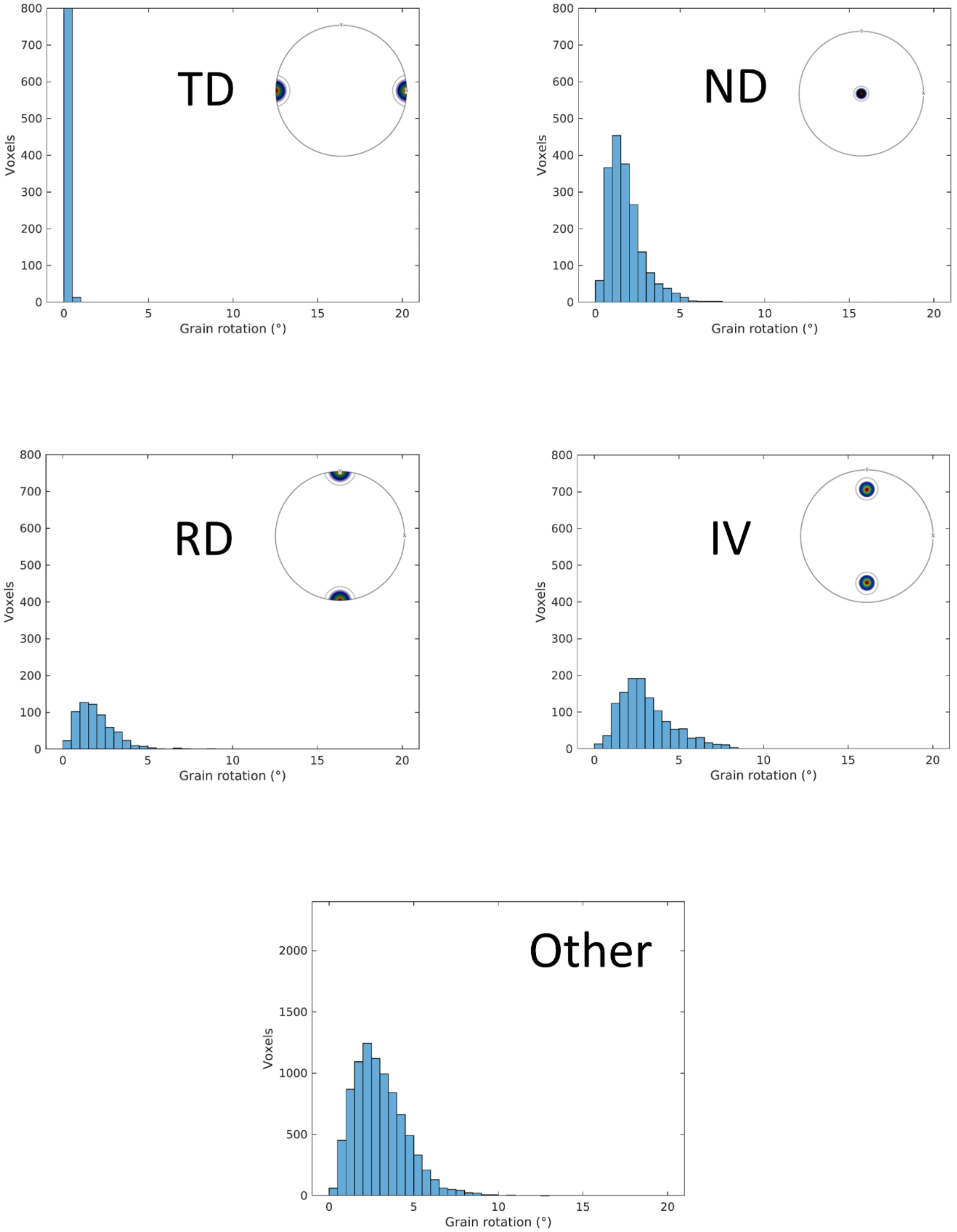

Figure 55: Lattice rotations within voxels of grains segmented by texture fibre, in a textured synthetic polycrystal containing a 5 x 5 x 1 macrozone, deformed to 7.5% biaxial tension along Y and compression along Z.

7 Discussion

7.1 Do macrozones in Ti-6Al-4V deform by twinning during hot rolling?

7.1.1 Evidence from Ti-6Al-4V bars rolled to 30% and 75% thickness reduction

In no EBSD mapping of the rolled materials presented in chapter 5 is any evidence of twinning visible (Figure 30 and Figure 34). The grain boundary misorientation maps do not show any macrozone α grains with neighbouring non-macrozone grains separated by a misorientation fitting any of the four twinning systems observed in titanium (compressive C1 64.6°, compressive C2 57.2°, tensile T1 84.8°, or tensile T2 35.1°). From the histograms of misorientations present in the bars rolled to 75% thickness reduction (Figure 38), the characteristic misorientations resulting from neighbouring BOR variants are clearly seen at all temperatures, indicating the inheritance of the texture through the α → β-phase transformation is dominant. Below 900 °C, the 10.529° variant misorientation is absent. The misorientations that indicate deformation twinning are not associated with any peaks on the histograms for bars rolled at 850 °C or above, which is to be expected since twinning in titanium alloys is thought to occur only at room temperatures (Philippe, Esling and Hoicheid, 1988; Zheng *et al.*, 2019). If any twinning has occurred at these temperatures, it only seems possible according to the hypothesis proposed by G. C. Obasi *et al.*, (2012), that twins propagate and consume their entire parent grain.

For bars rolled at 750 and 800 °C, a small peak is observed in the misorientation histogram below 60°, which might indicate some C2 twinning activity present in these bars. Given that die chill of around 200 °C has occurred (Figure 45), this is possible. However, under ND compression, macrozone grains are well oriented for < a > basal and prismatic slip, and this reorientation is not large enough to produce a (0002) | | ND fibre even if we assume that C2 deformation twinning has occurred within the macrozone laths. Only the T1 twinning mode has a reorientation large enough to reproduce the (0002) | | ND fibre from macrozone laths, with its reorientation of 84.8°. I do not interpret any evidence of T1 twinning in any of these results.

7.1.2 Evidence from CP-FFT simulations

The textures instanced in synthetic microstructures have not evolved any new fibres after 25% deformation in any of the three loading conditions modelled in section 6.3.1 (page 118, Figure 50). The

T1 tension twinning shear rates for the final deformation increments were an order of magnitude lower than the largest slip shear rate in all fibres (Table 12). As a 25% thickness reduction is as large as any rolling passes which were achieved, this confirms the absence of T1 twinning during the rolling trials discussed in section 7.1.1.

The consolidation of the macrozones into a contiguous unit did not result in any T1 twinning within the macrozones at 7.5% strain (Table 15 and Table 16), even when all slip modes were suppressed. As this loading condition is analogous to a single rolling pass, this further justifies why no texture flip is seen during the hot rolling experiments.

The CRSS values for slip systems have been calculated through experimental yield behaviour (Lerch and Arnold, 2016), adjusting the phenomenological CRSS values obtained by Zambaldi *et al.*, (2012) as described in section 6.1. But the twinning CRSS was estimated at 125% of the value of the < c + a > pyramidal in line with the relative strengths used in Taylor modelling by Philippe *et al.*, (1995), and therefore did not change significantly in favourability when the material properties were adjusted to high temperatures. Accurate empirical measurements of twinning CRSS values for the available twinning modes in Ti-6Al-4V could potentially produce a different result, but I think that this is unlikely given the twin CRSS values I have seen used in hcp crystal plasticity modelling are greater than the < a > basal and prismatic slip CRSS values (Abdolvand, Daymond and Mareau, 2011).

The decreases in CRSS values for slip families in titanium at high temperature are well known and demonstrate the decreased stresses required to activate slip on all systems at high-temperatures, when compared to room temperature deformation (as observed in Figure 9, and Lutjering and Williams, 2007). The easily activated < a > type slip systems require an additional deformation mode to enable plastic deformation along the < c > axis. At room temperature (i.e. during cold rolling), this deformation mode is twinning (Philippe, Esling and Hoicheid, 1988; Zheng *et al.*, 2019). However, at high temperatures, the reduced difficulty of < c + a > pyramidal slip supplants twinning. I surmise that a critical temperature exists at which the twinning and < c + a > pyramidal slip activities are equally favourable. The use of physically based, temperature-dependent slip and twinning constitutive equations would improve crystal plasticity modelling in this regard, enabling accurate prediction of textures as a function of temperature.

The application of macroscopic stress relaxation through the deviatoric shear stresses of the loading condition did not have a substantial effect on the lattice rotations observed (Table 11, Table 13 and Table 14), although the YZ biaxial loading conditions requiring deviatoric relaxation did not converge at 25% total strain. Due to the similar magnitudes of lattice rotation seen across the texture fibres in the other simulations, it is clear that the phenomenon of preferential twinning and < c + a > slip in (0002) | | ND grains observed in Taylor-FC modelling by Philippe *et al.*, (1995) does not occur in DAMASK. Since the stress and strain partitioning in the CP-FFT method is controlled by the constitutive parameters, with twinning assigned the CRSS value of largest magnitude, I find this result unsurprising.

7.2 The absence of a (0002) || ND texture fibre in rolled Ti-6Al-4V

7.2.1 Shortcomings of the rolling procedure

The furnaces were set to the intended rolling temperature before any as-received material was inserted, and the furnace adjusted in increments of 5 °C until the furnace interior was within 5 °C of the intended temperature. Once this was achieved, the bars were inserted into the furnace. However, during the 1 hour of heating the bar, in all cases the furnace became cooler, with all except the 850 °C recording a lower temperature than intended (Table 17). The difference between the intended temperature and the furnace interior was 11 °C or lower.

Intended rolling temperature (°C)	30% rolling thickness reduction furnace interior temperature (°C)	75% rolling thickness reduction trial furnace interior temperature (°C)
750	768	739
800	N/A	796
850	N/A	853
900	904	896
950	N/A	942

Table 17: Specified furnace temperatures, and furnace interior temperatures used to heat bars of Ti-6Al-4V prior to rolling, measured using a thermocouple.

However, during the transfer of a second 950 °C heated bar to the rolling mill, the bar had cooled by over 150 °C. This discrepancy increases the fraction of α present during the rolling, which results in difficulty achieving the intended thickness reduction of 15% per pass. At no temperature was this successfully achieved.

Tables of the mill rolling gaps for each trial are present in appendix 1 (page 162). The details of the rolling trials are outlined in section 5.2.1 (page 87).

For the 950 °C rolling trial, after a sizing pass at a rolling gap of 15 mm, a thickness reduction of 75.08% from a room temperature thickness of 15.01 mm, measured by Vernier callipers was achieved in five reductions of 15% of the original thickness, and one final correction pass, all at a rolling speed of 20 revolutions per minute. For passes 2-5, the bar was reheated in the furnace for two minutes. On the 6th pass, corresponding to a strain of 38%, the rolling mill stalled at the first two attempts, passing the bar partially through the mill. The bar was extracted by setting the mill to reverse, pushing the bar out of the front end. The bar was reheated for an additional 10 minutes between attempts, and the bar was successfully rolled through the mill at the third attempt.

For the 900 °C rolling trial, I increased the speed of the rolling mill to 30 revolutions per minute, in an attempt to reduce the heat losses due to die chill of the bar. However, this was insufficient to avoid the mill stalling during the final rolling pass. For passes 2-4, the reheat time was 2 minutes. On the 5th pass, the bar was reheated for 5 minutes, but stalled in the mill after passing 3/4s of the way through. After another 5 minutes of reheating, the bar was successfully rolled through the mill. The 6th pass, at 38% strain after a 2 minute reheat, stalled the mill immediately. As further passes were unlikely to succeed, I increased the rolling gap by 0.5 mm, to a strain of 29% for the adjusted pass. After a 5 minute reheat, the mill stalled again with approximately half the bar accepted through the rollers. As part of that amount passed through on the first failed attempt, I again decided to increase the rolling gap by 0.5 mm. This corresponds to an equivalent strain of 24%, notwithstanding the deformation already imparted to the bar on the two failed passes. After 5 minutes of reheating, the bar was successfully rolled through the mill. With a further 2 minutes of reheating, the bar was successfully rolled down to the target thickness in a correction step.

As the 800 °C rolling trial could be expected to be harder, I adjusted the rolling profile in advance, so that no rolling pass would require more than 20% strain, with the mill running at 30 revolutions per minute. After a sizing pass, the bar thickness was measured at 15.62 mm. With a 2 minute reheat, the 2nd, 4th and 7th passes, the mill stalled while the bar was approximately 2/3s of the way through.

Given the difficulties encountered with the 800 °C rolling trial, I chose to be cautious with the rolling profile for the 750 °C trial, with no pass attempting a greater strain than 12%. After a sizing pass, the bar was measured to be 15.49 mm in thickness. Between all passes from 2-13, the bar was reheated for 2 minutes, without stalling the mill. The 13th pass was a repeat of the rolling gap of the 12th pass, to correct the bar down to the target thickness. As the bar had warped significantly, it was reheated for a further two minutes and straightened using a 5-ton force on a fly-press.

To completely demonstrate the behaviour of Ti-6Al-4V across the range of temperatures from 750 °C to 950 °C, an additional rolling trial at 850 °C is necessary to conclude even steps of 50 °C across that interval. Starting from the rolling schedule that was used for 800 °C, I anticipated that the same rolling gaps would be achievable at the slightly higher temperature. The 3rd and 8th rolling passes stalled partway through the mill, requiring reheating for longer than 2 minutes and repeated rolling to achieve the thickness reduction of that pass. After measuring the thickness with Vernier callipers, I placed the bar on the steel pad of the fly-press to cool in air. Immediately after it had been set down, the temperature of the bar was found to be below 300 °C, indicating that the air cooling of the bar was effective almost immediately.

As my intention was to ensure that the final thickness reduction of the bar to 75% was achieved as closely as possible, the per-pass reduction deviated from the plan in all cases. This results in a very different and unpredictable internal stresses and strain rates for the final pass. In the motivating work by G.C. Obasi *et al.*, (2012) the final pass imposes a strain along ND of -38%. However, as the material I rolled at 950 °C required a second pass at its final rolling gap, the plastic strain for that pass was only -8%. For the 900 °C rolled material, the final pass strain was -24.5%, and for the 850 rolling the final pass achieved -19% strain. The 800 °C and 750 °C rolling trials also required a repeated final pass, correcting the thickness reduction with an unchanged roll gap. Their final-step thickness reductions were 20% and 5% respectively. The 750 °C rolling in particular could only be achieved with 12 passes, all of which achieved -15% strain or less, which may contribute to the formation of very fine secondary α and β grains at room temperature, similar to the martensitic structures formed by Chao, Hodgson and Beladi, (2016). It is my view that the strain rate of the final pass has a very important influence on the resulting rolling texture. A good way to examine this would be a comparison of 75% thickness reduction rolling trials at 950 °C with variation of the number of passes, and a uniaxial compression test. One possible experiment would be measurement of the texture by neutron diffraction, with in-situ heating and compression, at a facility such as the ENGIN-X beamline at the ISIS pulsed neutron and muon source.

7.2.2 Mechanisms affecting grain orientations

Observations of lattice rotation in simple bicrystal CP-FFT models demonstrate the controlling effect of the local texture. Grains which preferentially slip in a direction not parallel to the principal macroscopic shear experience the largest lattice rotations when strains are partitioned preferentially to them (Figure 47). Following uniaxial compression, or biaxial compression and tension of synthetic RVEs with several texture fibres, the largest magnitudes of grain rotation are not seen in in the TD texture fibre, which is well oriented for < a > basal and prismatic slip in all loading conditions (Figure 51, Table 11). The off-RD fibre (IV) and non-fibre grains have large magnitudes of rotation under all loading conditions. The RD fibre contains large lattice rotations in the biaxial loading cases yet does not in the case of uniaxial compression. Despite this, the largest slip shear rate of any fibre is found in the RD fibre (Table 12). This indicates that the Burgers vector of the most active slip system was aligned towards the Z axis. Since the RD fibre and TD fibre should have similar Schmid factors on their slip systems under this loading condition, as the rotation from one orientation to the other is centred around the compression axis, I find it surprising that the average slip shear rate in the TD fibre is one third of the magnitude of the average slip shear rate in the RD fibre. Their average lattice rotations are similar in magnitude. This indicates that the local stress partitioning controls the onset of slip during uniaxial compression of a polycrystal, which demonstrates the necessity of MDF control when instancing an RVE for a textured polycrystal.

As the rotation of macrozone laths through β-penetration has not been modelled, the emergence of new fibres from within the macrozones cannot be predicted by the CP-FFT methods used in chapter 6 (Semiatin, Seetharaman and Weiss, 1997; Roy, Madhavan and Suwas, 2014). This mechanism remains a possible explanation for the "texture flip" observed by G.C. Obasi *et al.*, (2012), and dual-phase simulations of Ti-6Al-4V could address this, informed by investigating the dual-phase morphology of Ti-6Al-4V at high temperature through in-situ heating and characterisation.

Considering the strength of the inherited β (110) texture in the α (0002) pole figure for the rolled and unrolled Ti-6Al-4V material heated to 950 °C, I consider the thermal transformation of the material through variant selection of the α → β → α transformation to be the dominant mechanism changing the texture of the rolled material. For the lower temperatures, the compliance of the β matrix surrounding the macrozone primary α is demonstrated by the consistent broadening of the (0002) | | TD fibre in the α pole figures. I would expect to see no off-RD fibre in an 800 °C heat-treated material, which would indicate that the fibre has formed through mechanical working, rather than through phase transformation. The β matrix surrounding off-macrozone primary α grains, as seen in the EDS measurements, is allowing for whole-grain rotation of macrozone α grains during rolling. At 950 °C, the material is almost entirely comprised of β during rolling which accounts for the reduction in the off-RD α fibre area fraction compared to the lower rolling temperatures.

7.2.3 Uncertainty of the retained β-phase fraction

My characterisation of the as-received material with a coarse beam raster increment of 1 μm in x and y observed a retained β fraction of 21.71%, albeit with 17.37% of the patterns measured not indexed to α-titanium or β-titanium. After a 1-hour heat treatment at 950 °C, both the fraction of patterns indexed as β and the fraction of patterns which did not index were reduced significantly, to 2.64% and 3.93% respectively. I do not believe that this represents a physical change in the retained β fraction, as the thermodynamic favourability of the α and β-phases is related to the local aluminium and vanadium content. However, as the heat treatment causes a relaxation of residual stresses within the material, the increase in fraction of this sample whose patterns are indexed is reasonable, even considering the very large step size of acquisition. Since "beam wobble" during acquisition results in the convolution of patterns across the area inspected by the electron beam, it is more difficult to obtain patterns from samples with a refined grain morphology with a large step size. The dramatic α grain growth, particularly the elimination of small grains within the macrozones (Figure 25), has resulted in easier pattern acquisition and indexing. Considering the pattern quality and phase maps during rolling to 30% thickness reduction (Figure 32 and Figure 33), there is a spatial association of reduced pattern quality with the presence of retained β-phase. This indicates that the retained β is more difficult to index, even in the most favourable conditions which result from the heat treatment.

A question I asked myself while collecting the EBSD maps was "where has all the β-phase gone?" Of the five 75% thickness reduction rolling trials, the 750 °C rolled material indexed the largest fraction of the surface as β-phase, at 9.47%, (Table 18). This would be expected for Ti-6Al-4V at room temperature (Pilchak, Sargent and Semiatin, 2018), but increased rolling temperature resulted in a reduction in the indexed β-phase, despite the higher β-phase fraction during rolling. This reduction in retained β motivated my investigation of the phase composition through direct backscatter imaging in section 3.1.4

Direct backscatter (p 57). As I calculated the β-phase fraction to be 13.0% ± 7.56 for the as-received material, 6 of the 13 maps lie outside this interval, including the EBSD characterisation of the as-received material itself.

Temperature (° C)	Total thickness reduction (%)	Step size (μm)	Indexed Ti-α (%)	Indexed Ti-β (%)	Not indexed (%)
As received	0	0.99	60.91	21.71	17.37
950	0	1.00	93.43	2.64	3.93
750	10	1.00	95.29	2.87	1.84
750	20	1.00	74.63	**7.95**	17.43
750	30	0.86	81.04	**11.69**	7.27
900	10	1.00	84.42	**9.20**	6.38
900	20	1.00	91.63	4.62	3.75
900	30	1.00	76.94	**11.29**	11.77
750	75	0.05	84.93	**9.47**	5.60
800	75	0.16	81.28	**5.69**	13.03
850	75	0.30	74.88	**7.93**	17.19
900	75	1.04	86.80	4.89	8.31
950	75	0.17	95.28	1.89	2.83

Table 18: Indexed fractions of EBSD maps presented in (results chapter 2), with beta fractions within the range expected from DBS imaging shown in bold.

Several of the maps have large fractions which have not indexed, which could be caused by systematic misindexing of the β-phase and thus account for the reduced β-phase fraction. However, the difference of specific examples such as 950 °C/75% and 750 °C/10% indicates that in some maps, the α-phase is over-represented. Although several of the 75% thickness reductions required a very small step size to ensure an acceptable indexing rate, the β-phase fraction does not appear to be related to the step size. At 75% thickness reduction, an increase in temperature generally seems associated with a decrease in the indexed β-phase fraction. The samples rolled to this thickness reduction at 900 and 950 °C both have a lower indexed β-fraction than could be expected, with the 950 °C rolled sample indexing at a sufficient rate to discount preferential indexing of α-phase due to a highly deformed β-phase.

7.2.4 Formation of the off-RD texture fibre

As close to the β-transus, 980 °C, the bar will be almost entirely comprised of β within the mill, slip is occurring primarily within β grains, which are softer than the α grains. However, considering the effect of die chill reduces the mill temperature by at least 200 °C (Figure 45), the material temperature for the 800 °C rolling trial is sufficiently below the transus that α grains have recrystallised, but still is hot enough that the β matrix is still present. As the equiaxed off-macrozone grains have improved pattern quality compared to the macrozone α and the β grains (Figure 36) the EDS spectroscopy demonstrating the presence of vanadium enrichment near off-macrozone α grains suggests that these grains have been rotated as a whole grain within a compliant β matrix, with β-penetration at points of significant shear within the laths (Figure 44). The small, bright grains and laths in the pattern quality map after rolling at 900 and 950 °C demonstrates the recrystallisation of β grains during cooling but are not present in the maps obtained after rolling at 850 °C or lower. The possibility of the RD texture fibre forming through recrystallisation can be rejected, since their moderate pattern quality indicates some lattice curvature, due to the presence of dislocations arising from deformation by slip.

7.2.5 Mobility of alloying elements

Applying the diffusion rates for vanadium and aluminium in titanium obtained by Semiatin *et al.*, (2004) to Fick's law, the largest magnitude of diffusion should be expected at temperatures between 900 – 950 °C. As the material used in the rolling trials is heated first for a one-hour soak, there is potential for diffusion of aluminium and vanadium atoms by an average of 33 μm, as addressed in section 2.2.7. For the 750 °C soak, the diffusion will be negligible.

Given that the formation of the off-RD texture fibre requires local enrichment of vanadium and depletion of aluminium, the diffusion of vanadium into an equilibrium spatial distribution may be the cause of the lack of an off-RD fibre after rolling to 75% thickness reduction at 900 and 950 °C (Figure 35). Since this fibre is forming through β-penetration of macrozone laths, reducing the soak duration will minimise the diffusion of vanadium, and may result in the formation of an off-RD fibre during rolling close to the transus.

Considering a 950 °C heat treatment of several hours, a microstructure and texture similar to Figure 25 will be obtained, dominated by coarse macrozones and large equiaxed primary-α grains. The macrozones will still deform by < a > basal and prismatic slip, which will not enable a "texture flip".

7.3 Viability of instancing virtual microstructures for texture evolution

7.3.1 Obtaining a representative surface morphology

In the TCVT method, the overdetermination of the near-surface seeds is constrained by the ratio of edge grains and interior grains, (Equation (32), page 55). If this criterion is not met, the computation of new near-surface Voronoi seeds which satisfy the reference surface will not converge, resulting in the trivial, original solution with all seeds fixed on the Z = 0 plane. This was the case when I attempted to model the surface containing 157 grains, which limited my model to the 23-grain reference surface. This limits the grain size distribution to a small number of large grains which dominate the ODF.

In order to improve the representation of the surface geometry, a change to the method of separating the surface into subsections would increase the number of grains that could be modelled. This reduces the volume fraction of each surface grain, which increases the total number of subsurface grains which are generated in the model, improving the representation of the texture through the MDF. This method gives complete freedom over the resolution of the overall surface, with as many grains being introduced as desired. It will also allow the introduction of complex morphological features such as macrozone laths.

A drawback of this method is the introduction of artefact grains at the boundaries where each subsection is joined together. As the Laguerre tessellation can only produce convex shapes, the artifacts will form a concave morphological unit of two grains with the same crystallographic orientation, similar to the multi-seed Voronoi tessellation used in Neper (Quey, Dawson and Barbe, 2011). However, since these artifacts are spatially located along the subsection boundaries, it will be important to control their placement to reduce their influence on the stress and strain partitioning.

The near-surface morphology instanced through the TCVT method is not completely columnar, which would result in anomalously large variation in the stress and strain partitioning at grain boundaries (Diehl *et al.*, 2016). Comparing the vertical inclination of grains instanced through the TCVT method and Voronoi tessellation, around half of the grain boundaries in a model constructed from reference surface of 23 grains are inclined by less than 10° (Figure 20 and Figure 21). Since the model with 157 grains in its reference surface produced a trivial columnar solution, this indicates the difficulty of modelling the reference surface within a 3D RVE. The Humphreys criterion of 500-1500 independent measurements of orientations in order to faithfully represent texture suggests that 157 grains is a poor representation of the texture of a surface, which motivates the modelling of reference surfaces containing a greater number of grains (Humphreys, 2001b).

The ODF of the subsurface grains was instanced directly by sampling orientations directly from the reference surface, which has been shown by P. Eisenlohr and Roters, (2008) to strengthen the texture of the most frequent orientations when a small number of grains are sampled. This effect is seen in Figure 22e. However, the ability to reproduce significantly larger surfaces with more grains, by reproducing the reference surface through several subsections should ensure enough grains are instanced to correct this. The increased number of surface grains is necessary in order to generate enough subsurface grains to appropriately control the MDF.

7.3.2 Controlling the instanced texture through the MDF

The MDF fitting for a small number of subsurface grains is extremely difficult, as seen in figure (Figure 22c). The reference surface of 23 grains was instanced into a RVE containing 97 grains, of which only 74 are subsurface grains whose orientations may be altered. As the cost function for texture optimisation (Figure 22g) only produced 114 operations which improved the texture representation after 20000 attempts, there is significant computational cost in computing a representative MDF using a small number of grains through a Monte Carlo method, since a satisfactory texture is difficult to obtain at random, if it is possible at all. If the iteration limit of 20000 is a necessary restriction of the computation, it is an appropriate interpretation that the number of available grains was not sufficient for texture optimisation.

The surface containing 157 grains generated a volume with over 1000 grains, described by the same number of voxels as the 97 grain RVE. Its initial starting MDF (Figure 22e) closely resembles a random, Mackenzie-like distribution of orientations. After 20000 attempts at optimising the texture, the MDF is reproduced with a much better agreement than in the 97 grain RVE. There is therefore a tension between the requirements of obtaining a good surface morphology with reasonable representation of the near-surface grains and providing an appropriate representation of the texture through the subsurface MDF.

An extension of the subsurface dimension to contain many more voxels than either of the surface in-plane dimensions, the number of subsurface grains available to produce the MDF is increased. However, this increases the requirement in computational memory when generating the RVE and computing the CP-FFT simulation. The grains of the subsurface will also be spatially separated from the constrained surface, which is disadvantageous when considering the effect of subsurface texture on the stress and strain partitioning on the surface. It is necessary to investigate the effect of Saint-Venant's principle with respect to both morphology and texture before making this alteration to the method.

The macroscopic stress and strain behaviours are identical for the CP-FFT models with both a controlled and an uncontrolled MDF (Figure 23). This demonstrates the inadequacy of measuring local effects through macroscopic measurements of mechanical properties, as they cannot be differentiated across that lengthscale. The segregation of the largest strain differences to grain boundaries and triple junctions (Figure 24) indicates the potential for crack initiation leading to failure. The local stress differences between the models are greater than the magnitude of the CRSS at these locations, indicating that plastic deformation cannot be accurately modelled without a full description of the crystallographic texture. As optimising the subsurface MDF causes such a significant difference in micromechanical behaviour, failing to account for it in a crystal plasticity model with the intention of predicting material performance failure is inadequate.

7.3.3 Compensating for periodic boundary conditions in CP-FFT simulations

Through the inhibition of stress and strain transfer across the domain boundaries (Figure 24), the isotropic medium embedding method demonstrates its value when utilising CP-FFT methods to simulate local effects. However, when modelling the texture evolution of individual fibres during rolling of Ti-6Al-4V, this was not necessary (Figure 48), as homogenisation of the RVE was desirable. The constraint of periodic boundary conditions must be either utilised or ameliorated in CP-FFT simulations. An investigation of the embedded domain method should be conducted in future to demonstrate the effect of Saint-Venant's principle when attempting to eliminate periodic artifacts in the CP-FFT method.

8 Conclusion

In this thesis I have examined the formation of texture in the titanium alloy Ti-6Al-4V through hot rolling, by characterising rolled material through EBSD, and examining the mechanisms of plastic deformation through CP-FFT simulations. I have shown the effect of rolling temperature on the morphology of Ti-6Al-4V, between the range of 750 and 950 °C, to a thickness reduction of 75%.

By developing a "TCVT" toolkit for synthetic generation of RVEs for DAMASK CP-FFT simulations, using limited statistical information obtained through surface EBSD characterisation, I present a method to examine the effect of subsurface texture on stress and strain partitioning, using the method of constraining a reference surface of grains innovated by Qiu, (2016) and the method of controlling subsurface texture through the MDF innovated by Saylor, Fridy, El-Dasher, Jung, & Rollett, (2004). Instancing two reference surfaces through the TCVT method, I have demonstrated the effect of subsurface texture on stress and strain partitioning in the constrained reference surface during simulations of uniaxial tension to 0.5% strain. The TCVT method can be expanded further to generate more representative microstructures, connecting simulation and experiment.

In order to control the MDF of the subsurface texture, an RVE must be constructed containing an order of magnitude more grains with a free choice of orientation, compared to the number of grains in its reference surface. With a decrease in the average area fraction of the surface grains, it became easier to reproduce the subsurface MDF.

Localised variations in stresses at grain boundaries, of the magnitude of the CRSS in the material are seen between RVEs with the same grain morphology and surface texture, and a different subsurface texture. This coincides with differences in strain partitioning at grain boundaries and triple junction, demonstrating a difference in the plastic behaviour of the two models and indicating the potential for material failure through crack initiation. The macroscopic stress and strain behaviours of the RVEs were equivalent. This indicates the importance of accurately characterising the texture throughout an RVE in order to draw any conclusion about material deformation modes (e.g. texture evolution and performance).

The number of grains that can be accurately represented in a cell diagram reproduced through near-surface seeds is constrained by an overdetermination criterion derived from Euler's formula of the faces, edges and vertices of a polyhedron. The number of central grains of the surface must be no greater than 1/6th of the number of grains at the domain boundary for the surface layer. This is in opposition to the requirement of many grains on the surface, which is necessary in order to populate many subsurface grains to control the MDF. Alternative methods could be established to instance surfaces with many grains, such as a partitioning of the reference surface into subsections of equal size.

Within the materials, the morphologies of the microstructure and crystallographic texture have been examined through EBSD mapping, chosen due to its capability of simultaneously characterising spatial and orientation information. This allowed me to generate pole figures and describing the material texture, and IPF maps presenting grain structures and their orientations. Grain boundary misorientations were computed from these maps and indirectly describe the twinning and phase transformation behaviour of the material. The area fraction and misorientations were segmented according to the texture fibres of the constituent material grains, informing the partitioning of plastic deformation behaviour and texture evolution within the fibres of the material.

In bars of Ti-6Al-4V rolled to a total thickness reduction of 75%, the macrozones of lenticular α-phase titanium laths with (0002) || TD are seen in EBSD characterisation after rolling at temperatures between 750 and 950 °C. These macrozones dominate the texture observed through pole figures, with minimal contributions from a "flipped" texture of (0002) || ND which has been seen in literature, and attributed to whole-grain twinning by G.C. Obasi *et al.*, (2012).

No evidence of twinning during hot-rolling has been observed, since the misorientation distributions after all rolling trials indicate that the predominant method of texture evolution is the inheritance of α-phase orientations from the β-phase through the BOR, and no characteristic twin-parent misorientations are seen.

A texture fibre not present in the as-received material emerges during deformation by rolling, with (0002) planes aligned 20° away from the rolling direction. Measurement of the elemental composition surrounding the grains of this texture fibre indicates an enrichment of vanadium, which is a β-stabilising element in titanium alloys. This indicates the potential for formation of this texture fibre through whole grain rotation of macrozone laths following β-penetration of the macrozones. This fibre is strongest in intensity at rolling temperatures well below the β-transus, and is lower in intensity during rolling at 900 or 950 °C.

Through CP-FFT simulations of textured synthetic polycrystals, I have examined the plastic deformation behaviour and texture evolution in RVEs representing the rolled Ti-6Al-4V textures characterised by EBSD. This was motivated by my lack of observation of a "texture flip" following hot rolling experiments, and thus lattice rotations arising from crystal slip were examined in the model following uniaxial compression and biaxial tension and compression, through partitioning of the volume according to texture fibres. The (0002) || TD fibre is seen to wholly deform through crystal slip during uniaxial compression and biaxial tension and compression to strains equivalent to a single reduction pass of a rolling procedure.

With constitutive parameters obtained through phenomenological measurements of yield behaviour in Ti-6Al-4V, deformation by twinning is not seen in any of the experimentally observed texture fibres in rolled Ti-6Al-4V. This supports the lack of a "flipped" texture fibre observed through characterisation of rolled bars and is evidence against a mechanism of whole-grain twinning in hot-rolled Ti-6Al-4V.

This thesis has presented an investigation of micromechanical behaviour during deformation of Ti-6Al-4V by rolling. At temperatures close to the β-transus, crystal slip is shown to be the only active mode of plastic deformation, with texture evolution arising from the deformation of β-phase grains are inherited through the BOR. This will enable metallurgical manufacturers to understand the performance of their material and the risks of component failure. The influence of texture on the plastic deformation of crystals reaches far beyond a single unit in a neighbourhood.

Future Work

The RVE instantiation method detailed in chapter 3 and used in chapter 4 to describe a copper microstructure can be developed to reproduce a Ti-6Al-4V macrozone, within a network of equiaxed primary-α grains. This will enable the use of Ti-6Al-4V EBSD maps in order to investigate the effects of the texture fibres discovered in chapter 5 upon the stress and strain partitioning in grains of known morphology and texture. However, in order to reproduce the many lenticular grains of the colony structures seen in titanium microstructures, the algorithm of describing the reference surface as a 3D Voronoi tessellation must be partitioned, such that each section of the surface whose Voronoi seed points are optimised fit the constraint of overdetermination (equation 30, page 59).

In order to appropriately reproduce the morphology of subsurface macrozones, the automated instantiation of the "hamburger" and "frankfurter" geometries described in Figure 49 (page 118) can be included into the instantiation model, constraining the morphology and location of the grains contributing to the (0002) ||TD fibre.

The effect of relaxed and constrained CP-FFT boundary conditions is uncertain. I have observed small differences in the average lattice rotation in the texture fibres after deformation to 7.5% strain, as seen in Table 11 (page 123), Table 13 (page 125), and Table 14 (page 125). Further investigation into the local stress and strain partitioning under different boundary conditions could provide context when interpreting texture evolution in CP-FFT simulations.

EBSD characterisation of Ti-6Al-4V heat treated at 800 °C for one hour and air cooled would investigate the possibility of a thermal mechanism contributing to the emergence of a (0002) || ND texture fibre. Since the 950 °C heat treatment conducted in chapter 5 (Figure 26, page 81) demonstrates the formation of this fibre through inheritance of β-phase texture through the BOR, a heat treatment at 800 °C could eliminate the BOR as a possible mechanism for the "texture flip" reported by G.C. Obasi *et al.*, (2012).

Bibliography

Abdolvand, H., Daymond, M. R. and Mareau, C. (2011) 'Incorporation of twinning into a crystal plasticity finite element model: Evolution of lattice strains and texture in Zircaloy-2', *International Journal of Plasticity*. Pergamon-Elsevier Science Ltd., 27(11), pp. 1721–1738. doi: 10.1016/j.ijplas.2011.04.005.

Ahmed, T. and Rack, H. J. (1998) 'Phase transformations during cooling in α+β titanium alloys', *Materials Science and Engineering: A*. Elsevier, 243(1–2), pp. 206–211. doi: 10.1016/S0921-5093(97)00802-2.

Araki, H. *et al.* (1994) 'Anomalous diffusion of Aluminum inβ-Titanium', *Metallurgical and Materials Transactions A*, 25(4), pp. 874–876. doi: 10.1007/BF02665465.

Aurenhammer, F. (1987) 'Power Diagrams: Properties, Algorithms and Applications.', *SIAM Journal on Computing*. SIAM Publications, 16(1), pp. 78–96. doi: 10.1137/0216006.

Bachmann, F., Hielscher, R. and Schaeben, H. (2011) 'Grain detection from 2d and 3d EBSD data—Specification of the MTEX algorithm', *Ultramicroscopy*. North-Holland, 111(12), pp. 1720–1733. doi: 10.1016/J.ULTRAMIC.2011.08.002.

Baggerly, R. G., Paton, N. E. and Williams, J. C. (1976) *Deformation and Solid Solution Strengthening of Titanium-Aluminum Single Crystals*.

Beladi, H., Chao, Q. and Rohrer, G. (2014) 'Variant selection and intervariant crystallographic planes distribution in martensite in a Ti–6Al–4V alloy', *Acta Materialia*, 80, pp. 478–489. doi: 10.1016/j.actamat.2014.06.064.

Le Biavant, K., Pommier, S. and Prioul, C. (2002) 'Local texture and fatigue crack initiation in a Ti-6Al-4V titanium alloy', *Fatigue & Fracture of Engineering Materials & Structures*. John Wiley & Sons, Ltd (10.1111), 25(6), pp. 527–545. doi: 10.1046/j.1460-2695.2002.00480.x.

Bishop, J. F. W. and Hill, R. (1951) 'CXXVIII. A theoretical derivation of the plastic properties of a polycrystalline face-centred metal', *The London, Edinburgh, and Dublin Philosophical Magazine and Journal of Science*. Taylor & Francis, 42(334), pp. 1298–1307. doi: 10.1080/14786444108561385.

Borgh, I. *et al.* (2013) 'On the three-dimensional structure of WC grains in cemented carbides', *Acta Materialia*. Pergamon, 61(13), pp. 4726–4733. doi: 10.1016/J.ACTAMAT.2013.05.008.

Boyle, K. P. (2005) 'Latent Hardening in Copper and Copper Alloys', in *Textures of Materials - ICOTOM 14*. Trans Tech Publications (Materials Science Forum), pp. 1043–1048.

Burgers, W. G. (1934) 'On the process of transition of the cubic-body-centered modification into the hexagonal-close-packed modification of zirconium', *Physica*, 1(7–12), pp. 561–586. doi: 10.1016/S0031-8914(34)80244-3.

Chao, Q., Hodgson, P. D. and Beladi, H. (2016) 'Microstructure and Texture Evolution During Symmetric and Asymmetric Rolling of a Martensitic Ti-6Al-4V Alloy', *Metallurgical and Materials Transactions A*, 47(1), pp. 531–545. doi: 10.1007/s11661-015-3211-y.

Courant, R. (1943) 'Variational methods for the solution of problems of equilibrium and vibrations', *Bull. Amer. Math. Soc.* American Mathematical Society, 49(1), pp. 1–23. Available at: https://projecteuclid.org:443/euclid.bams/1183504922.

Cromwell, P. (1997) *Polyhedra*. Cambridge: Cambridge University Press.

Dawson, P. R. and Boyce, D. E. (2015) 'FEpX -- Finite Element Polycrystals: Theory, Finite Element Formulation, Numerical Implementation and Illustrative Examples'. Available at: http://arxiv.org/abs/1504.03296 (Accessed: 23 August 2017).

Diehl, M. *et al.* (2016) 'Neighborhood influences on stress and strain partitioning in dual-phase microstructures', *Meccanica*, 51(2), pp. 429–441. doi: 10.1007/s11012-015-0281-2.

Dunne, F. P. E. and Petrinic, N. (2005) *Introduction to Computational Plasticity*. Oxford University Press.

Dunne, F. P. E., Rugg, D. and Walker, A. (2007) ‘Lengthscale-dependent, elastically anisotropic, physically-based hcp crystal plasticity: Application to cold-dwell fatigue in Ti alloys’, *International Journal of Plasticity*, 23(6), pp. 1061–1083. doi: 10.1016/j.ijplas.2006.10.013.

Eisenlohr, P. *et al.* (2013) ‘A spectral method solution to crystal elasto-viscoplasticity at finite strains’, *International Journal of Plasticity*. Elsevier Ltd, 46, pp. 37–53. doi: 10.1016/j.ijplas.2012.09.012.

Eisenlohr, P. and Roters, F. (2008a) ‘Selecting a set of discrete orientations for accurate texture reconstruction’, *Computational Materials Science*, 42(4), pp. 670–678. doi: 10.1016/j.commatsci.2007.09.015.

Eisenlohr, P. and Roters, F. (2008b) ‘Selecting a set of discrete orientations for accurate texture reconstruction’, *Computational Materials Science*, 42(4), pp. 670–678. doi: 10.1016/j.commatsci.2007.09.015.

Eshelby, J. D. (1957) ‘The Determination of the Elastic Field of an Ellipsoidal Inclusion, and Related Problems’, *Proceedings of the Royal Society of London A: Mathematical, Physical and Engineering Sciences*, 241(1226), pp. 376–396. Available at: http://rspa.royalsocietypublishing.org/content/241/1226/376.abstract.

Follansbee, P. S. and Gray, G. T. (1989) ‘An analysis of the low temperature, low and high strain-rate deformation of Ti−6Al−4V’, *Metallurgical Transactions A*, 20(5), pp. 863–874. doi: 10.1007/BF02651653.

Galán-López, J. and Verleysen, P. (2018) ‘Simulation of the plastic response of Ti–6Al–4V thin sheet under different loading conditions using the viscoplastic self-consistent model’, *Materials Science and Engineering: A*. Elsevier, 712, pp. 1–11. doi: 10.1016/J.MSEA.2017.11.070.

Gey, N. and Humbert, M. (2002) ‘Characterization of the variant selection occurring during the α→β→α-phase transformations of a cold rolled titanium sheet’, *Acta Materialia*. Pergamon, 50(2), pp. 277–287. doi: 10.1016/S1359-6454(01)00351-2.

Gibbs, G. B. (1969) ‘Thermodynamic analysis of dislocation glide controlled by dispersed local obstacles’, *Materials Science and Engineering*, 4(6), pp. 313–328. doi: 10.1016/0025-5416(69)90026-3.

Glavicic, M. G. *et al.* (2003) ‘Texture evolution in vacuum arc remelted ingots of Ti-6Al-4V’, *Materials Science and Engineering: A*. Elsevier, 346(1–2), pp. 8–18. doi: 10.1016/S0921-5093(02)00525-7.

Goldstein, J. I. *et al.* (2018) *Scanning Electron Microscopy and =X-Ray Microanalysis*. 4th edn. New York: Springer.

Groeber, M. A. *et al.* (2006) ‘3D reconstruction and characterization of polycrystalline microstructures using a FIB–SEM system’, *Materials Characterization*. Elsevier, 57(4–5), pp. 259–273. doi: 10.1016/J.MATCHAR.2006.01.019.

Groves, G. W. and Kelly, A. (1963) ‘Independent slip systems in crystals’, *The Philosophical Magazine: A Journal of Theoretical Experimental and Applied Physics*. Taylor & Francis, 8(89), pp. 877–887. doi: 10.1080/14786436308213843.

Hémery, S. *et al.* (2019) ‘A 3D analysis of the onset of slip activity in relation to the degree of micro-texture in Ti-6Al-4V’, *Acta Materialia*. Pergamon. doi: 10.1016/J.ACTAMAT.2019.09.028.

Hémery, S. and Villechaise, P. (2019) ‘In situ EBSD investigation of deformation processes and strain partitioning in bi-modal Ti-6Al-4V using lattice rotations’, *Acta Materialia*. Pergamon, 171, pp. 261–274. doi: 10.1016/J.ACTAMAT.2019.04.033.

Van Houtte, P. (1988) ‘A Comprehensive Mathematical Formulation of an Extended Taylor–Bishop–Hill Model Featuring Relaxed Constraints, the Renouard–Wintenberger Theory and a Strain Rate Sensitivity Model’, *Textures and Microstructures*, 8–9, pp. 313–350.

Van Houtte, P. *et al.* (2012) ‘Multi-scale modelling of the development of heterogeneous distributions of stress, strain, deformation texture and anisotropy in sheet metal forming’, *Procedia IUTAM*, 3, pp. 67–75. doi: 10.1016/j.piutam.2012.03.005.

Humbert, M. *et al.* (2006) ‘Study of the variant selection in sharp textured regions of bimodal IMI 834 billet’, *Materials Science and Engineering: A*. Elsevier, 430(1–2), pp. 157–164. doi: 10.1016/J.MSEA.2006.05.047.

Humphreys, F. J. (2001a) ‘Review Grain and subgrain characterisation by electron backscatter diffraction’, *Journal of Materials Science*, 36(16), pp. 3833–3854. doi: 10.1023/A:1017973432592.

Humphreys, F. J. (2001b) ‘Review Grain and subgrain characterisation by electron backscatter diffraction’, *Journal of Materials Science*, 36(16), pp. 3833–3854. doi: 10.1023/A:1017973432592.

Hutchinson, J. W. (1976) ‘Bounds and Self-Consistent Estimates for Creep of Polycrystalline Materials’, *Proceedings of the Royal Society of London. A. Mathematical and Physical Sciences*, 348(1652), pp. 101 LP – 127. Available at: http://rspa.royalsocietypublishing.org/content/348/1652/101.abstract.

James, D. W. and Moon, D. M. (1970) ‘The artensitic transformation in titanium binary alloys and its effect on mechanical properties’, *The Science, Technology and Application of Titanium*. Pergamon, pp. 767–778. doi: 10.1016/B978-0-08-006564-9.50083-X.

Jia, H., Marthinsen, K. and Li, Y. (2019) ‘Revealing abnormal {112¯1} twins in commercial purity Ti subjected to split Hopkinson pressure bar’, *Journal of Alloys and Compounds*. Elsevier, 783, pp. 513–523. doi: 10.1016/J.JALLCOM.2018.12.092.

Jones, I. P. and Hutchinson, W. B. (1981) ‘Stress-state dependence of slip in Titanium-6Al-4V and other H.C.P. metals’, *Acta Metallurgica*. Pergamon, 29(6), pp. 951–968. doi: 10.1016/0001-6160(81)90049-3.

Karthikeyan, T. *et al.* (2010) ‘Effect of cooling rate on transformation texture and variant selection during β → α transformation in Ti–5Ta–1.8Nb alloy’, *Materials Science and Engineering: A*. Elsevier, 528(2), pp. 549–558. doi: 10.1016/J.MSEA.2010.09.055.

Karthikeyan, T., Saroja, S. and Vijayalakshmi, M. (2006) ‘Evaluation of misorientation angle-axis set between variants during transformation of bcc to hcp phase obeying Burgers orientation relation', *Scripta Materialia*. Pergamon, 55(9), pp. 771–774. doi: 10.1016/J.SCRIPTAMAT.2006.07.022.

Kocks, F., Tomé, C. and Wenk, H.-R. (2000) *Texture and Anisotropy. Preferred Orientations in Polycrystals and Their Effect on Material Properties*.

Kolli, P. R. and Devaraj, A. (2018) 'A Review of Metastable Beta Titanium Alloys', *Metals*. doi: 10.3390/met8070506.

Lebensohn, R. A. (2001) 'N-site modeling of a 3D viscoplastic polycrystal using Fast Fourier Transform', *Acta Materialia*, 49(14), pp. 2723–2737. doi: 10.1016/S1359-6454(01)00172-0.

Lebensohn, R. A., Sanchez, P. V. and Pochettino, A. A. (1994) 'Modelling texture development of zirconium alloys at high temperatures', *Scripta Metallurgica et Materialia*, 30(4), pp. 481–486. doi: 10.1016/0956-716X(94)90607-6.

Lebensohn, R. A. and Tomé, C. N. (1993) 'A self-consistent anisotropic approach for the simulation of plastic deformation and texture development of polycrystals: Application to zirconium alloys', *Acta Metallurgica et Materialia*, 41(9), pp. 2611–2624. doi: 10.1016/0956-7151(93)90130-K.

Leo Prakash, D. G. *et al.* (2010) 'Deformation twinning in Ti-6Al-4 V during low strain rate deformation to moderate strains at room temperature', *Materials Science and Engineering: A*. Elsevier, 527(21–22), pp. 5734–5744. doi: 10.1016/J.MSEA.2010.05.039.

Leo Prakash, D. G. *et al.* (2015) 'Microstructure and texture evolution during thermomechanical processing of β-quenched Zr', *Acta Materialia*, 88, pp. 389–401. doi: 10.1016/j.actamat.2014.12.033.

Lerch, B. A. and Arnold, S. M. (2016) *Viscoplastic characterization of Ti-6-4: Experiments*. Cleveland, OH.

Lienert, U. *et al.* (2011) 'High-energy diffraction microscopy at the advanced photon source', *Jom*, 63(7), pp. 70–77. doi: 10.1007/s11837-011-0116-0.

Liu, B. *et al.* (2010) 'Comparison of finite element and fast Fourier transform crystal plasticity solvers for texture prediction', *Modelling and Simulation in Materials Science and Engineering*, 18(8), p. 085005. doi: 10.1088/0965-0393/18/8/085005.

Lutjering, G. and Williams, J. C. (2007) *Titanium*. 2nd ed. Berlin: Springer (Engineering materials and processes).

Ma, R. *et al.* (2018) 'Modeling the evolution of microtextured regions during α/β processing using the crystal plasticity finite element method', *International Journal of Plasticity*. Pergamon, 107, pp. 189–206. doi: 10.1016/J.IJPLAS.2018.04.004.

Maiti, T. and Eisenlohr, P. (2018) 'Fourier-based spectral method solution to finite strain crystal plasticity with free surfaces', *Scripta Materialia*, 145(Supplement C), pp. 37–40. doi: https://doi.org/10.1016/j.scriptamat.2017.09.047.

McKie, D. and McKie, C. (1986) *Essentials of Crystallography*. Blackwell Science Ltd.

Michel, J. C., Moulinec, H. and Suquet, P. (2001) 'A computational scheme for linear and non-linear composites with arbitrary phase contrast', *5th U.S. National Congress on Computational Mechanics, 4-6 Aug. 1999*, 52, pp. 139–160. doi: 10.1002/nme.275.

Mironov, S. *et al.* (2009) 'Microstructure evolution during warm working of Ti–6Al–4V with a colony-α microstructure', *Acta Materialia*. Pergamon, 57(8), pp. 2470–2481. doi: 10.1016/J.ACTAMAT.2009.02.016.

Morii, K. *et al.* (1986) 'Stability of the texture of Ti-6Al-4V during rolling in the two phase field', *Scripta Metallurgica*. Pergamon, 20(12), pp. 1795–1800. doi: 10.1016/0036-9748(86)90291-7.

Motz, C. *et al.* (2008) 'Micro-bending tests: A comparison between three-dimensional discrete dislocation dynamics simulations and experiments', *Acta Materialia*, 56(9), pp. 1942–1955. doi: 10.1016/j.actamat.2007.12.053.

Moulinec, H. and Suquet, P. (1998) ‘A numerical method for computing the overall response of nonlinear composites with complex microstructure’, *Computer Methods in Applied Mechanics and Engineering*, 157(1–2), pp. 69–94. doi: 10.1016/S0045-7825(97)00218-1.

Newkirk, J. B. and Geisler, A. H. (1953) ‘Crystallographic aspects of the beta to alpha transformation in titanium’, *Acta Metallurgica*. Pergamon, 1(3), pp. 370–374. doi: 10.1016/0001-6160(53)90113-8.

Obasi, G. C., Birosca, S., Quinta da Fonseca, J., *et al.* (2012) ‘Effect of β Grain Growth on Variant Selection and Texture Memory Effect during α→β→α-phase Transformation in Ti–6Al–4V’, *Acta Materialia*, 60, pp. 1048–1058. doi: 10.1016/j.actamat.2011.10.038.

Obasi, G. C., Birosca, S., Leo Prakash, D. G., *et al.* (2012a) ‘The influence of rolling temperature on texture evolution and variant selection during α→β→α-phase transformation in Ti–6Al–4V’, *Acta Materialia*, 60(17), pp. 6013–6024. doi: 10.1016/j.actamat.2012.07.025.

Obasi, G. C., Birosca, S., Leo Prakash, D. G., *et al.* (2012b) ‘The influence of rolling temperature on texture evolution and variant selection during α → β → α-phase transformation in Ti-6Al-4V’, *Acta Materialia*. PERGAMON-ELSEVIER SCIENCE LTD, 60(17), pp. 6013–6024. doi: 10.1016/j.actamat.2012.07.025.

Paramatmuni, C. and Kanjarla, A. K. (2019) ‘A crystal plasticity FFT based study of deformation twinning, anisotropy and micromechanics in HCP materials: Application to AZ31 alloy’, *International Journal of Plasticity*. Pergamon, 113, pp. 269–290. doi: 10.1016/J.IJPLAS.2018.10.007.

Pederson, R. *et al.* (2003) ‘Use of high temperature X-ray diffractometry to study phase transitions and thermal expansion properties in Ti-6Al-4V’, *Materials Science and Technology*. Taylor & Francis, 19(11), pp. 1533–1538. doi: 10.1179/026708303225008013.

Peirce, D., Asaro, R. J. and Needleman, A. (1982) ‘An analysis of nonuniform and localized deformation in ductile single crystals’, *Acta Metallurgica*, 30(6), pp. 1087–1119. doi: 10.1016/0001-6160(82)90005-0.

Philippe, M. J. *et al.* (1995) ‘Modelling of texture evolution for materials of hexagonal symmetry—II. application to zirconium and titanium α or near α alloys’, *Acta Metallurgica et Materialia*. Pergamon, 43(4), pp. 1619–1630. doi: 10.1016/0956-7151(94)00329-G.

Philippe, M. J., Esling, C. and Hoicheid, B. (1988) ‘Role of Twinning in Texture Development and in Plastic Deformation of Hexagonal Materials’, *Textures and Microstructures*, 7(4), pp. 265–301.

Pilchak, A. L. *et al.* (2013) ‘Characterization of Microstructure, Texture, and Microtexture in Near-Alpha Titanium Mill Products’, *Metallurgical and Materials Transactions A*, 44(11), pp. 4881–4890. doi: 10.1007/s11661-013-1804-x.

Pilchak, A. L., Sargent, G. A. and Semiatin, S. L. (2018) ‘Early Stages of Microstructure and Texture Evolution during Beta Annealing of Ti-6Al-4V’, *Metallurgical and Materials Transactions A*, 49(3), pp. 908–919. doi: 10.1007/s11661-017-4444-8.

Prakash, A. and Lebensohn, R. A. (2009) ‘Simulation of micromechanical behavior of polycrystals: finite elements versus fast Fourier transforms’, *Modelling and Simulation in Materials Science and Engineering*, 17(6), p. 064010. doi: 10.1088/0965-0393/17/6/064010.

Qiu, Y. (2016) *Efficient Modelling of Deformation using Spectral Methods – Extending to 3D*. Imperial College London.

Quey, R., Dawson, P. R. and Barbe, F. (2011) ‘Large-scale 3D random polycrystals for the finite element method: Generation, meshing and remeshing’, *Computer Methods in Applied Mechanics and Engineering*. North-Holland, 200(17–20), pp. 1729–1745. doi: 10.1016/J.CMA.2011.01.002.

Redenbach, C., Shklyar, I. and Andrä, H. (2012) ‘Laguerre tessellations for elastic stiffness simulations of closed foams with strongly varying cell sizes’, *International Journal of Engineering Science*. Pergamon, 50(1), pp. 70–78. doi: 10.1016/J.IJENGSCI.2011.09.002.

Renversade, L. *et al.* (2016) ‘Comparison between diffraction contrast tomography and high-energy diffraction microscopy on a slightly deformed aluminium alloy’, *IUCrJ*, 3(1), pp. 32–42. doi:

10.1107/S2052252515019995.

Rice, J. R. (1971) ‘Inelastic constitutive relations for solids: An internal-variable theory and its application to metal plasticity’, *Journal of the Mechanics and Physics of Solids*, 19(6), pp. 433–455. doi: 10.1016/0022-5096(71)90010-X.

Romero, J., Preuss, M. and Quinta da Fonseca, J. (2009) ‘Texture memory and variant selection during phase transformation of a zirconium alloy’, *Acta Materialia*. Acta Materialia Inc., 57(18), pp. 5501–5511. doi: 10.1016/j.actamat.2009.07.046.

Roters, F., Eisenlohr, P., Bieler, T. R., *et al.* (2010) *Crystal Plasticity Finite Element Methods*, *Crystal Plasticity Finite Element Methods*. WILEY-VCH Verlag. doi: 10.1002/9783527631483.

Roters, F., Eisenlohr, P., Hantcherli, L., *et al.* (2010) ‘Overview of constitutive laws, kinematics, homogenization and multiscale methods in crystal plasticity finite-element modeling: Theory, experiments, applications’, *Acta Materialia*. Acta Materialia Inc., 58(4), pp. 1152–1211. doi: 10.1016/j.actamat.2009.10.058.

Roters, F. *et al.* (2012) ‘DAMASK: the Düsseldorf Advanced MAterial Simulation Kit for studying crystal plasticity using an FE based or a spectral numerical solver’, *Procedia IUTAM*, 3, pp. 3–10. doi: 10.1016/j.piutam.2012.03.001.

Roters, F. *et al.* (2019) ‘DAMASK – The Düsseldorf Advanced Material Simulation Kit for modeling multi-physics crystal plasticity, thermal, and damage phenomena from the single crystal up to the component scale’, *Computational Materials Science*, 158, pp. 420–478. doi: https://doi.org/10.1016/j.commatsci.2018.04.030.

Roy, S., Madhavan, R. and Suwas, S. (2014) ‘Crystallographic texture and microstructure evolution during hot compression of Ti–6Al–4V–0.1B alloy in the (α + β)-regime’, *Philosophical Magazine*. Taylor & Francis, 94(4), pp. 358–380. doi: 10.1080/14786435.2013.853141.

Roy, S. and Suwas, S. (2017) ‘Orientation dependent spheroidization response and macro-zone formation during sub β-transus processing of Ti-6Al-4V alloy', *Acta Materialia*. Pergamon, 134, pp. 283–301. doi: 10.1016/J.ACTAMAT.2017.04.071.

Rugg, D., Dixon, M. and Dunne, F. P. E. (2007) 'Effective structural unit size in titanium alloys', *The Journal of Strain Analysis for Engineering Design*. IMECHE, 42(4), pp. 269–279. doi: 10.1243/03093247JSA273.

Sachs, G. (1928) 'Plasticity problems in metals', *Trans. Faraday Soc.* The Royal Society of Chemistry, 24(0), pp. 84–92. doi: 10.1039/TF9282400084.

Saylor, D. M. *et al.* (2004) 'Statistically representative three-dimensional microstructures based on orthogonal observation sections', *Metallurgical and Materials Transactions A*, 35(7), pp. 1969–1979. doi: 10.1007/s11661-004-0146-0.

Semiatin, S. L. *et al.* (2003) 'Microstructure evolution during alpha-beta heat treatment of Ti-6Al-4V', *Metallurgical and Materials Transactions A: Physical Metallurgy and Materials Science*, 34 A(10), pp. 2377–2386. doi: 10.1007/s11661-003-0300-0.

Semiatin, S. L. *et al.* (2004) 'Diffusion coefficients for modeling the heat treatment of Ti-6Al-4V', *Metallurgical and Materials Transactions A: Physical Metallurgy and Materials Science*, 35 A(9), pp. 3015–3018. doi: 10.1007/s11661-004-0250-1.

Semiatin, S. L., Seetharaman, V. and Weiss, I. (1997) 'The thermomechanical processing of alpha/beta titanium alloys', *JOM*, 49(6), pp. 33–39. doi: 10.1007/BF02914711.

Simmons, G. and Wang, H. (1971) *Single crystal elastic constants and caluclated aggregate properties*. M.I.T. Press.

Steglich, D. *et al.* (2012) 'Biaxial deformation behaviour of AZ31 magnesium alloy: Crystal-plasticity-based prediction and experimental validation', *International Journal of Solids and Structures*. Pergamon, 49(25), pp. 3551–3561. doi: 10.1016/J.IJSOLSTR.2012.06.017.

Sweeney, C. A. *et al.* (2013) ‘The role of elastic anisotropy, length scale and crystallographic slip in fatigue crack nucleation’, *Journal of the Mechanics and Physics of Solids*, 61. doi: 10.1016/j.jmps.2013.01.001.

Taylor, G. I. (1938) ‘Plastic Strain in Metals’, *Journal of the Institute of Metals*, 62, pp. 307–324.

Timet UK Ltd. (1997) *Timet Ltd. titanium alloys specification*. Available at: http://www.timet.com/assets/local/documents/technicalmanuals/TiAlloys.pdf (Accessed: 19 September 2019).

Timet UK Ltd. (2019) *Timet UK Ltd. Internal report*.

Tomé, C. N. and Christodoulou, N. (2000) ‘Analysis of accelerated irradiation growth in Zr-2.5% Nb pressure tubes’, *Philosophical Magazine A*, 80(6), pp. 1407–1424. doi: 10.1080/01418610008212127.

Tomé, C. N. and Kocks, U. F. (1985) ‘The yield surface of h.c.p. crystals’, *Acta Metallurgica*, 33(4), pp. 603–621. doi: 10.1016/0001-6160(85)90025-2.

Upadhyay, M. V. *et al.* (2016) ‘Study of lattice strain evolution during biaxial deformation of stainless steel using a finite element and fast Fourier transform based multi-scale approach’, *Acta Materialia*, 118, pp. 28–43. doi: 10.1016/j.actamat.2016.07.028.

Voce, E. (1955) ‘A Practial Strain-hardening Function’, *A Practial Strain-hardening Function*, pp. 219–226.

Warwick, J. L. W. *et al.* (2012) ‘Effect of texture on load partitioning in Ti-6Al-4V’, *Acta Materialia*, 60(10), pp. 4117–4127. doi: 10.1016/j.actamat.2012.03.039.

Weiss, I. *et al.* (1986) ‘Modification of alpha morphology in Ti-6Al-4V by thermomechanical processing’, *Metallurgical Transactions A*, 17(11), pp. 1935–1947. doi: 10.1007/BF02644991.

Wielewski, E., Siviour, C. R. and Petrinic, N. (2012) ‘On the correlation between macrozones and twinning in Ti–6Al–4V at very high strain rates', *Scripta Materialia*. Pergamon, 67(3), pp. 229–232. doi: 10.1016/J.SCRIPTAMAT.2012.04.026.

Wilkinson, A. J. and Britton, T. B. (2012) 'Strains, planes, and EBSD in materials science', *Materials Today*. Elsevier, 15(9), pp. 366–376. doi: 10.1016/S1369-7021(12)70163-3.

Williams, J. C., Baggerly, R. G. and Paton, N. E. (2002) 'Deformation behavior of HCP Ti-Al alloy single crystals', *Metallurgical and Materials Transactions A*, 33(13), pp. 837–850. doi: 10.1007/s11661-002-1016-2.

Woan, G. (2000) *The Cambridge Handbook of Physics Formulas*. Cambridge University Press.

Zambaldi, C. *et al.* (2012) 'Orientation informed nanoindentation of α-titanium: Indentation pileup in hexagonal metals deforming by prismatic slip', *Journal of Materials Research*. 2011/12/16. Cambridge University Press, 27(1), pp. 356–367. doi: 10.1557/jmr.2011.334.

Zeghadi, A. *et al.* (2007) 'Ensemble averaging stress–strain fields in polycrystalline aggregates with a constrained surface microstructure – Part 1: anisotropic elastic behaviour', *Philosophical Magazine*. Taylor & Francis, 87(8–9), pp. 1401–1424. doi: 10.1080/14786430601009509.

Zhang, C. *et al.* (2015) 'Effect of realistic 3D microstructure in crystal plasticity finite element analysis of polycrystalline Ti-5Al-2.5Sn', *International Journal of Plasticity*, 69, pp. 21–35. doi: 10.1016/j.ijplas.2015.01.003.

Zhang, K. *et al.* (2015) 'Fatigue crack initiation in as forged Ti–6Al–4V bars with macrozones present', *International Journal of Fatigue*. Elsevier, 80, pp. 288–297. doi: 10.1016/J.IJFATIGUE.2015.05.020.

Zhang, P., Balint, D. and Lin, J. (2011) 'An integrated scheme for crystal plasticity analysis: Virtual grain structure generation', *Computational Materials Science*, 50, pp. 2854–2864. Available at: http://www.sciencedirect.com/science/article/pii/S0927025611002655 (Accessed: 29 March 2017).

Zheng, X. *et al.* (2019) 'Twinning and sequential kinking in lamellar Ti-6Al-4V alloy', *Acta Materialia*.

Pergamon, 181, pp. 479–490. doi: 10.1016/J.ACTAMAT.2019.10.010.

Zheng, Z. (2017) *Internal report*.

Zienkiewicz, O. C. and Cheung, Y. K. (1967) *The Finite Element Method in Structural and Continuum Mechanics*. McGraw-Hill.

Zwicker, U. (1974) *Titan und Titanlegierungen*. Berlin: Springer-Verlag.

Appendix 1 Thickness measurements of rolled Ti-6Al-4V

A1.1 Small-strain rolling procedure

All six samples characterised have been cut from Ti-6Al-4V plate supplied by TIMET, 16 mm in thickness. The rolling bars are cut to 25 mm in width and 50 mm in length by electric discharge machining, and then milled down to 15 mm in thickness.

Thickness reductions of 10%, 20%, and 30% were achieved using a rolling mill with 5” diameter steel rollers.

Temperature (°C)	Total Strain for 10% aim (%)	Total Strain for 20% aim (%)	Total Strain for 30% aim (%)
768 (750)	9.73 ± 0.01	19.93	29.87
904 (900)	10.93	20.67	29.87

A1.1.1 750°C rolling

After the first bar was rolled, the thickness was notably below the target of 10% thickness reduction, at 14.4 mm. In order to achieve the intended thickness reduction, the bar was reheated for a further two minutes and rolled again at the same rolling gap.

	Target				Achieved			
Pass No	Strain per pass (%)	Total Strain (%)	Roll Gap (mm)	Reduction (mm)	Strain per pass (%)	Achieved Total Strain (%)	Achieved (mm)	Reduction (mm)
1	-10	10	13.5	1.5	4.00	4.00	14.40	0.60
2	0	10	13.5	0	5.73	9.73	13.54	0.86

Between the two passes which achieved a 20% reduction, the bar was reheated for two minutes.

	Target				Achieved			
Pass No	Strain per pass (%)	Total Strain (%)	Roll Gap (mm)	Reduction (mm)	Strain per pass (%)	Achieved Total Strain (%)	Achieved (mm)	Reduction (mm)
1	-10	10	13.5	1.5	12.73	12.73	13.09	1.91
2	-11.11	20	12.0	1.5	7.20	19.93	12.01	1.36

Between the three passes which achieved a 30% reduction, the bar was reheated for 2 minutes.

	Target				Achieved			
Pass No	Strain per pass (%)	Total Strain (%)	Roll Gap (mm)	Reduction (mm)	Strain per pass (%)	Achieved Total Strain (%)	Achieved (mm)	Reduction (mm)
1	-10	10	13.5	1.5	9.40	9.40	13.59	1.41
2	-11.11	20	12.0	1.5	11.41	19.73	12.04	1.55
3	-12.5	30	10.5	1.5	12.62	29.87	10.52	1.52

A1.1.2 900°C rolling

10% thickness reduction was achieved in a single pass.

	Target				Achieved			
Pass No	Strain per pass (%)	Total Strain (%)	Roll Gap (mm)	Reduction (mm)	Strain per pass (%)	Achieved Total Strain (%)	Achieved (mm)	Reduction (mm)
1	-10	10	13.5	1.5	10.93	10.93	13.36	1.64

Between the two passes which achieved a 20% reduction, the bar was reheated for 2 minutes.

	Target				Achieved			
Pass No	Strain per pass (%)	Total Strain (%)	Roll Gap (mm)	Reduction (mm)	Strain per pass (%)	Achieved Total Strain (%)	Achieved (mm)	Reduction (mm)
1	-10	10	13.5	1.5	10.67	10.67	13.40	1.60
2	-11.11	20	12.0	1.5	11.19	20.67	11.90	1.50

Between the three passes which achieved a 30% reduction, the bar was reheated for 2 minutes.

	Target				Achieved			
Pass No	Strain per pass (%)	Total Strain (%)	Roll Gap (mm)	Reduction (mm)	Strain per pass (%)	Achieved Total Strain (%)	Achieved (mm)	Reduction (mm)
1	-10	10	13.5	1.5	10.60	10.60	13.41	1.59
2	-11.11	20	12.0	1.5	11.26	20.67	11.90	1.51
3	-12.5	30	10.5	1.5	11.60	29.87	10.52	1.38

A1.2 Large-strain rolling procedure

All five bars were heated for 30 minutes at the stated temperature, then rolled to a total thickness reduction of 75%.

A1.2.1 950 °C rolling

For the 950 °C rolling trial, the furnace interior was measured to be 942 °C prior to rolling. After a sizing pass at a rolling gap of 15 mm, a thickness reduction of 75.08% from a room temperature thickness of 15.01 mm, measured by Vernier callipers was achieved in five reductions of 15% of the original thickness, and one final correction pass, all at a rolling speed of 20 revolutions per minute. For passes 2-5, the bar was reheated in the furnace for two minutes. On the 6th pass, corresponding to a strain of 38%, I decided the sample had been handled out of the furnace for too long, and increased the reheat time to 5 minutes. Despite this, the rolling mill stalled after passing approximately 1/3 of its length through the mill. The bar was extracted by setting the mill to reverse, pushing the bar out of the front end. The bar was reheated for an additional 10 minutes, then attempted to roll the bar for a second time. Again, the mill stalled, this time after passing approximately 2/3s of the bar length through the mill. After another reheat of 10 minutes, the bar was successfully rolled through the mill. Before the correction pass, the bar was reheated for a further 5 minutes.

	Target				Achieved			
Pass No	Strain per pass (%)	Total Strain (%)	Roll Gap (mm)	Reduction (mm)	Strain per pass (%)	Achieved Total Strain (%)	Achieved (mm)	Reduction (mm)
1	0	0.00	15	0	0	0.00	15.01	0
2	-15	15.00	12.75	2.25	9.06	9.06	13.65	1.36
3	-18	30.30	10.46	2.30	20.95	28.11	10.79	2.86
4	-21	44.94	8.26	2.20	18.54	41.44	8.79	2.00
5	-27	59.80	6.03	2.23	23.21	55.03	6.75	2.04
6	-38	75.08	3.74	2.29	38.81	72.49	4.13	2.62
7	-12	78.41	3.24	0.50	7.99	74.68	3.8	0.33

A1.2.2 900 °C rolling

For the 900 °C rolling trial, the furnace interior was measured to be 896 °C prior to rolling. After the 15 mm sizing pass, the thickness of the bar was measured to be 15.66 mm. I attempted the same thickness reductions as with the 950 °C trial, but I increased the speed of the rolling mill to 30 revolutions per minute, since at a temperature further below the beta transus, the bar will be harder to roll, and increasing the speed of the mill will reduce heat losses through die chill. For passes 2-4, the reheat time was 2 minutes. On the 5th pass, the bar was reheated for 5 minutes, but stalled in the mill after passing 3/4s of the way through. After another 5 minutes of reheating, the bar was successfully rolled through the mill. The 6th pass, at 38% strain after a 2 minute reheat, stalled the mill immediately. As further passes were unlikely to succeed, I increased the rolling gap by 0.5 mm, to a strain of 29% for the adjusted pass. After a 5 minute reheat, the mill stalled while rolling. As approximately half the bar had been processed, with some of that passed through on the first failed attempt, I again decided to increase the rolling gap by 0.5 mm. This corresponds to an equivalent strain of 24%, ignoring the deformation already incurred by the bar on the failed passes. After 5 minutes of reheating, the bar was successfully rolled through the mill. With a further 2 minutes of reheating, the bar was rolled down to the target thickness in a correction step.

	Target				Achieved			
Pass No	Strain per pass (%)	Total Strain (%)	Roll Gap (mm)	Reduction (mm)	Strain per pass (%)	Achieved Total Strain (%)	Achieved (mm)	Reduction (mm)
1	0	0.00	15	0	0	0.00	15.66	0
2	-15	15.00	12.75	2.25	12.20	12.20	13.75	1.91
3	-18	30.30	10.46	2.30	19.93	29.69	11.01	2.74
4	-21	44.94	8.26	2.20	17.80	42.21	9.05	1.96
5	-27	59.80	6.03	2.23	29.83	59.45	6.35	2.70
6	-38	75.08	3.74	2.29	37.80	74.78	3.95	2.40
7	-30	71.86	4.22	-0.48	32.13	72.48%	4.31	-0.36
8	-22	68.65	4.70	-0.48	22.99	68.77%	4.89	-0.58
9	-21	75.23	3.72	0.99	24.54	76.44%	3.69	1.20

A1.2.3 850 °C rolling

The temperature of the bar was measured to be 853 °C prior to rolling, with its width measured as 15.00 mm with Vernier callipers. Starting from the rolling schedule that was used for 800 °C, I anticipated that the same rolling gaps would be achievable at the slightly higher temperature. However, while after the sizing pass a reheat of 2 minutes was sufficient to ensure the 2nd pass was successful, the 3rd pass stalled in the mill after a reheat of 2 minutes. I reheated the bar for 5 minutes, after which the bar was accepted through the mill. Passes 4-7 were completed, following a reheat of 2 minutes for each. My measurement of the bar thickness after the 7th pass was slower than previous passes, so I chose to reheat for 3 minutes in total prior to the 8th pass, to ensure that the bar was returned to temperature. Following the 8th pass, the bar was reheated for 2 minutes, but then stalled halfway through the mill. After 5 minutes of reheating, the bar was accepted through the mill to its final thickness. After measuring the thickness with Vernier callipers, I placed the bar on the steel pad of the fly-press to cool in air. Immediately after it had been set down, the temperature of the bar was found to be below 300 °C, indicating that the air cooling of the bar was effective almost immediately.

	Target				Achieved			
Pass No	Strain per pass (%)	Total Strain (%)	Roll Gap (mm)	Reduction (mm)	Strain per pass (%)	Total Strain (%)	Achieved (mm)	Reduction (mm)
1	0	0.00	15	0	0	0.00	15.40	0
2	-15	15.00	12.75	2.25	13.64	15.64	13.30	2.10
3	-18	30.30	10.46	2.30	16.54	27.92	11.10	2.20
4	-17	42.15	8.68	1.78	15.32	38.96	9.40	1.70
5	-15	50.83	7.38	1.30	19.15	50.65	7.60	1.80
6	-15	58.20	6.27	1.11	13.16	57.14	6.60	1.00
7	-15	64.47	5.33	0.94	9.09	61.04	6.00	0.60
8	-15	69.80	4.53	0.80	20.00	68.83	4.80	1.20
9	-15	74.33	3.85	0.68	19.38	74.87	3.87	0.93

A1.2.4 800 °C rolling

As the 800 °C rolling trial could be expected to be harder, I adjusted the rolling profile in advance, so that no rolling pass would require more than 20% strain. The furnace interior was measured to be 796 °C prior to rolling. After a sizing pass, the bar thickness was measured at 15.62 mm. After a 2 minute reheat, the 2nd pass stalled the mill when the bar was almost completely through. After a five minute reheat, the bar was successfully passed through. Measuring the bar took slightly longer than expected, so prior to the 3rd pass, the bar was reheated for 3 minutes. On the 4th pass, at a strain of 17%, the mill stalled while the bar was approximately 2/3s of the way through. In order to reduce die chill, the rolling speed of the mill was increased to 40 revolutions per minute. After a 5 minute reheat, the bar was successfully passed through. The 5th and 6th passes were reheated for 2 minutes. The 7th pass was reheated for 2 minutes, then stalled the mill while almost completely through. After a 5 minute reheat it successfully passed through. Passes 8-10 were each reheated for 2 minutes, with the 10th pass being a repeat of the rolling gap of the 9th, to correct the bar down to the target thickness.

	Target				Achieved			
Pass No	Strain per pass (%)	Total Strain (%)	Roll Gap (mm)	Reduction (mm)	Strain per pass (%)	Total Strain (%)	Achieved (mm)	Reduction (mm)
1	0	0.00	15	0	0	0.00	15.49	0
2	-12	12.00	13.20	1.80	11.04	11.04	13.78	1.71
3	-12	22.56	11.62	1.58	11.10	20.92	12.25	1.53
4	-12	31.85	10.22	1.39	10.53	29.24	10.96	1.29
5	-12	40.03	9.00	1.23	13.87	39.06	9.44	1.52
6	-12	47.23	7.92	1.08	12.50	46.68	8.26	1.18
7	-12	53.56	6.97	0.95	12.11	53.13	7.26	1.00
8	-12	59.13	6.13	0.84	15.15	60.23	6.16	1.10
9	-12	64.04	5.39	0.74	10.88	64.56	5.49	0.67
10	-12	68.35	4.75	0.65	13.30	69.27	4.76	0.73
11	-12	72.15	4.18	0.57	11.97	72.95	4.19	0.57
12	-10	74.93	3.76	0.42	3.82	73.98	4.03	0.16
13	-10	74.93	3.76	0.00	5.46	75.40	3.81	0.00

A1.2.5 750 °C rolling

Given the difficulties encountered with the 800 °C rolling trial, I chose to be cautious with the rolling profile for the 750 °C trial, with no pass attempting a greater strain than 12%. The furnace was measured to be 739 °C. After a sizing pass, the bar was measured to be 15.49 mm in thickness. Between all passes from 2-13, the bar was reheated for 2 minutes, without stalling the mill. The 13th pass was a repeat of the rolling gap of the 12th pass, in order to correct the bar down to the target thickness. As the bar had warped significantly, it was reheated for a further two minutes and straightened using a 5-ton force equivalent fly-press.

	Target				Achieved			
Pass No	Strain per pass (%)	Total Strain (%)	Roll Gap (mm)	Reduction (mm)	Strain per pass (%)	Total Strain (%)	Achieved (mm)	Reduction (mm)
1	0	0.00	15	0	0	0.00	15.62	0
2	-15	15.00	12.75	2.25	14.85	14.85	13.3	2.32
3	-18	30.30	10.46	2.30	17.37	29.64	10.99	2.31
4	-17	42.15	8.68	1.78	12.65	38.54	9.6	1.39
5	-15	50.83	7.38	1.30	16.56	48.72	8.01	1.59
6	-15	58.20	6.27	1.11	16.73	57.30	6.67	1.34
7	-15	64.47	5.33	0.94	10.49	61.78	5.97	0.70
8	-15	69.80	4.53	0.80	17.09	68.31	4.95	1.02
9	-15	74.33	3.85	0.68	5.25	69.97	4.69	0.26
10	0	74.33	3.85	0.00	20.90	76.25	3.71	0.98

Appendix 2 Segmented EBSD maps of Ti-6Al-4V

These segmented figures accompany the results of section 5.3.2. Each of the quadrants correspond to the regions of the EBSD map which exist within 30° of the four fibres.

A2.1 950 °C rolling fibres

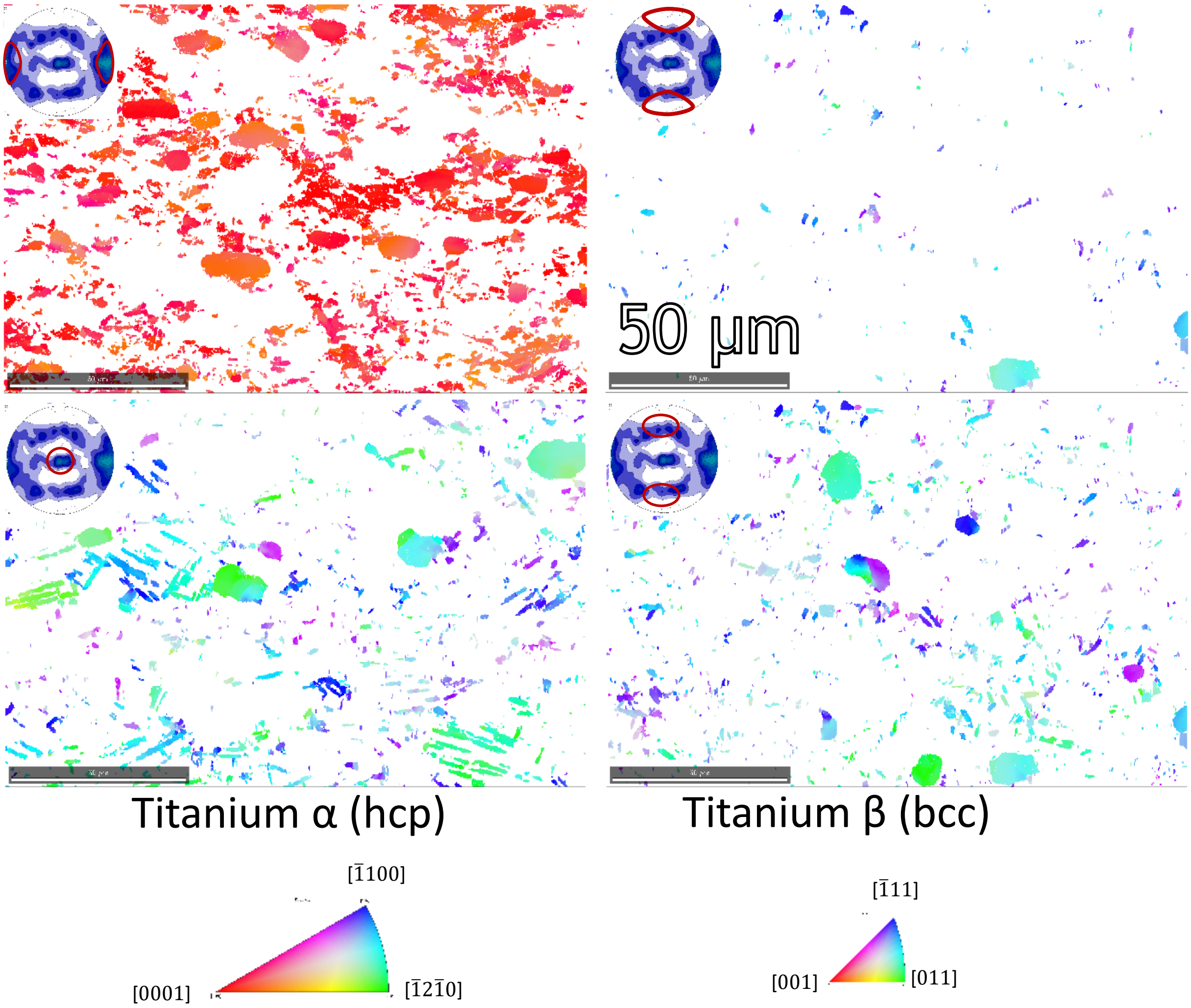

A2.2 900 °C rolling fibres

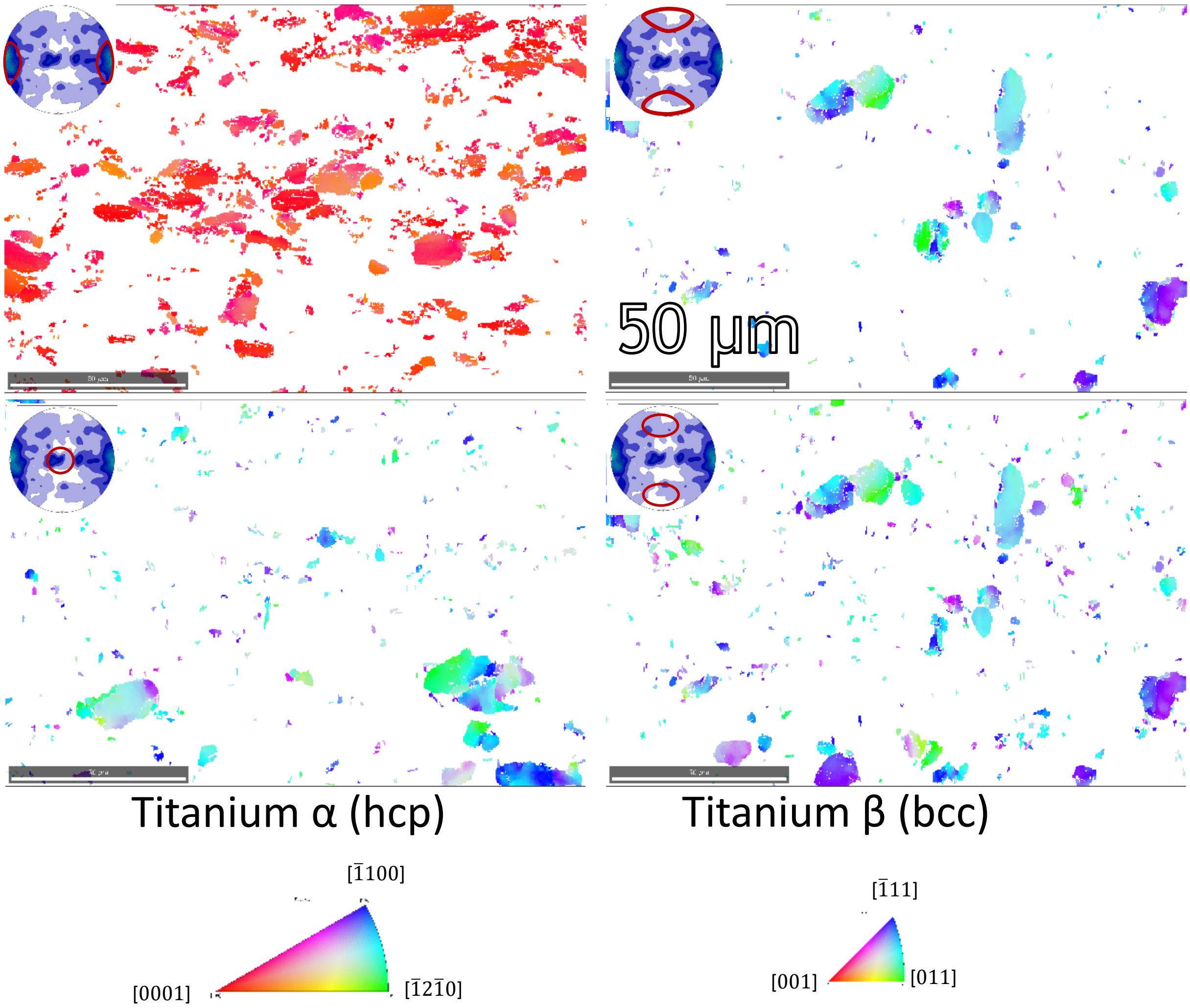

Titanium α (hcp)

Titanium β (bcc)

A2.3 850 °C rolling fibres

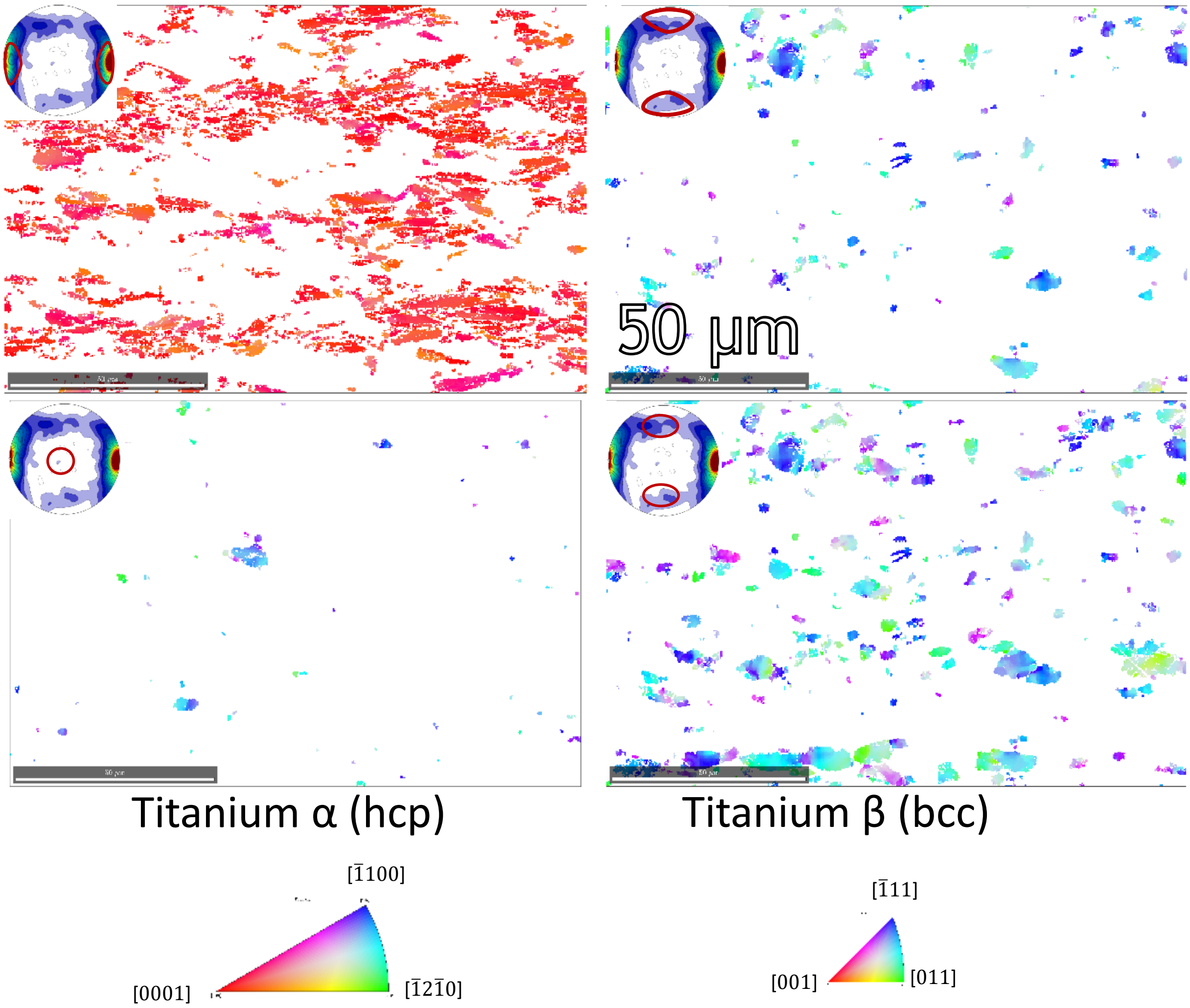

A2.4 800 °C rolling fibres

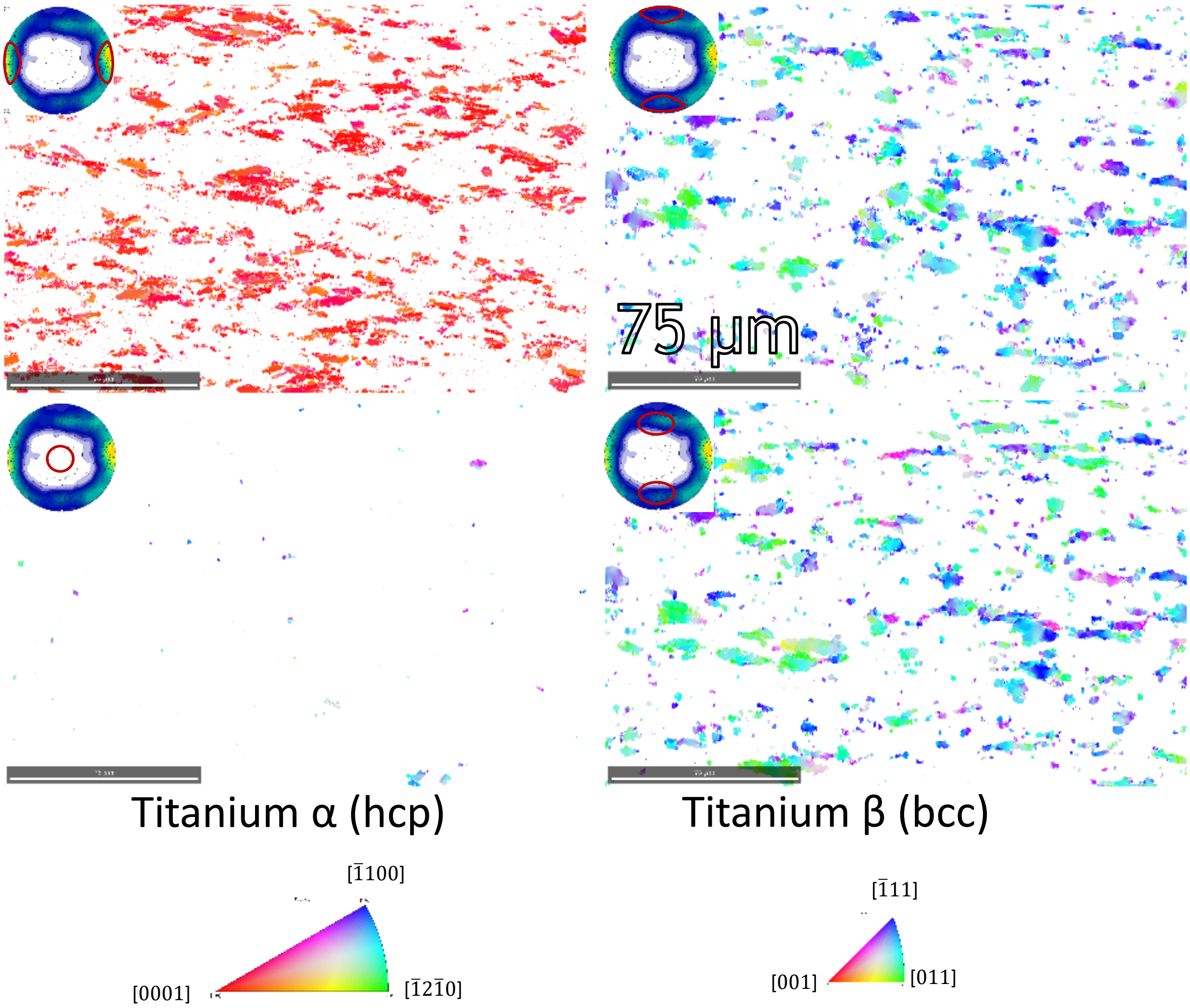

A2.5 750 °C rolling fibres

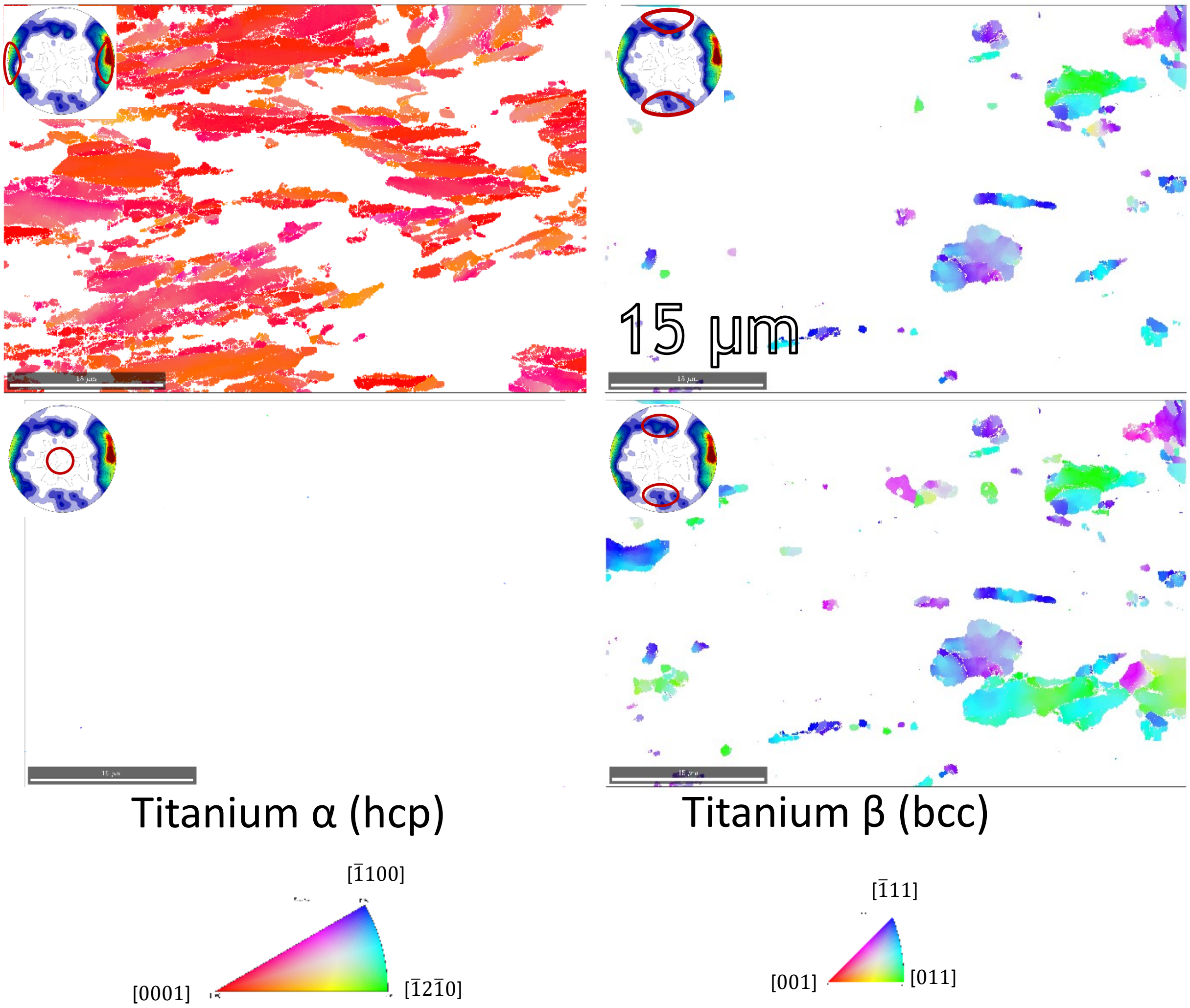

Titanium α (hcp)

Titanium β (bcc)